



**HAL**  
open science

# Qualification of numerical simulations by anisotropic mesh adaptation

Maxime Nguyen-Dinh

► **To cite this version:**

Maxime Nguyen-Dinh. Qualification of numerical simulations by anisotropic mesh adaptation. General Mathematics [math.GM]. Université Nice Sophia Antipolis, 2014. English. NNT : 2014NICE4012 . tel-00987202v2

**HAL Id: tel-00987202**

**<https://theses.hal.science/tel-00987202v2>**

Submitted on 14 May 2014

**HAL** is a multi-disciplinary open access archive for the deposit and dissemination of scientific research documents, whether they are published or not. The documents may come from teaching and research institutions in France or abroad, or from public or private research centers.

L'archive ouverte pluridisciplinaire **HAL**, est destinée au dépôt et à la diffusion de documents scientifiques de niveau recherche, publiés ou non, émanant des établissements d'enseignement et de recherche français ou étrangers, des laboratoires publics ou privés.

# THÈSE

pour obtenir le titre de  
Docteur en Sciences  
de l'UNIVERSITÉ de Nice-Sophia Antipolis  
Spécialité : Mathématiques appliquées

présentée et soutenue par :  
**Maxime NGUYEN-DINH**

## **Qualification des simulations numériques par adaptation anisotropique de maillages**

Thèse dirigée par **Jean-Antoine DÉSIDÉRI** et **Jacques PETER**  
soutenue le 19 mars 2014

JURY :

**M. Christophe CORRE**

Professeur, Université de Grenoble, Président

**M. Jean-Antoine DÉSIDÉRI**

Directeur de recherche, INRIA, Examineur

**M. Richard DWIGHT**

Maître de conférence, Université de Technologie de Delft, Rapporteur

**M. Bruno KOOBUS**

Professeur, Université de Montpellier II, Rapporteur

**M. Matthieu MEAUX**

Ingénieur de recherche, EADS-IW, Invité

**M. Jacques PETER**

Ingénieur de recherche, ONERA, Examineur

**M. Renaud SAUVAGE**

Ingénieur de recherche, Airbus Operations S.A.S, Examineur

**M. Michel VISONNEAU**

Directeur de recherche, CNRS, Rapporteur



## QUALIFICATION DES SIMULATIONS NUMERIQUES PAR ADAPTATION ANISOTROPIQUE DE MAILLAGES

**RESUMÉ :** La simulation numérique est largement utilisée pour évaluer les performances aérodynamiques des avions ainsi qu'en optimisation de forme. Ainsi l'objectif de ces simulations est souvent le calcul de fonctions aérodynamiques (*e.g.* les composantes du coefficient de traînée). L'objet de cette thèse est d'étudier des méthodes d'adaptation de maillages basées sur la dérivée totale de ces fonctions par rapport aux coordonnées du maillage (notée  $dJ/dX$ ). Celle-ci pouvant être calculée par la méthode adjointe discrète.

La première partie de cette étude concerne l'application de méthodes d'adaptation de maillages appliquées à des écoulements de fluides parfaits. Le sensor qui détecte les zones de maillage à raffiner s'appuie sur la norme de la dérivée  $dJ/dX$ . Cette étude a confirmé la pertinence de l'utilisation de cette dérivée pour adapter des maillages pour le calcul d'une fonction  $J$ .

La seconde partie du travail est la construction et l'étude de critères plus fiables basés sur  $dJ/dX$  pour d'une part adapter des maillages et d'autre part estimer si un maillage est bien adapté ou non pour le calcul de la fonction  $J$ . De plus une méthode de remaillage plus efficace basée sur une EDP elliptique est aussi présentée. Cette nouvelle méthode est appliquée pour des écoulements bidimensionnels découlements de fluides parfaits ainsi que pour un écoulement décrit par les équations RANS.

La dernière partie de l'étude est consacrée à l'application de la méthode proposée à des cas tridimensionnels d'écoulements RANS sur des géométries d'intérêt industriel.

**MOTS CLÉS :** Mécanique des fluides - Adaptation de maillages - Méthode adjointe discrète - Écoulement stationnaire compressible - Schéma volumes finis.

---

## QUALIFICATION OF NUMERICAL SIMULATIONS BY ANISOTROPIC MESH ADAPTATION

**ABSTRACT:** Numerical simulation is widely used for the assessment of aircraft aerodynamic performances and shape optimizations. Hence the objective of these simulations is often to compute aerodynamic outputs (*e.g.* the drag coefficient components). The purpose of this thesis is to study mesh adaptation methods based on the total derivative of the outputs with respect to mesh coordinates (denoted  $dJ/dX$ ). This derivative can be computed using the discrete adjoint method.

The first part of this study is about the application of mesh adaptation methods applied for Eulerian flows. The mesh locations to refine are detected using a sensor based on the norm of the derivative  $dJ/dX$ . This study confirmed that this derivative is relevant in order to adapt a mesh for the computation of the output  $J$ .

The second part of this work is the construction and the study of more reliable criteria based on  $dJ/dX$  for both mesh adaptation and the quality assessment of a given mesh for the computation of the output  $J$ . Moreover a more efficient remeshing method based on an elliptic PDE is presented too. This new method is applied for both two-dimensional Eulerian flows and a flow described by the RANS equations.

The last part of the study is devoted to the application of the proposed method to three-dimensional RANS flows on geometries of industrial interest.

**KEY WORDS:** Fluid mechanics - Mesh adaptation - Discrete adjoint method - Steady compressible flow - Finite volume scheme.



# Contents

Nomenclature	1
<i>Introduction</i>	5
Introduction	7
<i>1 Stratégie d'adaptation de maillages pour le calcul de fonctions</i>	9
<b>1 Goal oriented mesh adaptation strategies</b>	<b>13</b>
1.1 Aerodynamic functions estimation using numerical simulations . . . . .	14
1.1.1 The equations of fluid mechanics . . . . .	14
1.1.2 The aerodynamic outputs . . . . .	17
1.1.3 Discretization of the equations of fluid mechanics . . . . .	18
1.2 The discrete adjoint method . . . . .	19
1.2.1 Gradient computation with the discrete adjoint method . . . . .	19
1.2.2 Numerical resolution of the adjoint equation . . . . .	21
1.2.3 The numerical scheme differentiability issue . . . . .	21
1.3 Mesh adaptation strategies for the reduction of the discretization error . .	23
1.3.1 The method of Pierce and Giles . . . . .	23
1.3.2 The method of Venditti and Darmofal . . . . .	24
1.3.3 The method of Dwight . . . . .	26
1.4 Conclusions . . . . .	27
<i>2 Adaptation de maillages basée sur <math>dJ/dX</math></i>	<b>29</b>
<b>2 Mesh adaptation based on the goal derivative w.r.t. mesh coordinates</b>	<b>33</b>
2.1 The total derivative of aerodynamic functions w.r.t. mesh coordinates . . .	33
2.2 The proposed methodology applied to Eulerian flows . . . . .	36
2.3 The complete approach . . . . .	70
2.3.1 Mesh adaptation without parametrization . . . . .	70
2.3.2 Influence of the smoothing operator . . . . .	72
2.4 Conclusions . . . . .	73
<i>3 Qualification de maillages et adaptations locales</i>	<b>75</b>
<b>3 Mesh qualification and local adaptations</b>	<b>79</b>
3.1 Mesh qualification and local adaptations applied for Eulerian flows . . . . .	79
3.2 Enhancement of the elliptic remeshing method . . . . .	121
3.2.1 The issue of mesh anisotropy . . . . .	121
3.2.2 Treatment of the mesh close to solid walls . . . . .	122

3.2.3	The mesh folding issue . . . . .	122
3.2.4	Construction of the control functions for mesh adaptation . . . . .	125
3.3	Local adaptations for RANS flows . . . . .	125
3.3.1	RAE2822 test case . . . . .	125
3.3.2	Mesh adaptations . . . . .	127
3.3.3	The remeshing method influence . . . . .	134
3.4	Conclusions . . . . .	134
<b>4</b>	<b><i>Application à des cas industriels tridimensionnels</i></b>	<b>137</b>
<b>4</b>	<b>Application to three-dimensional industrial cases</b>	<b>141</b>
4.1	General presentation of the XRF-1 test case . . . . .	141
4.1.1	The XRF-1 configuration and the mesh hierarchy . . . . .	141
4.1.2	Introduction of a computable spatial mean for 3D applications . . . . .	144
4.1.3	Flow conditions and outputs . . . . .	144
4.2	Numerical results on the XRF-1 mesh hierarchy . . . . .	144
4.2.1	Numerical scheme and aerodynamic flow-field . . . . .	144
4.2.2	Reference values for the outputs . . . . .	146
4.2.3	Criteria $\theta$ and $\tilde{\theta}$ on the mesh hierarchy . . . . .	147
4.3	Mesh adaptations on the XRF-1 configuration . . . . .	149
4.3.1	Adaptation process . . . . .	149
4.3.2	Adaptation for the pressure drag coefficient . . . . .	149
4.3.3	Adaptation for the pressure lift coefficient . . . . .	152
4.3.4	Conclusions . . . . .	154
4.4	Application to the Generic Modern Aircraft configuration . . . . .	155
4.4.1	General presentation of the test case . . . . .	155
4.4.2	Visualization of mesh sensitivities . . . . .	156
4.4.3	Conclusions . . . . .	160
4.5	Conclusions . . . . .	160
	<b><i>Conclusions</i></b>	<b>163</b>
	<b>Conclusions</b>	<b>165</b>
	<b>Appendices</b>	<b>167</b>
<b>A</b>	<b>The anisotropic smoothing method</b>	<b>167</b>
A.1	Isotropic smoothing operator . . . . .	167
A.2	Anisotropic smoothing operator . . . . .	168
A.3	Impact of the smoothing on the remeshing . . . . .	169
<b>B</b>	<b>Comparison with feature-based mesh adaptation</b>	<b>171</b>
B.1	Construction of a feature-based sensor . . . . .	171
B.2	Feature-based mesh adaptation . . . . .	173
	<b>Bibliography</b>	<b>175</b>

# Nomenclature

## Notations relative to the fluid mechanics

$AoA$	Angle of attack
$c$	Chord of airfoil
$Cd$	Drag coefficient
$C_p, C_v$	Specific heat constant under constant pressure and under constant volume
$CD_p, CD_f, CD_w$	Pressure drag coefficient, friction drag coefficient and wave drag
$CD_v, CD_{vp}$	Viscous drag coefficient and viscous pressure drag coefficient
$CD_{sp}$	Spurious drag coefficient
$CD_{sp,irr}, CD_{sp,rev}$	Irreversible and reversible spurious drag coefficients
$D_p, D_f$	Pressure drag and friction drag
$\vec{e}_\infty$	Unit vector tangential to the upstream velocity
$E$	Total energy
$\mathcal{F}$	Euler inviscid flux density
$\bar{\mathcal{F}}$	Euler flux in the direction $n = (n_x, n_y, n_z)$
$\mathcal{F}^\nu$	Viscous flux density
$k_t$	Turbulent kinematic energy
$K_T$	Thermal conductivity coefficient
$L_p$	Contribution of pressure forces to the lift
$M, M_\infty$	Mach number and Mach number of far-field flow
$n$	Normal vector to solid wall, support of $J$ or outer boundary
$p$	Static pressure
$P_a$	Mean stagnation pressure over airfoil or wing contour
$Pr, Pr_t$	Prandtl number and turbulent Prandtl number
$p_a, p_{a\infty}$	Stagnation pressure and stagnation pressure of far-field flow
$p, p_\infty$	Static pressure and static pressure of far-field flow
$\bar{q}, \bar{q}_t$	Heat flux and turbulent heat flux
$S_{ref}$	Reference surface for the computation of drag and lift coefficients
$T, T_\infty$	Temperature and reference temperature
$T$	Characteristic time scale for time-averaging of the RANS equations
$\bar{V} = (V_x, V_y, V_z)$	Velocity vector
$V_\infty$	Velocity of far-field flow
$w$	State variable of direct model problem (continuous flow-field)
$\gamma$	Specific heat ratio
$\rho, \rho_\infty$	Density and density of far-field flow
$\mu, \mu_\infty$	Dynamic viscosity and dynamic viscosity at the reference temperature $T_\infty$
$\bar{\tau}, \bar{\tau}_R$	Viscous shear stress tensor and Reynolds tensor

**Notations relative to the discrete equations of the fluid mechanics**

$A$	Roe's matrix
$F, F^2, F^4$	Finite-volume flux, two-point flux formula and four-point flux formula
$F^R, F^J$	Roe and Jameson's flux formula, components $F^{R,k}$ and $F^{J,k}$ ( $k \in \{1, 4\}$ )
$F^{J,AD}$	Artificial dissipation term of the Jameson scheme
$k^2, k^4$	Artificial dissipation coefficients of Jameson <i>et. al.</i> scheme
$N_W$	Size of vectors $W$ and $R$
$\mathbf{r}$	Reference variable of the Taylor expansion surrounding one node
$R$	Numerical scheme (finite-volume flux balance)
$S = (S^X, S^Z)$	Surface vectors
$W$	Discrete conservative variables
$W_l, W_r$	Left state and right states
$W^{Roe}$	Roe's mean state
$W_b$	Conservative variables extrapolated on the wall
$\phi^{VA}$	Van Albada limiting function

**Notations relative to the discrete adjoint equations**

$J(J_m)$	Aerodynamic function as function of flow field $W$ (and $W_b$ ) and volume mesh $X$
$J(J_m)$	Aerodynamic function as function of volume mesh $X$
$\mathcal{J}(\mathcal{J}_m)$	Aerodynamic function as function of a vector of design parameters $\alpha$
$\mathcal{P}(dJ/dX)$	Projection of $dJ/dX$ cancelling components orthogonal to function support and solid walls
$\overline{\mathcal{P}(dJ/dX)}$	Spatial mean of $\mathcal{P}(dJ/dX)$
$N_\alpha$	Number of design parameters
$N_J$	Number of functions to be differentiated
$\lambda$	Adjoint variable of model problem (continuous adjoint function)
$\Lambda(\Lambda_m)$	Adjoint vector of $J$ ( $J_m$ ) for scheme $R$ , component $\Lambda^k$ ( $\Lambda_m$ ) ( $k \in \{1, 4\}$ )

**Notations relative to the meshes or the remeshing methods**

$B_{q,l}$	$(q+1)^{th}$ Bernstein polynomial of degree $l$
$\mathcal{B}$	Linear interpolation operator in the reference fine mesh
$c_i$	Mesh refinement criterion for mesh lines $i$ (resp. of planes $i$ )
$\bar{c}_{i+1/2}$	Mesh refinement criterion for rows of cells $i$
$C$	Computational space $C = [0, 1]^2$ (resp. $C = [0, 1]^3$ ) in 2D (resp. 3D)
$D$	Physical space $D \subset \mathbb{R}^2$ (resp. $D \subset \mathbb{R}^3$ ) in 2D (resp. 3D)
$g_i, g^i$	Covariant and contravariant base vectors
$g_{ij}, g^{ij}$	Covariant and contravariant metric tensors
$H, h$	Characteristic mesh size of coarse ( $H$ ) and fine ( $h$ ) grid
$i, j, (, k)$	Mesh indices of a 2D (resp. 3D) mesh
$\bar{i}, \bar{j}, (\bar{, } \bar{k})$	Reduced mesh indices in $[0, 1]^2$ (resp. $[0, 1]^3$ )
$L$	Characteristic size of a mesh deformation
$N_i, N_j, (, N_k)$	Number of mesh lines (resp. planes) of the structured mesh in each direction

## NOMENCLATURE

$P$	Parametric space $P = [0, 1]^2$ (resp. $P = [0, 1]^3$ ) in 2D (resp. 3D)
$P_k, \tilde{P}_{ij}^k$	Control functions associated to the $k^{th}$ topological direction only and to the $k^{th}$ topological direction and node $(i, j)$
$Q$	Maximum number of mesh lines (resp. planes) to be added between two lines (resp. planes) of current mesh
$S$	Solid body surface mesh
$\mathcal{S}$	Smoothing matrix for implicit smoothing of cell width
$X$	Volume mesh
$\alpha$	Vector of design parameters
$\beta$	Vector of parameters of mapping $\Phi$
$\alpha, \beta, \delta, \phi$	Parameters of the mesh families
$\epsilon$	Width of cell a cell row (in parameter space)
$\Gamma$	Airfoil contour (length $L(\Gamma)$ )
$\Phi, \tilde{\Phi}$	Mapping functions
$\chi_{N_i, N_j, (N_k)}$	Linear function mapping $[0, 1]^2$ (resp. $[0, 1]^3$ ) in $[1, N_i] \times [1, N_j]$ (resp. $[1, N_i] \times [1, N_j] \times [1, N_k]$ )

### Notations relative to the criteria and sensors

$\mathcal{D}_{(X_{ij}, L)}$	Disk of radius $L$ centered in $X_{ij}$
$ds_{ij}$	Surface element attachable to the point $X_{ij}$
$dX, dXC$	Admissible mesh variations and regular function such that $dX_{ij} = dXC(X_{ij}) \forall i, j \in \{1, N_i\} \{1, N_j\}$
$r$	Half the radius of the circle (resp. sphere) inscribed in the cells surrounding one node
$\gamma_{ijL}$	Discrete estimation of the part of the disk centered in the node $X_{ij}$ that is included in the fluid domain
$\mu_J$	Mean of $\ \mathcal{P}(dJ/dX)\ $ field
$\theta_J$	Bound of first order variation of $J$ for a specific displacement of nodes (criterion based on $\mathcal{P}(dJ/dX)$ )
$\bar{\theta}_J$	Criterion based on the spatial mean $\overline{\mathcal{P}(dJ/dX)}$
$\tilde{\theta}$	Criterion based on a spatial mean of $\mathcal{P}(dJ/dX)$ by topological directions
$\Omega$	Fixed surface inside the fluid domain (boundary $\partial\Omega$ )
$\Psi_L$	Radial function of support $\mathcal{D}_{(0, L)}$



# Introduction

L'évaluation des performances aérodynamiques des avions a une importance capitale en ingénierie aéronautique. La consommation en carburant est directement liée au coefficient de traînée qui est donc un important paramètre commercial. En effet un écart de 1% sur la traînée totale d'un avion long courrier équivaut, sur une distance parcourue de 10000 km, à une quantité de kérozène consommée de 800 kg, ce qui correspond à cinq passagers en moins et un manque à gagner de 2% pour les compagnies aériennes [3]. Ainsi les évaluations de ces fonctions aérodynamiques doivent être suffisamment précises. De nos jours les essais en soufflerie restent la référence. Cependant un très grand nombre d'estimations de ces fonctions est effectué dans la pratique. Ceci comprenant à la fois l'évaluation des performances aérodynamiques (environ un millier de calculs pour une configuration figée) et aussi pour les optimisations de forme. En conséquence, la simulation numérique est largement utilisée.

Dans ce contexte, la question de la précision de ces simulations pour le calcul de fonctions aérodynamiques a une grande importance. Les erreurs ont différentes origines. La première est l'erreur de modélisation qui est la différence entre le champ aérodynamique réel et la solution exacte des équations qui décrivent la physique. La seconde est l'erreur de discrétisation qui est la différence entre la solution exacte du modèle mathématique et la solution des équations discrètes. Et enfin la dernière source d'erreur est l'erreur de convergence liée à la précision machine dans la mesure où les calculs sont effectués informatiquement. L'erreur de discrétisation a elle-même deux origines. La première dépend de la précision du schéma numérique et la seconde dépend de la discrétisation du domaine de calcul avec un maillage. Ainsi l'une des approches possibles pour réduire l'erreur commise par les simulations numériques est d'effectuer des adaptations de maillage. Ces méthodes d'adaptation, destinées à améliorer les estimations de fonctions d'intérêt, sont généralement qualifiées de "goal oriented".

Plusieurs stratégies sont d'ores et déjà présentes dans la littérature. Les méthodes dites de h-raffinement consistent à ajouter de nouveaux nœuds dans les régions d'intérêt et éventuellement d'en supprimer dans d'autres régions. Les méthodes dites de r-raffinement consistent à déplacer les nœuds du maillage existant dans les régions d'intérêt afin d'y augmenter la densité de nœuds. Ces deux approches nécessitent de détecter les zones du maillage dans lesquelles il est nécessaire d'augmenter la densité de nœuds afin d'améliorer la précision de la solution. Les méthodes "goal oriented" sont développées depuis les années 1990 et la détection des zones du maillage à raffiner se fait souvent à l'aide d'estimations d'erreur *a posteriori*. Dans le cadre des éléments finis, nous pouvons citer les travaux de Johnson *et al.* [25, 6, 7], Giles *et al.* [18], Prudhomme et Oden [55], Larson et Barth [31], Machiels *et al.* [36], Hartmann *et al.* [21, 33, 20], Alauzet, Dervieux *et al.* [35] et Fidkowski et Roe [16]. Dans le cadre des volumes finis et des différences finis les contributions importantes sont celles de Pierce et Giles [53, 54], Venditti et Darmofal

[73, 74, 75] et Dwight [13, 14].

D'autre part, en 2005 Nielsen et Park ont introduit la dérivée totale de fonctions aérodynamiques par rapport aux coordonnées du maillage [43]. Leur objectif était d'éviter le coûteux stockage en mémoire des sensibilités de maillage par rapport aux paramètres de forme. Ce stockage complet est impossible pour la plupart des optimisations de forme dans l'industrie étant donné le grand nombre de paramètres considérés. La dérivée totale qu'ils ont introduite (notée  $dJ/dX$ ) est un lien entre la fonction aérodynamique et le maillage qui est utilisé pour la simulation numérique. Ainsi cette quantité semble fournir des informations pertinentes pour mettre en œuvre des méthodes d'adaptation de maillage "goal oriented".

Dans ce contexte, l'objet de cette thèse est d'utiliser cette dérivée  $dJ/dX$  pour construire des méthodes d'adaptation de maillage et également de développer des critères de qualité de maillage pour le calcul de fonctions. Autrement dit, le premier aspect des travaux présentés dans cette thèse est de définir un senseur basé sur  $dJ/dX$  qui est destiné à mettre en évidence les zones du maillage qui sont sensibles pour le calcul de la fonction  $J$  et ainsi d'adapter le maillage en conséquence. Le second aspect est de définir des critères scalaires basés sur  $dJ/dX$  qui ont pour but d'estimer si un maillage est bien adapté ou non pour le calcul de la fonction  $J$ .

Dans la pratique tous les cas tests considérés dans cette étude sont des écoulements externes et les fonctions d'intérêt sont des intégrales sur les contours des objets solides. Tous les maillages utilisés sont structurés et le solveur utilisé pour le calcul direct ainsi que pour le calcul adjoint est le logiciel *elsA* [10] qui est un code de volumes finis "cell centered" développé à l'ONERA depuis 1997.

Le plan de la thèse est le suivant. Le contexte général de l'étude est présenté dans le premier chapitre. En particulier ce chapitre inclut la présentation des équations de la méthode adjointe (utilisée pour le calcul de la dérivée  $dJ/dX$ ) ainsi qu'une revue de la bibliographie traitant des méthodes déjà existantes. Le second chapitre est une présentation de la première utilisation de  $dJ/dX$  dans le cadre de l'adaptation de maillage "goal oriented". Cette étude ayant conduit à la publication d'un article [49], ce dernier est le corps du chapitre. L'objectif principal de cette étude était d'évaluer la pertinence de l'utilisation de  $dJ/dX$  en adaptation de maillage dans le cas d'écoulements décrits par les équations d'Euler. Des écoulements bidimensionnels et tridimensionnels ont été considérés. La question du développement de critères scalaires de qualité de maillage est traitée dans le chapitre 3. Ce chapitre présente également une introduction à une méthode de remaillage plus efficace. Cette méthode est basée sur un système d'équations aux dérivées partielles elliptiques. Cette approche a l'avantage de permettre plus d'adaptations locales par rapport à la méthode utilisée dans le chapitre 2. Cette méthode a été appliquée pour des cas bidimensionnels d'écoulements décrits par les équations d'Euler ainsi que les équations RANS. Enfin le dernier chapitre présente une application de la méthode proposée pour des cas tests tridimensionnels industriels. Le cas test retenu pour l'adaptation de maillage a été la configuration XRF-1. Une étude du critère proposé a également été effectuée sur un maillage autour de la configuration "Generic Modern Aircraft" pour évaluer la pertinence du senseur proposé sur une configuration complexe. Cette étude est présentée dans le dernier chapitre.

# Introduction

The assessment of aircraft aerodynamic performances is of major interest in aeronautical engineering. As an example, the fuel consumption is directly connected to the drag coefficient which is hence a major commercial parameter. Indeed an error of 1% on the total drag of a long range aircraft corresponds to a kerosene consumption of  $800kg$  on a distance of  $10000 km$  which is the equivalent of five passengers and represents a loss of income of 2% for the airlines [3]. Therefore the evaluations of these aerodynamic outputs have to be accurate enough. Nowadays the wind tunnel tests are the reference. However a very large number of output estimations has to be done. This includes the assessment of the aerodynamic performances (roughly a thousand calculations for a fixed configuration) and also the application of shape optimizations. Therefore the use of numerical simulations appears to be useful.

In this context the issue of the accuracy of these simulations for the computation of aerodynamic outputs is of major interest. In actual facts the error has several origins. The first one is the modeling error that is the difference between a real flow and the exact solution of the equations that describes the physic. The second one is the discretization error that is the difference between the exact solution of the mathematical model and the discretized equations. And finally the convergence error that is connected to the machine precision level. The discretization error has itself two origins. The first one depends on the accuracy of the numerical scheme and the second one depends on the discretization of the computational domain on a mesh. Hence it appears that a way to reduce the error of the numerical simulations is to carry out mesh adaptations. The corresponding methods that aim to improve the estimations of functional outputs are the so-called “goal oriented” mesh adaptations methods.

Several strategies already exist in the literature. The h-refinement methods consist in the addition of new mesh nodes in regions of interest and possibly the suppression of nodes in other regions. And the r-refinement methods that consist in the displacement of the mesh nodes in order to get a higher node density in the regions of interest. Both approaches require to detect the mesh locations where the node density has to be increased in order to improve the solution accuracy. The goal oriented mesh adaptation has been developed since the 1990s and the detection of the mesh locations to refine were often based on *a posteriori* error estimations. In the framework of finite elements we can cite the work of Johnson and co-workers [25, 6, 7], Giles and co-workers [18], Prudhomme and Oden [55], Larson and Barth [31], Machiels *et. al.* [36], Hartmann and co-workers [21, 33, 20], Alauzet, Dervieux and co-workers [35] and Fidkowski and Roe [16]. In the framework of finite-volume and finite-difference methods the major contributions are the ones of Pierce and Giles [53, 54], Venditti and Darmofal [73, 74, 75] and Dwight [13, 14].

Moreover in 2005, Nielsen and Park introduced the total derivative of aerodynamic outputs with respect to the volume mesh coordinates [43]. The objective was to avoid the

expensive storage of the volume mesh sensitivities with respect to the design parameters. This storage being almost impossible for industrial shape optimizations according to the large number of parameters that are used. The total derivative that they introduced (denoted by  $dJ/dX$ ) is a connection between the aerodynamic function of interest that is computed and the mesh that is used for the numerical simulation. Hence this quantity seems to provide a relevant information for goal oriented mesh adaptations.

Following that remark, the purpose of this thesis is to use the total derivative  $dJ/dX$  to build up goal oriented mesh adaptation methods and to develop mesh quality criteria. In other words the first aspect of the following works is to define local sensors based on  $dJ/dX$  that aim to show up the sensitive mesh locations for the computation of the output  $J$  and then to adapt the mesh accordingly. The second aspect is to define scalar criteria, also based on  $dJ/dX$ , that aim to estimate if a mesh is adapted or not for the computation of the functional output.

In practice all the considered test cases in this thesis are external flows and the functional outputs are surface integrals over the walls. All the considered meshes are structured and the solver used for both the direct and adjoint problems is the CFD software *elsA* [10] that is a finite volume cell-centered code developed at ONERA since 1997.

The present thesis is organized as follow. The general context of the work is presented in the first chapter. In particular that includes the presentations of the adjoint equations (used for the computation of the derivative  $dJ/dX$ ) and a review of the most relevant existing methods in the literature. The second chapter is devoted to the presentation of the first use of  $dJ/dX$  for goal oriented mesh adaptation. This work lead to an article [49] that is the body of this chapter. The main objective of this study was to evaluate the relevance of the use of  $dJ/dX$  for mesh adaptation in the case of flows described by the Euler equations. Both two-dimensional and three-dimensional cases were considered. The issue of the construction of scalar criteria of mesh quality is treated in the chapter 3. This chapter also includes the introduction of a more efficient remeshing method based on an elliptic system of PDEs. This method has the advantage to allow more local remeshing in comparison to the one used in the previous applications. The method was assessed in the case of two-dimensional Euler and RANS flows. Finally the last step was to apply the proposed method for three-dimensional industrial cases. This is the topic of the last chapter. The proposed mesh adaptation method has been applied for a flow around the XRF-1 configuration. Moreover a study of the proposed local criterion has been carried out on a mesh around the Generic Modern Aircraft configuration in order to evaluate the proposed sensor on a complex configuration. This study is presented in the last chapter.

# Chapitre 1

## Stratégie d'adaptation de maillages pour le calcul de fonctions

### Résumé :

L'évaluation de fonctions aérodynamiques telles que les composantes du coefficient de traînée, la portance ou les moments a un intérêt majeur en ingénierie aéronautique. En effet, dans la mesure où la consommation en carburant des avions est directement liée à son coefficient de traînée, sa réduction à l'aide d'optimisations de forme a une importance cruciale. D'autre part, ces fonctions d'intérêt doivent également être estimées en chaque point du domaine de vol (de l'ordre du millier pour une configuration figée). Dans ce contexte même si les essais en soufflerie restent la référence, le grand nombre d'estimations à effectuer conduit à utiliser largement la simulation numérique.

Ainsi la précision de ces simulations a une importance particulière. L'erreur commise a différentes origines : l'erreur de modélisation qui est la différence entre un écoulement réel et la solution exacte des équations qui décrivent la physique (*e.g.* les équations RANS) ; l'erreur de discrétisation qui est la différence entre la solution exacte du modèle mathématique et la solution des équations discrétisées ; l'erreur de convergence provenant de la précision machine.

L'erreur de discrétisation est liée à la précision du schéma numérique mais aussi à la discrétisation du domaine de calcul en un maillage. Ainsi l'une des approches possibles pour réduire cette source d'erreur est de développer des méthodes d'adaptation de maillages pour le calcul de fonctions. Dans ce contexte de nombreuses méthodes s'appuient sur les vecteurs adjoints des fonctions d'intérêt. Les méthodes développées dans ces travaux se basent également sur ces vecteurs.

La section 1 présente les équations de la méthode adjointe discrète pour le calcul de gradient des fonctions d'intérêt par rapport à des paramètres de forme (appelé plus succinctement "calcul de gradient" dans la suite). Ces équations étant à la base des méthodes développées par la suite. La section 2 est une succincte présentation des principales méthodes présentes dans la littérature.

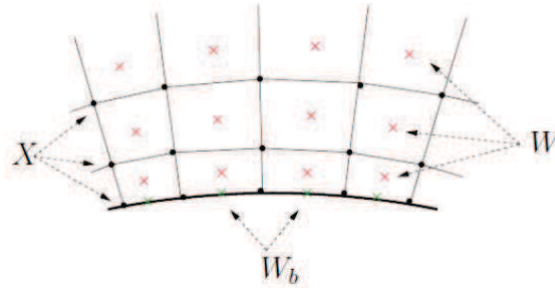
## 1. Calcul de gradient par méthode adjointe

Les équations discrétisées de la mécanique des fluides sont notées  $R$ . Il s'agit d'un vecteur de dimension  $N_W$  (nombre de cellules du maillage) correspondant au bilan de flux en chaque cellule. Dans les études qui suivent deux schémas ont été considérés, le schéma décentré de Roe [58] ainsi que le schéma centré de Jameson *et. al.* [24]. Le solveur utilisé est le code volumes finis *elsA* développé à l'ONERA [10].

Le champ aérodynamique discrétisé est noté  $W$  et le maillage volumique est noté  $X$ . A l'état stationnaire ces champs sont liés par la relation :

$$R(W, X) = 0$$

D'autre part le champ aérodynamique peut être extrapolé aux parois des objets solides (comme illustré sur la figure suivante), ce champ est noté  $W_b$ .



La fonction d'intérêt (*e.g.* coefficient de traînée, portance,...) dépend de  $W$ ,  $W_b$  et  $X$  et est notée  $J$ . D'autre part supposons que la forme de l'objet solide est paramétrée par un vecteur  $\alpha$  (de taille  $N_\alpha$ ) et que  $X$  est une fonction  $C^1$  de  $\alpha$ . Ainsi, si  $\det(\partial R / \partial W)(W, X(\alpha)) \neq 0$  pour tout  $\alpha$  alors le théorème des fonctions implicites permet de considérer  $W$  comme une fonction  $C^1$  du maillage  $X$ . La fonction d'intérêt dépendant de  $\alpha$  est notée  $\mathcal{J}$  et vérifie :

$$\mathcal{J}(\alpha) = J(W(\alpha), W_b(W(\alpha), X(\alpha)), X(\alpha))$$

La différentiation des ces équations conduit aux relations :

$$\begin{aligned} \frac{d\mathcal{J}}{d\alpha} &= \frac{\partial J}{\partial X} \frac{dX}{d\alpha} + \frac{\partial J}{\partial W_b} \frac{dW_b}{dX} \frac{dX}{d\alpha} + \Lambda^T \frac{\partial R}{\partial X} \frac{dX}{d\alpha} \\ \left( \frac{\partial R}{\partial W} \right)^T \Lambda &= - \left( \frac{\partial J}{\partial W} + \frac{\partial J}{\partial W_b} \frac{dW_b}{dW} \right)^T \end{aligned}$$

où  $\Lambda$  est le vecteur adjoint de  $J$  pour la discrétisation  $R$ .

Cette méthode de calcul de gradient a l'avantage de ne nécessiter la résolution du problème adjoint que pour chaque fonction indépendamment du nombre de paramètres de forme  $N_\alpha$ . Dans la pratique de l'optimisation aérodynamique le nombre de fonctions est bien inférieur au nombre de paramètres de forme. Ainsi, la méthode adjointe s'avère être plus avantageuse que les méthodes dont la complexité est en  $N_\alpha$  (méthode linéarisée, méthode des différences finies).

D'autre part, il est important de noter que l'hypothèse de régularité de  $R$  (fonction de classe  $C^1$ ) ne peut être omise. Or les schémas de type volumes finis comportent souvent des termes non différentiables comme des valeurs absolues ou des fonctions *max*. C'est

## 1. STRATÉGIES D'ADAPTATION DE MAILLAGES POUR LE CALCUL DE FONCTIONS

notamment le cas du schéma de Jameson. Il a ainsi été mis en évidence que des cas d'écoulements symétriques peuvent conduire à des solutions non symétriques. Il s'avère donc judicieux de modifier localement le schéma au voisinage des points auxquels  $R$  n'est pas différentiable pour s'assurer de la régularité  $C^1$ .

## 2. Méthodes d'adaptation de maillages pour le calcul de fonctions

La méthode adjointe décrite précédemment pour le calcul de gradient est aussi utilisée en adaptation de maillage pour le calcul de fonction dans la mesure où le vecteur adjoint permet également de relier l'erreur locale du problème direct à l'erreur globale sur l'estimation de la fonction. En effet la formule suivante peut être démontrée [73, 74, 75] :

$$J_h(W_h, X_h) = J_h(W_h^H, X_h) + (\Lambda_h \Big|_{W_h^H})^T R_h(W_h^H, X_h) + \mathcal{O}(\|W_h - W_h^H\|^2)$$

où  $X_h$  et  $W_h$  sont respectivement un maillage fin et le champ aérodynamique correspondant ( $R_h(W_h, X_h) = 0$ ). Le champ  $W_h^H$  est une reconstruction du champ aérodynamique sur le maillage fin à partir de calculs issus d'un maillage plus grossier.

Le résidu  $R_h(W_h^H, X_h)$  est lié à l'erreur commise sur le problème direct :

$$R_h(W_h^H, X_h) \simeq R_h(W_h, X_h) + \frac{\partial R_h}{\partial W} \Big|_{W_h} (W_h^H - W_h)$$

$$\|R_h(W_h^H, X_h)\| \leq \left\| \frac{\partial R}{\partial W} \Big|_{W_h} \right\| \|W_h^H - W_h\|$$

Or le terme  $(\Lambda_h \Big|_{W_h^H})^T R_h(W_h^H, X_h)$  du développement de  $J_h$  correspond à l'erreur au premier ordre entre la valeur de  $J$  obtenue sur le maillage fin  $X_h$  et celle obtenue en extrapolant le champ aérodynamique sur le maillage fin  $W_h^H$ . Ce terme fait apparaître le lien entre l'erreur commise sur le problème direct et celle commise sur l'estimation de la fonction d'intérêt.

Cette approche est à la base de la méthode de Venditti et Darmofal [73, 74, 75] qui proposent, pour les applications pratiques, d'estimer le vecteur adjoint  $(\Lambda_h \Big|_{W_h^H})$  à partir du vecteur adjoint calculé sur le maillage grossier. Cette méthode fournit ainsi un terme de correction de la valeur de  $J$ . La méthode d'adaptation de maillage proposée par Venditti et Darmofal s'appuie sur une estimation de l'erreur commise sur cette correction. Cette méthode est la référence des méthodes d'adaptation de maillage pour le calcul de fonctions. Son principal inconvénient est la nécessité d'utiliser deux niveaux de maillage.

Une autre méthode d'adaptation de maillage basée sur l'adjoint est celle proposée par Dwight [13, 14]. Cette méthode est liée au schéma de Jameson dans lequel des coefficients de dissipation artificielle  $k^2$  et  $k^4$  sont utilisés. La majeure partie de l'erreur commise sur l'estimation de  $J$  est attribuée à cette dissipation artificielle. La méthode de Dwight consiste à considérer des valeurs différentes de ces coefficients en chaque cellule de sorte à équidistribuer l'indicateur suivant :

$$\eta = k^2 \frac{dJ}{dk^2} + k^4 \frac{dJ}{dk^4}$$

# 1. STRATÉGIES D'ADAPTATION DE MAILLAGES POUR LE CALCUL DE FONCTIONS

Cet indicateur ne peut être calculé que par méthode adjointe :

$$\eta = \Lambda \left( k^2 \frac{\partial R}{\partial k^2} + k^4 \frac{\partial R}{\partial k^4} \right)$$

Cette approche ne nécessite pas deux niveaux de maillage comme pour celle de Venditti et Darmofal et fournit également une correction à la valeur de la fonction d'intérêt :  $J - k^2 dJ/dk^2 - k^4 dJ/dk^4$ . Néanmoins le principal inconvénient est que la méthode s'applique uniquement pour le schéma de Jameson.

## Conclusions

La réduction de l'erreur de discrétisation pour le calcul de fonctions aérodynamiques issues de simulations volumes finis a conduit au développement de plusieurs méthodes depuis le début des années 2000. Ces méthodes sont souvent basées sur le vecteur adjoint de la fonction d'intérêt. Ces approches ont été appliquées à de nombreux problèmes et ont conduit à de significatives améliorations des valeurs de fonction. Des méthodes d'adaptation de maillages ont également été mises en œuvre.

La méthode de Venditti et Darmofal ainsi que celle de Dwight sont applicables pour des problèmes non-linéaires ainsi que pour des fonctions non-linéaires. Néanmoins chacune présente un inconvénient notable : l'utilisation de deux niveaux de maillage pour la méthode de Venditti et Darmofal ; la nécessité d'utiliser un schéma numérique particulier pour celle de Dwight. Ainsi le développement d'une nouvelle méthode qui ne nécessite pas l'utilisation d'un maillage fin et qui n'est pas liée à l'utilisation d'un schéma en particulier est l'objectif principal des présents travaux.

L'idée principale est d'utiliser la dérivée totale de la fonction d'intérêt par rapport aux coordonnées des nœuds du maillage. Cette dérivée peut être calculée dans le cadre de la méthode adjointe discrète. Cette quantité est un lien direct entre la fonction d'intérêt et le maillage qui est utilisé pour la simulation numérique. La présentation des premiers développements de cette méthode est l'objet du chapitre 2.

# Chapter 1

## Goal oriented mesh adaptation strategies

The evaluation of aerodynamic outputs such as the drag coefficient components is a major issue in aeronautical engineering. As the fuel consumption is a major commercial parameter and as this output is directly connected to the drag coefficient, its reduction by shape optimization is of major interest. Moreover the aerodynamic forces and momenta also have to be estimated for every points of the flight domain (roughly a thousand calculations for a fixed configuration). In this context, even if the wind tunnel tests are the reference, the huge number of output evaluations that is required makes the use of numerical simulations a necessary solution to this issue.

The accuracy of these numerical simulations is then a major issue. The error has several origins: the modeling error that is the difference between a real flow and the exact solution of the equations describing the physic (*e.g.* RANS equations) ; the discretization error that is the difference between the exact solution of the mathematical model and the discretized equations ; the convergence error that is the error that comes from the machine computation of the solution of the discretized equations. The discretization error is connected to the accuracy of the scheme but also to the discretization of the computation domain on a mesh. In the framework of intensive output evaluations, a way to reduce the error in numerical simulations is to develop methods that reduce the discretization error for the outputs by adapting the meshes (this technique is called “goal oriented mesh adaptation”).

Most often these methods involve the adjoint vector of the goal. The methods developed in this work are also based on the adjoint vector. The following section is devoted to the generalities about the computation of the output using numerical simulations and presents several tools used thereafter. The section 1.2 is devoted to the discrete adjoint method for the computation of functional output gradient with respect to design parameters (succinctly called “gradient computation” thereafter). Finally the section 1.3 presents generalities about the different existing strategies for the reduction of the discretization error. The proposed methodology will then be presented in the next chapter.

## 1.1 Aerodynamic functions estimation using numerical simulations

This section is devoted to the presentation of the general process for the computation of aerodynamic outputs using numerical simulation. Thus the tools used in all the works of this thesis are also presented here.

### 1.1.1 The equations of fluid mechanics

The equations that describe compressible, turbulent and viscous flows are presented in the followings. These flows are described by the Navier-Stokes equations but if the viscous effects are neglected then these equations lead to the Euler equations. Many applications considered in the following chapters use these equations that are hence presented here after.

**The Euler equations** Inviscid flows are described by the Euler equations. It is a set of five non-linear partial differential equations describing the conservation of mass, momentum and energy. The conservative form of these equations is:

$$\frac{\partial w}{\partial t} + \text{div}(\mathcal{F}) = 0$$

where  $w$  is the continuous flow field and  $\mathcal{F}$  is the Euler flux density:

$$\mathcal{F} = \begin{pmatrix} \rho \bar{V} \\ \rho \bar{V} \otimes \bar{V} + p \bar{I} \\ (\rho E + p) \bar{V} \end{pmatrix}$$

where  $\rho$  is the density,  $\bar{V} = (V_x, V_y, V_z)$  is the velocity,  $E$  is the total energy and  $p$  is the static pressure. Finally these equations are completed by the perfect gas law:

$$p = (\gamma - 1) \rho \left( E - \frac{\|\bar{V}\|^2}{2} \right)$$

where  $\gamma = C_p/C_v$  is the specific heat ratio (which is equal to 1.4 for the air).

**The Navier-Stokes equations** Viscous flows are described by the Navier-Stokes equations whose equation in the conservative form is:

$$\frac{\partial w}{\partial t} + \text{div}(\mathcal{F} - \mathcal{F}^V) = 0, \tag{1.1}$$

where  $\mathcal{F}^V$  is the viscous flux density given by:

$$\mathcal{F}^V = \begin{pmatrix} 0 \\ \bar{\tau} \\ \bar{\tau} \bar{V} - \bar{q} \end{pmatrix}$$

where  $\bar{q}$  is the heat flux and  $\bar{\tau}$  is the viscous shear stress tensor given by:

$$\bar{\tau} = -\frac{2}{3}\mu \operatorname{div}(\bar{V})\bar{I} + \mu(\nabla\bar{V} + \nabla\bar{V}^T)$$

where  $\mu$  is the dynamic viscosity. In the case of perfect gas,  $\mu$  satisfy the Sutherland law:

$$\frac{\mu}{\mu_\infty} = \left(\frac{T}{T_\infty}\right)^{3/2} \frac{T_\infty + s}{T + s}$$

where  $\mu_\infty$  is the viscosity at the reference temperature  $T_\infty$  and  $s$  is a constant equal to 110.4 K for the air. The heat flux  $\bar{q}$  is given by the Fourier law:

$$\bar{q} = -K_T \nabla T$$

where  $T$  is the temperature and  $K_T$  is the thermal conductivity coefficient. If the Prandtl number ( $Pr$ ) is constant ( $Pr = 0.72$  for the air) then the thermal conductivity coefficient  $K_T$  is constant too and we have:

$$K_T = \frac{\mu C_p}{Pr}$$

where  $C_p$  is the specific heat constant under constant pressure. The fluid temperature is calculated thanks to the relation:

$$T = \frac{1}{C_v} \left( E - \frac{\|\bar{V}\|^2}{2} \right)$$

where  $C_v$  is the specific heat constant under constant volume.

**The RANS equations** For high Reynolds numbers, turbulent zones with multidimensional and instationary structures appear close to the solid walls and in the wakes. Most often the scale of these structures is too small to be directly computed by numerical simulations. Therefore it is useful to consider equations averaged in time. The idea is to split up the physical quantity  $f(x, t)$  (pressure, velocity, density, etc.) into a mean part  $\bar{f}(x, t)$  and a fluctuating one  $f'(x, t)$ :

$$f(x, t) = \bar{f}(x, t) + f'(x, t)$$

The time-averaged quantity  $\bar{f}(x, t)$  is defined by:

$$\bar{f}(x, t) = \frac{1}{T} \int_{-T/2}^{T/2} f(x, t + \tau) d\tau$$

where  $T$  is chosen to be large enough in comparison to the characteristic time scale of the turbulence. Moreover one can notice that the mean of the fluctuating part is null.

This time average is well suited for incompressible flows but in the case of compressible flows, several other terms appear. These terms are connected to a correlation between the density and other variables. Therefore it is useful to consider a density-weighted average, called Favre-averaging:

$$\tilde{f} = \frac{\overline{\rho f}}{\bar{\rho}}$$

This leads to the following decomposition:

$$f = \tilde{f} + f'' \quad \text{and} \quad \overline{\rho f''} = 0$$

## 1.1. AERODYNAMIC FUNCTIONS ESTIMATION USING NUMERICAL SIMULATIONS

The RANS equations are built up using the Favre means in the equations (1.1) and by applying the Favre mean properties. Using the classical simplifications where the third order term  $\overline{\rho V''^2 V^2}$  is neglected, as well as  $\overline{\tau V''}$ , the equations are:

$$\begin{aligned} \frac{\partial \bar{\rho}}{\partial t} + \text{div}(\bar{\rho} \tilde{V}) &= 0 \\ \frac{\partial \bar{\rho} \tilde{V}}{\partial t} + \text{div}(\bar{\rho} \tilde{V} \otimes \tilde{V} + \bar{p} \bar{I}) &= \text{div}(\bar{\bar{\tau}} + \bar{\tau}_R) \\ \frac{\partial \bar{\rho}(\tilde{E} + k_t)}{\partial t} + \text{div}(\bar{\rho}(\tilde{E} + k_t)\tilde{V} + \bar{p}\tilde{V}) &= \text{div}((\bar{\bar{\tau}} + \bar{\tau}_R)\tilde{V} - \tilde{q} - \bar{q}_t) \end{aligned}$$

where  $\bar{\tau}_R$  is the Reynolds tensor,  $k_t$  is the turbulent kinematic energy and  $\bar{q}_t$  is the turbulent heat flux. These quantities are defined by:

$$\bar{\tau}_R = -\overline{\rho V'' \otimes V''} \quad k_t = \frac{\overline{\rho V''^2}}{2\bar{\rho}} \quad \bar{q}_t = \overline{p V''} + \overline{\rho e'' V''}$$

The time-averaged shear stress tensor  $\bar{\bar{\tau}}$  is given by:

$$\bar{\bar{\tau}} = -\frac{2}{3}\mu \text{div}(\tilde{V})\bar{I} + \mu(\nabla \tilde{V} + \nabla \tilde{V}^T)$$

The time-averaged heat flux  $\tilde{q}$  is given by:

$$\tilde{q} = -K_T \nabla \tilde{T}$$

In order to close the RANS equations, the effects of turbulence on the mean flow have to be modeled. The Boussinesq hypothesis leads to the relations:

$$\begin{aligned} \bar{\tau}_R &= -\frac{2}{3}(\bar{\rho}k_t + \mu_t \text{div}(\tilde{V}))\bar{I} + \mu_t(\nabla \tilde{V} + \nabla \tilde{V}^T) \\ \bar{q}_t &= -\frac{C_p \mu_t}{Pr_t} \nabla T \end{aligned}$$

where  $\mu_t$  is the turbulent viscosity coefficient and  $Pr_t$  is the turbulent Prandtl number. In practice  $Pr_t$  is a constant independent of the temperature that is equal to 0.9.

Therefore, the Boussinesq hypothesis reduces the turbulence modeling to the two terms  $\mu_t$  and  $k_t$ . Several methods are available for the calculation of these terms: algebraic models and models with transport equations.

**The Spalart-Allmaras turbulence model** The turbulence model used in this work for the RANS applications is the one proposed by Spalart-Allmaras [63] based one transport equation for the kinematic turbulent viscosity  $\tilde{\nu} = \mu_t/\rho$ . This equation is the following one:

$$\underbrace{\frac{\partial \rho \tilde{\nu}}{\partial t} + \text{div}(\rho \tilde{\nu} \bar{V})}_{\text{convection}} = \underbrace{c_{b1} \tilde{S} \rho \tilde{\nu}}_{\text{production}} + \underbrace{\frac{1}{\sigma_{SA}} [\text{div}((\mu + \rho \tilde{\nu}) \nabla \tilde{\nu}) + c_{b2} \nabla(\rho \tilde{\nu}) \nabla \tilde{\nu}]}_{\text{diffusion}} - \underbrace{c_{w1} f_w \frac{\rho \tilde{\nu}^2}{d^2}}_{\text{destruction}}$$

where:

$$\mu_t = \rho \tilde{\nu} f_{v1} \quad \chi = \frac{\tilde{\nu}}{\nu} \quad f_{v1} = \frac{\chi^3}{\chi^3 + c_{v1}^3} \quad f_{v2} = 1 - \frac{\chi}{1 + \chi f_{v1}}$$

$$\tilde{S} = |\nabla \wedge \bar{V}| + \frac{\tilde{\nu}}{\kappa^2 d^2} f_{v2} \quad f_w = g \left[ \frac{1 + c_{w3}^6}{g^6 + c_{w3}^6} \right]^{\frac{1}{6}} \quad g = \tilde{r} + c_{w2}(\tilde{r}^6 - \tilde{r}) \quad \tilde{r} = \frac{\tilde{\nu}}{\tilde{S} \kappa^2 d^2}$$

and the constants are:

$$c_{b1} = 0.1355 \quad c_{b2} = 0.622 \quad \sigma_{SA} = \frac{2}{3} \quad \kappa = 0.41$$

$$c_{w1} = \frac{c_{b1}}{\kappa^2} + \frac{1 + c_{b2}}{\sigma_{SA}} \quad c_{w2} = 0.3 \quad c_{w3} = 2 \quad c_{v1} = 7.1$$

### 1.1.2 The aerodynamic outputs

The aerodynamic functions of interest considered are basically the drag and lift coefficients. These coefficients can be computed with a near-field approach that consists in integrations over the solid shape, or with a far-field approach [12]. The near-field pressure lift coefficient is given by the following relation:

$$CL_p = \frac{L_p}{\frac{1}{2} \rho_\infty V_\infty^2 S_{ref}}$$

where  $L_p$  is the lift obtained by integration of the pressure forces over the solid shape. The drag coefficient can be computed thanks to a near-field approach with the relation:

$$Cd = CD_p + CD_f$$

where  $CD_p$  is the pressure drag coefficient and  $CD_f$  is the skin-friction drag coefficient given by:

$$CD_p = \frac{D_p}{\frac{1}{2} \rho_\infty V_\infty^2 S_{ref}} \quad CD_f = \frac{D_f}{\frac{1}{2} \rho_\infty V_\infty^2 S_{ref}}$$

where  $D_p$  is the pressure drag,  $D_f$  is the friction drag,  $\rho_\infty$  and  $V_\infty$  are respectively the density and the velocity of far-field flow and  $S_{ref}$  is a reference surface.

The far-field drag breakdown is based on the following decomposition:

$$Cd = \underbrace{CD_p + CD_f}_{Near-field} = \underbrace{CD_w + CD_i + CD_{vp} + CD_f + CD_{sp}}_{Far-field}$$

where  $CD_w$  is the wave drag coefficient that comes from shock waves at transonic and supersonic conditions,  $CD_i$  is the induced drag produced by the trailing vortex wake,  $CD_{vp}$  is the viscous pressure drag coefficient that comes from viscous effects and  $CD_{sp}$  is the spurious drag coefficient that is a non-physical drag component that comes from numerical dissipation. Moreover the viscous drag coefficient  $CD_v$  is defined as follows:

$$CD_v = CD_f + CD_{vp}$$

In two dimensions the induced drag  $CD_i$  is produced at the far-field subfaces that are not far enough from the body and is then assimilated to spurious drag. This component is called the reversible drag (or fictitious induced drag) and is denoted  $CD_{sp,rev}$ . This component is proportional to the inverse of the distance between the body and the far-field and proportional to the square of the lift coefficient. Moreover in two dimensions the

## 1.1. AERODYNAMIC FUNCTIONS ESTIMATION USING NUMERICAL SIMULATIONS

other component of the spurious drag is the irreversible drag coefficient denoted  $CD_{sp,irr}$ . This lead to the following far-field drag breakdown in two dimensions:

$$Cd = CD_w + CD_{vp} + CD_f + CD_{sp,irr} + CD_{sp,rev}$$

In practice, for many cases, these aerodynamic outputs have been computed thanks to the tool *Zapp* at Airbus, for the near-field coefficients. The far-field coefficients have been computed using the software *FFD72* [12] developed at ONERA.

### 1.1.3 Discretization of the equations of fluid mechanics

The solver used in this work is *elsA* [10] that is developed at ONERA since 1997 for numerical simulations in aerodynamics. This code uses finite-volume cell-centered second order schemes on multiblock structured meshes. Two schemes were used in this work, the Roe's scheme [58] extended to second order thanks to MUSCL reconstruction of Van Leer [70] with the limiting function of Van Albada [69] and the Jameson *et. al.* scheme [24].

**The Roe's scheme** Roe's numerical flux is denoted by  $F^R$  and is defined by [58]:

$$F^R(W_l, W_r) = \frac{1}{2} (\bar{\mathcal{F}}(W_l) + \bar{\mathcal{F}}(W_r)) - \frac{1}{2} |A| (W_l - W_r)$$

where  $W_l$  (resp.  $W_r$ ) stands for the left state (resp. right state) and  $\bar{\mathcal{F}}$  is the Euler flux in the direction  $n = (n_x, n_y, n_z)$  ( $\bar{\mathcal{F}} = \mathcal{F}.n$ ). Finally,  $|A| = Mdiag(\lambda_A)M^{-1}$  with  $diag(\lambda_A)$  standing for the diagonal matrix composed by the eigenvalue of the Roe's matrix  $A = A(W_l, W_r)$ . This matrix is built up in order to be diagonalizable with real eigenvalues, to be the differential of  $\bar{\mathcal{F}}$  w.r.t.  $W$  and to satisfy:

$$A(W_l, W_r)(W_l - W_r) = \bar{\mathcal{F}}(W_l) - \bar{\mathcal{F}}(W_r)$$

The Roe's matrix  $A$  is the Jacobian of  $\bar{\mathcal{F}}$  evaluated at a mean state  $W^{Roe}$  given by:

$$W^{Roe} = \left[ \begin{array}{ccccc} \sqrt{\rho_l \rho_r} & \frac{\sqrt{\rho_l} u_l + \sqrt{\rho_r} u_r}{\sqrt{\rho_l} + \sqrt{\rho_r}} & \frac{\sqrt{\rho_l} v_l + \sqrt{\rho_r} v_r}{\sqrt{\rho_l} + \sqrt{\rho_r}} & \frac{\sqrt{\rho_l} w_l + \sqrt{\rho_r} w_r}{\sqrt{\rho_l} + \sqrt{\rho_r}} & \frac{\sqrt{\rho_l} (E_l + \frac{p_l}{\rho_l}) + \sqrt{\rho_r} (E_r + \frac{p_r}{\rho_r})}{\sqrt{\rho_l} + \sqrt{\rho_r}} \end{array} \right]^T$$

This scheme can be extended to second order using the MUSCL technique that consists in a linear reconstruction of the flow field [70]. The primitive variables are extrapolated on each interface using the following relations:

$$\begin{aligned} W_{i+\frac{1}{2},j,k}^l &= W_{i,j,k}^{prim} + \frac{1}{2} \phi^{VA}(W_{i,j,k}^{prim} - W_{i-1,j,k}^{prim}, W_{i+1,j,k}^{prim} - W_{i,j,k}^{prim}) \\ W_{i+\frac{1}{2},j,k}^r &= W_{i,j,k}^{prim} - \frac{1}{2} \phi^{VA}(W_{i+1,j,k}^{prim} - W_{i,j,k}^{prim}, W_{i+2,j,k}^{prim} - W_{i+1,j,k}^{prim}) \end{aligned}$$

where  $W_{i+\frac{1}{2},j,k}^l$  (resp.  $W_{i+\frac{1}{2},j,k}^r$ ) stands for the extrapolated primitive variables on the left side (resp. right side) of the interface  $(i + \frac{1}{2}, j, k)$  and  $W_{i,j,k}^{prim}$  the primitive variable at the cell  $(i, j, k)$ . Finally  $\phi^{VA}$  is a the Van Albada limiting function given by [69]:

$$\phi^{VA}(a, b) = \frac{(b^2 + \epsilon)a + (a^2 + \epsilon)b}{a^2 + b^2 + 2\epsilon}$$

where  $\epsilon$  is a small constant.

**The Jameson *et. al.* scheme** The numerical flux of Jameson *et. al.* scheme is denoted by  $F^J$  and is given by [24]:

$$F_{i-\frac{1}{2},j,k}^J(W_l, W_r) = \frac{1}{2} (\bar{\mathcal{F}}(W_l) + \bar{\mathcal{F}}(W_r)) + F_{i-\frac{1}{2},j,k}^{J,AD}$$

where  $F^{J,AD}$  is an artificial dissipation term given by:

$$F_{i-\frac{1}{2},j,k}^{J,AD} = -\epsilon_{i-\frac{1}{2},j,k}^{(2)} \bar{\rho}_{i-\frac{1}{2},j,k} \delta_{i-\frac{1}{2},j,k} + \epsilon_{i-\frac{1}{2},j,k}^{(4)} \bar{\rho}_{i-\frac{1}{2},j,k} \Delta_{i-\frac{1}{2},j,k} \quad (1.2)$$

with:

$$\bar{\rho}_{i-\frac{1}{2},j,k} = |\bar{V} \cdot S| + c ||S|| \quad \epsilon_{i-\frac{1}{2},j,k}^{(2)} = k^2 \max(\nu_i, \nu_{i-1}) \quad \text{and} \quad \epsilon_{i-\frac{1}{2},j,k}^{(4)} = \max(0, k^4 - \epsilon_{i-\frac{1}{2},j,k}^{(2)})$$

where  $k^2$  and  $k^4$  are artificial dissipation coefficients and  $\nu_i$  is a sensor build up in order to detect shocks and is defined by:

$$\nu_i = \frac{|p_{i+1,j} - 2p_{ij} + p_{i-1,j}|}{|p_{i+1,j}| + 2|p_{ij}| + |p_{i-1,j}|}$$

## 1.2 The discrete adjoint method

This section is devoted to a general presentation of the adjoint method and some technical issues associated with. This method initially developed for the computation of output gradient w.r.t. design parameters in the framework of shape optimization [23, 47] is also often used for goal oriented mesh adaptation [53, 54, 73, 74, 75, 13, 14] (that is presented in more details in the section 1.3). In the same way, the proposed methodology developed in this work, and presented in the next chapter, is based on the adjoint method.

### 1.2.1 Gradient computation with the discrete adjoint method

We denote by  $R$  (vector of size  $N_W$ ) the discretized equations of the fluid mechanics that is basically the finite-volume flux balance at each cell of the mesh. It is supposed that  $R$  has  $C^1$  regularity w.r.t. its two arguments. At the steady state the flow-field  $W$  and the volume mesh  $X$  satisfy:

$$R(W, X) = 0 \quad (1.3)$$

We denote by  $W_b$  the flow-field extrapolated at the boundaries of the solid walls as illustrated on the following figure.

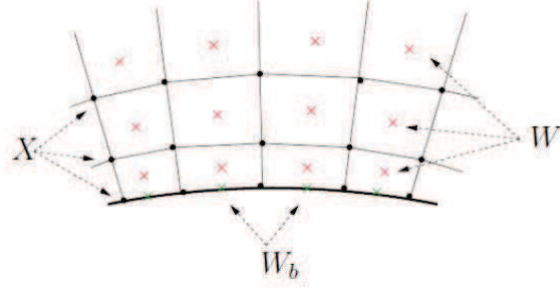


Figure 1.1: Localizations of the variables,  $X$  the mesh,  $W$  the cell-centered flow-field and  $W_b$  the flow-field extrapolated at the boundaries.

The aerodynamic function that depends on  $W$ ,  $W_b$  and  $X$  is denoted by  $J$ . Moreover the solid shape depends on design parameters  $\alpha$  (vector of size  $N_\alpha$ ) and it is supposed that  $X$  is a  $C^1$  regular function of  $\alpha$ . Hence, if  $\det(\partial R/\partial W)(W, X(\alpha)) \neq 0$  for all  $\alpha$ , the implicit function theorem allows to consider  $W$  as a  $C^1$  function of  $X$ . The aerodynamic function that depends on the parameters  $\alpha$  is denoted by  $\mathcal{J}$ , so we have:

$$\mathcal{J}(\alpha) = J(W(\alpha), W_b(W(\alpha), X(\alpha)), X(\alpha))$$

The differentiation of this relation and (1.3) leads to:

$$\begin{aligned} \frac{d\mathcal{J}}{d\alpha} &= \frac{\partial J}{\partial W} \frac{dW}{d\alpha} + \frac{\partial J}{\partial W_b} \frac{dW_b}{dW} \frac{dW}{d\alpha} + \frac{\partial J}{\partial W_b} \frac{dW_b}{dX} \frac{dX}{d\alpha} + \frac{\partial J}{\partial X} \frac{dX}{d\alpha} \\ &\quad \frac{\partial R}{\partial W} \frac{dW}{d\alpha} + \frac{\partial R}{\partial X} \frac{dX}{d\alpha} = 0 \end{aligned}$$

Multiplying this last equation by an arbitrary vector  $\Lambda^T$  of size  $N_W$  and adding this relation to the first one leads to:

$$\frac{d\mathcal{J}}{d\alpha} = \left( \Lambda^T \frac{\partial R}{\partial W} + \frac{\partial J}{\partial W} + \frac{\partial J}{\partial W_b} \frac{dW_b}{dW} \right) \frac{dW}{d\alpha} + \frac{\partial J}{\partial X} \frac{dX}{d\alpha} + \frac{\partial J}{\partial W_b} \frac{dW_b}{dX} \frac{dX}{d\alpha} + \Lambda^T \frac{\partial R}{\partial X} \frac{dX}{d\alpha}$$

The vector  $\Lambda$  is chosen such that the first term vanishes. The gradient  $d\mathcal{J}/d\alpha$  is then given by the following relations:

$$\frac{d\mathcal{J}}{d\alpha} = \frac{\partial J}{\partial X} \frac{dX}{d\alpha} + \frac{\partial J}{\partial W_b} \frac{dW_b}{dX} \frac{dX}{d\alpha} + \Lambda^T \frac{\partial R}{\partial X} \frac{dX}{d\alpha} \quad (1.4)$$

$$\left( \frac{\partial R}{\partial W} \right)^T \Lambda = - \left( \frac{\partial J}{\partial W} + \frac{\partial J}{\partial W_b} \frac{dW_b}{dW} \right)^T \quad (1.5)$$

The vector  $\Lambda$  is the adjoint vector of  $J$  for the discretization  $R$ .

The main advantage of this gradient computation method is that it requires to solve a linear system for all functions of interest independently of the number of design parameters that is not the case with the finite difference method or the direct differentiation method. In industrial context, the number of design parameters is by far greater than the number of functions of interest. Hence the adjoint method is most often chosen for gradient computations.

## 1.2.2 Numerical resolution of the adjoint equation

The adjoint equation (1.5) resolution requires to inverse the matrix  $\partial R/\partial W$  which is a large and sparse matrix. Hence the linear system cannot be solved directly for 3D large configurations. Thus the resolution of the adjoint equation is done thanks to a Newton iterative algorithm based on the following relation:

$$\frac{\partial R}{\partial W}{}^{T(APP)} (\Lambda^{n+1} - \Lambda^n) = - \left( \frac{\partial R}{\partial W}{}^{T(EXA)} \Lambda^n + \left( \frac{\partial J}{\partial W} + \frac{\partial J}{\partial W_b} \frac{dW_b}{dW} \right)^T \right),$$

where  $(\partial R/\partial W)^{(APP)}$  is an approximate Jacobian and  $(\partial R/\partial W)^{(EXA)}$  is the exact one. The resolution of this system can be done for example using the LU-SSOR method.

## 1.2.3 The numerical scheme differentiability issue

The discrete adjoint method is associated with the discretized equations  $R$  that models the physics. Moreover it allows to compute the gradient of a function of interest for a mesh  $X$  independently of the method used to compute the corresponding steady state flow-field  $W$  on this mesh. Nevertheless the discrete equations  $R$  need to have  $C^1$  regularity. This condition is necessary to ensure the well-posedness of the previously introduced equations. Unfortunately the numerical fluxes widely used in the framework of finite-volume schemes are not always  $C^1$  regular. As an example the Jameson *et. al.* scheme, it involves absolute values and *max* functions that are not differentiable. This can lead to unexpected behavior. For instance for symmetrical test cases, an asymmetrical adjoint field can be computed. The figure 1.2 illustrates such a case. The flow considered is a transonic ( $M_\infty = 0.8$ ) Eulerian flow with null incidence around the NACA0012 airfoil. The figure 1.2(a) illustrates the adjoint field for the variable  $\rho$  and the figure 1.2(b) illustrates the corresponding total derivative of the pressure drag coefficient  $CD_p$  w.r.t. the mesh nodes coordinates.

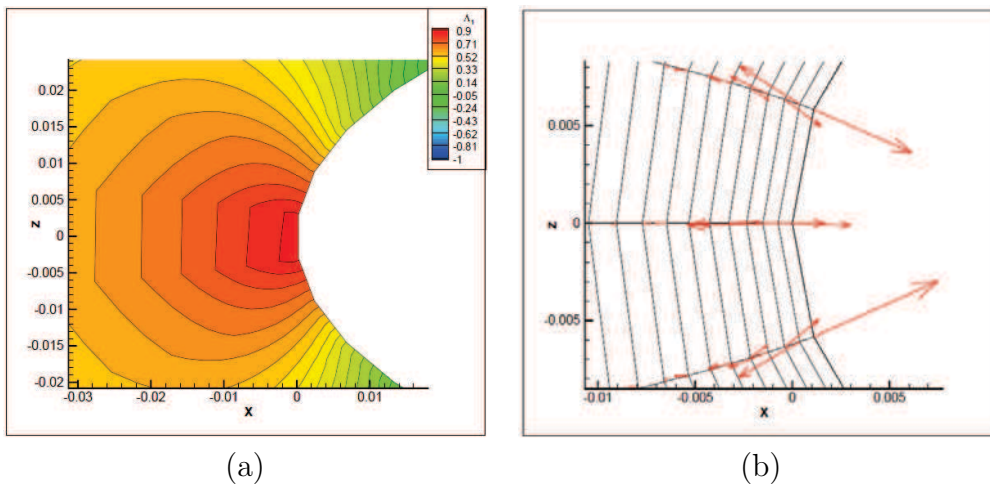


Figure 1.2: Leading edge of the NACA0012 airfoil, AoA = 0°,  $M_\infty = 0.8$  ; (a) Adjoint field for the variable  $\rho$  (b)  $dCD_p/dX$  field

An asymmetrical adjoint field can be observed and hence the same behavior also appears on the total derivative  $dCD_p/dX$ . However the differentiation of the numerical scheme can be slightly modified at the neighbourhood of non-differentiable point in order to avoid these effects. For example the differentiation of  $\bar{\rho}$  (in equation (1.2)) w.r.t. the  $x$ -component of the interface normal vector in the Jameson *et. al.* scheme is:

$$\frac{\partial \bar{\rho}}{\partial n_x} = \begin{cases} -\|S\|u & \text{if } \bar{V}.S < 0 \\ \|S\|u & \text{if } \bar{V}.S > 0 \end{cases}$$

There is an indetermination in the case where  $\bar{V}.S = 0$  thus this formula may be replaced by:

$$\frac{\partial \bar{\rho}}{\partial n_x} = \begin{cases} -\|S\|u & \text{if } \bar{V}.S < -2\epsilon \\ \frac{\|S\|u \bar{V}.S + \|S\|u}{\epsilon} & \text{if } -2\epsilon \leq \bar{V}.S \leq -\epsilon \\ 0 & \text{if } -\epsilon \leq \bar{V}.S \leq \epsilon \\ -\frac{\|S\|u \bar{V}.S + \|S\|u}{\epsilon} & \text{if } \epsilon \leq \bar{V}.S \leq 2\epsilon \\ \|S\|u & \text{if } 2\epsilon < \bar{V}.S \end{cases}$$

where  $\epsilon$  is a small constant. In the same way the function  $(a, b) \mapsto \max(a, b)$  can also be estimated differently in order to avoid the indetermination in the case where  $a = b$  with the following formula:

$$\max'(a, b) = \begin{cases} a & \text{if } (1 + \epsilon)b < (1 - \epsilon)a \\ \frac{(a-b)^2}{4\epsilon(a+b)} + \frac{a+b}{2} + \frac{\epsilon(a+b)}{4} & \text{if } -\epsilon(a+b) < a-b < \epsilon(a+b) \\ b & \text{if } (1 + \epsilon)a < (1 - \epsilon)b \end{cases}$$

These slight modifications of the differentiation formulas lead to more consistent results as illustrated on the following figures that are the counterpart of figures 1.2 with these corrected differentiation formulas.

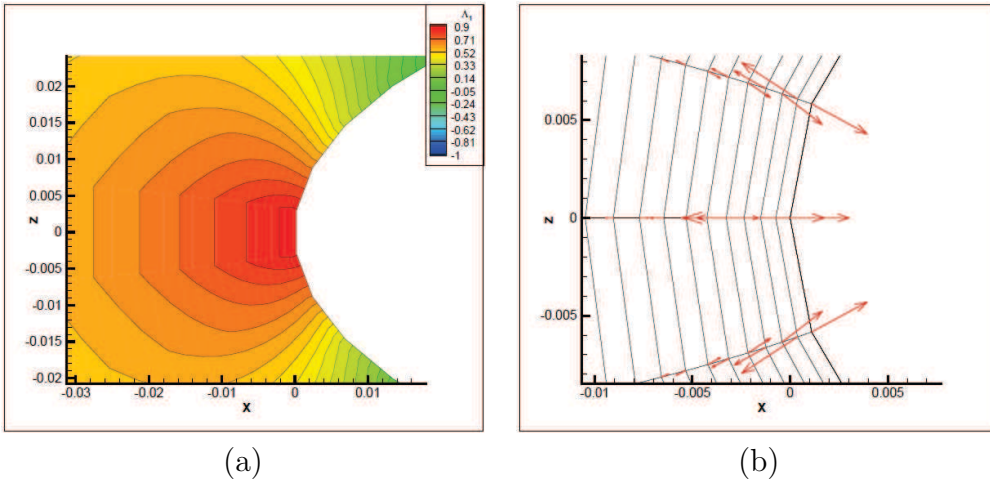


Figure 1.3: Leading edge of the NACA0012 airfoil,  $AoA = 0^\circ$ ,  $M_\infty = 0.8$  ; (a) Adjoint field for the variable  $\rho$  with the corrected differentiation formulas (b)  $dCD_p/dX$  field with the corrected differentiation formulas

In this case the numerical scheme is actually a  $C^1$  regular function. We observe slight modifications of the adjoint field in comparison to the previous case. However, as expected, this symmetrical test case effectively leads to a symmetrical adjoint field.

### 1.3 Mesh adaptation strategies for the reduction of the discretization error

As one of the error source in the aerodynamic output estimation comes from the discretization of the geometrical domain on meshes, it is useful to adapt them in order to reduce this error. Since many years several approaches were considered. Many of them use the adjoint vector, presented in the previous section, in order to build up output error estimators and to derive corresponding mesh adaptation methods. The subsection 1.3.1 is about the method proposed by Pierce and Giles for linear problems and linear outputs. The subsection 1.3.2 focuses on the method of Venditti and Darmofal that is the reference nowadays for goal oriented mesh adaptation methods involving the adjoint vector. This method can be applied for non-linear problems and non-linear functions. Another method based on the adjoint method is the one of Dwight and is presented in the subsection 1.3.3.

#### 1.3.1 The method of Pierce and Giles

The method of Pierce and Giles was developed at the end of the 1990s [52, 53, 54]. The direct problem is the following linear differential equation:

$$\mathcal{L}w = f$$

It is supposed that  $w$  and  $f$  belong to an Hilbert space  $\mathcal{H}$  whose inner product is denoted  $(\cdot, \cdot)$  and  $\mathcal{L}$  is a continuous linear differential operator. The output is the product of  $w$  with another vector  $g$  and then the corresponding adjoint problem can be defined:

$$\mathcal{L}^*\lambda = g$$

The operator  $\mathcal{L}^*$  is defined (if it exists) such that  $(\mathcal{L}^*\lambda, w) = (\lambda, \mathcal{L}w)$  for all  $\lambda$  and  $w$  that belong to  $\mathcal{H}$ . Thus the goal can be computed using the adjoint vector  $\lambda$ :

$$(g, w) = (\mathcal{L}^*\lambda, w) = (\lambda, \mathcal{L}w) = (\lambda, f)$$

Hence if the goal is estimated thanks to an approximated solution  $w_h$  of the direct problem then the error can be expressed as follows:

$$\begin{aligned} (g, w) - (g, w_h) &= (g, w - w_h) \\ &= (\mathcal{L}^*\lambda, w - w_h) \\ &= (\lambda, \mathcal{L}(w - w_h)) \\ &= (\lambda, f - \mathcal{L}w_h) \end{aligned}$$

If the adjoint problem has also been approximated then the error is expressed as:

$$(g, w) - (g, w_h) = (\lambda_h, f - \mathcal{L}w_h) + (\lambda - \lambda_h, f - \mathcal{L}w_h) \quad (1.6)$$

The first term is a computable correction to the output value. Pierce and Giles considered that the approximate solution of the direct and adjoint problems ( $w_h$  and  $\lambda_h$ ) are build up from discrete approximations  $W_h$  and  $\Lambda_h$  (obtained on a mesh of characteristic cell length  $h$ ) using a reconstruction operator  $\bar{R}$ :

$$w_h = \bar{R}W_h \quad \text{and} \quad \lambda_h = \bar{R}\Lambda_h$$

### 1.3. MESH ADAPTATION STRATEGIES FOR THE REDUCTION OF THE DISCRETIZATION ERROR

Thus the residual error are expected to satisfy:

$$\|\lambda - \lambda_h\| = \mathcal{O}(h^{\min(p,r)}) \quad \text{and} \quad \|f - \mathcal{L}w_h\| = \mathcal{O}(h^{\min(p,r-n)}),$$

where  $n$  is the derivation order of the operator  $\mathcal{L}$ ,  $p$  is the discretization order and  $r$  the order of the reconstruction operator  $\bar{R}$ . Thus the error of the corrected output value obtained with equation (1.6) is expected to satisfy:

$$|(g, w) - (g, w_h) - (\lambda_h, f - \mathcal{L}w_h)| = |(\lambda - \lambda_h, f - \mathcal{L}w_h)| \leq |\lambda - \lambda_h| \|f - \mathcal{L}w_h\| = \mathcal{O}(h^{\min(p,r) + \min(p,r-n)})$$

Pierce and Giles applied this method for a wide range of problems. This approach provides a corrected output value but can be applied only for linear functions and linear direct problems.

#### 1.3.2 The method of Venditti and Darmofal

The approach of Venditti and Darmofal was developed since the 2000s [73, 74, 75]. Their method consists in approximating the output that would be computed on a fine grid using computations performed on a coarser one. The output estimation that would be computed on the fine mesh is supposed to be precise enough but prohibitively expensive to compute whereas the computation on the coarse mesh is affordable but provides an output estimation that is not precise enough. The error estimation is build up using a flow-field and the adjoint vectors computed on the coarse mesh.

The subscript  $h$  stands for the fine mesh and  $H$  for the coarse one. Therefore the estimation of the aerodynamic output on the fine grid can be done using a Taylor's expansion:

$$J_h(W_h, X_h) = J_h(W_h^H, X_h) + \left( \frac{\partial J_h}{\partial W} \Big|_{W_h^H} \right) (W_h - W_h^H) + \mathcal{O}(\|W_h - W_h^H\|^2), \quad (1.7)$$

where  $W_h^H$  is an approximation of the flow-field on the fine mesh from a calculation done on the coarse one. Moreover the following adjoint-like equation can be defined:

$$(\Lambda_h|_{W_h^H})^T \left( \frac{\partial R_h}{\partial W} \Big|_{W_h^H} \right) = - \frac{\partial J_h}{\partial W} \Big|_{W_h^H} \quad (1.8)$$

Thus using this relation in equation (1.7) leads to:

$$J_h(W_h, X_h) = J_h(W_h^H, X_h) - (\Lambda_h|_{W_h^H})^T \left( \frac{\partial R_h}{\partial W} \Big|_{W_h^H} \right) (W_h - W_h^H) + \mathcal{O}(\|W_h - W_h^H\|^2)$$

Moreover the following equation holds:

$$R_h(W_h^H, X_h) = - \left( \frac{\partial R_h}{\partial W} \Big|_{W_h^H} \right) (W_h - W_h^H) + \mathcal{O}(\|W_h - W_h^H\|^2)$$

As a consequence the output can be estimated as follows:

$$J_h(W_h, X_h) = J_h(W_h^H, X_h) + (\Lambda_h|_{W_h^H})^T R_h(W_h^H, X_h) + \mathcal{O}(\|W_h - W_h^H\|^2)$$

Unfortunately the computation of the adjoint field  $\Lambda_h \Big|_{W_h^H}$  on the fine grid is not affordable if the one of  $W_h$  is not (in practice it is as expensive as the computation of the flow-field on this mesh). Hence the method consists in replacing this adjoint vector by an interpolated one  $(\Lambda_h^H)$  from a computation done on the coarse mesh. This leads to:

$$J_h(W_h, X_h) \simeq J_h(W_h^H, X_h) + \underbrace{(\Lambda_h^H)^T R_h(W_h^H, X_h)}_{\text{computable correction}} + \underbrace{\left( (\Lambda_h \Big|_{W_h^H})^T - (\Lambda_h^H)^T \right) R_h(W_h^H, X_h)}_{\text{error in computable correction}}$$

This method provides a correction estimation for the output value. One can notice the deep connection between this formulation and the one of Pierce and Giles given by the equation (1.6). This approach requires to estimate fields on the fine mesh from fields computed on the coarse one. Hence this method requires interpolation operators. Venditti and Darmofal proposed to use linear and quadratic operators (denoted by  $L_h^H$  and  $Q_h^H$  respectively) for the prolongation of the primal solution. They also introduced the corresponding interpolation operator for the adjoint vector (denoted by  $\bar{L}_h^H$  and  $\bar{Q}_h^H$ ).

Moreover Venditti and Darmofal also proposed a mesh adaptation method that aims to reduce an upper bound of an estimated remaining error. This bound is built as follows. First of all one can notice that the error in the computable correction can be written in a different form:

$$\begin{aligned} & \left( (\Lambda_h \Big|_{W_h^H})^T - (\Lambda_h^H)^T \right) R_h(W_h^H, X_h) \\ &= (\Lambda_h \Big|_{W_h^H})^T R_h(W_h^H, X_h) - (\Lambda_h^H)^T R_h(W_h^H, X_h) \\ &\simeq -(\Lambda_h \Big|_{W_h^H})^T \left( \frac{\partial R_h}{\partial W} \Big|_{W_h^H} \right) (W_h - W_h^H) + (\Lambda_h^H)^T \left( \frac{\partial R_h}{\partial W} \Big|_{W_h^H} \right) (W_h - W_h^H) \quad (1.9) \\ &= \left( \frac{\partial J_h}{\partial W} \Big|_{W_h^H} + (\Lambda_h^H)^T \left( \frac{\partial R_h}{\partial W} \Big|_{W_h^H} \right) \right) (W_h - W_h^H) \\ &= R_h^\Lambda (\Lambda_h^H) (W_h - W_h^H) \end{aligned}$$

where:

$$R_h^\Lambda(\cdot) = \frac{\partial R_h}{\partial W}^T(\cdot) + \frac{\partial J_h}{\partial W}^T$$

One can notice than  $R_h^\Lambda$  is the residual of the adjoint equation (1.8). The following adaptation parameter is defined for all elements  $k$  of the coarse mesh:

$$\epsilon_k = \frac{1}{2} \sum_{l(k)} \left\{ \left| [R_h^\Lambda(\bar{L}_h^H \Lambda_H)]_{l(k)}^T [Q_h^H W_H - L_h^H W_H]_{l(k)} \right| + \left| [\bar{Q}_h^H \Lambda_H - \bar{L}_h^H \Lambda_H]_{l(k)}^T [R_h(L_h^H W_H)]_{l(k)} \right| \right\},$$

where  $l(k)$  is the set of all cells of the fine mesh that belong to the cell  $k$  of the coarse mesh. The two terms of the sum estimate a bound of the error in the computable correction with the formulations given by (1.9) for the cell  $k$ . The adaptation parameter  $\epsilon_k$  is the average of these two estimations of this bound. A global bound  $\epsilon$  is defined as follows:

$$\epsilon = \sum_k \epsilon_k$$

In this framework the method of Venditti and Darmofal for mesh adaptation consists in equidistributing the adaptation parameter throughout the domain while reducing this upper bound estimation.

### 1.3. MESH ADAPTATION STRATEGIES FOR THE REDUCTION OF THE DISCRETIZATION ERROR

This method can be applied for non-linear direct problems and for non-linear functions. Venditti and Darmofal applied it for a wide range of problems including for two-dimensional viscous flows [75]. An advantage of this method is that it provides a correction term to the output value computed on the coarse mesh. However, the main drawback is that two levels of mesh are required.

#### 1.3.3 The method of Dwight

Another adjoint-based method for goal oriented mesh adaptation is the one proposed by Dwight [13, 14] at the end of the 2000s. This approach is based on the fact that the artificial dissipation in the Jameson *et. al.* scheme is an unphysical term. Extrapolations have been made (such that  $k^2, k^4 \rightarrow 0$ ) and have shown up that the artificial dissipation is responsible of the major part of the outputs error. A study on several mesh sizes shows that more than 90% of the error of discretization is due to the dissipation term. From this consideration a measure of error has been proposed:

$$\eta = k^2 \frac{dJ}{dk^2} + k^4 \frac{dJ}{dk^4},$$

where  $k^2$  and  $k^4$  are the artificial dissipation coefficients of the Jameson *et. al.* scheme [24]. The derivatives that appear in this relation can be computed using the adjoint method and leads to:

$$\frac{dJ}{dk^2} = \Lambda^T \frac{\partial R}{\partial k^2} \quad \text{and} \quad \frac{dJ}{dk^4} = \Lambda^T \frac{\partial R}{\partial k^4}$$

Thus the error measure can be rewritten:

$$\eta = \Lambda \left( k^2 \frac{\partial R}{\partial k^2} + k^4 \frac{\partial R}{\partial k^4} \right)$$

The method for mesh adaptation consists in defining the dissipation coefficients  $k^2$  and  $k^4$  independently for each cell ( $k_i^2$  and  $k_i^4$  for the cell  $i$ ). The coefficients on interfaces being define as the average of the coefficients of the adjacent cells. Thus a local dissipation error indicator is defined for each cell:

$$\eta_i = \Lambda \left( k_i^2 \frac{\partial R}{\partial k_i^2} + k_i^4 \frac{\partial R}{\partial k_i^4} \right)$$

This local indicator is then used to refine the mesh in order to minimize the dissipation error. Moreover  $J - k^2 dJ/dk^2 - k^4 dJ/dk^4$  is considered as a corrected output value. This method can be applied for non-linear problems and non-linear functions and has the advantage not to require several levels of mesh. However, the main drawback is that this method is connected to a particular numerical scheme.

## 1.4 Conclusions

The reduction of the discretization error for the computation of aerodynamic outputs has led to the development of several methods since many years. In this context strategies have been developed in the framework of finite-volume schemes and most often these methods use the adjoint vector of the output. These approaches were applied for a wide range of problems and lead to methodologies providing significant improvements of the output estimations and mesh adaptations strategies too.

The methods of Venditti and Darmofal and the one of Dwight are applicable for non-linear problems and for non-linear functions but each one has a disadvantage. The use of two levels of mesh for the method of Venditti and Darmofal and the use of a particular scheme for the method of Dwight. The development of a new strategy based on the adjoint vector and that does not require a fine mesh and that is not associated to a particular numerical scheme is the main objective of the present work.

In this framework the idea is to use the total derivative of the output w.r.t. the mesh nodes coordinates. This derivative can be computed thanks to the adjoint method. This quantity is a direct link between the output and the mesh used for the numerical simulation. The presentation of the first development of this approach is the topic of the next chapter.

## 1.4. CONCLUSIONS

# Chapitre 2

## Adaptation de maillages basée sur $dJ/dX$

### Résumé :

Des méthodes d'adaptation de maillages pour le calcul de fonctions sont développées depuis de nombreuses années et sont souvent basées sur le vecteur adjoint des fonctions d'intérêt. Déjà présentée dans le chapitre précédent, la méthode de référence est celle de Venditti et Darmofal [73, 74, 75] qui fournit une correction à la valeur de la fonction et permet également de mettre en œuvre une stratégie d'adaptation de maillage afin de réduire l'erreur commise sur cette correction. Le principal inconvénient de cette approche est la nécessité d'utiliser deux niveaux de maillage. Une autre approche est celle de Dwight [13, 14] qui ne nécessite pas deux niveaux de maillage mais qui est liée à l'utilisation du schéma de Jameson.

D'autre part Nielsen et Park ont introduit la dérivée totale de la fonction d'intérêt par rapport aux coordonnées du maillage ( $dJ/dX$ ) dans le cadre de l'optimisation de forme [43]. Ceci afin de réduire le coûteux stockage en mémoire des sensibilités de maillage par rapport aux paramètres de forme. Cette dérivée ( $dJ/dX$ ) est un lien entre la fonction d'intérêt  $J$  et le maillage  $X$  qui est utilisé pour la simulation numérique. Cette grandeur est à la base des méthodes développées dans ces travaux pour d'une part construire une méthode d'adaptation de maillage sur un seul niveau de maillage et qui n'est pas liée à l'utilisation d'un schéma en particulier et d'autre part pour construire des indicateurs de qualité de maillage pour le calcul de fonctions.

### 1. La dérivée totale de fonctions aérodynamiques par rapport aux coordonnées du maillage

L'expression du gradient d'une fonction objectif  $J$  par rapport aux paramètres de forme  $\alpha$  fait apparaître l'expression de la dérivée totale de  $J$  par rapport aux coordonnées du maillage :

$$\frac{dJ}{dX} = \underbrace{\frac{\partial J}{\partial X} + \frac{\partial J}{\partial W_b} \frac{dW_b}{dX}}_{\text{Dérivée géométrique}} + \underbrace{\Lambda^T \frac{\partial R}{\partial X}}_{\text{Dérivée aérodynamique}}$$

Cette relation fait apparaître deux termes. Le premier est la dérivée géométrique qui correspond à la sensibilité de la fonction d'intérêt par rapport aux nœuds de son support.

Le second terme est la dérivée aérodynamique qui correspond à la sensibilité de la fonction d'intérêt par rapport aux nœuds du maillage due à la sensibilité du champ aérodynamique par rapport au maillage.

Ainsi la dérivée totale  $dJ/dX$  correspond à la sensibilité de la fonction d'intérêt par rapport à chaque nœud du maillage. Cette grandeur semble intéressante en vue construire des indicateurs de qualité de maillage pour le calcul d'une fonction (qualification de maillage) d'une part et d'autre part pour adapter les maillages afin d'améliorer les estimations de ces fonctions.

Une étude théorique de  $dJ/dX$  a été menée dans le cas où  $J$  est une force intégrée par sommation sur le contour de l'objet solide et où  $R$  est un bilan de flux. Il est observé que le champ adjoint converge vers un champ régulier quand le maillage est raffiné. D'autre part l'ordre des différents termes de  $dJ/dX$  donnés dans l'équation précédente a également été étudié. Le premier terme ( $\partial J/\partial X$ ) est d'ordre un. Le second terme ( $\Lambda^T \partial R/\partial X$ ) est quant à lui d'ordre deux. En effet la sensibilité de la fonction  $J$  par rapport à la coordonnée  $x_{ij}$  due à la sensibilité du champ aérodynamique est donnée par :

$$\begin{aligned} \Lambda \frac{\partial R}{\partial x_{i,j}} = & \sum_{k=1}^{k=4} [(\Lambda_{i+1/2,j+1/2}^k - \Lambda_{i+1/2,j-1/2}^k) \frac{\partial F^{R,k}}{\partial S^Z} (W_{i+1/2,j-1/2}^L, W_{i+1/2,j+1/2}^R, S_{i+1/2,j}^X, S_{i+1/2,j}^Z) \\ & (\Lambda_{i-1/2,j+1/2}^k - \Lambda_{i-1/2,j-1/2}^k) \frac{\partial F^{R,k}}{\partial S^Z} (W_{i-1/2,j-1/2}^L, W_{i-1/2,j+1/2}^R, S_{i-1/2,j}^X, S_{i-1/2,j}^Z) \\ & (\Lambda_{i+1/2,j+1/2}^k - \Lambda_{i-1/2,j+1/2}^k) \frac{\partial F^{R,k}}{\partial S^Z} (W_{i-1/2,j+1/2}^L, W_{i+1/2,j+1/2}^R, S_{i,j+1/2}^X, S_{i,j+1/2}^Z) \\ & (\Lambda_{i+1/2,j-1/2}^k - \Lambda_{i-1/2,j-1/2}^k) \frac{\partial F^{R,k}}{\partial S^Z} (W_{i-1/2,j-1/2}^L, W_{i+1/2,j-1/2}^R, S_{i,j-1/2}^X, S_{i,j-1/2}^Z)] \end{aligned}$$

où  $(S^X, S^Z)$  est le vecteur surface,  $F^{R,k}$  ( $k \in \{1, 4\}$ ) sont les composantes du flux de Roe et  $W^L$  et  $W^R$  sont respectivement l'état de gauche et l'état de droite utilisés pour calculer les flux. Or  $\Lambda$  tend vers un champ limite et  $\partial F^{R,k}/\partial S^Z$  tend vers la densité de flux d'Euler dans la direction  $z$  quand la taille caractéristique du maillage diminue. Ainsi chaque terme du membre de droite de cette équation est du premier ordre. Dans la mesure où les termes de la somme sont des différences de deux termes dont les indices sont décalés, la somme est du second ordre.

## 2. Adaptations de maillages basées sur $dJ/dX$ pour des écoulements de fluides parfaits

La première utilisation de  $dJ/dX$  dans le cadre de l'adaptation de maillage a été effectuée pour des écoulements de fluides parfaits et a été décrite dans un article dans le journal *Computers & Fluids* [49].

### 2.1 Adaptation par ajout de nœuds

Une approche d'adaptation de maillage consiste à le raffiner en ajoutant de nouveaux nœuds dans des zones détectées par un senseur. Cette approche a été mise en œuvre. Dans la mesure où les maillages considérés étaient structurés, le raffinement était basé

## 2. ADAPTATION DE MAILLAGES BASÉE SUR $dJ/dX$

sur des ajouts de lignes de maillage en 2D et ajout de plans en 3D. Le senseur detectant les rangées de cellules entre lesquelles les nouveaux nœuds sont ajoutés était basé sur  $dJ/dX$  et donné par les formules suivantes (dans le cas 2D) :

$$\bar{c}_{i+1/2} = \frac{c_i + c_{i+1}}{2} \quad c_i = \left( \frac{1}{N_j} \sum_{j=1}^{N_j} \|\mathcal{P}(dJ/dX)_{ij}\|^2 \right)^{\frac{1}{2}}$$

où  $\bar{c}_{i+1/2}$  est la valeur du senseur associé à la rangée de cellules comprise entre la ligne  $i$  et  $i+1$  et  $c_i$  est un critère associé à la ligne  $i$ . Après la détection de ces rangées de cellules, de nouvelles lignes (ou plans en 3D) y sont ajoutées uniformément, puis une étape de lissage est réalisée pour réduire les irrégularités de maillage introduites par l'ajout de nœuds.

Cette méthode a été appliquée à des écoulements de fluide parfait en 2D autour du profil NACA0012 sans incidence en régime subsonique ( $M_\infty = 0,5$ ) et transsonique ( $M_\infty = 0,8$ ). Les maillages utilisés étaient des maillage en O issus d'une étude de Vassberg et Jameson [71, 72]. Les fonctions considérées étaient la traînée de pression  $CD_p$  et l'intégrale de la pression d'arrêt sur le contour du profil adimensionnée par les grandeurs à l'infini ( $P_a$ ). Les valeurs théoriques de ces fonctions sont connues dans le cas subsonique ( $CD_p = 0$  et  $P_a = 1$ ) et ont été extrapolées dans le cas transsonique après une étude de convergence en maillage (dont le maillage le plus fin a une taille de  $4097 \times 4097$ ).

Le maillage initial était de taille  $129 \times 129$  et le maillage adapté de taille  $257 \times 257$ . La valeur de  $CD_p$  obtenue sur le maillage adapté est  $0,380 \cdot 10^{-4}$  à comparer à la valeur obtenue sur le maillage régulier de même taille  $10,331 \cdot 10^{-4}$  et celle obtenue sur un maillage de même taille dont les lignes sont resserrées autour du profil selon une loi classique  $1,079 \cdot 10^{-4}$ .

La méthode a également été appliquée à un cas tridimensionnel pour un écoulement de fluide parfait autour de l'aile M6. Les maillages utilisés ont été construits par D. Destarac (ONERA/DAAP) à partir des maillages en O de l'étude en 2D. L'écoulement considéré est transsonique ( $M_\infty = 0,84$ ) avec une incidence  $AoA = 3,06^\circ$ . Les fonctions d'intérêt sont les mêmes que dans l'étude 2D ( $CD_p$  et  $P_a$ ) et les valeurs limites ont également été extrapolées à l'aide d'une étude de convergence en maillage (dont le maillage fin était de taille  $513 \times 513 \times 257$ ). Le maillage initial est de taille  $65 \times 65 \times 33$  et le maillage adapté de taille  $129 \times 129 \times 65$ . La valeur limite de  $CD_p$  est  $122,3 \cdot 10^{-4}$ . La valeur de  $CD_p$  sur le maillage adapté est  $129,6 \cdot 10^{-4}$  à comparer à la valeur obtenue sur le maillage régulier de même taille  $154,9 \cdot 10^{-4}$  et celle obtenue sur un maillage de même taille dont les plans sont resserrés selon une loi classique autour de l'aile  $133,1 \cdot 10^{-4}$ .

### 2.2 Adaptation par déplacements de nœuds

L'approche consistant à déplacer les nœuds existants a également été considérée. Cette méthode s'appuie sur une paramétrisation du maillage. Plus précisément la paramétrisation détermine la position des lignes du maillage entre celles d'un maillage fin. Des polynômes de Bernstein ont été utilisés pour paramétrer indépendamment la position des lignes du maillage dans les différentes directions topologiques tout en préservant une contrainte de régularité. En notant  $\beta$  ces paramètres, il est possible de calculer la dérivée de la fonction d'intérêt par rapport à  $\beta$  à l'aide de  $dJ/dX$  :

$$\frac{d\mathcal{J}}{d\beta} = \frac{dJ}{dX} \frac{dX}{d\beta}$$

Ainsi en se plaçant dans le cas où la fonction d'intérêt est affectée de façon monotone par la dissipation numérique, la méthode consistait à maximiser ou minimiser la fonction à l'aide d'un algorithme de descente. Plus précisément la méthode consistait à minimiser  $CD_p$  et à maximiser  $P_a$  dans le cas subsonique et à maximiser  $P_a$  dans le cas transsonique.

Dans le cas 2D subsonique, la valeur de  $CD_p$  est passée de  $10,331 \cdot 10^{-4}$  à  $0,739 \cdot 10^{-4}$  soit une réduction de 92,85% de l'erreur. Pour le cas transsonique la valeur de  $P_a$  est passée de 0,97744 à 0,99280. D'autre part il a été observé que la valeur de  $CD_p$  a également été améliorée au cours de cette adaptation. Dans le cas 3D la valeur de  $P_a$  est passée de 0,9746 à 0,9881 (à comparer à la valeur limite extrapolée de 0,9949).

La méthode consistant à maximiser ou minimiser la fonction directement à l'aide de  $dJ/dX$  sans paramétrisation a été mise en œuvre [51]. Cette approche a conduit à de mauvais résultats : les maillages obtenus présentaient d'importantes irrégularités locales. Des adaptations sans paramétrisation utilisant un champ  $dJ/dX$  moyenné a conduit à des maillages plus réguliers mais les valeurs de fonctions étaient comparables.

### 2.3 Critères de qualité de maillage pour le calcul de fonctions

Le dérivée totale  $dJ/dX$  peut également être utilisée pour construire des indicateurs scalaires destinés à évaluer la qualité globale d'un maillage pour le calcul de la fonction  $J$ . Le premier indicateur considéré est la moyenne de  $\|dJ/dX\|$  de l'ensemble des nœuds du maillage (noté  $\mu_J$ ). Une autre approche est de prendre en compte les déplacements admissibles de chacun des nœuds en multipliant la norme  $\|dJ/dX\|$  de chaque nœud par la moitié de la distance au nœud voisin le plus proche. Le second indicateur est la moyenne de ce champ (noté  $\theta_J$ ). Il a été observé que ces indicateurs sont plus faibles sur les maillages adaptés.

## Conclusions

Les premiers résultats d'adaptation de maillages basés sur la dérivée totale de fonctions aérodynamiques par rapport aux coordonnées du maillage confirment la pertinence de cette grandeur pour réduire l'erreur de discrétisation commise sur l'estimation de ces fonctions. D'autre part des critères de qualité de maillage  $\mu_J$  et  $\theta_J$  ont été étudiés et montrent que cette dérivée peut aussi être utilisée pour construire des indicateurs globaux de qualité de maillage. Ces indicateurs globaux étaient basés soit sur la moyenne de la norme de  $dJ/dX$  soit sur la moyenne de  $dJ/dX$  multipliée par une longueur caractéristique en chaque nœud. Une étude plus approfondie de critères de ce type est effectuée dans le chapitre 3, où les critères locaux associés sont utilisés pour effectuer les adaptations de maillage.

D'autre part la présente étude montre également que les méthodes de remaillage utilisées ont une influence particulière. En effet les maillages considérés dans cette étude étant structurés, les remaillages se faisaient par ajout (ou déplacement) de lignes entières. Ainsi elles operaient une augmentation de la densité de nœuds dans les zones détectées par le senseur et simultanément dans des zones qui ne nécessitent par forcément un raffinement. D'où l'intérêt de mettre en œuvre des méthodes d'adaptation de maillage plus efficaces permettant d'effectuer des adaptations plus locales. Une telle méthode basée sur un système d'équations aux dérivées partielles elliptiques a été étudié et utilisée. Cette méthode est présentée dans le chapitre 3.

## Chapter 2

# Mesh adaptation based on the goal derivative w.r.t. mesh coordinates

As introduced in the previous chapter, the goal oriented mesh adaptation methods developed since many years often use the adjoint vector of the functions of interest. Some of these methods can be applied for both linear and non-linear problems and for both linear and non-linear functions. The reference strategy in the literature is the one of Venditti and Darmofal. They use the adjoint vector in order to build up a correction estimation of the output value. The main drawback of this approach is the need of two levels of grids. Another strategy using the adjoint vector is the one proposed by Dwight. This method consists in building error indicator based on the dissipation coefficient of the Jameson *et. al.* scheme. The drawback of this approach is that the method is connected to the use of a particular scheme.

Nielsen and Park introduced the total derivative of the function of interest w.r.t. mesh node coordinates ( $dJ/dX$ ) [43] in the framework of shape optimization in order to avoid the huge storage of the mesh sensitivities. This technique has been used by several authors [41, 27].

This derivative is a link between the functional output  $J$  and the mesh  $X$  that is used for the numerical simulation. This derivative is at the basis of all the methods developed in this work. Therefore more details about this quantity is presented in the following section. This presentation is followed in section 2.2 by the introduction of the first methodology based on  $dJ/dX$  that has been developed. Finally more details about intuitive, but not fruitful, approaches are presented in the last section of this chapter.

## 2.1 The total derivative of aerodynamic functions w.r.t. mesh coordinates

The derivative  $dJ/dX$  is a vector at each node that is the sensitivity of the functional output estimation w.r.t. the node. Hence this quantity is a link between the function of interest and the mesh that is used for the numerical simulation. The following figures illustrate the total derivative of the pressure drag coefficient  $CD_p$  around the NACA0012 airfoil for a subsonic inviscid flow.

## 2.1. THE TOTAL DERIVATIVE OF AERODYNAMIC FUNCTIONS W.R.T. MESH COORDINATES

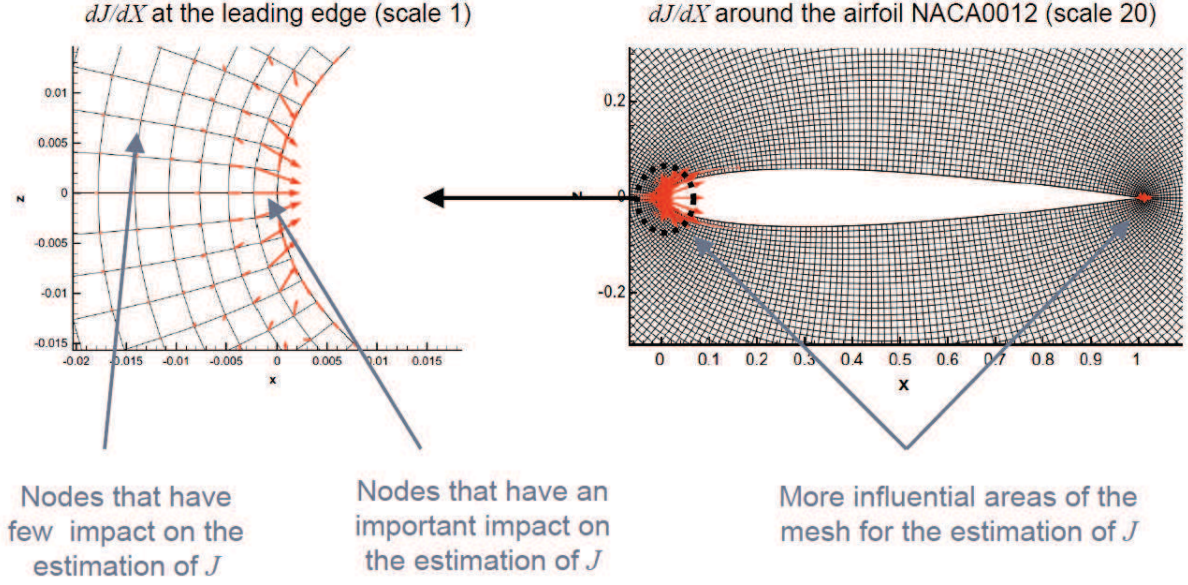


Figure 2.1:  $dC_{D_p}/dX$  field around the NACA0012 airfoil (Eulerian flow,  $M_\infty = 0.5$ ,  $\text{AoA} = 0^\circ$ )

We notice that  $dC_{D_p}/dX$  allows to identify the most sensitive areas of the mesh for the computation of the function (in this case the leading and the trailing edges). Therefore this derivative is a reliable quantity for goal oriented mesh adaptation and also for the construction of mesh quality criteria for the computation of  $J$ .

The expression of  $d\mathcal{J}/d\alpha$  computed thanks to the adjoint vector, presented in subsection 1.2.1 (equation (1.4)), allows to identify  $dJ/dX$ :

$$\begin{aligned} \frac{d\mathcal{J}}{d\alpha} &= \frac{\partial J}{\partial X} \frac{dX}{d\alpha} + \frac{\partial J}{\partial W_b} \frac{dW_b}{dX} \frac{dX}{d\alpha} + \Lambda^T \frac{\partial R}{\partial X} \frac{dX}{d\alpha} \\ &= \left( \frac{\partial J}{\partial X} + \frac{\partial J}{\partial W_b} \frac{dW_b}{dX} + \Lambda^T \frac{\partial R}{\partial X} \right) \frac{dX}{d\alpha} \\ &= \frac{dJ}{dX} \frac{dX}{d\alpha} \end{aligned}$$

In the expression of  $dJ/dX$  computed by the adjoint method two terms appear:

$$\frac{dJ}{dX} = \underbrace{\frac{\partial J}{\partial X} + \frac{\partial J}{\partial W_b} \frac{dW_b}{dX}}_{\text{Geometrical derivative}} + \underbrace{\Lambda^T \frac{\partial R}{\partial X}}_{\text{Aerodynamic derivative}} \quad (2.1)$$

The first term is the “geometrical derivative” that corresponds to the sensitivity of the output w.r.t. the position of the nodes of its support. The second one is the “aerodynamic derivative” that corresponds to the sensitivity of the output w.r.t. mesh nodes location due to the sensitivity of the aerodynamic field w.r.t. the mesh nodes location. As an example the following figures illustrate a mesh around the NACA64A212 airfoil (size 257) and the isochores of a Eulerian flow with  $M_\infty = 0.75$ ,  $\text{AoA} = 2.5^\circ$ .

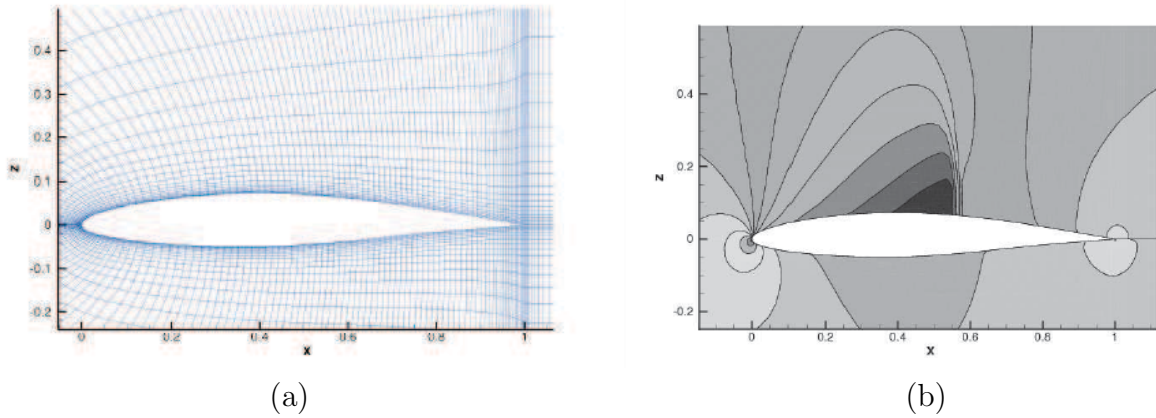


Figure 2.2: (a) C-type grid around the NACA64A212 airfoil (size 257) (b) Isochores of a Eulerian flow with  $M_\infty = 0.75$ ,  $AoA = 2.5^\circ$

A shock wave is located on the extrados of the airfoil. The wave drag  $CD_w$  can be computed using the code *FFD72*. The integration contour is illustrated on the figure 2.3(a).

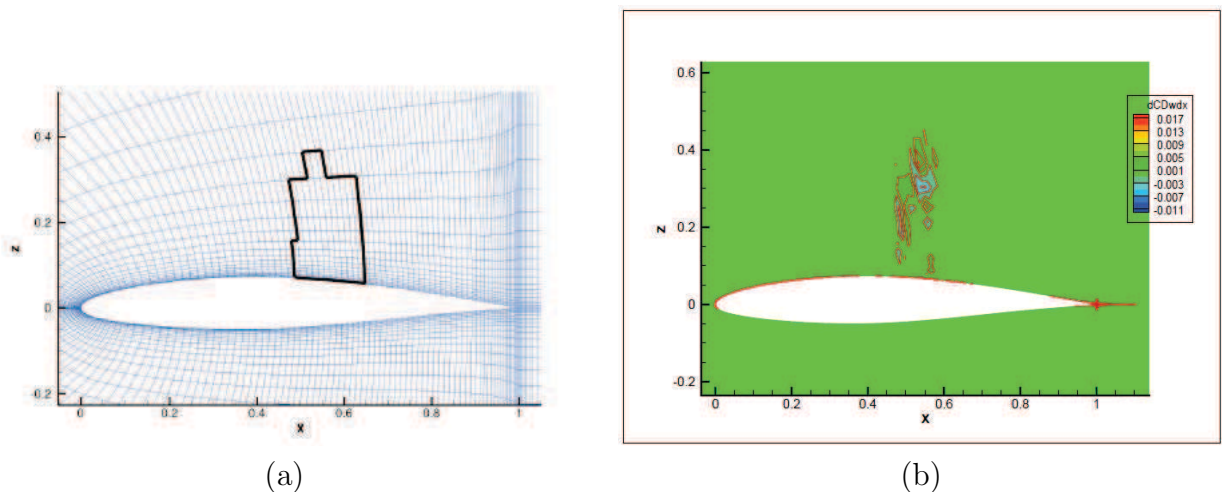


Figure 2.3: (a) Integration contour for the computation of the wave drag  $CD_w$  (b)  $x$ -component of the total derivative  $dCD_w/dX$

The figure 2.3(b) shows the  $x$ -component of the total derivative  $dCD_w/dX$ . We notice that important values are located on the support of the function and also around the airfoil and near the trailing edge. Moreover the following figures illustrate the breakdown of this derivative according to equation (2.1).

## 2.2. THE PROPOSED METHODOLOGY APPLIED TO EULERIAN FLOWS

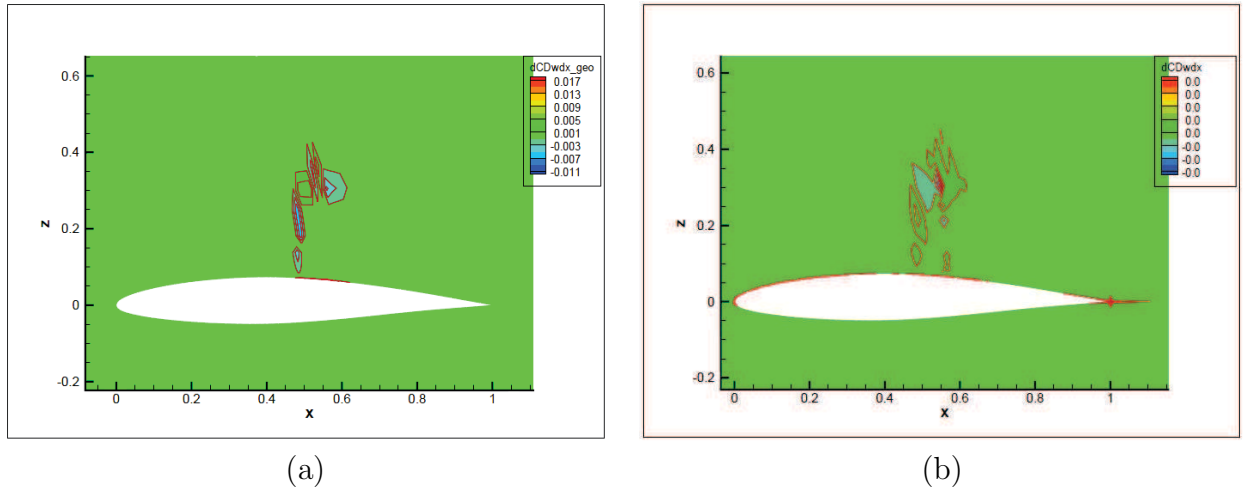


Figure 2.4: (a) Geometrical derivative of  $dC_{D_w}/dX$  (b) Aerodynamic derivative of  $dC_{D_w}/dX$

We notice that the high values of the geometrical derivative are obviously located only on the support of the function and that the other high values present on the complete derivative actually come from the aerodynamic derivative.

## 2.2 The proposed methodology applied to Eulerian flows

This section presents the first use of  $dJ/dX$  for goal oriented mesh adaptation. These results have been presented in an article in the journal *Computers & Fluids* [49] that is the body of the section. After recalling in more details the state of the art, a strategy based on the derivative  $dJ/dX$  is presented. The mesh adaptation methods used are both based on mesh node displacements and mesh refinement and they have been applied for both 2D and 3D Eulerian flows computation. Indicators of mesh quality are also introduced.

Goal oriented mesh adaptation using total derivative of aerodynamic functions with respect to mesh coordinates. With applications to Euler flows.

Jacques Peter<sup>a,\*</sup>, Maxime Nguyen-Dinh<sup>b</sup>, Pierre Trontin<sup>a</sup>

<sup>a</sup>ONERA/DSNA. 29, av. de la Division Leclerc, 92322 Chatillon Cedex, France

<sup>b</sup>AIRBUS Opérations S.A.S. 316, route de Bayonne, 31060 Toulouse Cedex 09, France

**Abstract**

In aeronautical CFD, engineers require accurate predictions of the forces and moments but they are less concerned with the accuracy of the detailed flow-field. Hence, the so-called “goal oriented” mesh adaptation strategies have been introduced to get satisfactory values of functional outputs at an acceptable cost, using local node displacement and insertion of new points rather than mesh refinement guided by uniform accuracy. Most often, such methods involve the adjoint vector of the function of interest. Our purpose is precisely to present new goal oriented mesh adaptation strategies in the framework of finite-volume schemes and a discrete adjoint method. It is based on the total derivative of the goal with respect to (w.r.t.) mesh nodes. More precisely, a projection of the goal derivative, removing all components corresponding to geometrical changes in the solid walls or the support of the output, is used to adapt the meshes either by inserting new nodes or by displacing current mesh nodes. The methods are assessed in the case of 2D and 3D Euler flow computations.

*Keywords:* Goal oriented mesh adaptation, Discrete adjoint method, Steady compressible equations, Finite-Volume scheme.

**Nomenclature**

AoA	Angle of attack
$B_{q,l}$	$(q + 1)^{th}$ Bernstein polynomial of degree $l$
$\mathcal{B}$	Linear interpolation operator in the reference fine mesh
$c$	Chord of airfoil
$CDp$	Drag coefficient
$c_i$	Mesh refinement criterion for mesh lines $i$ (resp. of planes $i$ )
$\bar{c}_{i+1/2}$	Mesh refinement criterion for rows of cells $i$
$E$	Total energy
$F$	Finite-volume flux
$F^R$	Roe’s flux formula, components $F^{R,k}$ ( $k \in \{1, 4\}$ )
$H, h$	Characteristic mesh size of coarse ( $H$ ) and fine ( $h$ ) grid
$i, j$ ( $, k$ )	Mesh indices of a 2D (resp. 3D) mesh
$\bar{i}, \bar{j}$ ( $, \bar{k}$ )	Reduced mesh indices in $[0, 1]^2$ (resp. $[0, 1]^3$ )
$J$ ( $J_m$ )	Aerodynamic function as function of flow field and volume mesh
$J$ ( $J_m$ )	Aerodynamic objective function as function of volume mesh
$\mathcal{J}$ ( $\mathcal{J}_m$ )	Aerodynamic function as function of a vector of design parameters
$\mathcal{P}(dJ/dX)$	Projection of $dJ/dX$ canceling components orthogonal to function support and solid walls
$k^2, k^4$	Artificial dissipation coefficients of Jameson <i>et al.</i> scheme [32]
$M, M_\infty$	Mach number and Mach number of far-field flow

\*Corresponding author Phone +33 1 46 73 41 84 Fax +33 1 46 73 41 66

Email addresses: [jacques.peter@onera.fr](mailto:jacques.peter@onera.fr) (Jacques Peter), [maxime.nguyen-dinh@airbus.com](mailto:maxime.nguyen-dinh@airbus.com) (Maxime Nguyen-Dinh), [pierre.trontin@onera.fr](mailto:pierre.trontin@onera.fr) (Pierre Trontin)

## 2.2. THE PROPOSED METHODOLOGY APPLIED TO EULERIAN FLOWS

$n$	Normal vector to solid wall, support of $J$ or outer boundary
$N_\alpha$	Number of design parameters
$N_i, N_j, N_k$	Number of mesh lines (resp. planes) of the structured mesh in each direction
$N_J$	Number of functions to be differentiated
$N_W$	Size of vectors $W$ and $R$
$p$	Static pressure
$P_a$	Mean stagnation pressure over airfoil or wing contour
$p_a, p_{a\infty}$	Stagnation pressure and stagnation pressure of far-field flow
$Q$	Maximum number of mesh lines (resp. planes) to be added between two lines (resp. planes) of current mesh
$r$	Half the radius of the circle (resp. sphere) inscribed in the cells surrounding one node
$R$	Finite-volume numerical scheme
$S(S^X, S^Z)$	Surface vector
$w$	State variable of direct model problem
$W$	Discrete conservative variables
$X$	Volume mesh
$\alpha$	Vector of design parameters
$\beta$	Vector of parameters of mapping $\Phi$
$\epsilon$	Array of cell-widths (in parameter space)
$\varepsilon$	Width of a cell row (component of $\epsilon$ )
$\gamma$	Specific heat ratio
$\Gamma$	Airfoil contour (length $L(\Gamma)$ )
$\lambda$	Adjoint variable of model problem
$\Lambda$ ( $\Lambda_m$ )	Adjoint vector of $J$ ( $J_m$ ) for scheme $R$ , component $\Lambda^k$ ( $\Lambda_m^k$ ) ( $k \in \{1, 4\}$ )
$\mu_J$	Mean of $\ \mathcal{P}(dJ/dX)\ $ field
$\theta_J$	Bound of first-order variation of $J$ for a specific displacement of nodes
$\rho$	Density
$\Phi$	Mapping function
$\chi_{N_i, N_j, N_k}$	Linear function mapping $[0, 1]^2$ (resp. $[0, 1]^3$ ) in $[1, N_i] \times [1, N_j]$ (resp. $[1, N_i] \times [1, N_j] \times [1, N_k]$ )
$\Omega$	Fixed surface inside the fluid domain (boundary $\partial\Omega$ )

### 1. Introduction

In many cases, engineers require accurate predictions of functional outputs based on a numerical simulation but they are less concerned with the accuracy of the whole field of state variables. Hence, the so-called “goal oriented” mesh adaptation strategies have been introduced to get satisfactory values of these functions at an acceptable cost, using local node displacement and insertion of new points rather than mesh refinement over the entire computational domain.

In the context of finite elements, a successful theory of *a posteriori* error and goal oriented mesh adaptation has been developed since the mid 90’s. Important contributions include the work of Johnson, Rannacher, Becker and co-workers [1, 2, 3], Giles, Pierce and co-workers [4], Prudhomme et al. [5], Larson and Barth [6], Machiels et al. [7], Hartman and co-workers [8, 9, 10] and Alauzet, Dervieux and co-workers [11]. In the framework of finite-difference/finite-volume methods contributions are less numerous. The main ones are described in subsection one before the proposed methods are briefly described (subsection two) and the outline of this text is presented (subsection three).

#### 1.1. Goal oriented mesh adaptation for finite-volume schemes. State of the art

At the end of the 90’s, Pierce and Giles introduced adjoint-based error estimation for functions in a very broad framework [12, 13]. It is simply supposed, that in a Hilbert space  $\mathcal{H}$ , whose inner product is denoted  $(\cdot, \cdot)$ : (a) a well-posed “direct” linear differential equation  $Lw = f$  can be solved, exactly or approximately, before computing the scalar product of the (possibly approximate) solution by another vector  $g$  of  $\mathcal{H}$ ; (b) a corresponding adjoint problem  $L^*\lambda = g$  is well defined and can be solved exactly or approximately, before

computing the dot product of the (possibly approximate) solution by  $f$ .

The error in the estimation of the common goal  $(g, w) = (L^* \lambda, w) = (\lambda, Lw) = (\lambda, f)$ , by the approximate solution  $w_h$  ( $h$  denoting the average mesh size) of the direct problem is

$$(g, w) - (g, w_h) = (g, (w - w_h)) = (L^* \lambda, (w - w_h)) = (\lambda, L(w - w_h)) = (\lambda, f - Lw_h) \quad (1)$$

If the adjoint problem has also been approximately solved, the error can be expressed as

$$(g, w) - (g, w_h) = (\lambda_h, f - Lw_h) + (\lambda - \lambda_h, f - Lw_h) \quad (2)$$

Pierce and Giles have given a detailed analysis of these formulas for a wide range of problems and numerical methods (including both finite-difference and finite-element methods). The main error term is  $(\lambda_h, f - Lw_h)$  and in common cases, the order of  $(\lambda - \lambda_h, f - Lw_h)$  is twice the order of the first term. At last, let us notice that the error in the function of interest,  $(\lambda_h, f - Lw_h)$ , is expressed as a weighted sum of the local residual errors of the direct problem with the adjoint variables as the weighting functions.

In a series of three articles [14, 15, 16], Venditti and Darmofal have proposed similar formulas for the specific case of finite differences/finite-volume and discrete adjoint and presented applications to compressible flow computations. Let us define the basic notations employed here for finite-volume CFD computations:  $W$  is the flow field (size  $N_W$ ),  $X$  is the volume mesh and  $R$  is the residual of the scheme. At steady state, these variables satisfy  $R(W, X) = 0$  (set of  $N_W$  nonlinear equations to be solved for  $W$ ). The method involves two grids: a coarse one of characteristic mesh size  $H$ , and a fine one of characteristic mesh size  $h$ . The full computation of the flow field and the output of interest on level  $H$  is supposed to be affordable, whereas it would be prohibitively expensive on level  $h$ . The subscripts  $h$  and  $H$  will be attached to  $R$ ,  $X$  and  $W$ . Lastly,  $W_h^H$  and  $\lambda_h^H$  represent the coarse-grid flow-field and adjoint vector reconstructed on the fine grid via some consistent projection operator. A Taylor's expansion of the functional output of interest  $J_h$  about the interpolated coarse-grid solution yields

$$J_h(W_h, X_h) = J_h(W_h^H, X_h) + \left( \frac{\partial J}{\partial W} \Big|_{W_h^H} \right) (W_h - W_h^H) + \mathcal{O}(\|W_h - W_h^H\|^2)$$

Using an adjoint-like equation solved on the fine grid (3) and then a Taylor's expansion of  $R$  about  $W_h^H$ :

$$(\Lambda_h \Big|_{W_h^H})^T \left( \frac{\partial R_h}{\partial W_h} \Big|_{W_h^H} \right) = - \frac{\partial J_h}{\partial W_h} \Big|_{W_h^H} \quad (3)$$

$$\begin{aligned} J_h(W_h, X_h) &= J_h(W_h^H, X_h) - (\Lambda_h \Big|_{W_h^H})^T \left( \frac{\partial R_h}{\partial W_h} \Big|_{W_h^H} \right) (W_h - W_h^H) + \mathcal{O}(\|W_h - W_h^H\|^2) \\ &= J_h(W_h^H, X_h) + (\Lambda_h \Big|_{W_h^H})^T R_h(W_h^H) + \mathcal{O}(\|W_h - W_h^H\|^2) \end{aligned} \quad (4)$$

Comparison of equations (1) and (4) demonstrates the link between the method of Pierce and Giles and that of Venditti and Darmofal. Besides, if the flow computation is not affordable on the fine grid, neither is the solution of equation (3) for  $(\Lambda_h \Big|_{W_h^H})^T$ . The alternative is to replace this adjoint field by the interpolated coarse-grid adjoint,

$$J_h(W_h, X_h) \simeq J_h(W_h^H, X_h) + \underbrace{(\Lambda_h^H)^T R_h(W_h^H)}_{\text{computable correction}} + \underbrace{((\Lambda_h \Big|_{W_h^H})^T - (\Lambda_h^H)^T) R_h(W_h^H)}_{\text{error in computable correction}}$$

The authors recommend to take  $J_h(W_h^H, X_h) + \Lambda_h^H R_h(W_h^H)$  as the function estimate and adapt the mesh by reducing uniformly the error in computable correction.

These formulas have raised a deep interest in the aeronautical CFD community (see references [18] to [31]). They were used for unstructured meshes [17, 18, 20, 22, 23, 24, 26, 28, 29], structured meshes [19, 21, 30, 31] and embedded-boundary Cartesian meshes [25, 27]. Most often Euler flows were considered [18, 19, 21, 25, 26, 27, 28, 29, 30] and very convincing results have been presented. Concerning Reynolds averaged Navier-Stokes (RANS) flows, Venditti and Darmofal have used the exact adjoint of RANS and Spalart-Allmaras

## 2.2. THE PROPOSED METHODOLOGY APPLIED TO EULERIAN FLOWS

one-equation model as coded in the FUN2D code and reported very good results for a RAE2822 airfoil (transonic flow conditions) and a three-element airfoil (subcritical flow conditions) [16]. Park et al. [17, 20], Kim et al. [22] and Balasubramanian et al. [24] have also presented satisfactory results for RANS flows around (respectively) an airfoil and the DLR-F6 wing-body, an isolated wing and an airfoil. Unfortunately, full linearization of RANS plus turbulence model equations often results for complex geometries in a dramatically poor conditioning of the Jacobian. This is why the “frozen turbulent viscosity” assumption is still often made. In this context, far less satisfactory results were reported by Tourrette et al. in [31]. Later on, Dwight has proposed a very different adjoint-based method attached to Jameson et al. scheme [32]. In a series of two articles [33, 34], he considered classical test cases for Euler flows. He ran computations using Jameson et al. scheme [32] on hierarchies of grids and for different sets of artificial dissipation coefficients ( $k^2, k^4$ ). The error for the functions of interest appeared to be mainly due to artificial dissipation. On this basis, the following measure for the approximation error in the Jameson et al. scheme has been proposed:

$$k^2 \frac{dJ}{dk^2} + k^4 \frac{dJ}{dk^4}$$

The dissipation coefficients are then interpreted as being defined independently for each control volume. This leads to a local indicator for dissipation-error in cell  $l$ :

$$k^2 \frac{dJ}{dk_l^2} + k^4 \frac{dJ}{dk_l^4}$$

The derivatives  $dJ/dk_l^2$  and  $dJ/dk_l^4$  can only be computed by the adjoint method. The field of local indicator for dissipation error is used as a mesh refinement indicator and  $J - k^2 dJ/dk^2 - k^4 dJ/dk^4$  is considered as the corrected output value.

A more detailed state of the art about output-based error estimation and mesh adaptation can be found in the recent review by Fidkowski and Darmofal [35].

### 1.2. Proposed methods

The aim of this study is to define new methods for finite-volume goal oriented mesh adaptation, in which only one base grid is used, on that is not restricted to a specific scheme.

For the sake of clarity, a distinction is first made between two ways of considering the same aerodynamic output of interest: (a) using standard dependencies, the output  $J$  is a function of the flow field and the volume mesh ; (b) as the equations of the finite-volume scheme define the flow field from the mesh, the output – then denoted  $J$  – can be viewed as a function of the mesh only. The total derivative of the goal  $J$  w.r.t. volume mesh coordinates, which is also the Jacobian of  $J$ ,  $dJ/dX$ , is the basis of the proposed method. This vector field indicates the variation of the output with the coordinates of the mesh nodes.

Nevertheless, the  $dJ/dX$ -field may include components orthogonal to the solid walls, which are obviously not usable in the framework of mesh adaptation. In the common case where  $J$  is a line integral (in 2D) or a surface integral (in 3D), its total derivative w.r.t. mesh nodes may also include components orthogonal to the integral support which cannot be taken into account during mesh adaptation. This leads to the definition of a projected field denoted  $\mathcal{P}(dJ/dX)$ . This field is analyzed in the simple case of near-field drag for a subcritical inviscid flow, using various meshes (coarse to fine, adapted/not adapted for  $CDp$  computation). This examination has let us to define two mesh-adaptation methods based on  $\mathcal{P}(dJ/dX)$ :

- a general heuristic node addition method consisting in adding nodes in areas of high  $\|\mathcal{P}(dJ/dX)\|$ -values ;
- a node-displacement method well-suited for specific flows for which a functional output is monotonically affected by numerical dissipation (like theoretical zero drag of subcritical Euler flows that is systematically overestimated in flow simulations due to numerical dissipation).

Finally, note that Yamaleev et al. also considered the total derivative of a functional output w.r.t. mesh coordinates in the framework of grid adaptation [36]. Their method focuses on the sensitivity of the error in an output and requires, in its present form, the exact value of this output. It is presented in the general framework of unsteady flow and moving meshes. In the applications carried out up to now, small displacements of nodes of unstructured meshes are achieved to reduce the error for steady state flows. The proposed node-displacement method is based on the same principle but can handle larger displacements of structured mesh lines/planes using parametrization. The proposed node addition method does not require the exact value of the output.

1.3. *Outline*

After recalling certain generalities about discrete sensitivity analysis, the Jacobian of the function  $J$  is identified and the projected field, relevant to  $J$ -oriented mesh adaptation, are derived and analyzed in the second section. The three following sections are devoted to application to 2D Euler flows: the geometry is presented in section three, where the relevance of drag minimization (for subcritical flow) and total pressure maximization (for subcritical and transonic flow conditions) is discussed. Mesh adaptation based on the projected total derivative of these functions are then presented in section four (with the line-addition method) and five (with the node displacement method). The last section is devoted to the assessment of the method for a 3D Euler flow.

**2. Projected total derivative of functional output w.r.t. mesh nodes**

The equations of discrete sensitivity computation are discussed in detail in subsection 2.1. This leads to the identification of the total derivative of aerodynamic functions w.r.t. volume mesh nodes in the second subsection. The derivation of a projection of this field, suitable for mesh adaptation, is the subject of the next subsection. Subsections 2.5 to 2.8 present both theoretical analysis of this field and its examination for meshes, schemes and a simple test case introduced in subsection 2.4.

2.1. *Discrete sensitivity analysis in the framework of finite-volume methods*

The basic notations for finite-volume CFD have been introduced in subsection (1.1): the state variables (aerodynamic conservative variables) are denoted  $W$  (vector of size  $N_W$ ), the volume mesh is denoted  $X$ . At steady state these vectors satisfy the discrete equations of fluid mechanics (a discrete form of Euler or RANS equations for example):

$$R(W, X) = 0 \tag{5}$$

(in general, a nonlinear set of  $N_W$  equations). In the context of sensitivity analysis, the volume mesh depends on a vector of design parameters  $\alpha \in D_\alpha \subset R^{N_\alpha}$ . Some more assumptions are required to compute first order derivatives:

- (1)  $X(\alpha)$  is supposed to be  $C^1$  regular;
- (2)  $R$  is supposed to have  $C^1$  regularity w.r.t. its two vector arguments;
- (3) the property  $\det[(\partial R/\partial W)](W, X(\alpha)) \neq 0$  is supposed to be true for all meshes of  $D_\alpha$  and corresponding steady state flows ( $R(W, X(\alpha)) = 0$ ).

Under assumptions (1),(2) and (3), the implicit function theorem allows us to define  $W$  as a  $C^1$  function of  $X$ , for all the volume meshes defined by  $\alpha \in D_\alpha$ .

In this context, an aerodynamic function  $J$ , that naturally appears has a function of the mesh  $X$  and the flow field  $W$  can be defined as a function  $J$  of mesh  $X$  only. Besides the same aerodynamic function, can be seen from the designer point of view as a function  $\mathcal{J}$  of the design parameters  $\alpha$ . These functions are linked by the simple equations

$$J(X) = J(W, X) \quad \text{where } R(W, X) = 0 \tag{6}$$

$$\mathcal{J}(\alpha) = J(W(\alpha), X(\alpha)) \quad \text{where } R(W(\alpha), X(\alpha)) = 0 \tag{7}$$

Sensitivity analysis typically aims to compute the derivatives of  $N_J$  aerodynamic functions  $\mathcal{J}_1, \mathcal{J}_2, \dots, \mathcal{J}_{N_J}$  w.r.t. to  $N_\alpha$  design parameters  $\alpha_l$ . These sensitivities are most often computed during shape optimizations ; in this context, one of the function is the objective whereas the others are the constraints or the active constraints depending on the optimization algorithm [37]. The subject of sensitivity computation for compressible flow simulations started with the landmark article of Jameson [38]; a recent article [39] gives a status on this topic after twenty years of research. In the framework of the discrete approach, the derivatives of interest can be computed by the direct differentiation method ( $DD$ ) [40, 41] or the discrete adjoint vector

## 2.2. THE PROPOSED METHODOLOGY APPLIED TO EULERIAN FLOWS

method (AV) [42] (provided  $J_m$   $m \in [1, N_J]$  are also  $C^1$  regular):

$$\begin{aligned} & \forall m \in [1, N_J] \quad \forall l \in [1, N_\alpha] \\ (DD) \text{ solve } & \frac{\partial R}{\partial W} \frac{dW}{d\alpha_l} = -\frac{\partial R}{\partial X} \frac{dX}{d\alpha_l} \end{aligned} \quad (8)$$

$$\text{compute } \frac{dJ_m}{d\alpha_l} = \frac{\partial J_m}{\partial X} \frac{dX}{d\alpha_l} + \frac{\partial J_m}{\partial W} \frac{dW}{d\alpha_l} \quad (9)$$

$$(AV) \text{ solve } \left(\frac{\partial R}{\partial W}\right)^T \Lambda_m = -\left(\frac{\partial J_m}{\partial W}\right)^T \quad (10)$$

$$\text{compute } \frac{dJ_m}{d\alpha_l} = \frac{\partial J_m}{\partial X} \frac{dX}{d\alpha_l} + \Lambda_m^T \left(\frac{\partial R}{\partial X} \frac{dX}{d\alpha_l}\right) \quad (11)$$

The derivatives given in equations (9) and (11) are sums of two terms. The first is a geometrical sensitivity (change in the function of interest due to the change of shape steered by the design parameter  $\alpha_l$ ). The second term is the aerodynamic sensitivity (change in the function of interest due to the change in the flow-field caused by the change of shape).

The CPU costly operation of (DD) and (AV) is the solution of the large linear systems of size  $N_W$  (equations (8) and (10)). The number of linear systems to be solved is equal to the number of design parameters ( $N_\alpha$ ) for (DD) as it is equal to the number of functions to differentiate ( $N_J$ ) for (AV). For almost all industrial shape optimizations, the number of design parameters is by far larger than the number of functions of interest. This is why the adjoint vector method raises much more interest than the direct differentiation method.

Concerning the memory requirement, both methods need the storage of the mesh sensitivities ( $dX/d\alpha_l$   $l \in [1, N_\alpha]$ ) which becomes the most stringent constraint for very large numbers of design parameters. These mesh sensitivities are needed at least for the computation of the geometrical part of the function sensitivities ( $(\partial J_m/\partial X)(dX/d\alpha_l)$ ). Concerning the geometrical sensitivity of the explicit residual ( $\partial R/\partial X)(dX/d\alpha_l)$ , it is most often estimated by second order finite differences using one of the two following formulas:

$$\begin{aligned} \frac{\partial R}{\partial X} \frac{dX}{d\alpha_l} & \simeq \frac{R(W(\alpha), X(\alpha + \delta\alpha_l)) - R(W(\alpha), X(\alpha - \delta\alpha_l))}{2\delta\alpha_l} \\ \frac{\partial R}{\partial X} \frac{dX}{d\alpha_l} & \simeq \frac{R(W(\alpha), X(\alpha) + \delta\alpha_l \frac{dX}{d\alpha_l}) - R(W(\alpha), X(\alpha) - \delta\alpha_l \frac{dX}{d\alpha_l})}{2\delta\alpha_l} \end{aligned}$$

This avoids the tedious differentiation of the numerical scheme w.r.t. metric terms. Conversely, this requires either the storage of shifted meshes  $X(\alpha + \delta\alpha_l)$  or, once again, the storage of mesh sensitivities ( $dX/d\alpha_l$ ). The adjoint mesh deformation of Nielsen and Park [43] recalled next subsection does not suffer from these demanding memory requirements. The total derivative of the functional outputs w.r.t. mesh nodes appears naturally in this context.

### 2.2. Total derivative of aerodynamic functions w.r.t. mesh nodes. Adjoint mesh deformation.

Now let us suppose that the numerical scheme  $R$  has been differentiated w.r.t. metric terms. The geometrical sensitivity of the scheme can then be expressed as a product of two Jacobian matrices and the sensitivity computed in adjoint mode (equation (11)) can be rewritten as:

$$\frac{dJ_m}{d\alpha_l} = \left(\frac{\partial J_m}{\partial X} + \Lambda_m^T \frac{\partial R}{\partial X}\right) \frac{dX}{d\alpha_l} \quad (12)$$

This clearly identifies the total derivative of the functions of interest w.r.t. the volume mesh coordinates

$$\frac{dJ_m}{dX} = \frac{\partial J_m}{\partial X} + \Lambda_m^T \frac{\partial R}{\partial X} \quad (13)$$

The meaning of the two terms of the function sensitivity w.r.t. a design parameter has been discussed before. A similar analysis can be done for equation (13): the first term,  $(\partial J_m/\partial X_k)$  corresponds to the direct dependency of function  $J_m$  on the location of node  $k$ , whereas the second term  $-\Lambda_m^T (\partial R/\partial X_k)$  corresponds to changes of the flow field on the support of function  $J_m$ , due to the change of node  $k$  location.

The first asset of this choice is that carrying out the sensitivity computation is possible using two successive computers (a) a fast, low memory computer to perform the computation of  $\Lambda_m$  and  $dJ_m/dX$  only, which does not require the storage of the volume mesh sensitivities  $dX/d\alpha_l$ ; (b) a possibly slower computer to solve the adjoint equations of the mesh deformation method (whose right hand-sides are  $\frac{dJ_m}{dX}$ ) or to directly compute the product  $(dJ_m/dX)(dX/d\alpha_l)$ . Other assets in the context of shape optimization exist (like multiple parametrizations) but are not discussed here in detail.

This was proposed by Nielsen and Park [43]. As storing volume mesh sensitivities is almost impossible for industrial shape optimizations with large numbers of parameters, this technique is now used by many authors (see for example [44, 45, 46, 47, 48, 49, 50, 51]).

### 2.3. Projection of goal derivative w.r.t. mesh nodes

When accurate predictions of a functional output  $J$  are required whereas accuracy of the whole flow field is not, goal oriented mesh adaptation strategies are the proper tools. In other circumstances, a satisfactory mesh can be characterized by the quality of approximation of an aerodynamic output. For example, for transonic Euler flows, a good mesh corresponds to a flow-field exhibiting low stagnation pressure losses or low entropy increase before and after shock waves. For subcritical Euler flows, low stagnation pressure losses or low entropy increase all over the fluid domain should be achieved.

In these two cases, the  $dJ/dX$  vector-field is an interesting input for a goal oriented mesh adaptation. Nevertheless it is not absolutely well-suited for the task: if  $J$  is a classical wall integral (like near field drag, lift...), for example, the plot of  $dJ/dX$  will presumably suggest wall-node displacements with components orthogonal to the wall, which are suitable for shape optimization but unacceptable for mesh adaptation. Hence a projected functional output gradient will be the basis of our mesh adaptation method.

Aerodynamic shape optimization for aircraft configurations is based at ONERA on far-field drag extraction [52]. In the formulas defined or casted by D. Destarac, all aerodynamic coefficients, drag components and moments are expressed as line integral in 2D and surface integrals in 3D. In the context of mesh adaptation, neither the solid shape of the body nor the integral support can be changed. Hence the total derivative of functional output w.r.t mesh nodes cannot be directly used to adapt the mesh. A projected output gradient field  $\mathcal{P}(dJ/dX)$  is defined as follows for 2D configurations

$\mathcal{P}(dJ/dX) = dJ/dX$                       Outside the support of  $J$  and solid walls contour

$\mathcal{P}(dJ/dX) =$   
 $dJ/dX - (dJ/dX \cdot n)n$                       Inside the support of  $J$ , along  
the walls, at the outer border (normal  $n$ )

$\mathcal{P}(dJ/dX) = 0$                               At a corner of the support of  $J$

The extension to 3D flows is straightforward.

### 2.4. Selected meshes, schemes and test cases for analysis of $dJ/dX$ and $\mathcal{P}(dJ/dX)$

In subsection 2.5, the order of magnitude w.r.t. a characteristic cell length  $h$  of  $dJ/dX$  terms is determined ; this requires the specification of the dependencies of the numerical flux. In subsection 2.6, the influence of mesh density, mesh quality and scheme on  $\mathcal{P}(dJ/dX)$  field is sought for. Hence the considered numerical schemes and meshes are presented from this subsection.

2D and 3D Euler flows are considered in the application sections. In this preliminary examination, only plots of  $dJ/dX / \mathcal{P}(dJ/dX)$  for a subcritical 2D flow ( $M_\infty = 0.5$  AoA=0°) around a slightly modified NACA0012 considered by Vassberg and Jameson [53, 54] are presented.

A hierarchy of meshes with O-topology was kindly provided by these authors. Each quadrilateral cell of these meshes has an aspect-ratio of one and the mesh-lines are orthogonal at each grid point. Based on these meshes, a second family was built, with aspect ratio 1/8 at the wall and power law for the width of the cells in the direction from wall to far-field [61]. The mesh size along the airfoil is minimum near  $z = 0$  (upstream of leading edge, downstream of trailing edge) and  $x = 0.5$  (shock location in the transonic case considered in section 3) at the upper and lower part of the airfoil. The ratio of the cell-width in this direction at these locations with the mean length in the other mesh direction is 1/3. The far-field boundary for both families is about 150 chord lengths away from the airfoil (see [53, 54]). In this preliminary study, meshes of sizes ranging from (129×129) nodes to (513×513) have been used.

## 2.2. THE PROPOSED METHODOLOGY APPLIED TO EULERIAN FLOWS

For this 2D test case, the number of mesh lines of the two families of structured lines is denoted  $N_i$  and  $N_j$ , the corresponding current indices are  $i$  and  $j$ . A plot of the NACA0012 is presented in figure 1(a) whereas figure 1(b) depicts the position of  $i$  and  $j$  mesh lines.

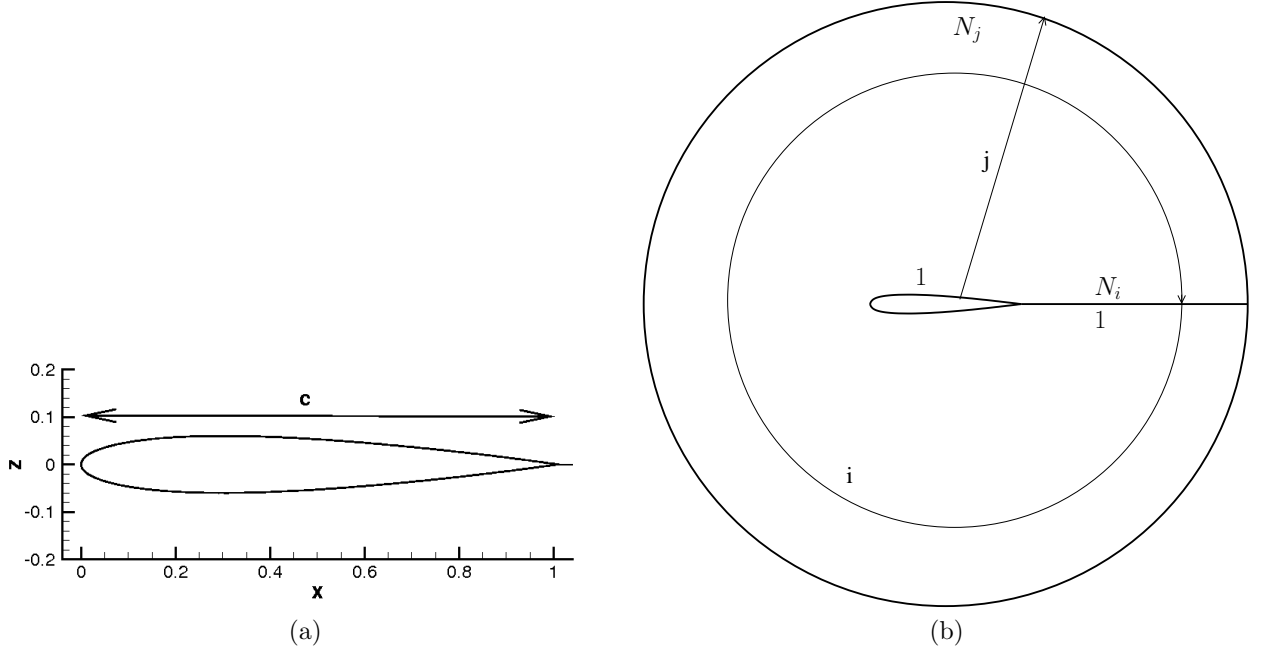


Figure 1: (a) NACA0012 airfoil configuration.  $c$  is the chord length ; (b) mesh topology of O-grids provided by Vassberg et al. [53, 54].

In most of the simulations, the Roe flux [55] has been used. Extension to second order is based on the classical MUSCL reconstruction of Van Leer [56] applied to primitive variables (density, velocity component, pressure). The selected limiting function is the one proposed by Van Albada [57]. (MUSCL formula are applied without corrections for irregular meshes) A parabolic entropy fix is included in Roe's flux formula to avoid null absolute value of eigenvalues; as a result, the numerical scheme is a  $C^1$  function of the flow field as required for discrete sensitivity computations. For the sake of comparison, a limited number of simulations was run with Jameson et al. scheme [32].

The support for this work is the *elsA* code [58], a finite-volume cell-centered code devoted to standard second order CFD analysis. Hence  $R$  is a field attached to cells (mean is not distinguished from cell-centered value as the scheme is only second-order). It is computed by standard flux balance without division by the volume.

### 2.5. Analysis of $dJ/dX$ and $\mathcal{P}(dJ/dX)$ fields

The terms in equation (13) are analyzed in the common case where the output of interest,  $J$ , is a force estimated by summation over solid walls, and  $R$  is the classical finite-volume flux balance. In this case, it can easily be checked that the dimensions of adjoint fields do not involve any length and it is actually observed that adjoint vectors converge towards regular fields as the mesh is refined.

It is also easily checked that  $(\partial J/\partial X)$  is then a first-order term in the size of the cells at the wall. Inversely the analysis of the second term of  $\Lambda^T(\partial R/\partial X)$ , is not straightforward. It is carried out for a 2D calculation and for the upwind flux of interest (Roe's flux extended to second order via MUSCL technique). The numerical flux of one face depends (a) concerning the geometry, only on the local surface vector (b) concerning the flow field, on the two extrapolated states (denoted  $W^R$  and  $W^L$  with the index of the face used as subscript). The usual  $(x, z)$  coordinates most often used for airfoils are retained.

All terms of  $\Lambda^T(\partial R/\partial x_{i,j})$  where  $(i, j)$  is a generic point inside the domain will be estimated. Using the

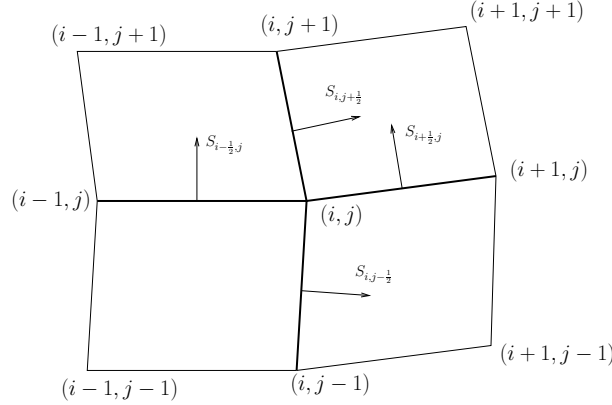


Figure 2: Notations for finite volume discretization. In bold, mesh lines connected to  $X_{ij} = (x_{ij}, z_{ij})$

notations of figure 2, the surface vector coordinates are

$$S_{i-1/2, j} \equiv \begin{pmatrix} S_{i-1/2, j}^X \\ S_{i-1/2, j}^Z \end{pmatrix} = \begin{pmatrix} z_{i-1, j} - z_{i, j} \\ x_{i, j} - x_{i-1, j} \end{pmatrix}$$

$$S_{i, j-1/2} \equiv \begin{pmatrix} S_{i, j-1/2}^X \\ S_{i, j-1/2}^Z \end{pmatrix} = \begin{pmatrix} z_{i, j} - z_{i, j-1} \\ x_{i, j-1} - x_{i, j} \end{pmatrix}$$

As stated before, the finite volume flux of face  $(i, j - 1/2)$  has following dependencies

$$F_{i, j-1/2} = F^R(W_{i, j-1/2}^L, W_{i, j-1/2}^R, S_{i, j-1/2}^X, S_{i, j-1/2}^Z)$$

(where  $F^R$  denotes Roe's flux whose components are denoted  $F^{R, k}$ ,  $k \in \{1, 4\}$ ). In order to differentiate w.r.t. node coordinates  $F_{i, j-1/2}$  may be also written

$$F_{i, j-1/2} = F^R(W_{i, j-1/2}^L, W_{i, j-1/2}^R, z_{i, j} - z_{i, j-1}, x_{i, j} - x_{i, j-1})$$

The corresponding formulas for the numerical flux in  $i$  mesh direction is

$$F_{i-1/2, j} = F^R(W_{i-1/2, j}^L, W_{i-1/2, j}^R, z_{i-1, j} - z_{i, j}, x_{i, j} - x_{i-1, j})$$

$R$  being the flux balance ( $R_{i+1/2, j+1/2} = F_{i+1, j+1/2} - F_{i, j+1/2} + F_{i+1/2, j+1} - F_{i+1/2, j}$ ), the sensitivity of the objective w.r.t. coordinate  $x_{i, j}$  through the changes in the flow field,  $\Lambda^T (\partial R / \partial x_{ij})$ , is then

$$\begin{aligned} \Lambda^T (\partial R / \partial x_{ij}) = & \\ & \sum_{k=1}^{k=4} ((\Lambda_{i+1/2, j+1/2}^k - \Lambda_{i+1/2, j-1/2}^k) \frac{\partial F^{R, k}}{\partial S^Z} (W_{i+1/2, j}^L, W_{i+1/2, j}^R, S_{i+1/2, j}^X, S_{i+1/2, j}^Z) \\ & - (\Lambda_{i-1/2, j+1/2}^k - \Lambda_{i-1/2, j-1/2}^k) \frac{\partial F^{R, k}}{\partial S^Z} (W_{i-1/2, j}^L, W_{i-1/2, j}^R, S_{i-1/2, j}^X, S_{i-1/2, j}^Z) \\ & - (\Lambda_{i+1/2, j+1/2}^k - \Lambda_{i-1/2, j+1/2}^k) \frac{\partial F^{R, k}}{\partial S^Z} (W_{i, j+1/2}^L, W_{i, j+1/2}^R, S_{i, j+1/2}^X, S_{i, j+1/2}^Z) \\ & + (\Lambda_{i+1/2, j-1/2}^k - \Lambda_{i-1/2, j-1/2}^k) \frac{\partial F^{R, k}}{\partial S^Z} (W_{i, j-1/2}^L, W_{i, j-1/2}^R, S_{i, j-1/2}^X, S_{i, j-1/2}^Z)) \end{aligned} \quad (14)$$

$\Lambda$  fields tend towards regular limiting fields as the mesh size decreases.  $\frac{\partial F^{R, k}}{\partial S^Z}$  tends toward Euler flux density in  $z$  direction as the mesh size decreases. Hence all terms of the right hand side of equation (14) are first-order in  $h$ . As two differences of two terms appear with one shifted index, the sum is second order in this scale. The theoretical order of the two parts of  $dJ/dX$  is checked for  $CDp$ , for the 2D subcritical flow on a hierarchy of three meshes. It is also verified that  $\|dCDp/dX\|$  and  $\|\mathcal{P}(dCDp/dX)\|$  have the same order of magnitude except close to the leading edge (see figures 3 and 4).

## 2.2. THE PROPOSED METHODOLOGY APPLIED TO EULERIAN FLOWS

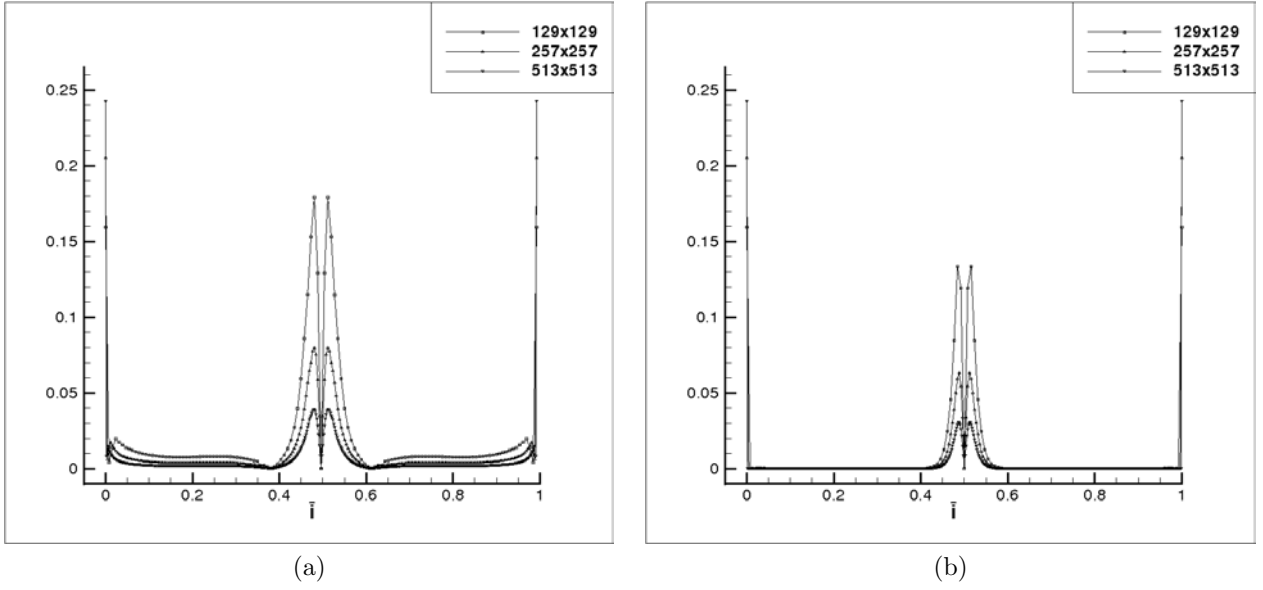


Figure 3: NACA0012. Subcritical flow. Quasi-Uniform meshes ( $129 \times 129$ ) ( $257 \times 257$ ) ( $513 \times 513$ ). (a)  $\|\mathcal{P}(dCDp/dX)\|$  along the wall (b)  $\|\mathcal{P}(dCDp/dX)\|$  along the wall

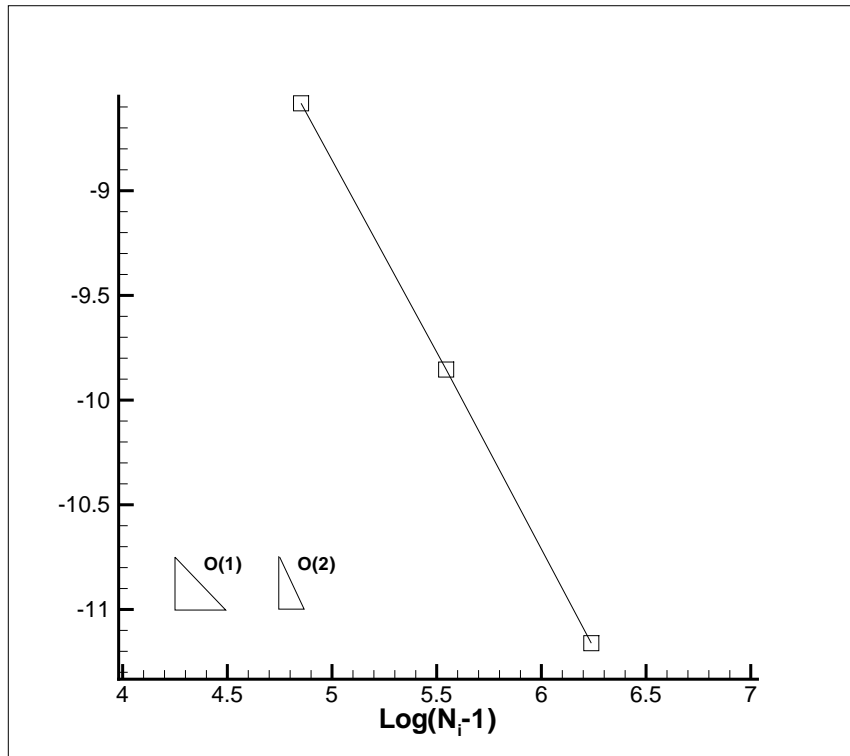


Figure 4: NACA0012. Subcritical flow. Quasi-Uniform meshes ( $129 \times 129$ ) ( $257 \times 257$ ) ( $513 \times 513$ ). log of mean of  $\|\Lambda_{CDp} \frac{\partial B}{\partial X}\|$  over the mesh

2.6. Influence of mesh density, mesh quality and scheme on the  $\mathcal{P}(dJ/dX)$  field

In order to gain intuition about the  $\mathcal{P}(dJ/dX)$  field,  $\mathcal{P}(dCDp/dX)$  and  $\mathcal{P}(dP_a/dX)$  are plotted for the upwind second order scheme for three grids – size  $(129 \times 129)$   $(257 \times 257)$   $(513 \times 513)$  – of the two families of meshes described in last but one subsection, for the subcritical Euler flow around NACA0012 airfoil ( $M_\infty = 0.5$ ,  $AoA=0^\circ$ ) – see figures 5 and 6.

The first family with quasi-uniform aspect-ratio of one and orthogonal mesh-lines, is well suited for grid convergence but not for efficient estimation of near field inviscid drag, that requires a mesh stretching close to the airfoil. The second one (right-side of the plot) precisely exhibits the stretching of classical structured meshes used for simulation of flows around airfoils.

At the scale of the wider plots of figure 5 and 6,  $\mathcal{P}(dCDp/dX)$  and  $\mathcal{P}(dP_a/dX)$  vectors can only be seen in the vicinity of the leading edge and for the point just behind the trailing edge. This is why they are plotted at the leading edge.

When examining the plots from coarse to fine meshes, it first to be noted that  $dJ/dX$  vectors are not actually much larger for the wall nodes (where they involve a first order component in space) than for the points of the interior of the domain (where they are second order in space) in the most sensitive area of the mesh (although the second order behavior is well observed for a global mean – figure 4 (b)).

As expected, for each mesh family,  $\|\mathcal{P}(dCDp/dX)\|$  and  $\|\mathcal{P}(dP_a/dX)\|$  decrease as the number of nodes increases. Besides, for the same mesh size, close to the leading edge,  $CDp$  and  $P_a$  have a significant sensitivity w.r.t. the coordinates of a larger number of points for the stretched grids (see the small plots, in particular). This suggests to consider  $J$ -oriented adaptation methods that move points towards zones of high  $\|\mathcal{P}(dJ/dX)\|$  or add points in corresponding zones. Concerning  $\|\mathcal{P}(dJ/dX)\|$  on stretched and quasi-uniform grids, at the same location it is not systematically lower for the stretched (better adapted) grid than for the quasi-uniform. Actually, for the considered test case, it is for  $CDp$  but not for  $P_a$ .

Besides, figure 7, presents a plot of  $\mathcal{P}(dCDp/dX)$ , on the  $(257 \times 257)$  meshes, for Jameson et al. scheme [32]. The comparison of the corresponding plots for the upwind second order scheme (figure 5, middle plots), indicates that  $CDp$  is less sensitive to the position of the node at the leading edge for the centered scheme. Nonetheless, the regions of high  $\|\mathcal{P}(dCDp/dX)\|$  are the same for the two schemes and, for the centered scheme,  $\|\mathcal{P}(dCDp/dX)\|$  is also lower on the stretched mesh than on the quasi-uniform mesh.

2.7. Proposed mesh adaptation methods. Proposed indicators.

As stated in subsection 2.3,  $\mathcal{P}(dJ/dX)$  is a projection of  $dJ/dX$  retaining all the degrees of freedom available for mesh adaptation. According to function  $J$  this field can be used in different ways:

(a) if a function  $J$  cannot simply correlated with numerical errors, a heuristic node addition method can be applied. As observed in previous subsection meshes adapted for the computation of  $J$  have a larger number of nodes in the zones sensitive for  $J$  evaluation. Hence an intuitive heuristic node addition procedure consists in adding nodes in the region of high  $\|\mathcal{P}(dJ/dX)\|$ -values.

(b) when the physics of the problem indicate that the maximum or minimum reachable value of  $J$  is optimal, a descent algorithm directly based on  $\mathcal{P}(dJ/dX)$  or associated with a mesh parametrization may seek meshes providing better values of the output of interest.

This usage of the field  $\mathcal{P}(dJ/dX)$  in cases (a) and (b) will be demonstrated in the application sections.

Finally, it seems useful to define scalar indicators based on  $dJ/dX$ : the mean over the mesh nodes of  $\|\mathcal{P}(dJ/dX)\|$  is denoted  $\mu_J$ . We wish to make a distinction between to types of meshes exhibiting locally high values of  $\|\mathcal{P}(dJ/dX)\|$ . If large vectors  $\mathcal{P}(dJ/dX)$  with the same direction are encountered in a zone where the mesh is coarse (figure 9 (b1)) the value of  $J$  would actually be affected by a possible nodes displacement in this zone, that should obviously be remeshed. Conversely, if the mesh is fine (figure 9 (b2)) it is not possible to determine an actual nodes displacement that would significantly affect the value of  $J$ . This is why a second indicator  $\theta_J$  is defined in complement to  $\mu_J$ .  $\theta_J$  is the mean  $\|\mathcal{P}(dJ/dX)\|$  times  $r$  defined as half the radius of the inscribed circle (see figure 9 (a)). It can be seen as an upper bound of the first order variation of  $J$  when the nodes move locally while preserving the topology of the mesh.

## 2.2. THE PROPOSED METHODOLOGY APPLIED TO EULERIAN FLOWS

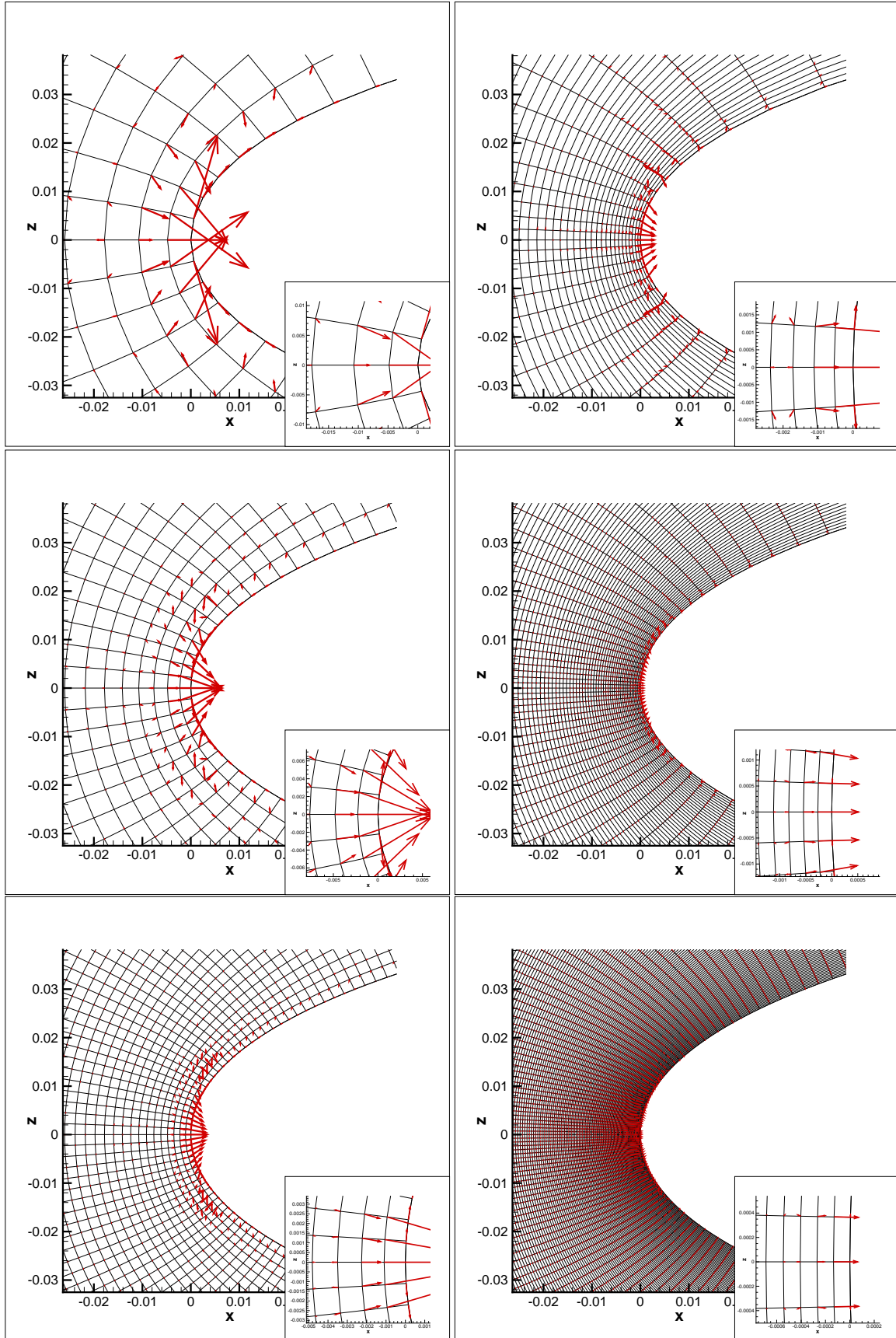


Figure 5: NACA0012, subcritical flow conditions. Examination of  $-\mathcal{P}(dCDp/dX)$  for  $(129 \times 129)$  (top)  $(257 \times 257)$  (middle)  $(513 \times 513)$  down for quasi-uniform (right) and stretched mesh (right) for Roe's scheme (same scale for all plots).

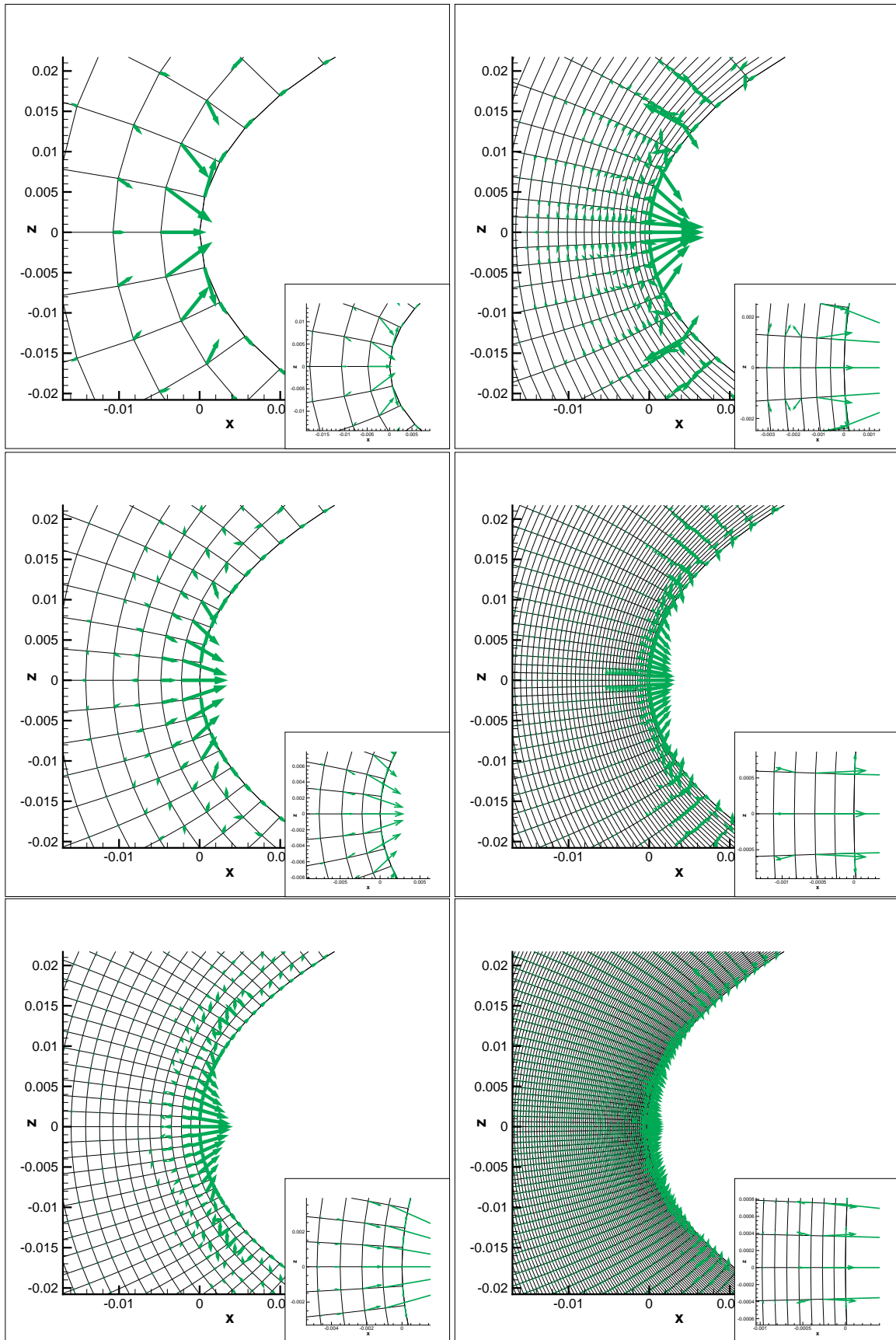


Figure 6: NACA0012, subcritical flow conditions. Examination of  $\mathcal{P}(dP_a/dX)$  for  $(129 \times 129)$  (top)  $(257 \times 257)$  (middle)  $(513 \times 513)$  down for quasi-uniform (right) and stretched mesh (right) for Roe's scheme (same scale for all plots).

## 2.2. THE PROPOSED METHODOLOGY APPLIED TO EULERIAN FLOWS

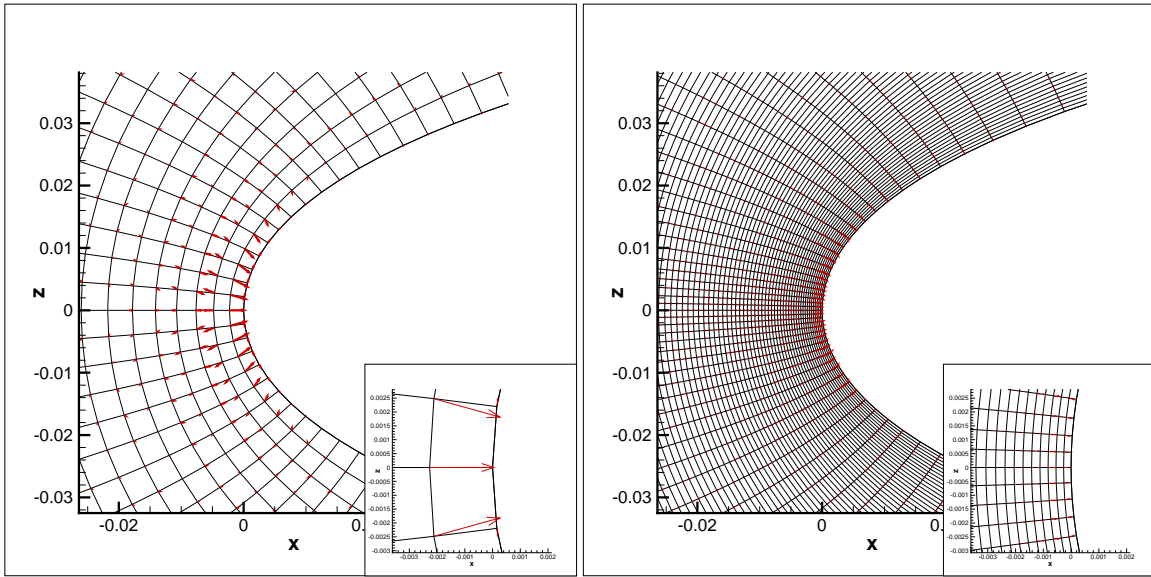


Figure 7: NACA0012, subcritical flow conditions. Examination of  $-\mathcal{P}(dCDp/dX)$  for  $(257 \times 257)$  quasi-uniform (right) and stretched mesh (left) for Jameson et al. scheme.

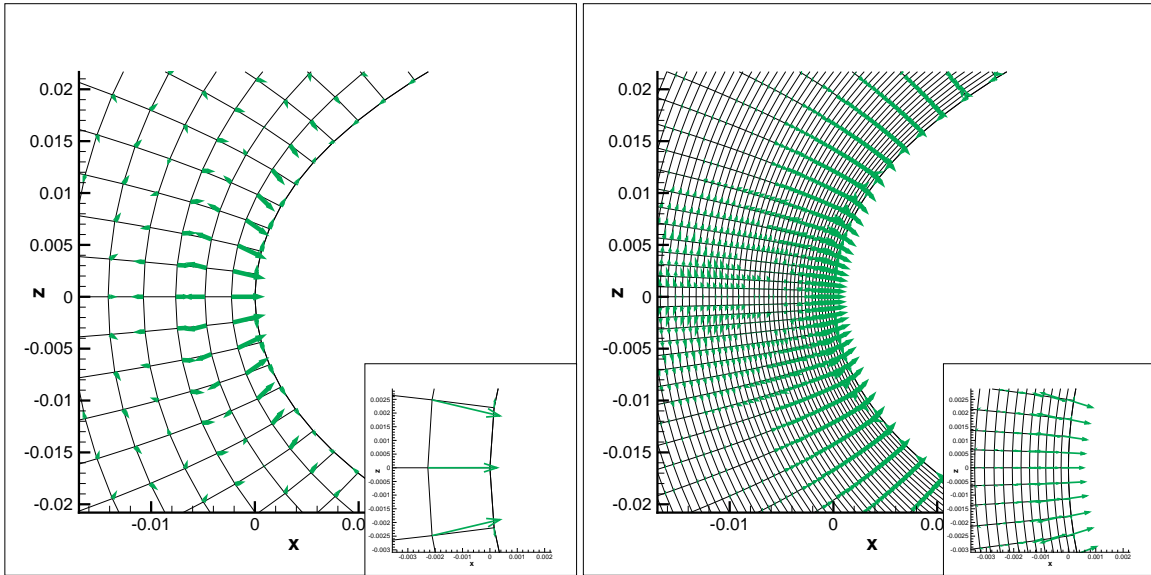


Figure 8: NACA0012, subcritical flow conditions. Examination of  $\mathcal{P}(dP_a/dX)$  for  $(257 \times 257)$  quasi-uniform (right) and stretched mesh (left) for Jameson et al. scheme.

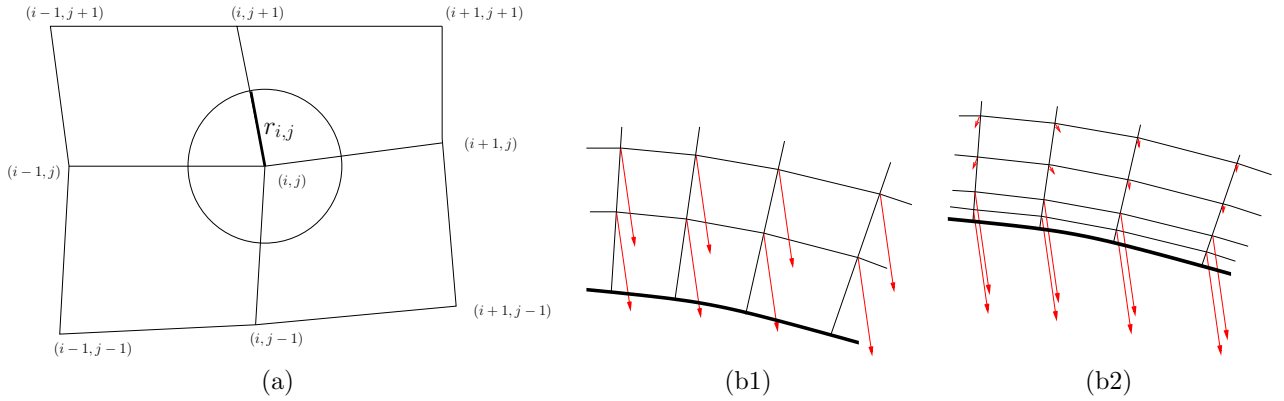


Figure 9: (a) Definition of the radius  $r_{i,j}$  involved in  $\theta_J$ ; (b1) large  $\mathcal{P}(dJ/dX)$  with large possible displacement of nodes; (b2) large  $\mathcal{P}(dJ/dX)$  without large possible displacement of nodes

### 2.8. Comparison of proposed mesh refinement indicator with classical indicators

The proposed heuristic mesh adaptation criterion is plotted for the upwind scheme and flow considered in subsection 2.6. The mesh is the quasi-uniform  $(257 \times 257)$  mesh described in the same subsection and the function of interest is the near-field drag. The iso-values of  $\|\mathcal{P}(dCDp/dX)\|$  are presented on the top-right of figure 10. It appears that this quantity, as it is adjoint based, if used as a refinement criterion, will induce refinement upwind the support of the function of interest (in this case, upwind the airfoil). The local quantity corresponding to the global indicator  $\theta_{CDp}$  ( $\|\mathcal{P}(dCDp/dX_{i,j})\| r_{i,j}$ ) exhibits almost the same iso-lines as  $\|\mathcal{P}(dCDp/dX)\|$ .

For the sake of comparison, a feature based criterion is plotted. The norm of the gradient of the stagnation pressure times the local size of the mesh is chosen as it may select areas with high numerical dissipation. As expected, this criterion is high around and downstream the airfoil and can not induce refinement upstream the airfoil. Finally, the broadly used criterion of Venditti and Darmofal is computed. Flow simulation and adjoint equation for  $CDp$  are converged on the coarse underlying  $(129 \times 129)$  grid and an interpolated flow field and two interpolated adjoint vectors (based on second and third-order operators in the index-space) are calculated in order to approximate the error in computable correction of Venditti and Darmofal's formula. It is plotted in the lower right part of figure 10. It presents approximately the same features (although with stronger values in the airfoil wake) than the proposed criterion.

## 3. 2D Euler test case. Limiting values for functions.

### 3.1. Test case

The slightly modified NACA0012 considered by Vassberg et al. [53, 54] is the selected airfoil. The two non-lifting flows of this study are retained:  $AoA=0^\circ$ ,  $M_\infty=0.5$  (subcritical flow) and  $AoA=0^\circ$ ,  $M_\infty=0.8$  (transonic flow). In the transonic case, a shock wave is located at  $x/c = 0.505$ .

### 3.2. Grids, functional outputs, reference values for the outputs.

Two families of meshes have been described in subsection 2.4. In most of this work, the number of grid nodes is  $(129 \times 129)$ ,  $(257 \times 257)$ ,  $(513 \times 513)$ ,  $(1025 \times 1025)$  and  $(2049 \times 2049)$ . A  $(4097 \times 4097)$  grid has been used once to computing limiting values of functional outputs in transonic flow conditions.

The two aerodynamic functions involved in the mesh adaptation are the near-field drag coefficient  $CDp$  and stagnation pressure  $P_a$  integrated over the airfoil. Let  $\Gamma$  denote the airfoil contour and  $L(\Gamma)$  denote its length. The functions of interest,  $CDp$  and  $P_a$ , are defined by:

$$CDp = \oint_{\Gamma} \frac{2}{\gamma M_\infty^2} \left( \frac{p}{p_\infty} - 1 \right) n \cdot e_x dl \quad (15)$$

$$P_a = \frac{1}{L(\Gamma)p_{a\infty}} \oint_{\Gamma} p_a dl \quad (16)$$

## 2.2. THE PROPOSED METHODOLOGY APPLIED TO EULERIAN FLOWS

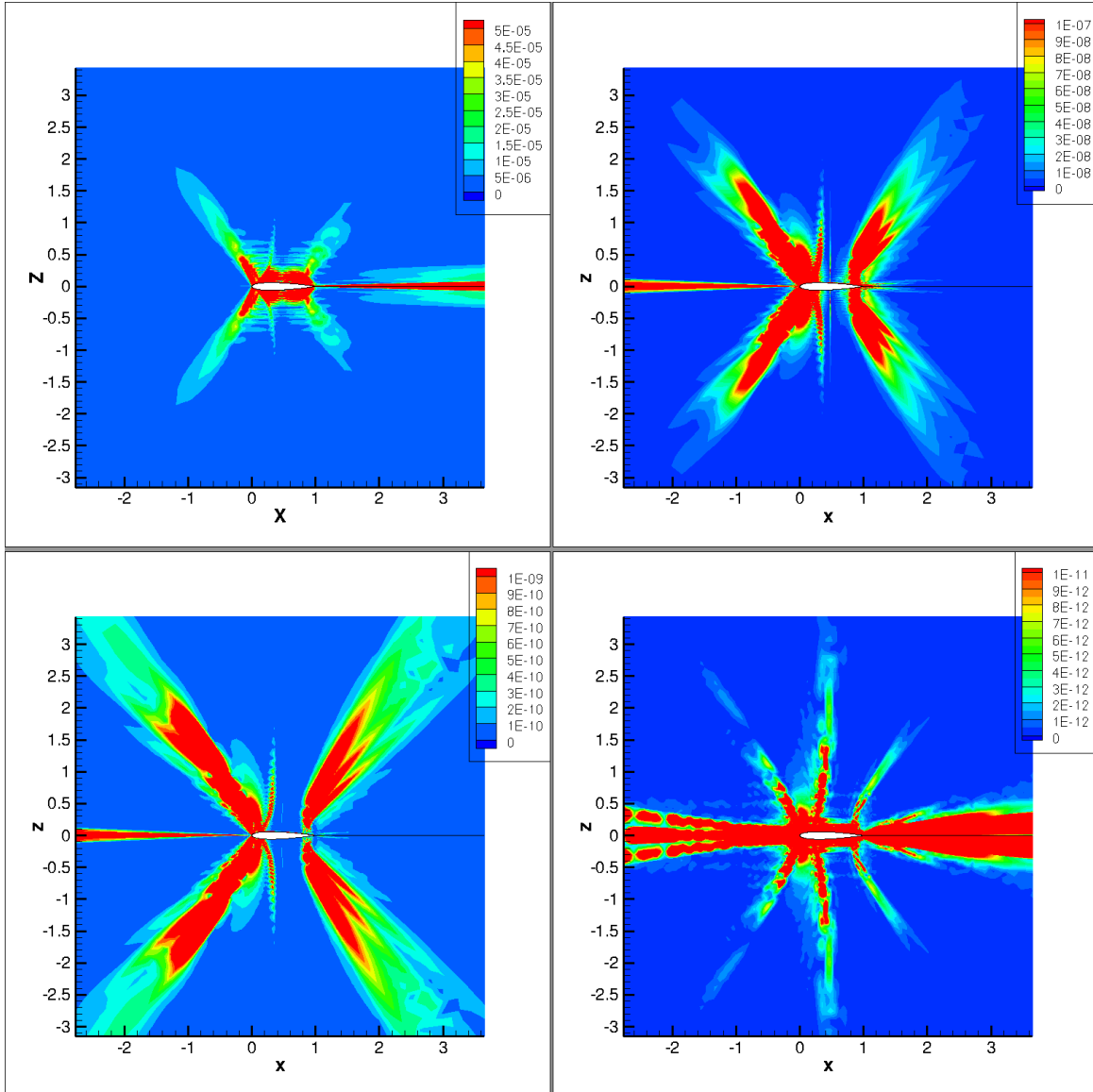


Figure 10: NACA0012, subcritical flow conditions. Comparison of mesh refinement criteria: feature based criterion, gradient of stagnation pressure times local characteristic length of cells (top left) ;  $\|\mathcal{P}(dCDp/dX)\|$  (top right) ;  $\|\mathcal{P}(dCDp/dX)\| \times r$  (down left) ; Venditti and Darmofal's criterion (down right).

	$CDp (\times 10^4)$	$\mu CDp$	$\theta_{CDp}$	$P_a$	$\mu P_a$	$\theta_{P_a}$
quasi-uniform grids						
<i>lim. value</i>	0.	—	—	1.	—	—
$2049 \times 2049$	0.169	$3.95 \cdot 10^{-8}$	$1.22 \cdot 10^{-11}$	0.99905	$6.70 \cdot 10^{-6}$	$1.24 \cdot 10^{-9}$
$1025 \times 1025$	0.674	$2.89 \cdot 10^{-7}$	$1.44 \cdot 10^{-10}$	0.99812	$2.96 \cdot 10^{-5}$	$3.75 \cdot 10^{-8}$
$513 \times 513$	2.634	$1.73 \cdot 10^{-6}$	$1.30 \cdot 10^{-9}$	0.99622	$1.02 \cdot 10^{-4}$	$7.55 \cdot 10^{-7}$
$257 \times 257$	10.331	$9.03 \cdot 10^{-6}$	$1.66 \cdot 10^{-8}$	0.99217	$3.19 \cdot 10^{-4}$	$1.04 \cdot 10^{-5}$
$129 \times 129$	40.986	$4.38 \cdot 10^{-5}$	$3.99 \cdot 10^{-7}$	0.98396	$1.05 \cdot 10^{-3}$	$9.75 \cdot 10^{-5}$
stretched grids						
$2049 \times 2049$	0.005	$1.52 \cdot 10^{-8}$	$3.16 \cdot 10^{-13}$	0.99983	$1.60 \cdot 10^{-5}$	$1.65 \cdot 10^{-9}$
$1025 \times 1025$	0.018	$6.20 \cdot 10^{-8}$	$3.17 \cdot 10^{-12}$	0.99973	$2.33 \cdot 10^{-5}$	$1.02 \cdot 10^{-8}$
$513 \times 513$	0.119	$3.68 \cdot 10^{-7}$	$5.45 \cdot 10^{-10}$	0.99950	$8.39 \cdot 10^{-5}$	$4.36 \cdot 10^{-8}$
$257 \times 257$	1.079	$2.72 \cdot 10^{-6}$	$1.15 \cdot 10^{-9}$	0.99898	$4.35 \cdot 10^{-4}$	$1.12 \cdot 10^{-7}$
$129 \times 129$	7.849	$2.47 \cdot 10^{-5}$	$1.65 \cdot 10^{-8}$	0.99784	$2.34 \cdot 10^{-3}$	$3.45 \cdot 10^{-6}$

 Table 1:  $CDp$  and  $P_a$  for baseline and stretched grids.  $M_\infty = 0.5$ .

where  $p_\infty$  and  $p_{a\infty}$  are respectively the upstream static pressure and stagnation pressure.

Table 1 presents the values of  $CDp$  and  $P_a$  for the subcritical test case, for the five different grids. The theoretical value for  $CDp$  is zero as the whole flow is subcritical and non-zero drag values observed in Tab. 1 are indicative of parasitic (numerical) drag. The theoretical value for  $P_a$  is one, and, similarly, every lower value shows the effect of numerical dissipation. Note that for the  $2049 \times 2049$  grid, Vassberg *et al.* [53, 54] obtained  $CDp = 0.162 \cdot 10^{-4}$  with the OVERFLOW code, which indicates that *elsA* results are quite good for fine meshes. The calculations on the stretched grids also lead to consistent results. The convergence of the functional outputs towards the theoretical limiting values is faster than for quasi-uniform meshes ; this indicates that the benefit of higher mesh density near the airfoil is superior to the degradation caused by the non regular cell-widths. In the mesh adaptation strategy, the objective is to adapt the quasi-uniform  $257 \times 257$  grid so as to decrease  $CDp$  or increase  $P_a$ .

Similar results are shown in Tab. 2 for  $M_\infty = 0.8$ . For this transonic test case, the computed drag is the sum of wave drag and spurious numerical drag (both positive contributions). In Vassberg *et al.* [53, 54] a value of  $83.502 \cdot 10^{-4}$  is found for the  $2049 \times 2049$  nodes grid, with the CFL3D code, and a limiting value of  $83.415 \cdot 10^{-4}$  is extrapolated. Hence, once again, the results obtained with *elsA* for the fine meshes (either quasi-uniform or stretched) are satisfactory. Besides, the shock wave induces a loss of stagnation pressure and the limit value of  $P_a$  is no longer one. In Fig. 11, the wall stagnation pressure  $p_a$  at the wall is represented *versus*  $x$ . Upstream of the shock, the numerical dissipation tends to diminish  $p_a$ . Downstream of the shock, the same trend is observed and the stagnation pressure at the wall decreases when numerical dissipation increases (ie. when the grid characteristic size decreases). This allows to maximize  $P_a$  not only for the subcritical test case but also for the transonic test case. Concerning the minimization of  $CDp$ , it is relevant for the subcritical case (as all the drag is spurious), but may be irrelevant in the transonic case (as the wave drag may be decreased while maintaining a significant level of spurious drag). Lastly, a limiting value of  $CDp$  equal to  $83.420 \cdot 10^{-4}$  is computed by fitting a second order formula  $CDp_{lim} + ah + bh^2$  to the estimation of the three finest quasi-uniform grids. This estimate belongs to the interval of the limiting values presented in [53, 54] ranging from  $83.415 \cdot 10^{-4}$  to  $83.423 \cdot 10^{-4}$ . A limiting value of 0.99306 is obtained for  $P_a$  by the same type of calculation. Its relative distance to the fine grid estimate is four times larger than the one of  $CDp$  limiting value (respectively 0.08% and 0.02%) and the difference between this estimate of  $P_a$  and slightly larger values obtained on adapted meshes is discussed later. As stated before, the calculations on the stretched grids provide consistent monotonic results. Nevertheless they lead to slightly different limiting values ( $83.433 \cdot 10^{-4}$  instead of  $83.420 \cdot 10^{-4}$  for  $CDp$  and 0.99324 instead of 99306 for  $P_a$ ), probably because the *elsA* code does not include any correction for irregular meshes.

In summary, the  $P_a$  maximization (for subcritical and transonic flow) and the  $CDp$  minimization (for subcritical flow) based on  $\mathcal{P}(dCDp/dX)$  and  $\mathcal{P}(dP_a/dX)$  fields are retained to adapt meshes by nodes displacement. Besides  $CDp$ - and  $P_a$ -oriented mesh adaptation by lines addition (based on  $\|\mathcal{P}(dCDp/dX)\|$  and

2.2. THE PROPOSED METHODOLOGY APPLIED TO EULERIAN FLOWS

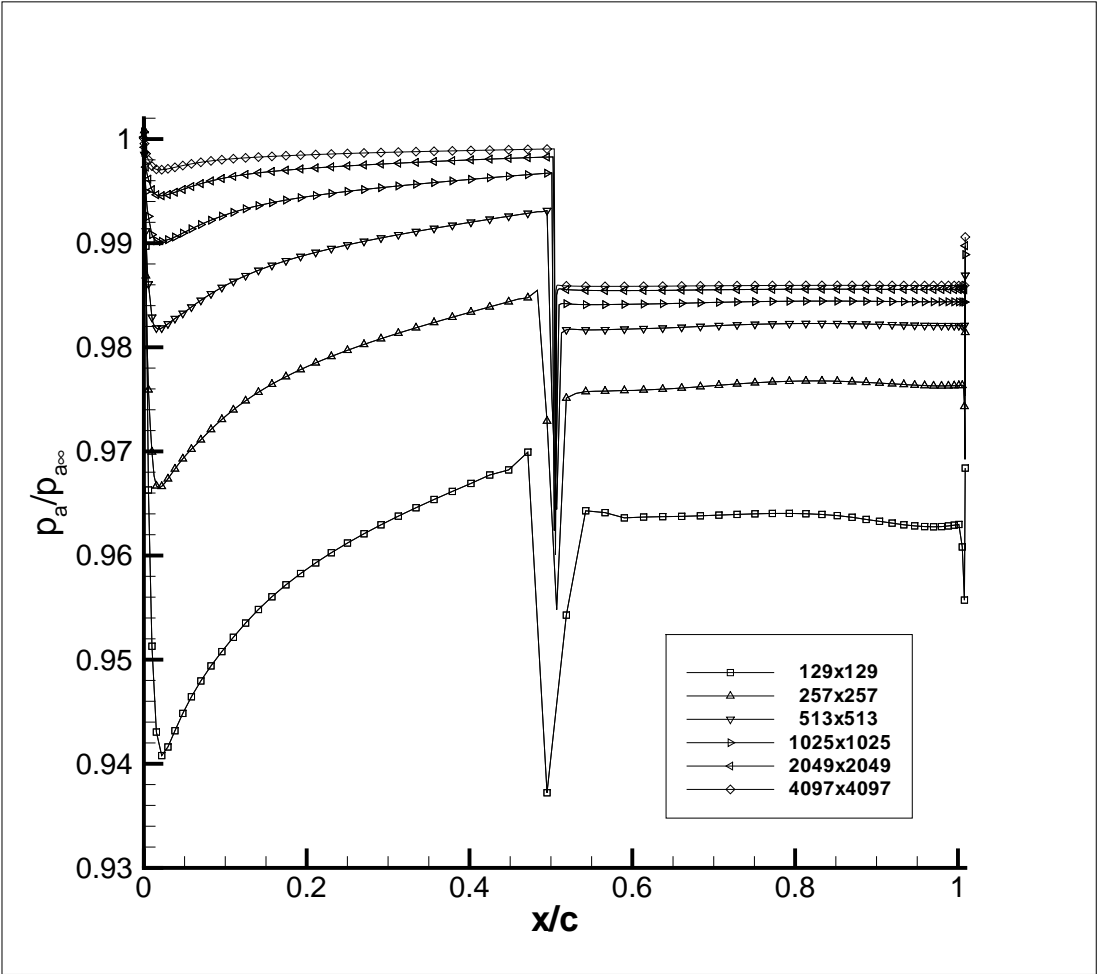


Figure 11: Stagnation pressure at the wall  $p_a/p_{a\infty}$  versus  $x/c$ .  $M_\infty = 0.8$ . Initial grids provided by Vassberg and Jameson[53, 54]

	$CDp (\times 10^4)$	$\mu_{CDp}$	$\theta_{CDp}$	$P_a$	$\mu_{P_a}$	$\theta_{P_a}$
quasi-uniform grids						
<i>lim. value</i>	83.420	—	—	0.99306	—	—
$4097 \times 4097$	83.439	*	*	0.99227	*	*
$2049 \times 2049$	83.514	$5.93 \cdot 10^{-8}$	$1.07 \cdot 10^{-11}$	0.99140	$7.63 \cdot 10^{-6}$	$8.18 \cdot 10^{-9}$
$1025 \times 1025$	83.832	$1.62 \cdot 10^{-7}$	$1.01 \cdot 10^{-10}$	0.98942	$2.69 \cdot 10^{-5}$	$2.48 \cdot 10^{-8}$
$513 \times 513$	85.047	$9.55 \cdot 10^{-7}$	$1.03 \cdot 10^{-9}$	0.98556	$9.95 \cdot 10^{-5}$	$4.04 \cdot 10^{-7}$
$257 \times 257$	89.865	$5.40 \cdot 10^{-6}$	$1.37 \cdot 10^{-8}$	0.97741	$3.76 \cdot 10^{-4}$	$5.12 \cdot 10^{-6}$
$129 \times 129$	109.576	$2.84 \cdot 10^{-5}$	$1.87 \cdot 10^{-7}$	0.96175	$1.15 \cdot 10^{-3}$	$3.41 \cdot 10^{-5}$
stretched grids						
$2049 \times 2049$	83.423	$1.24 \cdot 10^{-8}$	$1.26 \cdot 10^{-12}$	0.99295	$2.66 \cdot 10^{-5}$	$2.81 \cdot 10^{-9}$
$1025 \times 1025$	83.458	$5.14 \cdot 10^{-8}$	$9.66 \cdot 10^{-12}$	0.99291	$6.89 \cdot 10^{-5}$	$3.03 \cdot 10^{-8}$
$513 \times 513$	83.662	$2.92 \cdot 10^{-7}$	$1.03 \cdot 10^{-10}$	0.99235	$1.42 \cdot 10^{-4}$	$1.05 \cdot 10^{-7}$
$257 \times 257$	85.627	$2.06 \cdot 10^{-6}$	$1.73 \cdot 10^{-9}$	0.99113	$5.71 \cdot 10^{-4}$	$5.72 \cdot 10^{-7}$
$129 \times 129$	97.464	$1.60 \cdot 10^{-5}$	$3.33 \cdot 10^{-8}$	0.98833	$2.01 \cdot 10^{-3}$	$2.47 \cdot 10^{-6}$

Table 2:  $CDp$  and  $P_a$  for baseline and stretched grids.  $M_\infty = 0.8$ . The \* sign corresponds to calculations that could not be achieved due to huge CPU and memory requirements.

$\|\mathcal{P}(dP_a/dX)\|$ ) will be carried out for both, the transonic and the subcritical flow conditions.

### 3.3. Examination of criteria $\mu$ and $\theta$ for the two family of meshes

The values of the indicators  $\mu$  and  $\theta$  have been computed for the two functions and the two families of meshes. In the subcritical and in the transonic case, as expected and predicted by the analysis of subsection 2.5, for both functions and both families of meshes,  $\mu_{CDp}$  and  $\mu_{P_a}$  decrease as the mesh size is increased. For a given mesh size, it is observed that  $\mu$  is not systematically lower on the stretched meshes that are supposed to be more adapted to the calculation of the functions of interest. This seems to be function-dependent as  $\mu_{CDp}$  is lower on the stretched grids than on the corresponding quasi-uniform grids whereas  $\mu_{P_a}$  is higher on the stretched grids than on the corresponding quasi-uniform grids.

Finally, it is observed that criterion  $\theta$  decreases as the mesh size is increased and that this criterion is lower on the stretched grids than on the quasi-uniform grids (except for  $P_a$  on the  $1025 \times 1025$  grid).

## 4. Mesh adaptation by node addition. 2D Euler subcritical and transonic flows.

### 4.1. Line addition method

Only coarse meshes with lines interpolated in the reference fine mesh will be considered. Hence, an  $N_i \times N_j$  mesh may be fully defined by the position of its lines,  $(\varphi_i, \varphi_j)$ , with respect to those of the fine mesh. The position of the nodes is then evaluated by a bi-linear interpolation operator  $\mathcal{B}$ .

$$\begin{array}{ccc} \varphi & & \mathcal{B} \\ \{1, N_i\}\{1, N_j\} & \longrightarrow & [1, 2049][1, 2049] \longrightarrow \mathbb{R}^2 \\ (i, j) & & (\varphi_i, \varphi_j) \quad X(x, z) \end{array}$$

A three-step method is used to add mesh lines to a current mesh. The addition method is described here after in the case of  $i$ -lines. The extension to another mesh direction is straightforward. A criterion  $\bar{c}_{i+1/2}$  ( $i \in \{1, N_i - 1\}$ ) is defined by:

$$\bar{c}_{i+1/2} = \frac{c_i + c_{i+1}}{2} \quad c_i = \left( \frac{1}{N_j} \sum_{j=1}^{N_j} \|\mathcal{P}(dJ/dX)_{ij}\|^2 \right)^{\frac{1}{2}}$$

The criterion  $\bar{c}_{i+1/2}$  is hence assigned to a row of cells. Let  $N$  denote the number of  $i$ -lines to be added and  $Q$  the maximum number of lines to be inserted between two consecutive lines of the current mesh (for

## 2.2. THE PROPOSED METHODOLOGY APPLIED TO EULERIAN FLOWS

$Q$	$CDp (\times 10^4)$	$P_a$	$CD_w$	$CD_{sp}$
3	84.045	0.99325	83.209	0.837
4	83.935	0.99413	83.303	0.633
5	83.961	0.99409	83.258	0.704

Table 3:  $CDp$  and  $P_a$  after  $CDp$ -oriented lines addition.  $M_\infty = 0.8$ .

most of the tests  $Q$  was equal to 4). \*\*\*\* A simple algorithm is used to select rows where to add 1 to  $Q$  mesh lines depending on  $\bar{c}_{i+1/2}$  values [60]. A first larger mesh of  $(N_i + N) \times N_j$  nodes is built by adding regularly  $q$  mesh lines in the selected cell rows for  $q$  equal one to  $Q$ .\*\*\*\* The position of the mesh lines is then regularized by smoothing their width  $\varepsilon_i = (\varphi_{i+1} - \varphi_i)$  (we will denote  $\epsilon = \{\varepsilon_i\}$ ) as defined in the reference mesh. A smoothing operator is used. It is based on a third order dissipation flux and is explicit. A sequence of cell-widths  $\varepsilon_{i+\frac{1}{2}}^{n+1} = \varepsilon_{i+\frac{1}{2}}^n + D_{i+1}^4 - D_i^4$  is calculated until a convergence criterion is satisfied. The fluxes are defined by:

$$D_i^4 = -k^4(\varepsilon_{i+3/2} - 3\varepsilon_{i+1/2} + 3\varepsilon_{i-1/2} - \varepsilon_{i-3/2})$$

The fluxes  $D_1^4$  and  $D_{N_i}^4$  are set to zero and the fluxes  $D_2^4$  and  $D_{N_i-1}^4$  are defined by the previous formula with  $\varepsilon_{1/2} = \varepsilon_{3/2}$  and  $\varepsilon_{N_i+1/2} = \varepsilon_{N_i-1/2}$  respectively.

### 4.2. Results for the 2D transonic test case

The initial coarse mesh is the quasi-uniform grid with 129 nodes presented in the previous section. Meshes with 257  $i$ -lines and 257  $j$ -lines were built in six steps by adding successively  $j$ -lines and  $i$ -lines (44 lines were added for the four first steps and 40 lines for the two last ones so that multigrid calculations could be run). As the proposed node displacement method cannot handle a  $CDp$ -oriented mesh adaptation for transonic flow conditions, this test-case is retained for the first mesh adaptations by line addition.

The initial value of  $CDp$  on the 129 mesh is  $109.578 \cdot 10^{-4}$  to be compared with the limiting value of  $83.420 \cdot 10^{-4}$ . Mesh adaptations using the explicit cell-width smoothing have first been made. The corresponding results are presented in table 3. Fortunately, the method appeared to be almost insensitive to  $Q$  (maximum number of lines added in a cell row),  $k^4$  (equal to 0.064 for the final results) and to the convergence criterion on  $\epsilon^n$ . The final  $CDp$  values (84.045, 83.935, 83.961 for  $Q=3, 4, 5$ ) for the adapted meshes are almost as accurate as the one obtained on the quasi-uniform  $1025 \times 1025$  mesh (83.832) and significantly better than the one obtained on a classical  $257 \times 257$  stretched mesh (85.627). At last, it is checked using far-field drag breakdown [52], that the observed decrease in near-field drag is due to a reduction of the spurious drag (see two right columns of Tab. 3). The drag decomposition for the quasi-uniform  $129 \times 129$  mesh is  $(CD_p(109.578) = CD_w(82.596) + CD_{sp}(26.982))$  and the one of the  $257 \times 257$  mesh is  $(CD_p(89.865) = CD_w(83.175) + CD_{sp}(6.690))$ . So the mesh adaptation actually succeeded in decreasing the spurious drag and improving the near-field and far-field drag estimates. Besides, satisfactory values of  $P_a$  are indirectly obtained while conducting  $CDp$ -oriented mesh adaptation.

A  $P_a$ -oriented mesh adaptation was conducted using the selected enrichment method (local value of  $\mathcal{P}(dP_a/dX)$ , explicit smoothing,  $Q = 4$ ). It led to satisfactory values of  $P_a$  (0.99357) and  $CDp$  (84.008). Both mesh adaptation procedures tend to insert new  $j$  lines close to the wall while maintaining a regular distribution of  $i$  lines. The results are summarized in table 4.

It is observed that the bound of the first variation of  $CDp$  (for bounded node displacement as described in figure 9 (a))  $\theta_{CDp}$  is much lower for the adapted grids (about  $3 \cdot 10^{-10}$ ) than for the quasi-uniform grid of same size (about  $1.6 \cdot 10^{-8}$ ) or the corresponding standard stretched grid (about  $1 \cdot 10^{-9}$ ). Concerning  $P_a$ ,  $\theta_{P_a}$  is also much lower on the stretched and adapted grids than on the quasi-uniform grid.

### 4.3. Results for subcritical test cases

As in the transonic test case, the initial coarse mesh is the quasi-uniform 129 grid and a mesh with 257  $i$ -lines and 257  $j$ -lines is built in six steps by adding successively  $j$ -lines and  $i$ -lines (44 lines were added in the first four steps and 40 lines in the last two).

The initial value of  $CDp$  on the 129 mesh is  $40.986 \cdot 10^{-4}$  to be compared with the limiting value of 0. A

	$CDp (\times 10^4)$	$\mu_{CDp}$	$\theta_{CDp}$	$P_a$	$\mu_{P_a}$	$\theta_{P_a}$
subcritical flow conditions						
lim. values	0.	—	—	1.	—	—
quasi-uniform	10.331	$9.03 \cdot 10^{-6}$	$1.66 \cdot 10^{-8}$	0.99217	$3.19 \cdot 10^{-4}$	$1.04 \cdot 10^{-5}$
stretched	1.079	$2.72 \cdot 10^{-6}$	$1.15 \cdot 10^{-9}$	0.99898	$4.35 \cdot 10^{-4}$	$1.12 \cdot 10^{-7}$
adapted for $CDp$	0.380	$1.14 \cdot 10^{-6}$	$3.47 \cdot 10^{-10}$	0.99997	$8.07 \cdot 10^{-4}$	$3.07 \cdot 10^{-7}$
adapted for $P_a$	0.528	$1.22 \cdot 10^{-6}$	$3.55 \cdot 10^{-10}$	0.99982	$4.10 \cdot 10^{-4}$	$1.22 \cdot 10^{-7}$
transonic flow conditions						
lim. value	83.420	—	—	0.99306	—	—
quasi-uniform	89.865	$5.40 \cdot 10^{-6}$	$1.37 \cdot 10^{-8}$	0.97741	$3.76 \cdot 10^{-4}$	$5.12 \cdot 10^{-6}$
stretched	85.627	$2.06 \cdot 10^{-6}$	$1.73 \cdot 10^{-9}$	0.99113	$5.71 \cdot 10^{-4}$	$5.72 \cdot 10^{-7}$
adapted for $CDp$	83.935	$1.06 \cdot 10^{-6}$	$2.19 \cdot 10^{-9}$	0.99413	$1.50 \cdot 10^{-3}$	$8.39 \cdot 10^{-7}$
adapted for $P_a$	84.008	$1.17 \cdot 10^{-6}$	$1.05 \cdot 10^{-9}$	0.99357	$3.04 \cdot 10^{-3}$	$3.29 \cdot 10^{-7}$

Table 4:  $CDp$  and  $P_a$  for  $257 \times 257$  baseline, stretched and adapted grids (adaptation by nodes addition, explicit smoothing,  $Q=4$ )

mesh adaptation using the explicit cell-width smoothing (with  $Q=4$ ) is run. The result is presented in table (4). The  $CDp$  value is 0.380 for the adapted mesh. The result is more accurate than the value obtained on the quasi-uniform  $1025 \times 1025$  (0.674) mesh and the value obtained on a classical  $257 \times 257$  stretched mesh (1.079). The mean  $\mu_{CDp}$  is lower for the adapted grids (about  $1.14 \cdot 10^{-6}$ ) than for the quasi-uniform grid of same size ( $9.03 \cdot 10^{-6}$ ) or the corresponding standard stretched grid ( $2.72 \cdot 10^{-6}$ ). Lastly, the value of the mean stagnation pressure at the wall (0.99997) is very close to the theoretical one. Finally a  $P_a$ -oriented mesh adaptation was carried out, also leading to consistent results that are indicated in table 4.

Concerning the changes in mesh density, both mesh adaptation procedures have been observed to insert new  $j$  lines close to the wall, but  $CDp$  oriented adaptation maintained a quite regular distribution of  $i$  lines (although with a small tightening in front of leading edge) whereas  $P_a$ -oriented led to a very dense mesh upwind the leading edge.

As in the subcritical test case, it is observed the bound of the first variation of  $CDp$  and  $P_a$  (for the node displacement described in figure 9 (a))  $\theta_{CDp}$  and  $\theta_{P_a}$  are significantly lower on the stretched and adapted grids than on the quasi-uniform grid.

#### 4.4. Comparison with feature-based mesh adaptation

Dwight demonstrated that, even for 2D Euler flows, feature based mesh adaptation may fail to converge towards a satisfactory evaluation of goal [33, 34]. Nevertheless, the node addition method was also run with a feature based criterion. The comparison is presented in [60].

### 5. Mesh adaptation by node displacement. 2D Euler subcritical and transonic flows.

Iterative optimization algorithms are run to adapt the volume mesh about the NACA0012 while increasing  $P_a$  or decreasing  $CDp$ . A stage of the optimization is stopped after two successive steps with  $|\delta CDp|$  lower than 0.1 for  $CDp$  and  $|\delta P_a|$  lower than 0.0001 for  $P_a$ .

Mesh adaptation without parametrization was performed on this test case. Steepest descent iterations were carried out to decrease the drag  $CDp$  in the subcritical test case. The algorithm simply reads  $X^{(l)} = X^{(l-1)} - s^l \mathcal{P}(dCDp/dX)^{(l-1)}$ . Unfortunately, even for this simple problem, very irregular meshes has been obtained after a few iterations of the descent algorithm, while only a disappointing value of the function of interest has been reached. An extended presentation of these results can be found in [59]. After these tests, the projected gradient field was no longer used directly ; instead, it has been combined with suitable parametrizations.

## 2.2. THE PROPOSED METHODOLOGY APPLIED TO EULERIAN FLOWS

### 5.1. Mesh adaptation based on parametrized mappings

Considering the previous results, the coarse meshes to be optimized are now described by a smooth mapping function associated with the body-fitted coordinates of the  $2049 \times 2049$  mesh. A coarse mesh with  $N_i \times N_j$  mesh-lines is fully defined by its mapping  $\Phi$  and the following sequence of transformations

$$\begin{array}{ccccccc} \chi_{N_i, N_j}^{-1} & & \Phi & & \chi_{2049} & & \mathcal{B} \\ \{1, N_i\}\{1, N_j\} & \longrightarrow & [0, 1][0, 1] & \longrightarrow & [0, 1][0, 1] & \longrightarrow & [1, 2049][1, 2049] & \longrightarrow & \mathbb{R}^2 \\ (i, j) & & (\bar{i}, \bar{j}) & & (\Phi_i, \Phi_j) & & (\chi_i, \chi_j) & & X(x, z) \end{array}$$

where

$$\begin{aligned} \chi_{N_i, N_j}^{-1}(i, j) &= ((i-1)/(N_i-1), (j-1)/(N_j-1)) \\ \chi_{2049}(\Phi_i, \Phi_j) &= (1. + 2048\Phi_i, 1. + 2048\Phi_j) \end{aligned}$$

The position of the coarse nodes is calculated by the bi-linear interpolation  $\mathcal{B}$  from their relative position  $(\chi_i, \chi_j)$  in the  $2049 \times 2049$  O-grid defined by  $\chi_{2049} \circ \Phi \circ \chi_{N_i, N_j}^{-1}$  (input values are integers in  $\{1, N_i\}\{1, N_j\}$ ), or alternatively from  $\chi_{2049} \circ \Phi$  (input values are then  $((i-1)/(N_i-1), (j-1)/(N_j-1))$ ). The mapping corresponding to the construction of the coarse mesh by regular line extraction in the fine  $2049 \times 2049$  mesh is simply  $\Phi_i^r(\bar{i}, \bar{j}) = \bar{i}$   $\Phi_j^r(\bar{i}, \bar{j}) = \bar{j}$ . Moreover only non-lifting test-cases are considered and symmetry about horizontal axis should be maintained. This requires  $\Phi_i(1 - \bar{i}, \bar{j}) = 1 - \Phi_i(\bar{i}, \bar{j})$ .

### 5.2. Preliminary examination of the projected gradient fields

The projected gradient fields  $-\mathcal{P}(dCDp/dX)$  (left) and  $\mathcal{P}(dP_a/dX)$  (right) are examined on the baseline  $257 \times 257$  mesh for subcritical flow conditions (figure 12) and transonic flow conditions (figure 13).

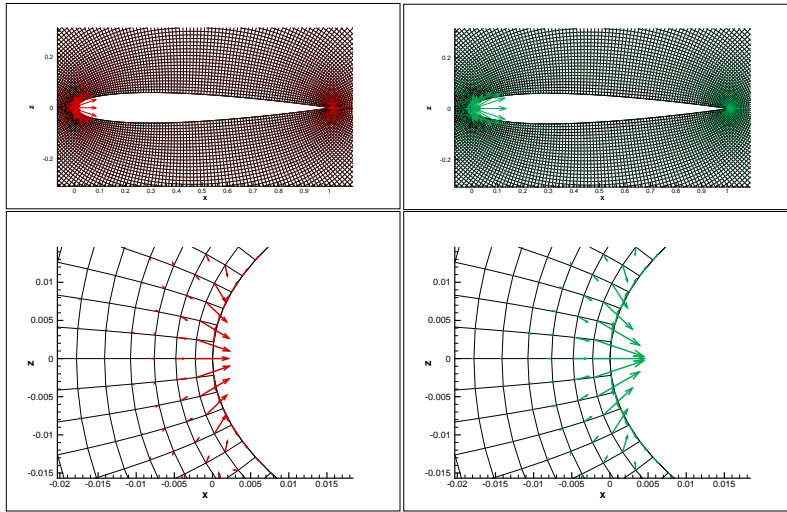


Figure 12: NACA0012, subcritical flow conditions. Examination of  $-\mathcal{P}(dCDp/dX)$  (left) and  $\mathcal{P}(dP_a/dX)$  (right) on quasi-uniform  $257 \times 257$  mesh. Top: general view. Down: leading edge. Respective scales of arrows are 20 (top figure) and 1 (down).

The plots of  $-\mathcal{P}(dCDp/dX)$  (left) and  $\mathcal{P}(dP_a/dX)$  (right) are first discussed for the subcritical flow. It clearly appears on the general views (top part of figures 12) that large values of  $\|\mathcal{P}(dCDp/dX)\|$  and  $\|\mathcal{P}(dP_a/dX)\|$  are observed at the leading and trailing edge. Near the leading edge (bottom part of figure 12),  $-\mathcal{P}(dCDp/dX)$  and  $\mathcal{P}(dP_a/dX)$  vectors are almost parallel. This indicates that moving the lines  $j = 2$  and  $j = 3$  towards the wall will diminish the (spurious) drag and increase the stagnation pressure. Near the trailing edge, the  $-\mathcal{P}(dCDp/dX)$  and  $\mathcal{P}(dP_a/dX)$  vectors are less similar and less coherently structured. Nonetheless, they indicate that moving line  $j = 2$  towards the wall will reduce the (spurious) drag and

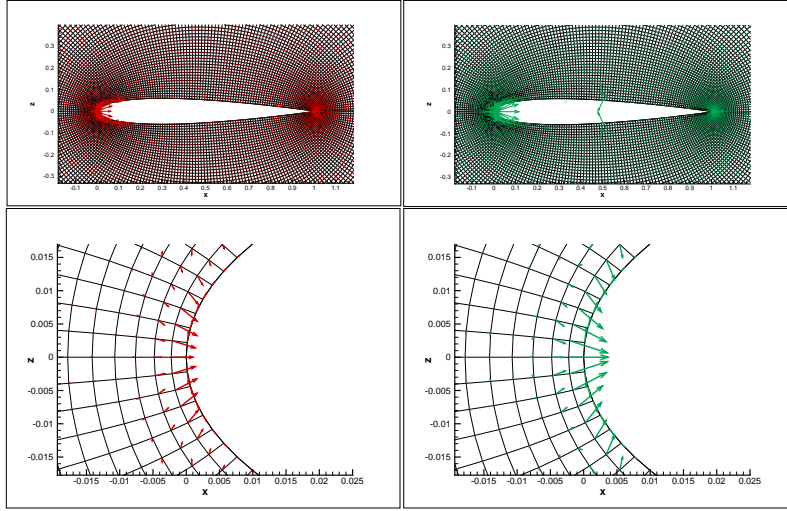


Figure 13: NACA0012, transonic flow conditions. Examination of  $-\mathcal{P}(dCDp/dX)$  (left) and  $\mathcal{P}(dPa/dX)$  (right) on quasi-uniform  $257 \times 257$  mesh. Top: general view. Down: trailing edge. Respective scales of arrows are 20 (top figure), and 1 (down).

increase the stagnation pressure at the wall.

The observations and conclusions are almost the same for the transonic flow (see figure 13) except that the  $\|\mathcal{P}(dPa/dX)\|$ -field also exhibits some large values in the shock-wave area. These isolated large vector norms cannot be used for structured mesh adaptation. Once again, moving the lines  $j = 2$  and  $j = 3$  towards the wall near the leading edge, and moving the line  $j = 2$  towards the wall near the trailing edge will raise the stagnation pressure at the wall, which is the selected objective for transonic flow conditions mesh adaptation. Simultaneously, these nodes displacement will reduce the drag. Whether the spurious drag or the wave drag is then reduced will be discussed in some detail later on. As a conclusion to the visual examination of the projected gradient fields, design parameters that smoothly make the first  $j$ -lines closer to the wall are defined.

### 5.3. Mesh adaptation with single variable Bernstein polynomials

In the framework described in the foreword of this section, Bézier curves and surfaces appear as very appropriate tools to define mapping functions. In a first attempt to use this family of functions, only single variable Bézier curves are used. In order to limit the number of coefficients to optimize, degree four curves are selected. As  $\Phi$  is a map of  $[0, 1] \times [0, 1]$  and satisfies the symmetry property  $\Phi_i(1 - \bar{i}, \bar{j}) = 1 - \Phi_i(\bar{i}, \bar{j})$ , it has to be defined as

$$\begin{aligned}\Phi_i^B(\beta)(\bar{i}, \bar{j}) &= \bar{i} + \beta(B_{1,4}(\bar{i}) - B_{3,4}(\bar{i})) \\ \Phi_j^B(\beta_1, \beta_2, \beta_3)(\bar{i}, \bar{j}) &= \bar{j} + \beta_1 B_{1,4}(\bar{j}) + \beta_2 B_{2,4}(\bar{j}) + \beta_3 B_{3,4}(\bar{j})\end{aligned}$$

where  $B_{q,l}$  is the  $(q + 1)^{th}$  Bernstein polynomial of degree  $l$ :  $B_{q,l}(t) = C_l^q t^q (1 - t)^{l-q}$  ( $C_l^q = l! / (q!(l - q)!)$ ). The derivatives of the functions of interest w.r.t the parameters are computed by the chain rule, e.g.:

$$\frac{d\mathcal{J}}{d\beta} = \frac{dJ}{dX} \frac{dX}{d\beta} = \frac{dJ}{dX} \frac{dX}{d\chi_{2049}} \frac{d\chi_{2049}}{d\Phi} \frac{d\Phi}{d\beta} \quad (17)$$

Besides, it appeared that optimizing the position of the iso- $j$  lines leads to much larger improvements than optimizing the position of the iso- $i$  lines. Hence, iso- $j$  mesh lines position is first modified. The algorithm for maximization and minimization is the steepest descent. The mesh to optimize is the  $(257 \times 257)$  O-grid.

– Subcritical test case. Minimization of  $CDp$ .

The optimal coefficients are  $(\beta_1, \beta_2, \beta_3) \simeq (-0.2501, -4.505 \cdot 10^{-3}, -2.727 \cdot 10^{-4})$   $\beta \simeq 0.2059$ . The correspond-

## 2.2. THE PROPOSED METHODOLOGY APPLIED TO EULERIAN FLOWS

ing  $\bar{\Phi}$  function is

$$\begin{aligned}\Phi_i^{B1}(\bar{i}, \bar{j}) &= 1.82353\bar{i} - 2.47060\bar{i}^2 + 1.64707\bar{i}^3 \\ \Phi_j^{B1}(\bar{i}, \bar{j}) &= -0.00055\bar{j} + 2.97462\bar{j}^2 - 2.94868\bar{j}^3 + 0.97461\bar{j}^4\end{aligned}$$

Surprisingly, it is not a mapping of the unit square in itself (see  $\partial\Phi_j^{B1}(\bar{i}, \bar{j})/\partial\bar{j}$ ). Nevertheless it defines a suitable structured mesh as  $\bar{\Phi}$  function is only evaluated for  $\chi_{257}^{-1}(\{1, 257\}, \{1, 257\})$ . The mapping of  $i$ -lines,  $\Phi_i^{B1}$ , corresponds to a less dense distribution behind the trailing edge and a tightened distribution in front of the leading edge. The mapping of  $j$ -lines,  $\Phi_j^{B1}$ , corresponds to a strong tightening of  $j$ -lines close to the wall. The initial value of  $CDp$  is 10.331. The value after five iso- $j$  lines optimization iterations is  $1.273 \cdot 10^{-4}$ . The final value after three steps iso- $i$  lines optimization iteration is  $0.739 \cdot 10^{-4}$ . A total 92.85% reduction of (spurious) drag is obtained. Besides, the stagnation pressure at the wall has been significantly increased by the optimization process. The final value of  $P_a$  is 0.99957 (whereas its initial value is 0.99217). Thus, the minimization of  $CDp$  leads to a better flow-field in terms of total pressure losses.

– Subcritical test case. Maximization of  $P_a$  .

The optimal coefficients are  $(\beta_1, \beta_2, \beta_3) \simeq (-0.2052, -2.546 \cdot 10^{-3}, -6.966 \cdot 10^{-6})$   $\beta \simeq 1.238 \cdot 10^{-3}$ . The corresponding  $\bar{\Phi}$  function is

$$\begin{aligned}\Phi_i^{B2}(\bar{i}, \bar{j}) &= 2.24526\bar{i} - 3.73579\bar{i}^2 + 249053\bar{i}^3 \\ \Phi_j^{B2}(\bar{i}, \bar{j}) &= -0.00066\bar{j} + 2.989567\bar{j}^2 - 2.977094\bar{j}^3 + 0.988189\bar{j}^4\end{aligned}$$

With this formulas, the same type of line displacement is achieved as with  $\Phi^{B1}$ . The initial value of  $P_a$  is 0.99217. After five iterations optimizing iso- $j$  mesh lines position, it gets 0.99921. The two iterations optimizing the coefficient of  $\Phi_i^{B2}$  have led to a very small additional increase, from 0.99921 to 0.99959. As the entire flow is subcritical, the ideal value of  $P_a$  is 1. and the discrepancy with 1. and actual values is due to numerical dissipation. The optimization reduced the error in  $P_a$  of 94.76%. Besides, the near-field drag has been significantly reduced by the optimization process. The final value of  $CDp$  is  $0.841 \cdot 10^{-4}$  (whereas the initial value is  $10.331 \cdot 10^{-4}$ ). Thus, the maximization of  $P_a$  leads to a better flow-field in terms of drag.

– Transonic test case. Maximization of  $P_a$  .

The optimal  $\bar{\Phi}$  function is defined by  $(\beta_1, \beta_2, \beta_3) \simeq (-0.2503, -2.546 \cdot 10^{-3}, 6.966 \cdot 10^{-6})$  and  $\beta \simeq 1.238 \cdot 10^{-3}$ . It reads

$$\begin{aligned}\Phi_i^{B3}(\bar{i}, \bar{j}) &= 1.00495\bar{i} - 0.01486\bar{i}^2 + 0.00991\bar{i}^3 \\ \Phi_j^{B3}(\bar{i}, \bar{j}) &= -0.001221\bar{j} + 2.988384\bar{j}^2 - 2.973078\bar{j}^3 + 0.985915\bar{j}^4\end{aligned}$$

The mapping of  $i$ -lines,  $\Phi_i^{B3}$ , corresponds to an approximately regular distribution of  $i$  lines. The mapping of  $j$ -lines,  $\Phi_j^{B3}$ , corresponds to a strong tightening of  $j$ -lines close to the wall. The initial value of  $P_a$  is 0.97744. After five iterations of optimization of iso- $j$  mesh lines position, it gets 0.99277. The two iterations optimizing the coefficient of  $\Phi_i^{B3}$  have led to a very small additional increase (from 0.99277 to 0.99280).

Besides, the drag for the final mesh is  $84.187 \cdot 10^{-4}$ , to be compared with  $89.865 \cdot 10^{-4}$  for the initial one. This drag estimate is quite close to the estimated limiting value ( $CDp = 83.420 \cdot 10^{-4}$ ). In order to check that this difference is due to a reduction of spurious drag, the position and strength of the shock wave is examined for initial and final  $257 \times 257$  grid and for the  $2049 \times 2049$  grid. The position of the sonic line of the shock is almost the same (initial coarse mesh:  $x=0.5043$  ; optimized coarse mesh:  $x=0.5050$ ; fine mesh:  $x=0.5055$  ) just as the Mach number upstream the shock wave (initial coarse mesh:  $M_u=1.246$ ; optimized coarse mesh:  $M_u=1.254$ ; fine mesh:  $M_u=1.254$ ). This is also confirmed by a far-field drag extraction [52] that estimates the spurious drag as  $CD_{sp} = 6.691 \cdot 10^{-4}$  for the initial mesh and  $CD_{sp} = 0.772 \cdot 10^{-4}$  for the final mesh.

Finally the changes in the global indicators based on  $\|dJ/dX\|$  are discussed: The values of  $\mu_{CDp}$ ,  $\theta_{CDp}$ ,  $\mu_{P_a}$  and  $\theta_{P_a}$  for the adapted grids and the corresponding quasi-uniform grids are reported in table 5. As for the line addition method,  $\theta_J$  is in general smaller for the  $J$ -adapted meshes than for the stretched grid, where it is smaller than on the quasi-uniform mesh.

The influence of mesh density on the mesh adaptation process was studied. Very similar results were obtained on a coarser  $129 \times 129$  grid. They are presented in another document [59].

	$CD_p (\times 10^4)$	$\mu CD_p$	$\theta_{CD_p}$	$P_a$	$\mu P_a$	$\theta_{P_a}$
subcritical flow conditions						
lim. values	0.	—	—	1.	—	—
quasi-uniform	10.331	$9.03 \cdot 10^{-6}$	$1.66 \cdot 10^{-8}$	0.99217	$3.19 \cdot 10^{-4}$	$1.04 \cdot 10^{-5}$
stretched	1.079	$2.72 \cdot 10^{-6}$	$1.15 \cdot 10^{-9}$	0.99898	$4.35 \cdot 10^{-4}$	$1.12 \cdot 10^{-7}$
adapted for $CD_p$	0.739	$1.42 \cdot 10^{-6}$	$6.83 \cdot 10^{-10}$	0.99957	$4.93 \cdot 10^{-4}$	$1.25 \cdot 10^{-6}$
adapted for $P_a$	0.841	$1.24 \cdot 10^{-6}$	$5.53 \cdot 10^{-10}$	0.99959	$4.01 \cdot 10^{-4}$	$1.11 \cdot 10^{-6}$
transonic flow conditions						
lim. value	83.420	—	—	0.99306	—	—
quasi-uniform	89.865	$5.40 \cdot 10^{-6}$	$1.37 \cdot 10^{-8}$	0.97741	$3.76 \cdot 10^{-4}$	$5.12 \cdot 10^{-6}$
stretched	85.627	$2.06 \cdot 10^{-6}$	$1.73 \cdot 10^{-9}$	0.99113	$5.71 \cdot 10^{-4}$	$5.72 \cdot 10^{-7}$
adapted for $P_a$	84.187	$1.48 \cdot 10^{-6}$	$2.43 \cdot 10^{-9}$	0.99280	$1.27 \cdot 10^{-3}$	$2.06 \cdot 10^{-6}$

 Table 5:  $CD_p$  and  $P_a$  for  $257 \times 257$  baseline, stretched and adapted grids (adaptation by nodes displacement)

## 6. Mesh adaptation of ONERA M6 wing

For the 3D test case, the number of mesh lines of the two families of structured lines is denoted  $N_i$ ,  $N_j$  and  $N_k$ . The corresponding current indices are  $i$ ,  $j$  and  $k$ .

### 6.1. 3D Euler test case

Finally the adaptation methods are applied in 3D to the ONERA M6 Wing [62]. The flow characteristics are  $M_\infty = 0.84$  and  $\text{AoA} = 3.06^\circ$ . A hierarchy of four O-O meshes was built. The wing grids have been derived from Vassberg and Jameson's NACA0012 airfoil grids through the following procedure: projection of the NACA0012 grid on the D airfoil, the unique generating airfoil of the M6 wing [62]; application of this grid in the symmetry plane; spanwise translation and smoothed rotation of this grid following the chord law of the M6 wing. The resulting grids have monoblock O-O topology, where  $j=1$  is the wing surface,  $j=j_{max}$  the far-field boundary (roughly a half-sphere of radius 120 root chord lengths),  $i=1$  and  $i=i_{max}$  the wing wake,  $k=1$  a surface in the horizontal mid-wing plane, beyond the wing tip,  $k=k_{max}$  the symmetry plane. The mesh sizes are  $65 \times 65 \times 33$  (coarse mesh,  $0.139 \cdot 10^6$  nodes),  $129 \times 129 \times 65$  (standard mesh,  $1.08 \cdot 10^6$  nodes),  $257 \times 257 \times 129$  (very fine mesh,  $8.52 \cdot 10^6$  nodes) and  $513 \times 513 \times 257$  (extremely fine mesh for mesh convergence studies,  $67.6 \cdot 10^6$  nodes). A plot of the wing is presented in Fig. 14 (left) whereas the right part of the same figure depicts the position of  $i$ ,  $j$  and  $k$  mesh-planes. Besides, a family of four meshes, stretched in the direction from wall to far-field, is built based on the extremely fine mesh. For this family, the size of the cells increases in the  $j$  mesh direction from wall to far-field, the ratio of the cell-width at the wall with the mean length in  $i$  mesh direction is  $1/8$ .

The functional outputs of interest are the pressure drag  $CD_p$  and mean stagnation pressure at the wall  $P_a$  (as in the 2D case). Unfortunately, the global forces were not measured on the ONERA M6 wing (only static pressure in different sections was considered) and, probably due to the lack of a common reference surface, a significant dispersion can be observed in the reference values of  $CD_p$  presented in the literature (112 drag counts in [34], 117 in [25], about 120 in [18], about 116 in [21]...) In this study, trailing edge closure, following Vassberg *et al.*, leads to a root chord of length 0.8131 instead of 0.8059 [62]. The reference surface chosen, 0.7532 corresponds to the trapezoidal part of the original M6 wing. Table 6 presents the values of  $CD_p$  and  $P_a$  for the two families of meshes. Considering the difference of function values between two consecutive meshes, two less digits for  $CD_p$  (than in the 2D test case) and one less digit for  $P_a$  are mentioned. As in the airfoil test case,  $CD_p$  decreases and  $P_a$  increases as the size of the cells decreases and limiting values are extrapolated from the finest three meshes ( $CD_p = 122.3$ , and  $P_a = 0.9941$ ) Besides, a plot of the iso-Mach number lines is presented in Fig. 15 for the three fine meshes. The classical  $\lambda$ -shock structure is observed.

Mesh-adaptation aims at building meshes of standard size about the wing ( $129 \times 129 \times 65$ , 1081665 nodes) that lead to an accurate evaluation of the functions of interest. Adaptation by mesh-planes addition, starting from the coarse  $65 \times 65 \times 33$  mesh, is presented in next subsection. Adaptation by mesh-planes displacement for the maximization of  $P_a$  is presented subsequently.

2.2. THE PROPOSED METHODOLOGY APPLIED TO EULERIAN FLOWS

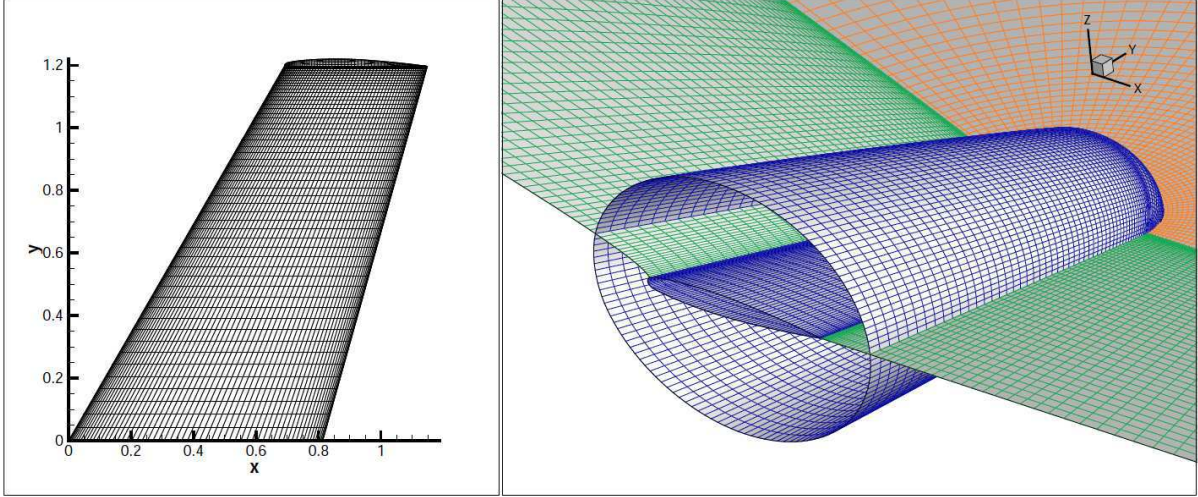


Figure 14: ONERA M6 Wing.  $129 \times 129 \times 65$  mesh. Left: solid wall. Right: mesh topology.  $i$ -mesh planes (green),  $j$ -mesh planes (blue),  $k_{min}$  mesh plane (orange).

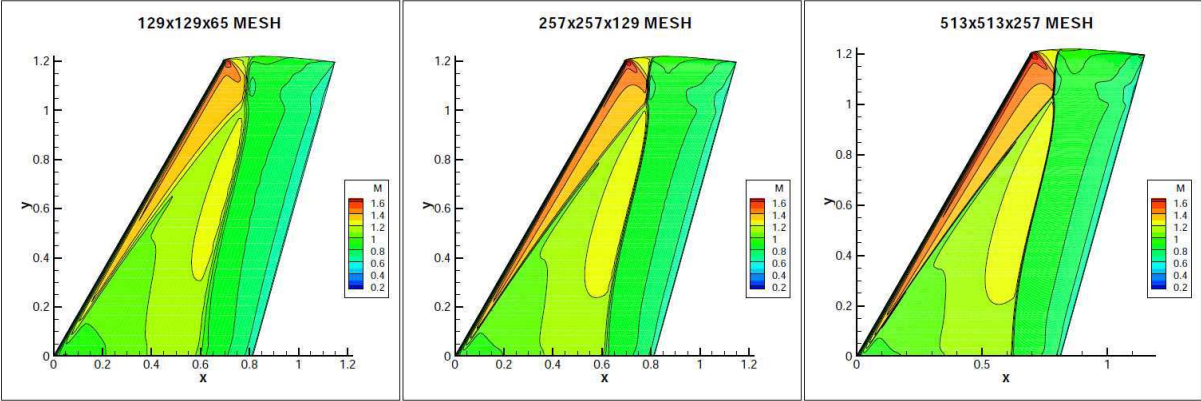


Figure 15: ONERA M6 Wing (upper side). iso-Mach number lines.

### 6.2. Mesh adaptation by mesh-plane addition

Only coarse meshes with planes interpolated in the fine  $257 \times 257 \times 129$  mesh will be considered. Hence, an  $N_i \times N_j \times N_k$  mesh may be fully defined by the position of its planes,  $(\varphi_i, \varphi_j, \varphi_k)$ , with respect to those of the fine mesh. The position of the nodes is then evaluated by a bi-linear interpolation operator  $\mathcal{B}$ .

$$\begin{array}{ccc} \varphi & & \mathcal{B} \\ \{1, N_i\}\{1, N_j\}\{1, N_k\} & \longrightarrow & [1, 257][1, 257][1, 129] \longrightarrow \mathbb{R}^3 \\ (i, j, k) & & (\varphi_i, \varphi_j, \varphi_k) \quad X(x, y, z) \end{array}$$

The plane-addition method is the extension of the one defined for 2D problems in subsection 4.1. The criteria  $c$  is now calculated for the three mesh directions. For example,  $c_j$  is defined as

$$\bar{c}_j = \frac{c_j + c_{j+1}}{2} \quad c_j = \left( \frac{1}{N_i N_k} \sum_{i=1}^{N_i} \sum_{k=1}^{N_k} \|\mathcal{P}(dJ/dX_{i,j,k})\|^2 \right)^{\frac{1}{2}} \quad (18)$$

In order to keep a matching join between  $k = 1 \quad i \leq (N_i + 1)/2$  and  $k = 1 \quad i \geq (N_i + 1)/2$ , the criteria for  $i$ -mesh planes needs to be changed in

$$\bar{c}'_i = \frac{\bar{c}_i + \bar{c}_{N_i-i}}{2}$$

The best parameters, selected in subsection 4.1 are retained ( $Q=4$  and explicit smoothing). Mesh adaptations, based on both  $\mathcal{P}(dCDp/dX)$  and  $\mathcal{P}(dP_a/dX)$  are conducted. The plots of  $c_i$ ,  $c_j$  and  $c_k$  on the initial  $65 \times 65 \times 33$  mesh indicate that the highest criteria values are obtained for  $j$ - and then  $i$ -mesh planes (see figure 16). In order to maintain the computational cost acceptable, a 6-step mesh-planes addition is retained starting by the family of planes of highest sensitivity: addition of 32  $j$ -planes, 32  $i$ -planes, 16  $k$ -planes, 32  $j$ -planes, 32  $i$ -planes, 16  $k$ -planes. The final function values for the  $\|\mathcal{P}(dCDp/dX)\|$ -based adaptation are  $CDp = 129.6 \cdot 10^{-4}$  and  $P_a = 0.9870$ . The corresponding values for the  $\|\mathcal{P}(dP_a/dX)\|$ -based adaptation are  $CDp = 130.0 \cdot 10^{-4}$  and  $P_a = 0.9888$ . For both mesh adaptation procedures, mesh planes were added in front of the leading edge ( $i$ -planes), close to the wall ( $j$ -planes) and close to symmetry plane ( $k$ -planes) (for  $k$  planes, planes location can be well seen in figure 16). These output values are closer to the reference ones than those obtained on the initial quasi-uniform grid (0.9567 and 154.9) and the classical stretched grid (0.9802 and 133.1) with the same number of nodes. All function values are presented in table 7 next to the far-field drag breakdown. It is checked that the spurious drag is significantly lower for the adapted meshes than for the quasi-uniform or stretched meshes of corresponding size.

### 6.3. Mesh adaptation by mesh-plane displacement

It is first carefully checked that the stagnation pressure at the wall is lower for the coarse mesh than for the finer, all over the solid wall (not only upwind but also downwind the shock-waves). A mesh adaptation by maximization of  $P_a$  can hence be considered.

As in the 2D case, the standard size mesh ( $129 \times 129 \times 65$ ) to be adapted is described by a smooth mapping function associated with the body-fitted coordinates of a finer mesh (in this case, the  $257 \times 257 \times 129$  mesh). The mesh of interest with  $N_i \times N_j \times N_k$  mesh-planes, is fully defined by its mapping  $\Phi$  and the following sequence of transformations

$$\begin{array}{ccccccc} \chi_{N_i, N_j, N_k}^{-1} & & \Phi & & \chi_{257, 257, 129} & & \mathcal{B} \\ \{1, N_i\}\{1, N_j\}\{1, N_k\} & \longrightarrow & [0, 1]^3 & \longrightarrow & [0, 1]^3 & \longrightarrow & [1, 257]^2 [1, 129] \longrightarrow \mathbb{R}^3 \\ (i, j, k) & & (\bar{i}, \bar{j}, \bar{k}) & & (\Phi_i, \Phi_j, \Phi_k) & & (\chi_i, \chi_j, \chi_k) \quad X(x, y, z) \end{array}$$

As in the previous section, only Bézier curves of degree four parametrized by a single variable are used and as  $\Phi$  is a map of  $[0, 1]^3$  and satisfies the symmetry property  $\Phi_i(1 - \bar{i}, \bar{j}) = 1 - \Phi_i(\bar{i}, \bar{j})$ , it has to be defined as

$$\begin{aligned} \Phi_i^B(\beta)(\bar{i}, \bar{j}, \bar{k}) &= \bar{i} + \beta(B_{1,4}(\bar{i}) - B_{3,4}(\bar{i})) \\ \Phi_j^B(\beta_{1j}, \beta_{2j}, \beta_{3j})(\bar{i}, \bar{j}, \bar{k}) &= \bar{j} + \beta_{1j}B_{1,4}(\bar{j}) + \beta_{2j}B_{2,4}(\bar{j}) + \beta_{3j}B_{3,4}(\bar{j}) \\ \Phi_k^B(\beta_{1k}, \beta_{2k}, \beta_{3k})(\bar{i}, \bar{j}, \bar{k}) &= \bar{k} + \beta_{1k}B_{1,4}(\bar{k}) + \beta_{2k}B_{2,4}(\bar{k}) + \beta_{3k}B_{3,4}(\bar{k}) \end{aligned}$$

## 2.2. THE PROPOSED METHODOLOGY APPLIED TO EULERIAN FLOWS

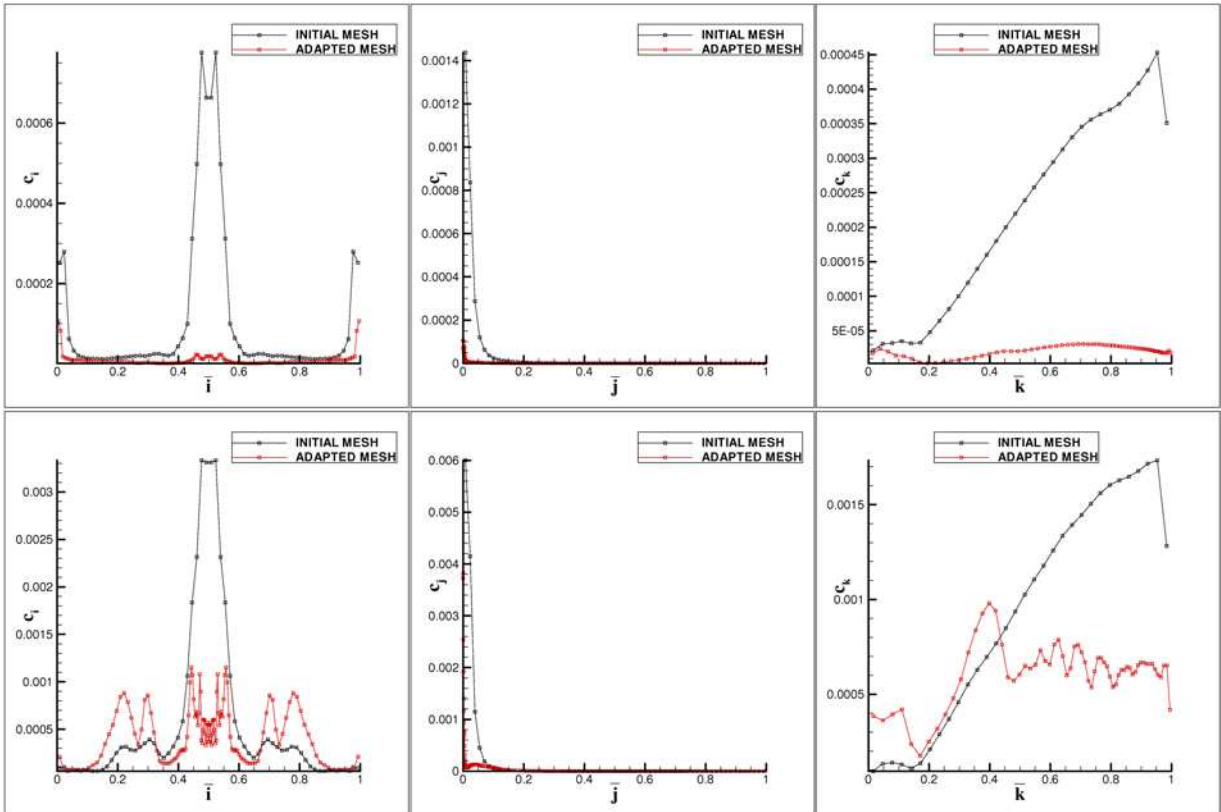
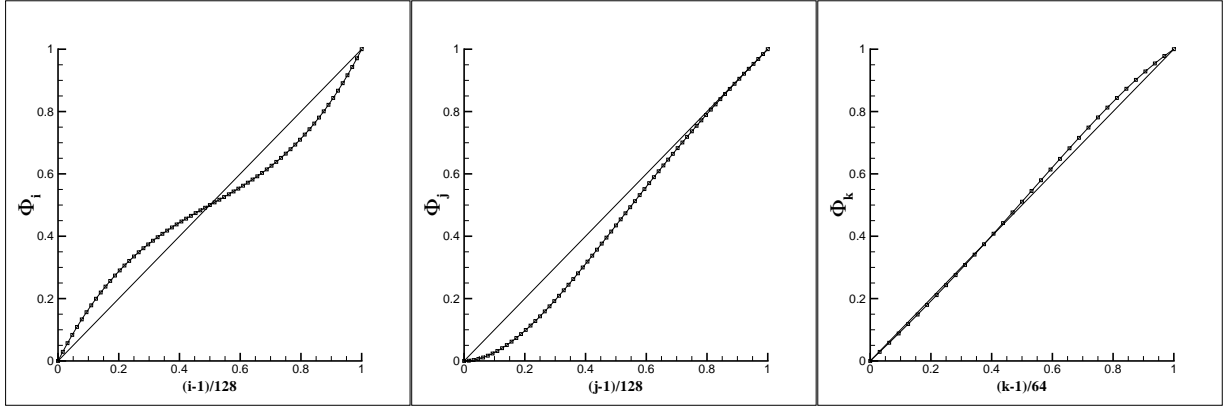


Figure 16: Up:  $(c_i, c_j, c_k)$  on the quasi-uniform  $65 \times 65 \times 33$  mesh at the beginning of  $\|\mathcal{P}(dCDp/dX)\|$ -based mesh adaptation by planes adjonction §(6.2) Down: same plots for  $\|\mathcal{P}(dP_a/dX)\|$ -based mesh adaptation §(6.2)


 Figure 17:  $(\Phi_i^B, \Phi_j^B, \Phi_k^B)$  defining the final mesh adapted by plane-displacement §(6.3)

The derivative of  $P_a$  w.r.t the seven parameters is computed by the chain rule just as before (eq. (17)). In order to lower the computational cost of the mesh adaptation, the seven parameters were advanced simultaneously. The descent method is the steepest descent as in the 2D case. It is stopped at the sixth step after a change in  $P_a$  that was less than 0.001. The value of  $P_a$  on the final adapted mesh is 0.9881 and the corresponding value of  $CDp$  is 129.9. Both values are closer to the reference ones than those obtained on the initial quasi-uniform grid (0.9567 and 154.9) and the classical stretched grid (0.9802 and 133.1) with the same number of nodes. The function values are presented in table 7 next to the far-field drag breakdown. Once again, the spurious drag is significantly lower for the adapted mesh than for the quasi-uniform or stretched meshes of corresponding size.

The final coefficient are  $(\beta, \beta_{1j}, \beta_{2j}, \beta_{3j}, \beta_{1k}, \beta_{2k}, \beta_{3k}) = (0.2285, -0.2491, -8.2453 \cdot 10^{-3}, -1.0252 \cdot 10^{-2}, -1.8916 \cdot 10^{-2}, 8.2601 \cdot 10^{-2})$ . The corresponding mapping function is

$$\begin{aligned} \Phi_i^B(\beta)(\bar{i}, \bar{j}, \bar{k}) &= 1.9074\bar{i} - 2.7222\bar{i}^2 + 1.8148\bar{i}^3 \\ \Phi_j^B(\beta_{1j}, \beta_{2j}, \beta_{3j})(\bar{i}, \bar{j}, \bar{k}) &= 0.0036\bar{j} + 2.9398\bar{j}^2 - 2.8904\bar{j}^3 + 0.9470\bar{j}^4 \\ \Phi_k^B(\beta_{1k}, \beta_{2k}, \beta_{3k})(\bar{i}, \bar{j}, \bar{k}) &= 0.9243\bar{k} + 0.1441\bar{k}^2 + 0.2961\bar{k}^3 - 0.3376\bar{k}^4 \end{aligned}$$

Fig. 17 presents plots of functions  $\Phi_i^B$ ,  $\Phi_j^B$ ,  $\Phi_k^B$  and identity. It clearly appears that  $i$ -planes came closer to the one in front of the leading edge plane (part of  $z = 0$ ,  $\Phi_i=0.5$ ),  $j$ -planes came closer to the wall whereas  $k$ -planes did not move significantly.

Finally the changes in the global indicators based on  $\|dJ/dX\|$  are discussed for the two adaptation methods: The values of  $\mu_{CDp}$ ,  $\theta_{CDp}$ ,  $\mu_{P_a}$  and  $\theta_{P_a}$  for the adapted grids and the corresponding quasi-uniform and stretched grids are reported in table 7.  $\theta_J$  is systematically smaller for the  $J$ -adapted meshes than for the stretched grid, where it is smaller than on the quasi-uniform mesh.

## 7. Conclusion

New approaches to adapting meshes in the framework of finite-volume goal-oriented CFD and discrete adjoint method have been introduced. They are based on a projection of the total derivative of the goal  $J$  w.r.t nodes location, denoted  $\mathcal{P}(dJ/dX)$  retaining all the degrees of freedom available for mesh adaptation. The visualization of this field gives an insight in the goal-oriented mesh-adaptation issue: If the  $\mathcal{P}(dJ/dX)$  vector field exhibits a zone of vectors of large magnitude pointing approximately in the same direction, the function of interest  $J$  is sensitive to a displacement in this zone. Moreover if the mesh is coarse and could be significantly displaced in this area (see figures 12, 13) then a neighboring acceptable mesh would lead to a significantly different value of  $J$  and, obviously, a local refinement is needed for a more stable estimation of  $J$ .

## 2.2. THE PROPOSED METHODOLOGY APPLIED TO EULERIAN FLOWS

	$CD_p (\times 10^4)$	$\mu_{CD_p}$	$\theta_{CD_p}$	$P_a$	$\mu_{P_a}$	$\theta_{P_a}$
quasi-uniform grids						
<i>lim. value</i>	122.3	—	—	0.9949	—	—
$513 \times 513 \times 257$	127.1	*	*	0.9844	*	*
$257 \times 257 \times 129$	132.9	$3.22 \cdot 10^{-7}$	$2.70 \cdot 10^{-10}$	0.9746	$2.80 \cdot 10^{-6}$	$4.09 \cdot 10^{-9}$
$129 \times 129 \times 65$	154.9	$2.33 \cdot 10^{-6}$	$5.46 \cdot 10^{-9}$	0.9567	$1.71 \cdot 10^{-5}$	$5.27 \cdot 10^{-8}$
$65 \times 65 \times 33$	233.4	$1.79 \cdot 10^{-5}$	$1.01 \cdot 10^{-7}$	0.9294	$8.54 \cdot 10^{-5}$	$5.73 \cdot 10^{-7}$
stretched grids						
$513 \times 513 \times 257$	125.5	*	*	.9921	*	*
$257 \times 257 \times 129$	126.8	$3.70 \cdot 10^{-7}$	$5.96 \cdot 10^{-11}$	0.9890	$6.99 \cdot 10^{-6}$	$1.82 \cdot 10^{-9}$
$129 \times 129 \times 65$	133.1	$2.43 \cdot 10^{-6}$	$1.25 \cdot 10^{-9}$	0.9802	$6.36 \cdot 10^{-5}$	$3.15 \cdot 10^{-8}$
$65 \times 65 \times 33$	157.6	$2.12 \cdot 10^{-5}$	$2.92 \cdot 10^{-8}$	0.9453	$4.84 \cdot 10^{-4}$	$4.08 \cdot 10^{-7}$

Table 6: ONERA M6 Wing.  $M_\infty = 0.84$  AoA=3.06°.  $CD_p$  and  $P_a$  for baseline and stretched grids. The \* sign corresponds to calculations that could not be achieved due to huge CPU and memory requirements.

	$CD_p (10^{-4})$	$\mu_{CD_p}$	$\theta_{CD_p}$	$P_a$	$\mu_{P_a}$	$\theta_{P_a}$	$CD_w$	$CD_i$	$CD_{sp}$
lim. value	122.3	—	—	0.9949	—	—	—	—	—
quasi-uniform	154.9	$2.33 \cdot 10^{-6}$	$5.46 \cdot 10^{-9}$	0.9774	$1.71 \cdot 10^{-5}$	$5.27 \cdot 10^{-8}$	48.5	69.0	37.4
stretched	133.1	$2.43 \cdot 10^{-6}$	$1.25 \cdot 10^{-9}$	0.9802	$6.36 \cdot 10^{-5}$	$3.15 \cdot 10^{-8}$	50.6	72.1	10.4
ad. for $P_a$ (§6.2)	130.0	$1.71 \cdot 10^{-6}$	$1.05 \cdot 10^{-9}$	0.9888	$7.46 \cdot 10^{-5}$	$1.92 \cdot 10^{-8}$	50.0	72.2	7.8
ad. for $CD_p$ (§6.2)	129.6	$2.51 \cdot 10^{-6}$	$1.03 \cdot 10^{-9}$	0.9870	$8.75 \cdot 10^{-5}$	$2.44 \cdot 10^{-8}$	50.7	72.2	6.7
ad. for $P_a$ (§6.3)	129.9	$1.47 \cdot 10^{-6}$	$1.45 \cdot 10^{-9}$	0.9881	$7.06 \cdot 10^{-5}$	$2.92 \cdot 10^{-8}$	50.7	72.7	6.5

Table 7: ONERA M6 Wing.  $M_\infty = 0.84$  AoA=3.06°.  $CD_p$ ,  $P_a$ , far-field drag breakdown for (129×129×65) quasi-uniform, stretched and adapted meshes.

When dealing in particular with Eulerian flows, classical functional outputs reach their maximum/minimum value at the limit of fine meshes and mesh-adaptation by maximization/minimization of these outputs were successfully conducted. Besides, a heuristic mesh-adaptation method, consisting in adding mesh-lines in the zones of large  $\|\mathcal{P}(dJ/dX)\|$  was also successfully applied. Actually, adapted meshes presented lower mean value of  $\|\mathcal{P}(dJ/dX)\|$  times the local characteristic length of the cells.

Future work will include extension to RANS flows and application to more complex geometries as well as extension to unstructured [63, 64] meshes that provide a more powerful framework for mesh adaptation.

### Acknowledgments

The authors express their warm gratitude to J.C. Vassberg and A. Jameson for allowing the co-workers of D. Destarac to use their hierarchy of O-grids around the NACA0012 airfoil. They warmly thank D. Destarac who derived the M6 wing grids from Vassberg and Jameson's airfoil grids and carried out far-field drag extraction. They are also very grateful to J.A. Désidéri for his relevant recommendations.

### References

- [1] Johnson C, Rannacher R, Boman M. Numerics and hydrodynamics theory: towards error control in CFD, SIAM J Numer Anal 1995;32:1058–1079.
- [2] Becker R, Rannacher R. Weighted *a posteriori* error control in FE methods, in Proceedings of ENUMATH-97, Heidelberg, World Scientific Publishing, 1998.
- [3] Becker R, Rannacher R. An optimal control approach to *a posteriori* error estimation in finite element methods. Acta Numerica 2001:1–102.
- [4] Giles M, Larson MG, Levenstam JM, Süli E. Adaptive error control for finite element approximation of lift and drag coefficient in viscous flow. Tech. Rep. NA-97/06, Comlab, Oxford University, 1997.

- [5] Prudhomme S, Oden J. On goal oriented error estimation for elliptic problems: application to the control of pointwise error. *Computers Method in Applied Mechanics and Engineering* 1999;313–331.
- [6] Larson MG, Barth TJ. *A posteriori* error estimation for discontinuous Galerkin approximation of hyperbolic systems. NAS Technical Report. NAS 99-010. 1999.
- [7] Machiels L, Peraire J, Patera AT. *A posteriori* finite element output bounds for the incompressible Navier-Stokes equations; Application to a natural convection problem. *J Comput Phys* 2001;172:401–425.
- [8] Hartmann R, Houston P. Adaptive discontinuous Galerkin methods for the compressible Euler equations. *J Comput Phys* 2002;182(2):508–532.
- [9] Leicht T, Hartmann R. Error estimation and anisotropic mesh refinement for 3D laminar aerodynamic flow simulations. *J Comput Phys* 2010;229:7344–7360.
- [10] Hartmann R, Held J, Leicht T. Adjoint-based error estimation and adaptive mesh refinement for the RANS and (k- $\omega$ ) turbulence model equations. Accepted for publication in *J Comput Phys*.
- [11] Loseille A, Dervieux A, Alauzet F. Fully anisotropic goal-oriented mesh adaptation for 3D steady Euler equations. *J Comput Phys* 2010;229(2):2860–2897.
- [12] Pierce NA, Giles MB. Adjoint recovery of superconvergent functionals for PDE approximations. *SIAM Review* 2000;42:247–264.
- [13] Pierce NA, Giles MB. Adjoint and defect error bounding and correction for functional estimates. In: *AIAA paper series, Paper 2003-3846*; 2003.
- [14] Venditti DA, Darmofal DL. Adjoint error estimation and grid adaptation for functional outputs: Application to quasi-one-dimensional flow. *J Comput Phys* 2000;164:40–69.
- [15] Venditti DA, Darmofal DL. Grid adaptation for functional outputs: Application to two-dimensional inviscid flows. *J Comput Phys* 2002;176:40–69.
- [16] Venditti DA, Darmofal DL. Anisotropic grid adaptation for functional outputs: Application to two-dimensional viscous flows. *J Comput Phys* 2003;187:22–46.
- [17] Park MA. Three-dimensional turbulent RANS adjoint-based error correction In: *AIAA paper series, Paper 2003-3849*; 2003.
- [18] Park MA. Adjoint-based, three-dimensional error prediction and grid adaptation. *AIAA J* 2010;42(9):1854–1862.
- [19] N. Kroll, N. Gauger, J. Brezillon, K. Becker, V. Schultz. Ongoing activities in shape optimization within the german project Megadesign. in *Proceedings of ECCOMAS Congress, Jyvaskyla*. 2004.
- [20] Lee-Rausch EM, Park MA, Jones WT, Hammond DP, Nielsen EJ. Application of parallel adjoint-based error estimation and anisotropic grid adaptation for three-dimensional aerospace configurations In: *AIAA paper series, Paper 2005-4842*; 2005.
- [21] Barthet A, Airiau Ch, Braza M, Turrette L. Adjoint-based error correction applied to far-field drag breakdown on structured grid. In: *AIAA paper series, Paper 2006-3315*; 2006
- [22] Kim HJ, Nalhashi K. Output-based error estimation and adaptive mesh refinement using viscous adjoint method. In: *AIAA paper series, Paper 2006-1395*; 2006.
- [23] Jones WT, Nielsen EJ, Park MA. Validation of 3D adjoint-based error estimation and mesh adaptation for sonic boom prediction. In: *AIAA paper series, Paper 2006-1150*; 2006.
- [24] Balasubramanian R, Newman III JC. Comparison of adjoint-based and feature-based grid adaptation for functional outputs. *Int J Numer Methods Fluids* 2007;53:1541–1569.

## 2.2. THE PROPOSED METHODOLOGY APPLIED TO EULERIAN FLOWS

- [25] Nemec M, Aftosmis MJ. Adjoint error estimation and adaptive refinement for embedded-boundary cartesian mesh. In: AIAA paper series, Paper 2007-4187. 2007.
- [26] Rogé G, Borel-Sandou S. Improvement of observations, error estimation and mesh adaptation using an adjoint based approach for aerodynamic calculations. Proceedings of RTO-MP-AVT-147 symposium. 2007.
- [27] Nemec M, Aftosmis MJ, Wintzer M. Adjoint-based adaptive mesh refinement for complex geometries In: AIAA paper series, Paper 2008-725; 2008.
- [28] Rogé G, Martin L. Goal oriented anisotropic grid adaptation. C.R. Acad. Sci. Paris, Ser. I 346 pp. 1109–1112. 2008.
- [29] Park MA, Darmofal DL. Output-adaptive tetrahedral cut-cell validation for sonic boom prediction. In: AIAA paper series, Paper 2008-6594; 2008.
- [30] Peter J, Lazareff M, Couaillier V. Verification, validation and error estimation in CFD. Int J Engineering Systems Modeling and Simulation 2010;2(1/2):75–86.
- [31] Kroll N, Bieler H, Deconinck H, Couaillier V, van der Ven H, Sorensen K. ADIGMA. A European initiative on the development of adaptive higher-order methods variational methods for aerospace applications. Springer. 2010.
- [32] Jameson A, Schmidt W, Turkel E. Numerical solution of the Euler equations by finite volume methods using Runge-Kutta time stepping schemes. In: AIAA paper series, Paper 1981-1259; 1981.
- [33] Dwight RP. Goal-oriented mesh adaptation using a dissipation based error indicator Int J for Numer Methods Fluids 2007;56(8):1193–2000.
- [34] Dwight RP. Heuristic *a posteriori* estimation of error due to dissipation in finite volume schemes and application to mesh adaptation. J Comput Phys Vol 2008;227:2845–2863.
- [35] Fidkowski KJ, Darmofal DL. Output-Based Error Estimation and Mesh Adaptation in Computational Fluid Dynamics: Overview and Recent Results. AIAA J 2011;49(4):673–694.
- [36] Yamaleev NK, Diskin B, Pathak K. Error minimization via adjoint-based anisotropic grid adaptation. In: AIAA paper series; Paper 2010-4436. 2010.
- [37] Bompard M, Peter J. Local search methods for design in aeronautics. in RTO-AVT-167 Lecture series on Strategies for optimization and automated design of gas turbine engines 2010.
- [38] Jameson A. Aerodynamic design via control theory. J Sci Comput 1988;3:233–260.
- [39] Peter J, Dwight RP. Numerical sensitivity analysis: a survey of approaches. Comput and Fluids 2010;39(3):373–391.
- [40] A. Taylor III, V. Korivi, G. Hou. Sensitivity analysis applied to the Euler equations: a feasibility study with emphasis on variation of geometric shape. In: AIAA paper series; Paper 91-0173. 1991.
- [41] Baysal O, Eleshaky M. Aerodynamic design sensitivity analysis methods for the compressible Euler equations. J Fluids Eng 1991;113(4):681–688.
- [42] P. Frank, G. Shubin. A comparison of optimisation based approaches for a model computational aerodynamics design problem. J Comput Phys 1992;98:74–89.
- [43] Nielsen E, Park M. Using an adjoint approach to eliminate mesh sensitivities in aerodynamic design. AIAA J 2005;44(5):948–953.
- [44] Nielsen E, Kleb B. Efficient Construction of Discrete Adjoint Operators on Unstructured Grids by Using Complex Variables. In: AIAA paper series; Paper 2005-0324. 2005.

- [45] Alauzet F, Borel-Sandou S, Daumas L, Dervieux A, Dinh Q, Kleinveld S, Loseille A, Mesri Y, Rog G. Multi-model design strategies applied to sonic boom reduction”. *European J of Comput Mechanics*. 2007;10(1):1–20.
- [46] Truong AH, Oldfield CA, Zingg DW. Mesh movement for a discrete-adjoint Newton-Krylov algorithm for aerodynamic optimization. *AIAA J*, 2008;46(7):1695–1704.
- [47] Nielsen E, Lee-Rausch EM, Jones WT. Adjoint-based design of rotors in a non-inertial reference frame. *J Aircraft*, 2010;47(2):638–646.
- [48] Hicken, JE, Zingg DW, Aerodynamic optimization algorithm with integrated geometry parametrization and mesh movement, *AIAA J*, 2010;48(2):400–413.
- [49] Widhalm M, Brezillon J, Ilić C, Leicht T. Investigation of adjoint-based gradient computation for realistic 3d aero-optimization. In: *AIAA paper series; Paper 2010-9129*. 2010.
- [50] Nguyen-Dinh M, Trontin P, Meaux M, Peter J, Renac F. Total derivative of aerodynamics functions w.r.t. volume or wall mesh nodes for shape optimization and mesh adaptation. Nguyen-Dinh M, Trontin P, Meaux M, Peter J, Renac F. in *Proceedings of ODAS Congress, Toulouse*. 2011.
- [51] Kapadia S, Anderson WK, Burdyshaw C. Channel shape optimization of solid oxide fuel cells using advanced numerical techniques. *Comput and Fluids* 2011;41(1):41–50.
- [52] D. Destarac, *Far-Field / Near-Field Drag Balance and Applications of Drag Extraction in CFD*, VKI Lecture Series 2003, CFD-based Aircraft Drag Prediction and Reduction, Rhode Saint Genèse (Belgium), February 3-7, 2003, National Institute of Aerospace, Hampton (VA), November 3-7, 2003.
- [53] Vassberg JC, Jameson A. In pursuit of grid convergence, part I: two-dimensional Euler solution. In: *AIAA paper series, Paper 2009-4114*; 2009.
- [54] Vassberg JC, Jameson A. In pursuit of grid convergence for two-dimensional Euler solution. *J Aircraft*, 2010;47(4):1152–1166.
- [55] Roe PL. Approximate Riemann solvers, parameter vectors and difference schemes. *J Comput Phys* 1981;43:357–372.
- [56] van Leer B. Towards the ultimate conservative difference scheme. V - A second order sequel to Godunov’s method. *J Comput Phys* 1979;32:101–136.
- [57] van Albada GD, van Leer B, Roberts WW. A comparative study of computational methods in cosmic gas dynamics. *Astronomy and Astrophysics* 1982;108:76–84.
- [58] Cambier L, Veillot JP. Status of the *elsA* CFD software for flow analysis and multidisciplinary applications. In: *AIAA paper series, Paper 2008-664*; 2008.
- [59] Peter J, Trontin P, Nguyen-Dinh M. Goal oriented mesh adaptation using total derivative of aerodynamic functions with respect to mesh coordinates. In: *AIAA paper series. Paper 2011-30*; 2011
- [60] Peter J, Nguyen-Dinh M, Trontin P. Goal oriented mesh adaptation using total derivative of aerodynamic functions with respect to mesh coordinates. In: *AIAA paper series. Paper 2012-158*; 2011
- [61] Rizzi A. Computational Mesh for Transonic Airfoils, in *Numerical methods for the computation of transonic flow*, Arthur Rizzi and Henri Viviand editors, Vieweg, Braunschweig, 1981.
- [62] Schmitt V, Charpin A. Pressure distributions on the ONERA-M6-Wing at transonic Mach numbers. Experimental data base for computer program assessment. *AGARD-R-138*. 179.
- [63] Puigt G, Gazaix M, Montagnac M, Le Pape MC, de La Llave Plata M, Marmignon C, Boussuge JF, Couaillier V. Development of a new hybrid compressible solver inside the CFD *elsA* software. In: *AIAA paper series. Paper 2011-3379*; 2011
- [64] de La Llave Plata M, Couaillier V, Marmignon C, Le Pape MC, Gazaix M. Further developments in the multiblock hybrid CFD solver *elsA-H*. In: *AIAA paper series. Paper 2012-1112*; 2012

## 2.3 The complete approach

The works presented in the previous section are the main results of the first study of mesh adaptations based on the derivative  $dJ/dX$ . Nevertheless other approaches have also been studied but not included in this article [40]. These methods seemed to be more efficient but actually their applications did not lead to better results. This section is devoted to the presentation of some of them in order to provide a better understanding of some choices made in the previous work.

### 2.3.1 Mesh adaptation without parametrization

The mesh adaptation method by line displacements considered in the previous methodology is based on a parametrization of the mesh. The derivative of the goal w.r.t. the mesh parameters are computed thanks to the derivative  $dJ/dX$ . The meshes are then adapted in order to maximize (or minimize) the goal that is supposed to be monotonically affected by the numerical dissipation. In this framework one can ask if the mesh parametrization is really necessary. Indeed a mesh can be directly adapted without parametrization using a steepest descent. In other words a mesh sequence  $(X^l)$  can be defined by the relation:

$$X^l = X^{l-1} - s^l \mathcal{P} \left( \frac{dJ}{dX^{l-1}} \right)$$

where  $X^0$  is the initial mesh and  $s^l$  is set to its optimal value using three steady state computations in order to define a parabolic approximation of  $J$  as a function of  $s$ .

This method was applied to minimize  $CD_p$  for the  $257 \times 257$  mesh in the subsonic case ( $M_\infty = 0.5$ ). The figure 2.5(a) shows the values of the output for the eleven iterations that were carried out. The  $CD_p$  value decreases from  $10.33 \cdot 10^{-4}$  to  $6.33 \cdot 10^{-4}$ . The initial and the adapted meshes are illustrated on the figure 2.5(b) (respectively with dashed and solid lines). The adaptation has an impact only within four layer of nodes around the airfoil.

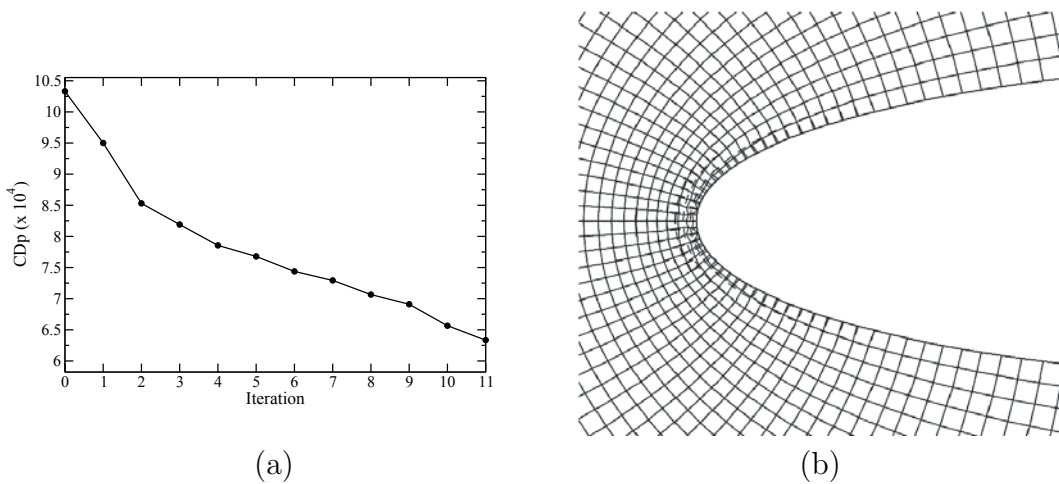


Figure 2.5: (a)  $CD_p$  vs. iteration of the mesh adaptation process (b) Dashed: initial grid ; Solid: adapted grid for  $CD_p$

The following figures 2.6 focus on the leading edge and the trailing edge. We observe that the local adaptation is active essentially at the leading edge.

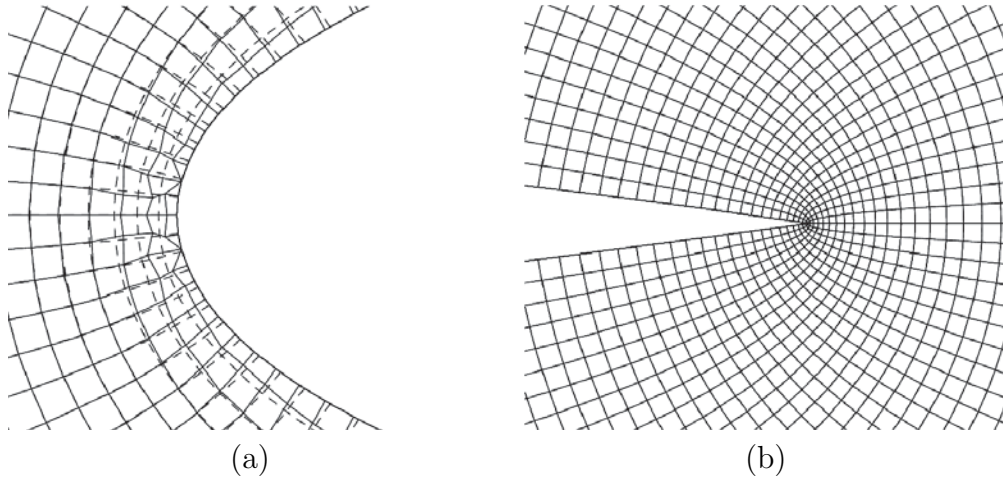


Figure 2.6: Dashed: initial grid ; Solid: adapted grid for  $CD_p$  ; (a) focus at the leading edge (b) focus at the trailing edge

We also observe that oscillations occur. Moreover two points are hitting the solid wall so that this grid is a local optimum at the border of the acceptable meshes domain. These results lead to consider a smoothing step in the adaptation process. The projected field  $\mathcal{P}(dJ/dX^{l-1})$  is replaced by a smoother one built in order to average the field where mesh lines  $j$  tends to oscillate. The figure 2.7(a) illustrates the  $CD_p$  values for the twelve iterations that were carried out and 2.7(b) shows the initial mesh and the adapted one at the leading edge of the airfoil.

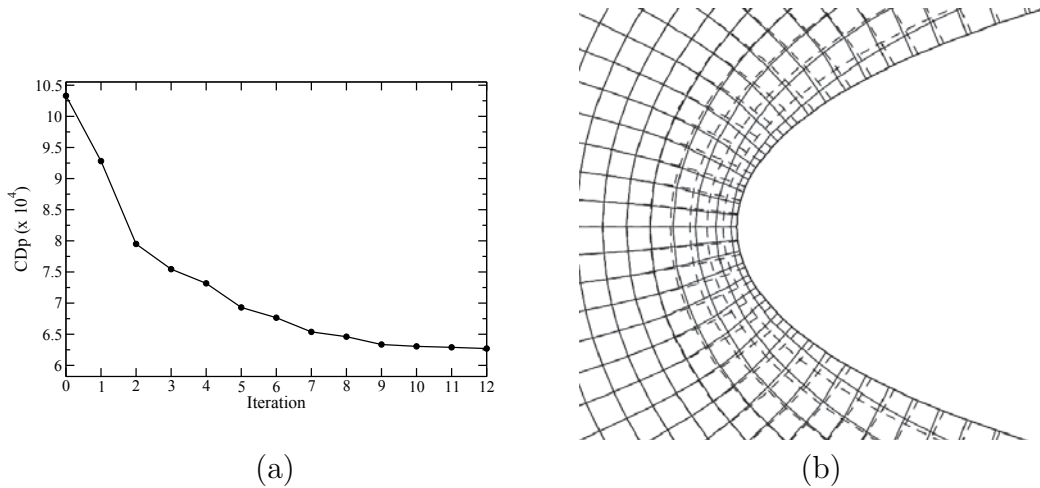


Figure 2.7: (a)  $CD_p$  vs. iteration of the mesh adaptation process with the smoothed field (b) Dashed: initial grid ; Solid: adapted grid for  $CD_p$

The  $CD_p$  value decreases from  $10.33 \cdot 10^{-4}$  to  $6.27 \cdot 10^{-4}$  which is close to the value obtained previously ( $6.33 \cdot 10^{-4}$ ). These results are significantly worse than those obtained using mesh parametrization ( $0.739 \cdot 10^{-4}$ ). This shows that  $dJ/dX$  can not be used directly to adapt meshes efficiently, the mesh adaptation method has a significant impact. The structured meshes have to be globally adapted while preserving its regularity.



## 2.4 Conclusions

The results obtained in the two-dimensional and three-dimensional test cases of Eulerian flows, presented in the present chapter, confirm that the total derivative  $dJ/dX$  is a useful quantity for mesh adaptation. Nevertheless several aspects of this work deserve a deeper study.

A result of the current study is that  $dJ/dX$  can also be used to build up global indicator of mesh quality for the computation of the outputs (the criteria  $\mu_J$  and  $\theta_J$ ). The mesh adaptations have been carried out on the basis of  $\mu_J$  but we observed that the criterion  $\theta_J$  decreased much more. Moreover it appeared that  $dJ/dX$  cannot be used directly. Indeed a mesh parametrization was necessary for the mesh displacement method. Therefore the development of more reliable indicators, that take into account these remarks, is a part of the study presented in the next chapter.

Another conclusion of the current study is that the remeshing strategy has an important impact on the method efficiency. Indeed even if the outputs values were improved for the different remeshing methods that have been considered, important differences can occur between these values according to the selected remeshing method. In this framework a more efficient mesh adaptation method for structured meshes is also a part of the next chapter. This method aims to allow more local refinement.

Finally, the application of this methodology to flows described by the RANS equations is also a part of the next chapter.

## 2.4. CONCLUSIONS

# Chapitre 3

## Qualification de maillages et adaptations locales

### Résumé :

Le chapitre précédent a montré l'intérêt d'utiliser la dérivée totale  $dJ/dX$  pour adapter des maillages dans le calcul de la fonction  $J$ . Cette étude a également mis en évidence la possibilité de construire des critères globaux de qualité de maillage pour le calcul de fonctions. Néanmoins cette étude a aussi montré l'influence de la méthode de remaillage utilisée et elle a été appliquée uniquement pour des écoulements de fluides parfaits. Ainsi l'étude de critères plus précis et la mise en œuvre d'une méthode de remaillage permettant d'adapter localement les maillages ont été effectués et appliqués dans le contexte d'écoulements de fluides parfaits ainsi que pour des écoulements décrits par les équations RANS.

### 1. Critères de qualification de maillages

L'étude précédente a mis en évidence certains points à prendre en compte pour construire un senseur fiable indiquant les zones de maillage à adapter. En effet les adaptations effectuées étaient basées sur la norme de  $dJ/dX$  (critère noté  $\mu_J$  dans l'étude précédente) alors qu'il a été observé que le critère qui diminue pour la fonction  $P_a$  était le critère qui prenait en compte la longueur caractéristique en chaque nœud (critère noté  $\theta_J$  dans l'étude précédente). Il s'avère nécessaire de prendre en compte les déplacements admissibles des nœuds du maillage ainsi que la régularité du champ  $dJ/dX$ . Dans ce contexte les critères développés dans ce chapitre s'appuient sur la relation suivante :

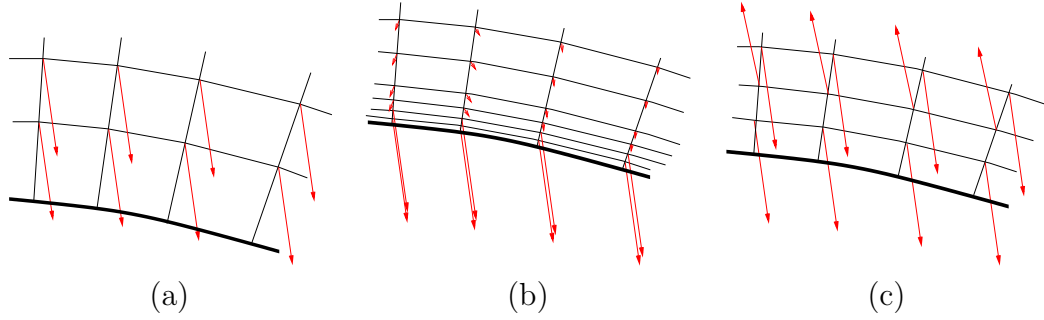
$$J(X + dX) - J(X) \simeq \frac{dJ}{dX} \cdot dX$$

où  $dX$  est un déplacement admissible des nœuds du maillage (c'est-à-dire tel que  $X + dX$  est effectivement un maillage et tel que la forme de l'objet solide n'est pas modifiée). Le membre de droite de cette relation peut être majoré en multipliant  $dJ/dX$  en chaque nœud par une longueur caractéristique d'un déplacement admissible du nœud (dans la pratique la moitié de la distance au nœud voisin le plus proche). Le critère ainsi obtenu est un critère de stabilité du maillage  $X$  pour le calcul de la fonction  $J$  dans la mesure où il majore la variation au premier ordre de l'estimation de fonction obtenue sur des maillages voisins  $X + dX$  et celle obtenue sur le maillage courant  $X$ .

### 3. QUALIFICATION DE MAILLAGES ET ADAPTATIONS LOCALES

Ce critère prend donc en compte les deux cas de figure suivants :

- De larges déplacements admissibles avec un champ  $\mathcal{P}(dJ/dX)$  régulier (figure (a) ci-dessous) indiquant qu'un déplacement local des nœuds du maillage aura un impact important sur l'estimation de  $J$ .
- De faibles déplacements admissibles avec un champ  $\mathcal{P}(dJ/dX)$  régulier (figure (b) ci-dessous) indiquant que peu de déplacements locaux sont admissibles et ainsi que l'impact sur l'estimation de  $J$  sera faible.



- (a) Large et régulier champ  $\mathcal{P}(dJ/dX)$  avec de larges déplacements admissibles des nœuds  
(b) Large et régulier champ  $\mathcal{P}(dJ/dX)$  avec peu de déplacements admissibles des nœuds  
(c) Large et non régulier champ  $\mathcal{P}(dJ/dX)$  avec de larges déplacements admissibles des nœuds

Néanmoins il est également possible que de larges déplacements soient admissibles avec un champ  $\mathcal{P}(dJ/dX)$  irrégulier (comme illustré sur la figure (c) ci-dessus). Dans ce cas un déplacement local des nœuds du maillage aura éventuellement peu d'impact sur l'estimation de  $J$  du fait des effets de compensation occasionnés par l'irrégularité de  $\mathcal{P}(dJ/dX)$ . Ces considérations ont conduit à construire le critère suivant :

$$\bar{\theta}(i, j) = \|\overline{\mathcal{P}(dJ/dX)}_{ij}\| r_{i,j} \quad \bar{\theta} = \frac{1}{N_i N_j} \sum_{i,j} \bar{\theta}(i, j)$$

où  $\overline{\mathcal{P}(dJ/dX)}$  est une moyenne spatiale de  $\mathcal{P}(dJ/dX)$  pour prendre en compte la régularité de ce champ et  $r_{i,j}$  est une longueur caractéristique d'un déplacement admissible du nœud  $(i, j)$ . Le réel  $\bar{\theta}$  défini comme la moyenne du critère scalaire  $\bar{\theta}(i, j)$  est candidat à être un critère global de qualité du maillage pour le calcul de la fonction  $J$ .

Afin d'évaluer ce critère, une famille paramétrée de maillages a été construite autour du profil NACA0012. Pour chacun des maillages, la fonction  $J$  a été calculée ainsi que le critère  $\bar{\theta}$  pour étudier la corrélation entre les bonnes estimations de fonctions et les faibles valeurs du critère.

## 2. Adaptations locales de maillages appliquées à des écoulements de fluides parfaits

Afin d'effectuer des adaptations de maillages plus locales qu'au chapitre précédent, une nouvelle méthode a été mise en œuvre. Cette méthode s'appuie sur un système

### 3. QUALIFICATION DE MAILLAGES ET ADAPTATIONS LOCALES

d'équations aux dérivées partielles elliptiques et s'inspire de la méthode de Soni *et al.* [62] qui utilise un senseur basé sur les caractéristiques de l'écoulement. Le principe de la méthode de remaillage repose sur le fait qu'un maillage structuré peut être considéré comme l'image d'un maillage cartésien du carré unité (ou cube unité en 3D) par une fonction solution de l'équation suivante (dans le cas 3D) :

$$\sum_{i,j=1}^3 g^{ij} x_{\xi^i \xi^j} + \sum_{k=1}^3 g^{kk} P_k x_{\xi^k} = 0$$

où  $x = (x_1, x_2, x_3)$  et  $\xi^i$  ( $i = 1, 2, 3$ ) sont les coordonnées curvilignes et  $g^{ij}$  ( $i, j = 1, 3$ ) le tenseur métrique contravariant et  $P_k$  les fonctions de contrôle. Le maillage ainsi généré est entièrement défini par ces fonctions de contrôle. À noter que ces fonctions peuvent être calculées même si le maillage n'a pas été généré par cette méthode.

Le remaillage basé sur cette équation consiste à modifier les fonctions de contrôle à partir du senseur local  $\bar{\theta}$  afin d'augmenter la densité de nœuds dans les zones du maillage présentant de fortes valeurs du critère.

Cette méthode a été appliquée aux mêmes cas tests qu'au chapitre précédent à savoir un écoulement subsonique ( $M_\infty = 0,5$ ) et un écoulement transsonique ( $M_\infty = 0,8$ ) de fluide parfait, sans incidence, autour du profil NACA0012. Le schéma utilisé est le schéma de Jameson et les fonctions d'intérêt considérées sont le coefficient de traînée de pression  $CD_p$  et l'intégrale autour du profil de la pression d'arrêt (notée  $P_a$ ). Dans le cas subsonique, la valeur de  $P_a$  passe de 0,99121 à 0,99949 (à comparer à la valeur théorique de 1).

Concernant l'adaptation pour  $CD_p$ , la valeur de fonction est passée de  $16,050 \cdot 10^{-4}$  sur le maillage initial à  $0,584 \cdot 10^{-4}$  sur le maillage adapté. Dans le cas transsonique, la valeur de  $P_a$  est passée de 0,97425 à 0,99179 (à comparer à la valeur limite de 0,99225). Concernant l'adaptation pour  $CD_p$ , la valeur de fonction est passée de  $94,361 \cdot 10^{-4}$  sur le maillage initial à  $83,422 \cdot 10^{-4}$  sur le maillage adapté (à comparer à la valeur limite de  $83,483 \cdot 10^{-4}$ ). À noter que les estimations de  $P_a$  sont également améliorées lors des adaptations pour  $CD_p$  et inversement. D'autre part, il a aussi été observé une diminution de la traînée artificielle  $CD_{sp}$  lors de ces adaptations.

## 3. Applications à un écoulement décrit par les équations RANS

La méthodologie présentée dans la section précédente a été mise en œuvre dans le contexte d'un écoulement décrit par les équations RANS. Le cas test sélectionné est un écoulement transsonique ( $M_\infty = 0,725$ ) autour du profil RAE2822 avec un angle d'attaque  $AoA = 2,466^\circ$  et un nombre de Reynolds par mètre  $Re.m^{-1} = 6,5 \cdot 10^6$ . Ce cas test a été considéré par Venditti et Darmofal [75]. Le maillage utilisé est un maillage en C composé de seize blocs dont la frontière se trouve à cent cordes du profil. Deux fonctions d'intérêt ont été considérées, à savoir le coefficient de traînée  $Cd$  et le coefficient de portance de pression  $CL_p$ . Des valeurs de référence de  $Cd$  et  $CL_p$  ont été extrapolées à l'aide d'une étude de convergence en maillage. Les valeurs ainsi obtenues sont en accord avec celles de Venditti et Darmofal [75]. Le processus d'adaptation a été arrêté lorsque la valeur du critère étudié augmente par rapport à sa valeur à l'itération précédente.

### 3. QUALIFICATION DE MAILLAGES ET ADAPTATIONS LOCALES

La méthode d'adaptation utilisée précédemment dans le cas d'écoulements de fluides parfaits a dû être améliorée pour traiter certaines spécificités de ce nouveau cas test. L'une de ces modifications visait à traiter l'anisotropie du maillage initial. En effet certaines zones de ce maillage sont initialement raffinées ce qui conduit à de faibles valeurs du senseur à ces endroits. Le maillage n'y est donc pas raffiné et n'y est, de même, que peu déraffiné. Ainsi ces zones du maillage où la densité de nœuds est élevée se conservent au cours des itérations d'adaptation. Il s'ensuit que ces zones sont denses non pas parce que le senseur les a détectées mais uniquement car elles l'étaient initialement. Pour éviter ce problème, les valeurs des fonctions de contrôle utilisées pour effectuer la première itération sont mises à zéro dans les zones du maillage où les valeurs du senseur sont inférieures à une valeur limite.

L'adaptation pour  $Cd$  a été effectuée en trois itérations. La valeur initiale de  $Cd$  était  $123,93 \cdot 10^{-4}$  (à comparer à la valeur limite de  $118,60 \cdot 10^{-4}$ ). La valeur obtenue sur le maillage adapté était  $119,41 \cdot 10^{-4}$  soit une réduction de l'erreur de 85% pour l'estimation champ proche. La valeur initiale de  $CL_p$  était  $0,73950$  et sa valeur sur le maillage adapté pour  $Cd$  était  $0,74194$  (à comparer à la valeur limite de  $0,75615$ ). Une amélioration indirecte de  $CL_p$  est donc observée. Les valeurs du critère  $\bar{\theta}[Cd]$  ont diminué lors de l'adaptation. Ainsi  $\bar{\theta}[Cd]$  valait  $2,9110 \cdot 10^{-7}$  sur le maillage initial et  $2,4371 \cdot 10^{-7}$  sur le maillage adapté. De même le critère associé à  $CL_p$  a également diminué en passant de  $5,2251 \cdot 10^{-10}$  à  $4,2025 \cdot 10^{-10}$ .

L'adaptation pour  $CL_p$  a été effectuée en quatre itérations. Sa valeur est passée de  $0,73950$  à  $0,74775$  (à comparer à la valeur limite de  $0,75615$ ). Une diminution de 50% de l'erreur a donc été observée. Une amélioration indirecte de l'estimation de  $Cd$  a également été observée, passant de  $123,93 \cdot 10^{-4}$  sur le maillage initial à  $119,99 \cdot 10^{-4}$  sur le maillage adapté (valeur limite de  $118,60 \cdot 10^{-4}$ ). Le critère  $\bar{\theta}[CL_p]$  est passé de  $5,2252 \cdot 10^{-10}$  à  $3,6104 \cdot 10^{-10}$ . De même le critère  $\bar{\theta}[Cd]$  a diminué en passant de  $2,9110 \cdot 10^{-7}$  à  $2,3458 \cdot 10^{-7}$ .

La méthode a conduit à un raffinement autour du profil ainsi qu'à l'amont du bord d'attaque et au niveau du sillage pour les deux adaptations. Néanmoins le raffinement dans le sillage amont a été plus fort pour l'adaptation pour  $CL_p$ .

D'autre part, dans les deux cas, il a été constaté que le coefficient de traînée de frottement ( $CD_f$ ) est la composante de la traînée qui a été la plus améliorée. En particulier, bien qu'une augmentation de la densité de nœud a été effectuée dans la zone du choc, le coefficient de traînée de choc ( $CD_w$ ) n'est pas amélioré de façon significative.

## Conclusions

Un senseur basé sur  $dJ/dX$  et prenant en compte la régularité de ce champ (via une moyenne spatiale) ainsi que les déplacements admissibles des nœuds lors d'un remaillage local a été construit. La corrélation entre les bonnes valeurs de fonctions et les faibles valeurs de critère a été étudiée sur une famille paramétrée de maillages et a montré une corrélation fiable bien qu'imparfaite. Le critère local correspondant a ensuite été utilisé pour effectuer des adaptations locales de maillage à l'aide d'une méthode elliptique. Ces adaptations ont conduit à des maillages induisant de bonnes estimations de fonctions à la fois pour des écoulements décrits par les équations d'Euler que pour des écoulements décrits par les équations RANS. L'étape suivante, qui fait l'objet du chapitre suivant, est l'application de cette méthodologie pour adapter un maillage tridimensionnel autour d'une configuration industrielle.

# Chapter 3

## Mesh qualification and local adaptations

The previous chapter was a presentation of the first application of the derivative  $dJ/dX$  for mesh adaptation. These results have confirmed the interest of this derivative for goal oriented mesh adaptation. However the adaptation methods lead to global refinements and hence they can induce an increase of the mesh density in areas that are not necessarily of interest. Moreover the quality indicator that was considered was the mean of the field  $\|\mathcal{P}(dJ/dX)\|$  (denoted by  $\mu$ ) but it was observed for  $P_a$  that the criterion that actually diminished was the bound of the first order variation of  $J$  for a specific allowable node displacement (denoted by  $\theta$ ). Hence it appeared that the actual node displacements have to be taken into account during a mesh adaptation process. Another phenomenon that has to be taken into account is a compensation effect that can occur for irregular  $\mathcal{P}(dJ/dX)$  fields.

More reliable criteria that take into account these phenomena and a local mesh adaptation method based on an elliptic system of PDEs are described and studied in the following section with application to two-dimensional Eulerian flows. Section 3.2 then presents the enhancements of the elliptic remeshing method that were found necessary to perform efficient adaptations of RANS flows. Finally Section 3.3 describes the application of this methodology to two-dimensional RANS flows on multiblock structured meshes. All these applications have been done for a particular point of the flight domain. The extension of the proposed method to this 2D RANS test case was an intermediate step before the application of the method to a three-dimensional case presented in the next chapter.

### 3.1 Mesh qualification and local adaptations applied for Eulerian flows

This section presents a more reliable criterion of mesh quality. The correlation of the low values of these criteria and the accurate values of functions are studied on families of parametrized meshes. These global criteria are connected to local ones that are well suited for mesh adaptation as they detect the mesh locations where the node location has an important impact on the output estimation. These local criteria are used with a local mesh adaptation method. This work has led to the publication of an article in the *European Journal of Mechanics - B/Fluids* that is the body of this section [39].

## Mesh quality assessment based on aerodynamic functional output total derivatives

Maxime Nguyen-Dinh<sup>a,\*</sup>, Jacques Peter<sup>b</sup>, Renaud Sauvage<sup>a</sup>, Matthieu Meaux<sup>c</sup>,  
Jean-Antoine Désidéri<sup>d</sup>

<sup>a</sup>*Airbus Operations S.A.S. 316, route de Bayonne, 31060 Toulouse Cedex 09, France*

<sup>b</sup>*ONERA/DSNA. 29, av. de la Division Leclerc, 92322 Chatillon Cedex, France*

<sup>c</sup>*EADS-IW. 18, rue Marius Terce - BP 13050 31025 Toulouse Cedex 03, France*

<sup>d</sup>*INRIA Sophia Antipolis-Méditerranée. 2004, route des Lucioles - BP 93 06902 Sophia Antipolis Cedex, France*

---

### Abstract

Our purpose is to develop a new goal oriented method based on the total derivative of the goal with respect to (w.r.t.) volume mesh nodes. The asymptotic behavior of this derivative as the characteristic cell size tends to zero is first studied. This behavior is assessed using numerical simulations on a hierarchy of meshes. Goal oriented criteria of mesh quality are then proposed based on the same derivative and the local characteristic cell length. Their relevance is assessed using several families of parametrized meshes. The criterion succeeds in sorting the better meshes for goal evaluation from the worse. Finally a local mesh adaptation strategy is proposed and validated. All demonstrations are done for 2D structured meshes with finite-volume schemes and cell-centered approach in the case of Eulerian flow computations.

*Keywords:* Goal oriented mesh adaptation, Discrete adjoint method, Steady compressible equations, Finite-Volume scheme, Mesh quality.

---

### Nomenclature

$AoA$	Angle of attack
$\mathcal{B}$	Linear interpolation operator in the reference fine mesh
$c$	Chord of airfoil
$C$	Computational space $C = [0, 1]^2$ (resp. $C = [0, 1]^3$ ) in 2D (resp. 3D)
$CD_p, CD_w, CD_{sp}$	Pressure drag coefficient, wave drag coefficient and spurious drag
$ds_{ij}$	Surface element attachable to the point $X_{ij}$
$dX, dXC$	Admissible mesh variations and regular function such that $dX_{ij} = dXC(X_{ij}) \forall i, j \in \{1, N_i\}\{1, N_j\}$
$D$	Physical space $D \subset \mathbb{R}^2$ (resp. $D \subset \mathbb{R}^3$ ) in 2D (resp. 3D)

---

\*Corresponding author Phone +33 5 61 18 48 01

*Email addresses:* maxime.nguyen-dinh@airbus.com (Maxime Nguyen-Dinh),  
jacques.peter@onera.fr (Jacques Peter), renaud.sauvage@airbus.com (Renaud Sauvage),  
matthieu.meaux@eads.net (Matthieu Meaux), jean-antoine.desideri@inria.fr (Jean-Antoine Désidéri)

$\mathcal{D}_{(X_{ij}, L)}$	Disk of radius $L$ centered in $X_{ij}$
$\vec{e}_\infty$	Unit vector tangential to the upstream velocity
$F^{(2)}$	Two-point Euler inviscid flux formula
$F^{(4)}$	Four-point Euler inviscid flux formula
$F^J$	Jameson flux formula
$\mathcal{F}$	Euler inviscid flux density
$g_i, g^i$	Covariant and contravariant base vectors
$g_{ij}, g^{ij}$	Covariant and contravariant metric tensors
$H, h$	Characteristic mesh size of coarse ( $H$ ) and fine ( $h$ ) grid
$i, j(, k)$	Mesh indices of a 2D (resp. 3D) mesh
$\bar{i}, \bar{j}(, \bar{k})$	Reduced mesh indices in $[0, 1]^2$ (resp. $[0, 1]^3$ )
$J$	Aerodynamic objective function as function of volume mesh
$J$	Aerodynamic function as function of flow field and volume mesh
$\mathcal{J}$	Aerodynamic function as function of a vector of design parameters
$k^{(2)}, k^{(4)}$	Artificial dissipation coefficients of Jameson <i>et al.</i> scheme
$L$	Characteristic size of a mesh deformation
$M_\infty$	Mach number of far-field flow
$n_\mu$	Number of design parameters
$\vec{n}$	Normal vector to solid wall, support of $J$ or outer boundary
$N_i, N_j$	Number of mesh lines of the structured mesh in each direction
$N_W$	Size of vectors $W$ and $R$
$p, p_\infty$	Static pressure and static pressure of far-field flow
$p_a, p_{a\infty}$	Stagnation pressure and stagnation pressure of far-field flow
$P$	Parametric space $P = [0, 1]^2$ (resp. $P = [0, 1]^3$ ) in 2D (resp. 3D)
$P_a$	Mean stagnation pressure over airfoil contour
$P_k, \tilde{P}_{ij}^k$	Control functions associated to the $k^{th}$ topological direction only and to the $k^{th}$ topological direction and the node $(i, j)$
$\mathcal{P}(dJ/dX)$	Projection of $dJ/dX$ cancelling components orthogonal to function support and solid walls
$\overline{\mathcal{P}(dJ/dX)}$	Spatial mean of $\mathcal{P}(dJ/dX)$
$r$	Reference variable of the Taylor expansion
$R$	Finite-volume flux balance
$s$	Sensor scalar field
$s^{(1)}, s^{(2)}, s^{(3)}$	Sensor fields connected to specific geometrical directions
$S$	Solid body surface mesh
$S = (S^X, S^Z)$	Interfaces surface vectors
$W$	Conservative variables (discrete)
$w$	Continuous flow-field
$X$	Volume mesh
$\alpha, \beta, \delta, \phi$	Parameters of the mesh families
$\gamma$	Specific heat ratio
$\gamma_{ijL}$	Discrete estimation of the part of disk centered in the node $X_{i,j}$ that is included in the fluid domain
$\Gamma$	Airfoil contour (length $L(\Gamma)$ )

$\theta$	Criterion based on $\mathcal{P}(dJ/dX)$
$\Lambda$	Adjoint vector of $J$ ( $J_k$ ) for scheme $R$
$\lambda$	Continuous limit of $\Lambda$ as the mesh size increases
$\mu$	Vector of design parameter
$\Phi$	Mapping function from $[0, 1]^2$ to $[0, 1]^2$
$\bar{\theta}$	Criterion based on a spatial mean of $\mathcal{P}(dJ/dX)$
$\chi_{N_i, N_j, (N_k)}$	Linear function mapping $[0, 1]^2$ (resp. $[0, 1]^3$ ) in $[1, N_i] \times [1, N_j]$ (resp. $[1, N_i] \times [1, N_j] \times [1, N_k]$ )
$\Psi_L$	Radial function of support $\mathcal{D}_{(0,L)}$

## 1. Introduction

In aeronautical CFD, engineers require accurate predictions of the forces and moments but they are less concerned with flow-field accuracy. Hence, the so-called “goal oriented” mesh adaptation strategies have been introduced to get satisfactory values of functional outputs at an acceptable cost, using local node displacement and insertion of new points rather than mesh refinement guided by uniform accuracy. Most often, such methods involve the adjoint vector of the function of interest.

The objective of this study is three-fold: we first study the asymptotic behavior of the total derivative of the goal w.r.t. volume mesh coordinates as characteristic cell size tends to zero (section 2). This asymptotic behavior is verified on a hierarchy of meshes (section 5). We then try to qualify the meshes that are well suited for the computation of  $J$  (the output of interest) based on one scalar indicator and to derive a corresponding local mesh refinement indicator, both global and local criteria being based on the previously mentioned total derivative of the goal (denoted  $J$ ) w.r.t. the volume mesh coordinates (denoted  $X$ ). Until now the Venditti and Darmofal method is the major reference on the last subject for finite-volume methods [1, 2, 3]; it has been applied by many authors but has the drawback to require two levels of meshes. For finite elements methods, many goal oriented mesh adaptation methods have been developed since the 1990s. Important contributions include the articles of Johnson and co-workers [4, 5, 6], Giles and co-workers [7], Prudhomme and Oden [8], Larson and Barth [9], Machiels et al. [10], Hartmann and co-workers [11, 12, 13] and Alauzet, Dervieux and co-workers [14]. The search for a criterion using the adjoint vector on a unique level of mesh was rarely considered in the literature. However we can notice the contribution of Dwight [15, 16] in which only one level of mesh is necessary but is limited to the classical Jameson *et al.* numerical scheme [17].

### 1.1. State of the art on goal oriented mesh adaptation for finite volume schemes

A recent detailed state of the art about output-based error estimation and mesh adaptation can be found in the review by Fidkowski and Darmofal [18]. This article covers both finite-element and finite volume methods. Here, a short presentation of classical adaptation methods for finite-volume schemes is made.

In a series of three articles [1, 2, 3], Venditti and Darmofal have proposed similar formulas for the specific case of finite differences/finite-volume and discrete adjoint, and presented applications to compressible flow computations. Let us define the basic notations employed here for finite-volume CFD computations:  $W$  is the flow field (size  $N_W$ ),  $X$  is the volume

mesh and  $R$  is the residual of the scheme. At steady state, these variables satisfy  $R(W, X) = 0$  (set of  $N_W$  nonlinear equations to be solved for  $W$ ).  $R$  is supposed to have  $C^1$  regularity w.r.t. its two vector arguments. The method involves two grids: a coarse one of characteristic mesh size  $H$ , and a fine one of characteristic mesh size  $h$ . The full computation of the flow field and the output of interest on level  $H$  is supposed to be affordable, whereas it would be prohibitively expensive on level  $h$ . The subscripts  $h$  and  $H$  will be attached to  $R$ ,  $X$  and  $W$ . Lastly,  $W_h^H$  and  $\lambda_h^H$  represent the coarse-grid flow-field and adjoint vector reconstructed on the fine grid *via* some consistent projection operator. A Taylor's expansion of the functional output of interest  $J_h$  about the interpolated coarse-grid solution writes:

$$J_h(W_h, X_h) = J_h(W_h^H, X_h) + \left( \frac{\partial J}{\partial W} \Big|_{W_h^H} \right) (W_h - W_h^H) + \mathcal{O}(\|W_h - W_h^H\|^2)$$

After solving an adjoint-like equation on the fine grid (1), a Taylor's expansion of  $R$  about  $W_h^H$  writes:

$$(\Lambda_h|_{W_h^H})^T \left( \frac{\partial R_h}{\partial W_h} \Big|_{W_h^H} \right) = - \frac{\partial J_h}{\partial W_h} \Big|_{W_h^H} \quad (1)$$

$$\begin{aligned} J_h(W_h, X_h) &= J_h(W_h^H, X_h) - (\Lambda_h|_{W_h^H})^T \left( \frac{\partial R_h}{\partial W_h} \Big|_{W_h^H} \right) (W_h - W_h^H) + \mathcal{O}(\|W_h - W_h^H\|^2) \\ &= J_h(W_h^H, X_h) + (\Lambda_h|_{W_h^H})^T R_h(W_h^H) + \mathcal{O}(\|W_h - W_h^H\|^2) \end{aligned} \quad (2)$$

If the flow computation is not affordable on the fine grid, neither is the solution of equation (1) for  $(\Lambda_h|_{W_h^H})$ . An alternative is to replace this adjoint field by the interpolated coarse-grid adjoint,

$$J_h(W_h, X_h) \simeq J_h(W_h^H, X_h) + \underbrace{(\Lambda_h^H)^T R_h(W_h^H)}_{\text{computable correction}} + \underbrace{((\Lambda_h|_{W_h^H})^T - (\Lambda_h^H)^T) R_h(W_h^H)}_{\text{error in computable correction}}$$

The authors recommend to take  $J_h(W_h^H, X_h) + \Lambda_h^H R_h(W_h^H)$  as the function estimate and adapt the mesh by reducing uniformly the error in computable correction. These formulas have raised a deep interest in the aeronautical CFD community. The main applications of this method are described in [19].

Later Dwight has proposed a very different adjoint-based method attached to Jameson *et al.* scheme [17]. In a series of two articles [15, 16], he considered classical test cases for Eulerian flows. He conducted computations using Jameson *et al.* scheme [17] on hierarchies of grids and for different sets of artificial dissipation coefficients ( $k^{(2)}, k^{(4)}$ ). The error for the functions of interest appeared to be mainly due to artificial dissipation. On this basis, the following measure for the approximation error in the Jameson *et al.* scheme has been proposed:

$$k^{(2)} \frac{dJ}{dk^{(2)}} + k^{(4)} \frac{dJ}{dk^{(4)}}$$

The dissipation coefficients are then interpreted as being defined independently for each control volume. This leads to a local indicator for dissipation-error in cell  $l$ :

$$k^{(2)} \frac{dJ}{dk_l^{(2)}} + k^{(4)} \frac{dJ}{dk_l^{(4)}}$$

### 3.1. MESH QUALIFICATION AND LOCAL ADAPTATIONS APPLIED FOR EULERIAN FLOWS

The derivatives  $dJ/dk_l^{(2)}$  and  $dJ/dk_l^{(4)}$  can only be computed by the adjoint method. The field of local indicator for dissipation error is used as a mesh refinement indicator and  $J - k^{(2)}dJ/dk^{(2)} - k^{(4)}dJ/dk^{(4)}$  is considered as the corrected output value.

#### 1.2. Basics on total derivative of a functional output w.r.t. volume mesh coordinates

In the neighbourhood of  $(W_i, X_i)$  at which  $R(W_i, X_i) = 0$ ,  $\det[\partial R/\partial W(W_i, X_i)] \neq 0$ , the implicit function theorem allows us to express  $W$  as a function of the mesh  $X$ . In this framework an aerodynamic function  $J(W, X)$  can be expressed as a function  $J$  of the mesh only  $J(X) = J(W(X), X)$ , whose derivative w.r.t.  $X$  is called here the total derivative of the functional output w.r.t. volume mesh coordinates. It naturally appears in the equation of sensitivity computation for shape optimization using the adjoint vector method: Denoting  $\mu$  the vector of design parameters (size  $n_\mu$ ) and  $\mathcal{J}$  the function of interest expressed as a function of the design parameters ( $\mathcal{J}(\mu) = J(W(X(\mu)), X(\mu))$ ), the classical equations of the adjoint vector method are:

$$\left(\frac{\partial R}{\partial W}\right)^T \Lambda = -\left(\frac{\partial J}{\partial W}\right)^T \quad \frac{d\mathcal{J}}{d\mu_l} = \frac{\partial J}{\partial X} \frac{dX}{d\mu_l} + \Lambda^T \left(\frac{\partial R}{\partial X} \frac{dX}{d\mu_l}\right) \quad l \in [1, n_\mu] \quad (3)$$

or

$$\frac{d\mathcal{J}}{d\mu_l} = \left[ \frac{\partial J}{\partial X} + \Lambda^T \frac{\partial R}{\partial X} \right] \frac{dX}{d\mu_l} \quad l \in [1, n_\mu]$$

This clearly identifies

$$\frac{dJ}{dX} = \frac{\partial J}{\partial X} + \Lambda^T \frac{\partial R}{\partial X} \quad (4)$$

This quantity was first introduced by Nielsen and Park in the framework of adjoint based sensitivity analysis for shape optimization [20]. In this context the CPU time required to evaluate the derivatives of the output of interest was (almost) independent of the number of design parameters but, the memory requirements inversely were proportional to the number of design parameters. Actually the storage of volume mesh sensitivity w.r.t. design variables was not possible for large configurations involving some hundreds design parameters and this limited the benefit of the adjoint method. Nielsen and Park proposed an elegant solution involving the adjoint of the explicit or implicit relationship between the deformation of the surface mesh denoted  $S$  and volume mesh deformation. The equations of the method read:  
– in the general case of an implicit dependence between  $X$  and  $S$ , denoted  $D(X, S) = 0$ :

$$\left(\frac{\partial R}{\partial W}\right)^T \Lambda = -\left(\frac{\partial J}{\partial W}\right)^T \quad \left(\frac{\partial D}{\partial X}\right)^T \Gamma = -\left(\frac{\partial J}{\partial X} + \Lambda^T \frac{\partial R}{\partial X}\right)^T = -\left(\frac{dJ}{dX}\right)^T$$

$$\frac{d\mathcal{J}}{d\mu_l} = \left[ \Gamma^T \frac{\partial D}{\partial S} \right] \frac{\partial S}{\partial \mu_l} \quad l \in [1, n_\mu]$$

(where the term in brackets is to be computed first)

– in case of an explicit dependence  $X = X(S)$ :

$$\left(\frac{\partial R}{\partial W}\right)^T \Lambda = -\left(\frac{\partial J}{\partial W}\right)^T \quad \frac{dJ}{dX} = \frac{\partial J}{\partial X} + \Lambda^T \frac{\partial R}{\partial X}$$

$$\frac{d\mathcal{J}}{d\mu_l} = \left[ \frac{dJ}{dX} \frac{dX}{dS} \right] \frac{dS}{d\mu_l} \quad l \in [1, n_\mu]$$

(where the term in brackets is to be computed first). These equations are used to replace equation (3).

The first term in equation (4),  $(\partial J / \partial X_k)$  corresponds to the direct dependency of function  $J$  on the location of node  $k$ , whereas the second term  $\Lambda^T(\partial R / \partial X_k)$  corresponds to changes of the flow field on the support of function  $J$ , due to the change of node  $k$  location.

Finally, it is easily checked that  $dJ/dX$  cannot be computed in the direct differentiation mode as this would require the (huge) derivative  $dW/dX$  to be calculated and stored.

### 1.3. Principle of proposed methods

The  $dJ/dX$  vector field can be plotted for simple configurations and classical functions (like near-field pressure drag  $CD_p$  of an airfoil or stagnation pressure integrated over the airfoil) [21, 19, 22]. Most often, the vector fields at wall nodes exhibit large components orthogonal to the wall that would change the solid shape if the mesh was deformed accordingly. Hence a projected field  $\mathcal{P}(dJ/dX)$ , retaining all components suitable for mesh adaptation, is defined:

$\mathcal{P}(dJ/dX) = dJ/dX$	Outside the support of $J$ and solid walls contour
$\mathcal{P}(dJ/dX) = dJ/dX - (dJ/dX \cdot \vec{n})\vec{n}$	Inside the support of $J$ , along the walls, at the outer border (normal $\vec{n}$ )
$\mathcal{P}(dJ/dX) = 0$	At a corner of the support of $J$

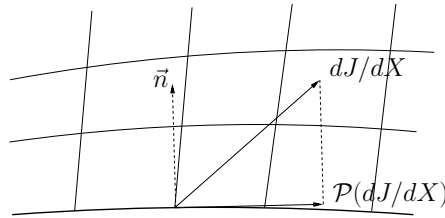


Figure 1: Projection of  $dJ/dX$  at the solid walls

Our objective is to define goal oriented mesh quality criteria based on first-order expansions, relatively to the calculation of a functional  $J$  in cases where the mesh deformation should satisfy certain local or global preservation properties. The first order variation of the output  $J$  in case of a mesh displacement  $dX$  is obviously

$$J(X + dX) - J(X) \simeq \frac{dJ}{dX} \cdot dX$$

In case we consider only variations  $dX$  that do not modify the solid walls, nor the boundaries of the mesh or the integration contour of the function of interest, the following relation also holds

$$J(X + dX) - J(X) \simeq \mathcal{P} \left( \frac{dJ}{dX} \right) \cdot dX \quad (5)$$

The principle of the proposed method is derived from equation (5) and the possible combina-

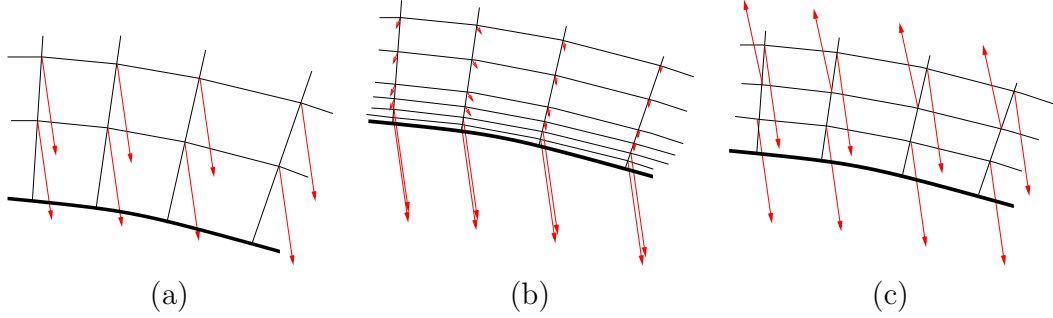


Figure 2: (a) large regular  $\mathcal{P}(dJ/dX)$  with large possible displacement of nodes ; (b) large regular  $\mathcal{P}(dJ/dX)$  without large possible displacement of nodes (c) large non-regular  $\mathcal{P}(dJ/dX)$  with large possible displacement of nodes

tion of local aspect of mesh and  $\mathcal{P}(dJ/dX)$  field (see figure 2). Figure (2)(a) is a typical case where equation (5) proves that a local mesh refinement is needed, as moving down the two mesh lines with high  $\|dJ/dX\|$  values would cause a significant increase of  $J$  value. Figure (2)(b) is a case of high sensibility of  $J$  value to the position of some nodes but, as these nodes cannot be significantly moved, the evaluation of  $J$  does not appear to be sensitive to a simple actual mesh deformation. Figure (2)(c) is a case of high sensitivity of  $J$  to the position of some nodes that can be significantly moved but the contribution of the different nodes in (5) tend to cancel out if they are moved coherently. Hence, it is not easy to decide whether this zone should be refined for a stable evaluation of the output of interest.

These considerations are the basis of  $J$ -oriented mesh adaptation methods described in next section.

#### 1.4. Outline

The section 2 provides an analysis of the asymptotic behavior of  $dJ/dX$  field. The criteria of mesh quality are presented in section 3 and a local mesh adaptation method using these criteria is presented in section 4. The three following sections are devoted to numerical applications. More precisely, the section 5 presents a numerical study of the asymptotic behavior of  $dJ/dX$  field and the section 6 is devoted to the study of the mesh quality criteria. Finally applications of local mesh adaptations based on these criteria are presented in section 7.

## 2. Asymptotic study of $dJ/dX$

This section presents a theoretical study of the asymptotic behavior of the total derivative  $dJ/dX$ . This vector field is at the basis of the goal oriented criteria proposed in the next section.

### 2.1. Framework for the analysis of the $dJ/dX$ field

The terms in equation (4) are analyzed for a 2D problem in the common place case where the output of interest,  $J$ , is a force estimated by summation over solid walls, and  $R$  is the

classical finite-volume flux balance:

$$R_{i,j} = F_{i+1/2,j} - F_{i-1/2,j} + F_{i,j+1/2} - F_{i,j-1/2},$$

where  $F$  is the numerical flux. In this case, it can easily be checked that the dimensions of adjoint fields do not involve any length and it is actually observed that adjoint vectors converge towards regular fields as the mesh is refined.

It is also easily checked that  $\partial J/\partial X$  is then a first-order term in the distance between two successive points on the wall [22].

Conversely the analysis of the second term  $\Lambda^T(\partial R/\partial X)$ , is not straightforward. It is carried out for a 2D calculation and for a numerical flux depending (a) concerning the geometry, only on the local surface vector (b) concerning the flow field, on two or four states on the same mesh line (denoted  $W_L, W_R$  in the first case or  $W_{2L}, W_L, W_R, W_{2R}$  in the second case). The usual  $(x, z)$  coordinates, most often used for airfoils, are retained. All terms of  $\Lambda^T(\partial R/\partial x_{i,j})$

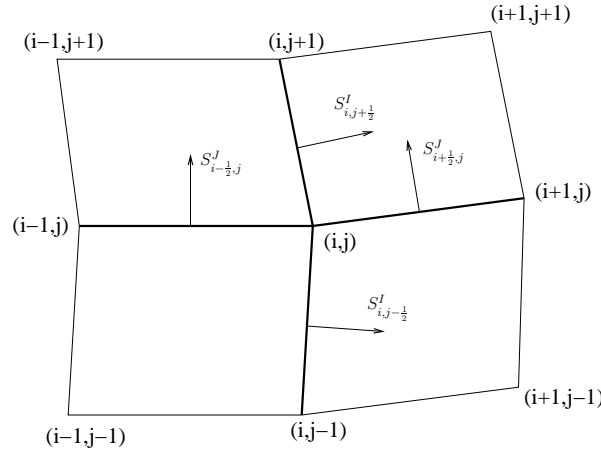


Figure 3: Notations for finite volume discretization. In bold, mesh lines connected to  $X_{i,j} = (x_{i,j}, z_{i,j})$

where  $(i, j)$  is a generic point inside the domain will be estimated. Using the notations of figure 3, the surface vector coordinates are

$$S_{i-1/2,j} \equiv \begin{pmatrix} S_{i-1/2,j}^X \\ S_{i-1/2,j}^Z \end{pmatrix} = \begin{pmatrix} z_{i-1,j} - z_{i,j} \\ x_{i,j} - x_{i-1,j} \end{pmatrix}$$

$$S_{i,j-1/2} \equiv \begin{pmatrix} S_{i,j-1/2}^X \\ S_{i,j-1/2}^Z \end{pmatrix} = \begin{pmatrix} z_{i,j} - z_{i,j-1} \\ x_{i,j-1} - x_{i,j} \end{pmatrix}$$

## 2.2. Asymptotic behaviour of $dJ/dX$ outside the support of $J$

We make the following statement:

**Statement:** A 2D finite-volume cell-centred scheme for Euler flows and for structured grids is considered. The numerical flux is supposed (a) to depend on the local surface vector and on two or four states of the corresponding mesh line either sides of the interface ; (b) to be  $C^2$  except at marginal locations where the absolute value has a zero argument, or min

### 3.1. MESH QUALIFICATION AND LOCAL ADAPTATIONS APPLIED FOR EULERIAN FLOWS

or max functions have equal arguments. The fixed node of interest  $X_{i,j}$ , is assumed to be located (a) outside of the support of  $J$  ; (b) in a zone of the fluid domain where the discrete flow-field  $W$  and the adjoint vector  $\Lambda$  tend towards  $C^1$  limiting functions  $w$  and  $\lambda$  ; (c) in a location such that the fluxes of the four surfaces attached to  $X_{i,j}$  are  $C^2$  functions of their aerodynamic and geometric arguments at the limit of small step sizes.

Under these assumptions, the total derivative of  $J$  w.r.t.  $X_{i,j}$  has the following asymptotic behaviour as the mesh is refined:

$$\begin{bmatrix} \frac{dJ}{dx_{i,j}} \\ \frac{dJ}{dz_{i,j}} \end{bmatrix} = ds_{ij} \sum_{k=1}^4 \begin{bmatrix} \frac{\partial \lambda^k}{\partial z} \frac{\partial \mathcal{F}_Z^k}{\partial w} \frac{\partial w}{\partial x} - \frac{\partial \lambda^k}{\partial x} \frac{\partial \mathcal{F}_Z^k}{\partial w} \frac{\partial w}{\partial z} \\ -\frac{\partial \lambda^k}{\partial z} \frac{\partial \mathcal{F}_X^k}{\partial w} \frac{\partial w}{\partial x} + \frac{\partial \lambda^k}{\partial x} \frac{\partial \mathcal{F}_X^k}{\partial w} \frac{\partial w}{\partial z} \end{bmatrix} + o(ds)$$

where  $\mathcal{F}_X$  (resp.  $\mathcal{F}_Z$ ) is the continuous Euler flux density in direction  $x$  (resp.  $z$ ) and  $ds_{ij}$  the surface attached to node  $X_{i,j}$  (one quarter of the surface of the four neighboring cells).

*Remark.* The assumption that the numerical flux should be  $C^1$  is already required in the mathematical framework of the discrete gradient computation. The  $C^2$  regularity is an additional assumption required for this property. More details are given in the subsection 2.4.

Thanks to this property, any goal oriented mesh refinement indicator or estimator based on  $dJ/dX$  can be approximated on a new grid from the calculation, with the same scheme, on another grid with a different mesh density.

#### 2.3. Derivation of asymptotic behaviour of $dJ/dX$ for a two-point flux formula

As the analysis of  $\Lambda^T \partial R / \partial X$  calculation is quite long, it is first carried out here for a two-point flux formula, denoted  $F^{(2)}$ , depending on the local surface vector and the two neighboring states  $W_{i-1/2,j-1/2}$  and  $W_{i+1/2,j-1/2}$ , so that the numerical flux is

$$F_{i,j-1/2} = F^{(2)}(W_{i-1/2,j-1/2}, W_{i+1/2,j-1/2}, S_{i,j-1/2}^X, S_{i,j-1/2}^Z)$$

For the sake of brevity  $\partial F^{(2)} / \partial S^Z$  is denoted  $F_Z^2$ . Due to these dependencies and the assumed local regularity of  $F^{(2)}$ , the expansion of  $\Lambda^T \partial R / \partial X$  is:

$$\begin{aligned} \Lambda \frac{\partial R}{\partial x_{i,j}} &= \sum_{k=1}^{k=4} T^k \\ T^k &= (\Lambda_{i+1/2,j+1/2}^k - \Lambda_{i+1/2,j-1/2}^k) F_Z^{2,k} (w_{i+1/2,j-1/2}, w_{i+1/2,j+1/2}, S_{i+1/2,j}^X, S_{i+1/2,j}^Z) \\ &\quad - (\Lambda_{i-1/2,j+1/2}^k - \Lambda_{i-1/2,j-1/2}^k) F_Z^{2,k} (w_{i-1/2,j-1/2}, w_{i-1/2,j+1/2}, S_{i-1/2,j}^X, S_{i-1/2,j}^Z) \\ &\quad - (\Lambda_{i+1/2,j+1/2}^k - \Lambda_{i-1/2,j+1/2}^k) F_Z^{2,k} (w_{i-1/2,j+1/2}, w_{i+1/2,j+1/2}, S_{i,j+1/2}^X, S_{i,j+1/2}^Z) \\ &\quad + (\Lambda_{i+1/2,j-1/2}^k - \Lambda_{i-1/2,j-1/2}^k) F_Z^{2,k} (w_{i-1/2,j-1/2}, w_{i+1/2,j-1/2}, S_{i,j-1/2}^X, S_{i,j-1/2}^Z) \end{aligned} \quad (6)$$

It is supposed, as observed when computing  $W$  and  $\Lambda$  for an output corresponding to an

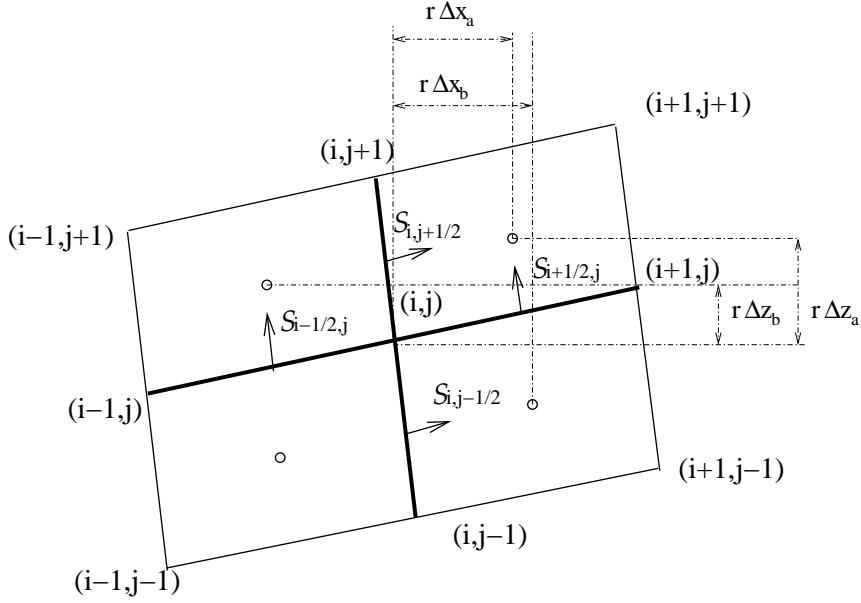


Figure 4: Notations for finite volume discretization on regular meshes

effort on a hierarchy of meshes that both fields tend to continuous functions, denoted  $w$  (corresponding to the solution of the flow equations) and  $\lambda$ . In this case (as in the search of the accuracy of a scheme or its equivalent equation) a Taylor expansion of equation (6) where discrete values have been replaced by the local values of the continuous functions, is carried out. In this calculations, it is supposed that  $X_{i,j}$  is fixed whereas the other point location around  $X_{i,j}$  shrink with a factor  $r$  ( $r$  being the reference variable of the Taylor expansion). At least, the continuous value of the flow field at the fixed point  $X_{i,j}$  is denoted  $\bar{w}$ . Due to the assumed local regularity of the limiting adjoint field, the differences like  $(\lambda_{i+1/2,j+1/2}^k - \lambda_{i+1/2,j-1/2}^k)$  are first order in  $r$ . The first order Taylor expansion of a flux derivative like  $F_Z^{2,k}(w_{i+1/2,j-1/2}, w_{i+1/2,j+1/2}, S_{i+1/2,j}^X, S_{i+1/2,j}^Z)$  is equal to  $F_Z^{2,k}(\bar{w}, \bar{w}, 0, 0)$  plus a first order term in  $r$ . As the sum

$$\begin{aligned}
 & (\lambda_{i+1/2,j+1/2}^k - \lambda_{i+1/2,j-1/2}^k) - (\lambda_{i-1/2,j+1/2}^k - \lambda_{i-1/2,j-1/2}^k) \\
 & - (\lambda_{i+1/2,j+1/2}^k - \lambda_{i-1/2,j+1/2}^k) + (\lambda_{i+1/2,j-1/2}^k - \lambda_{i-1/2,j-1/2}^k)
 \end{aligned}$$

is equal to zero, the expansion of  $T^k$  does not contain any first-order term in  $r$  and the second order term in  $r$  is only given by the product of the first order terms of the factors. Besides, as a structured mesh is infinitely refined, the cells locally tend to a set of identical parallelograms. The Taylor expansion, carried out in this framework, thus gives the dominant term in  $r$ . The notations for the positions of cell-centers w.r.t.  $X_{i,j}$  are defined on figure 4. It is easily checked that in this particular case

$$S_{i-1/2,j} = S_{i+1/2,j} = \begin{pmatrix} r(\Delta z_b - \Delta z_a) \\ r(\Delta x_a + \Delta x_b) \end{pmatrix} \quad S_{i,j-1/2} = S_{i,j+1/2} = \begin{pmatrix} r(\Delta z_a + \Delta z_b) \\ r(\Delta x_a - \Delta x_b) \end{pmatrix}$$

### 3.1. MESH QUALIFICATION AND LOCAL ADAPTATIONS APPLIED FOR EULERIAN FLOWS

The first order Taylor's expansion of the terms of the product in equation (6) can be calculated thanks to the local regularity assumptions for the limiting adjoint field and the flux formula:

$$\begin{aligned} \lambda_{i+1/2,j+1/2}^k - \lambda_{i+1/2,j-1/2}^k &= r(\Delta x_a - \Delta x_b) \frac{\partial \lambda^k}{\partial x} + r(\Delta z_a + \Delta z_b) \frac{\partial \lambda^k}{\partial z} + o(r) \\ F_Z^{2,k}(w_{i+1/2,j-1/2}, w_{i+1/2,j+1/2}, r(\Delta z_b - \Delta z_a), r(\Delta x_a + \Delta x_b)) &= F_Z^{2,k}(\bar{w}, \bar{w}, 0, 0) \\ &+ \frac{\partial F_Z^{2,k}}{\partial W_L} \left( r \Delta x_b \frac{\partial w}{\partial x} - r \Delta z_b \frac{\partial w}{\partial z} \right) + \frac{\partial F_Z^{2,k}}{\partial W_R} \left( r \Delta x_a \frac{\partial w}{\partial x} + r \Delta z_a \frac{\partial w}{\partial z} \right) \\ &+ r(\Delta z_b - \Delta z_a) \frac{\partial F_Z^{2,k}}{\partial S_X} + r(\Delta x_a + \Delta x_b) \frac{\partial F_Z^{2,k}}{\partial S_Z} + o(r) \end{aligned}$$

where all derivatives of  $F_Z$  are evaluated in  $(\bar{w}, \bar{w}, 0, 0)$ . The numerical flux of interest  $F^{(2)}$  is consistent with Eulerian Flux (denoted  $\mathcal{F}$ ). Hence his  $k^{th}$  component satisfies for all  $(S_X, S_Z)$

$$F^{(2,k)}(\bar{w}, \bar{w}, S_X, S_Z) = \mathcal{F}_X^k(\bar{w}) S_X + \mathcal{F}_Z^k(\bar{w}) S_Z$$

This yields

$$F_Z^{2,k}(\bar{w}, \bar{w}, S_X, S_Z) = \frac{\partial F^{(2,k)}}{\partial S_Z}(\bar{w}, \bar{w}, S_X, S_Z) = \mathcal{F}_Z^k(\bar{w})$$

and the derivatives of  $F_Z^{2,k}$  w.r.t.  $S_X$  and  $S_Z$  in  $(\bar{w}, \bar{w}, 0, 0)$  is null. This yields

$$\begin{aligned} \lambda_{i+1/2,j+1/2}^k - \lambda_{i+1/2,j-1/2}^k &= r(\Delta x_a - \Delta x_b) \frac{\partial \lambda^k}{\partial x} + r(\Delta z_a + \Delta z_b) \frac{\partial \lambda^k}{\partial z} + o(r) \\ F_Z^{2,k}(w_{i+1/2,j-1/2}, w_{i+1/2,j+1/2}, r(\Delta z_b - \Delta z_a), r(\Delta x_a + \Delta x_b)) &= F_Z^{2,k}(\bar{w}, \bar{w}, 0, 0) \\ &+ r \frac{\partial F_Z^{2,k}}{\partial W_L} \left( \Delta x_b \frac{\partial w}{\partial x} - \Delta z_b \frac{\partial w}{\partial z} \right) + r \frac{\partial F_Z^{2,k}}{\partial W_R} \left( \Delta x_a \frac{\partial w}{\partial x} + \Delta z_a \frac{\partial w}{\partial z} \right) + o(r) \end{aligned}$$

$$\begin{aligned} T^k &= r^2 \left[ \left( (\Delta x_a - \Delta x_b) \frac{\partial \lambda^k}{\partial x} + (\Delta z_a + \Delta z_b) \frac{\partial \lambda^k}{\partial z} \right) \left( \frac{\partial F_Z^{2,k}}{\partial w_L} \left( \Delta x_b \frac{\partial w}{\partial x} - \Delta z_b \frac{\partial w}{\partial z} \right) + \frac{\partial F_Z^{2,k}}{\partial w_R} \left( \Delta x_a \frac{\partial w}{\partial x} + \Delta z_a \frac{\partial w}{\partial z} \right) \right) \right. \\ &- \left( (\Delta x_a - \Delta x_b) \frac{\partial \lambda^k}{\partial x} + (\Delta z_a + \Delta z_b) \frac{\partial \lambda^k}{\partial z} \right) \left( \frac{\partial F_Z^{2,k}}{\partial w_L} \left( -\Delta x_a \frac{\partial w}{\partial x} - \Delta z_a \frac{\partial w}{\partial z} \right) + \frac{\partial F_Z^{2,k}}{\partial w_R} \left( -\Delta x_b \frac{\partial w}{\partial x} + \Delta z_b \frac{\partial w}{\partial z} \right) \right) \\ &- \left( (\Delta x_a + \Delta x_b) \frac{\partial \lambda^k}{\partial x} + (\Delta z_a - \Delta z_b) \frac{\partial \lambda^k}{\partial z} \right) \left( \frac{\partial F_Z^{2,k}}{\partial w_L} \left( -\Delta x_b \frac{\partial w}{\partial x} + \Delta z_b \frac{\partial w}{\partial z} \right) + \frac{\partial F_Z^{2,k}}{\partial w_R} \left( \Delta x_a \frac{\partial w}{\partial x} + \Delta z_a \frac{\partial w}{\partial z} \right) \right) \\ &\left. + \left( (\Delta x_a + \Delta x_b) \frac{\partial \lambda^k}{\partial x} + (\Delta z_a - \Delta z_b) \frac{\partial \lambda^k}{\partial z} \right) \left( \frac{\partial F_Z^{2,k}}{\partial w_L} \left( -\Delta x_a \frac{\partial w}{\partial x} - \Delta z_a \frac{\partial w}{\partial z} \right) + \frac{\partial F_Z^{2,k}}{\partial w_R} \left( \Delta x_b \frac{\partial w}{\partial x} - \Delta z_b \frac{\partial w}{\partial z} \right) \right) \right] \\ &+ o(r^2) \end{aligned}$$

It is easily checked that all  $\frac{\partial \lambda^k}{\partial x} \frac{\partial w}{\partial x}$  and  $\frac{\partial \lambda^k}{\partial z} \frac{\partial w}{\partial z}$  terms cancel out. The remaining terms are

$$\begin{aligned} T^k &= -2r^2(\Delta x_a \Delta z_b + \Delta x_b \Delta z_a) \frac{\partial \lambda^k}{\partial x} \left( \frac{\partial F_Z^{2,k}}{\partial w_L} + \frac{\partial F_Z^{2,k}}{\partial w_R} \right) \frac{\partial w}{\partial z} \\ &+ 2r^2(\Delta x_a \Delta z_b + \Delta x_b \Delta z_a) \frac{\partial \lambda^k}{\partial z} \left( \frac{\partial F_Z^{2,k}}{\partial w_L} + \frac{\partial F_Z^{2,k}}{\partial w_R} \right) \frac{\partial w}{\partial x} + o(r^2) \end{aligned}$$

The derivatives of  $F_Z^{2,k}$  are estimated in  $(\bar{w}, \bar{w}, 0, 0)$ . From the flux consistency, for all  $(S_X, S_Z)$

$$F_Z^{2,k}(\bar{w}, \bar{w}, S_X, S_Z) = \frac{\partial F^{(2,k)}}{\partial S_Z}(\bar{w}, \bar{w}, S_X, S_Z) = \mathcal{F}_Z^k(\bar{w})$$

Differentiating this relation w.r.t.  $\bar{w}$  in  $(\bar{w}, \bar{w}, 0, 0)$  leads to

$$\frac{\partial F_Z^{2,k}}{\partial w_L}(\bar{w}, \bar{w}, 0, 0) + \frac{\partial F_Z^{2,k}}{\partial w_R}(\bar{w}, \bar{w}, 0, 0) = \frac{d\mathcal{F}_Z^k}{dw}(\bar{w})$$

Besides it can easily be checked that  $2r^2(\Delta x_a \Delta z_b + \Delta x_b \Delta z_a) = ds_{ij}$  is the surface of the parallelogram defined by the four cell-centers about  $X_{i,j}$ . Hence a simpler expression for  $T^k$  is

$$T^k = ds_{ij} \left( \frac{\partial \lambda^k}{\partial z} \frac{d\mathcal{F}_Z^k}{dw} \frac{\partial w}{\partial x} - \frac{\partial \lambda^k}{\partial x} \frac{d\mathcal{F}_Z^k}{dw} \frac{\partial w}{\partial z} \right) + o(r^2)$$

Or

$$T^k = ds_{ij} \left( \frac{\partial \lambda^k}{\partial z} \frac{\partial \mathcal{F}_Z^k}{\partial x} - \frac{\partial \lambda^k}{\partial x} \frac{\partial \mathcal{F}_Z^k}{\partial z} \right) + o(r^2)$$

When computing the limit of  $\Lambda^T \partial R / \partial z_{ij}$  the counter part of equation (6) is obtained by substituting  $-F_X^{2,k}$  to  $F_Z^{2,k}$ . Hence, the asymptotic behaviour of  $dJ/dX$  outside the support of  $J$ , under the regularity assumptions stated above, is:

$$\frac{dJ}{dX_{ij}} = ds_{ij} \sum_{k=1}^4 \left[ \begin{array}{c} \frac{\partial \lambda^k}{\partial z} \frac{\partial \mathcal{F}_Z^k}{\partial x} - \frac{\partial \lambda^k}{\partial x} \frac{\partial \mathcal{F}_Z^k}{\partial z} \\ -\frac{\partial \lambda^k}{\partial z} \frac{\partial \mathcal{F}_X^k}{\partial x} + \frac{\partial \lambda^k}{\partial x} \frac{\partial \mathcal{F}_X^k}{\partial z} \end{array} \right]_{ij} + o(r^2)$$

#### 2.4. Assumption of local $C^2$ flux regularity for the asymptotic behaviour of $dJ/dX$

The usual flux formula, as defined for steady state or unsteady simulations, are not  $C^2$  functions of their aerodynamic and geometric arguments and the local  $C^2$  regularity required in the property of section 2.2 is questionable. This point is discussed here for a classical flux formula, Jameson et al. flux[17]. The arguments can be easily extended to the other classical inviscid flux formulas. Jameson et al. flux reads:

$$\begin{aligned} F_{i,j+\frac{1}{2}}^J &= \frac{1}{2} (\mathcal{F}_X(W_{i+\frac{1}{2},j+\frac{1}{2}}) + \mathcal{F}_X(W_{i-\frac{1}{2},j+\frac{1}{2}})) S_{X \ i,j+\frac{1}{2}} \\ &+ \frac{1}{2} (\mathcal{F}_Z(W_{i+\frac{1}{2},j+\frac{1}{2}}) + \mathcal{F}_Z(W_{i-\frac{1}{2},j+\frac{1}{2}})) S_{Z \ i,j+\frac{1}{2}} \\ &- k^2 \nu_{i,j+\frac{1}{2}} \rho_{i,j+\frac{1}{2}} (W_{i+\frac{1}{2},j+\frac{1}{2}} - W_{i-\frac{1}{2},j+\frac{1}{2}}) \\ &+ Max(k^4 - k^2 \nu_{i,j+\frac{1}{2}}, 0) \rho_{i,j+\frac{1}{2}} (W_{i+\frac{3}{2},j+\frac{1}{2}} - 3 W_{i+\frac{1}{2},j+\frac{1}{2}} + 3 W_{i-\frac{1}{2},j+\frac{1}{2}} - W_{i-\frac{3}{2},j+\frac{1}{2}}) \end{aligned}$$

with the spectral radius  $\rho_{i,j+\frac{1}{2}} = (|V \cdot S| + c|S|)_{i,j+\frac{1}{2}}$  and the sensor of strong gradient zones

$$\nu_{i,j+\frac{1}{2}} = Max(\nu_{i+\frac{1}{2},j+\frac{1}{2}}, \nu_{i-\frac{1}{2},j+\frac{1}{2}}) \quad \nu_{i+\frac{1}{2},j+\frac{1}{2}} = \frac{|p_{i+\frac{3}{2},j+\frac{1}{2}} - 2p_{i+\frac{1}{2},j+\frac{1}{2}} + p_{i-\frac{1}{2},j+\frac{1}{2}}|}{p_{i+\frac{3}{2},j+\frac{1}{2}} + 2p_{i+\frac{1}{2},j+\frac{1}{2}} + p_{i-\frac{1}{2},j+\frac{1}{2}}}$$

The mathematical framework of discrete gradient calculation requires that the flux balance  $R$  and hence the flux be  $C^1$  function of  $W$  and  $X$ . In practice, regularization of flux formulas or are not applied in actual codes without strong consequences on gradient values. If  $C^2$  regularization of max and absolute values are applied then, there is no issue with the assumption of  $C^2$  regularity. If only  $C^1$  regularization or no regularization is applied, then  $X_{i,j}$  shall not be located in a zone where

$$V.n_i \neq 0. \quad V.n_j \neq 0. \quad \frac{\partial^2 p}{\partial^2 s_i} \neq 0. \quad \frac{\partial^2 p}{\partial^2 s_j} \neq 0 \quad \frac{\partial}{\partial s_i} (1/p \frac{\partial^2 p}{\partial^2 s_i}) \neq 0. \quad \frac{\partial}{\partial s_j} (1/p \frac{\partial^2 p}{\partial^2 s_j}) \neq 0.$$

As concerning the *Max* term it disappears at the limit of small step size except for points exactly located in a discontinuity of the limiting flow that are excluded of section 2.2 statement by the local flow regularity assumption.

The apparent remaining issue is then that  $\|S\|$  is not a  $C^1$ -regular function of  $(S_X, S_Z)$  in the vicinity of  $(0, 0)$  but the Taylor expansion is carried out from the beginning for the variable  $r$ , the shrinking factor of a set of identical paralelogramms, corresponding to the local form of an infinitely refined structured mesh. Then this norm is expressed as  $\|(r S_X, r S_Z)\| = r \sqrt{S_X^2 + S_Z^2}$  that is a linear function of  $r$ .

### 3. Definition of goal oriented mesh quality criteria

The present section is devoted to the presentation of the proposed  $dJ/dX$ -based criteria of mesh quality. These criteria are used for both the assessment of the mesh quality for the computation of  $J$  and for the goal oriented mesh adaptations. The remeshing method used for the applications is presented in the next section.

#### 3.1. Former results about $\|dJ/dX\|$ field

A possible intuitive guess in  $J$ -oriented mesh adaptation based on  $dJ/dX$  is that  $\|dJ/dX_l\|$  (where  $l$  is a generic mesh index) should be made equal all over the mesh during the adaptation process (so that all nodes would cause an equal change in  $J$  when moving). Actually this cannot be achieved with structured meshes. For example in [19, 22], goal oriented mesh adaptations using a criterion based on  $\|dJ/dX\|$  have been carried out. In this study two families of structured meshes about the NACA0012 airfoil were considered and the fields of total derivative of two functions ( $P_a$ , the sum of the stagnation pressure over the airfoil and  $CD_p$ ) w.r.t. volume mesh nodes were studied. The standard deviation of  $\|dJ/dX_l\|$  divided by its mean appeared to be quite high even for adapted meshes satisfying both general and goal oriented quality criteria (30.7 on an adapted mesh for  $P_a$  of size  $257 \times 257$  to be compared to the value of 26.3 on the regular mesh of same size) and to increase with the density for a hierarchy of embedded grids (roughly height times higher on a mesh of size  $2049 \times 2049$  in comparison to the one of size  $257 \times 257$  for  $P_a$  and roughly twenty-two times higher for  $CD_p$ ).

A second possible intuitive guess is that  $\sum_l \|dJ/dX_l\|$  should be smaller for a mesh better adapted to the calculation of  $J$ . Actually this guess appeared to be wrong. In [19, 22], the sum of  $\|dP_a/dX_l\|$  over the mesh nodes is roughly height times higher for the adapted meshes of size  $257 \times 257$  (providing good estimations of  $P_a$ ) than for the regular meshes of same size (providing poor estimations of  $P_a$ ).

For the sake of brevity, these points are not further developed and all proposed criteria are based on equation (5).

### 3.2. Term-by-term bounds on $\mathcal{P}(dJ/dX).dX$ . Criterion $\theta$

Single block structured meshes are considered in the application sections. For 2D calculations, the number of lines in the meshing directions (denoted  $i$  and  $j$ ) are  $N_i$  and  $N_j$ . The definition of criteria are made in this case first and straightforwardly extended to 3D and multiblock meshes. A simple bound on the linearized first-order variation of  $J$  given by equation (5) is introduced. We denote  $dX$  an admissible mesh displacement (so that  $X + dX$  is a well-defined structured mesh if  $X$  is one) such that each node is to stay in a circle whose radius is equal to half the distance to the nearest node (radius denoted  $r_{i,j}$  for the node  $(i, j)$ , see figure 5).

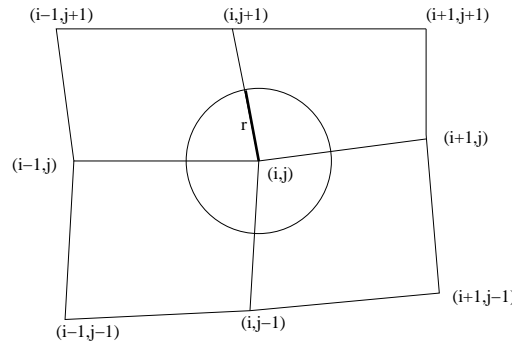


Figure 5: Allowable node displacement for criteria  $\theta(i, j)$

The absolute value of the first-order variation of  $J$  (equation (5)) due to the mesh displacement  $dX$  satisfies

$$\left| \mathcal{P} \left( \frac{dJ}{dX} \right) . dX \right| \leq \sum_{i=1}^{N_i} \sum_{j=1}^{N_j} \left\| \mathcal{P} \left( \frac{dJ}{dX} \right)_{i,j} \right\| r_{i,j}$$

Related notations are introduced:

$$\theta(i, j) = \left\| \mathcal{P} \left( \frac{dJ}{dX} \right)_{i,j} \right\| r_{i,j} \quad \theta = \frac{1}{N_i N_j} \sum_{i=1}^{N_i} \sum_{j=1}^{N_j} \theta(i, j)$$

So we can try to locally adapt the mesh in order to regularise  $\theta(i, j)$ , the (linearized) maximum change in  $J$  induced by the displacement of  $X_{i,j}$  described before (mesh adaptation) or see if the  $\theta$ -values corresponding to several meshes of same size are ordered as the accuracy of  $J$  evaluation (goal oriented mesh quality assessment).

NB: When considering several aerodynamic functions,  $[J]$  is added to the previous notations in order to indicate the function to which the criterion is related.

### 3.1. MESH QUALIFICATION AND LOCAL ADAPTATIONS APPLIED FOR EULERIAN FLOWS

#### 3.3. Spatial mean of $\mathcal{P}(dJ/dX)$ , $\overline{\mathcal{P}(dJ/dX)}$ . Criterion $\bar{\theta}$

The relevant mesh variation field  $dX$  (ie such that the mesh  $X + dX$  can really be used for an aerodynamic simulation) are regular fields whereas  $\mathcal{P}(dJ/dX)$  can be very irregular exhibiting approximately opposite vectors for neighboring vectors (see figure 6). Hence,  $|\mathcal{P}(dJ/dX).dX|$  is certainly overestimated in some cases by bounding separately the terms of the dot product. The regularity of the variation field  $dX$  is expressed to bring up a convolution based spatial mean  $\overline{\mathcal{P}(dJ/dX)}$  of  $\mathcal{P}(dJ/dX)$  in order to establish a more relevant bounding than in the previous section. The mean field  $\overline{\mathcal{P}(dJ/dX)}$  is built up such that the following relation holds for all variation field  $dX$  that can be well approximated by a linear function at a specific length scale  $L$

$$\mathcal{P}\left(\frac{dJ}{dX}\right).dX \simeq \overline{\mathcal{P}\left(\frac{dJ}{dX}\right)}.dX$$

The mean field  $\overline{\mathcal{P}(dJ/dX)}$  is a more regular vector field than  $\mathcal{P}(dJ/dX)$  (see figure 7). In practice at each node  $(i, j)$ ,  $\overline{\mathcal{P}(dJ/dX)}_{ij}$  is a discrete convolution between  $\mathcal{P}(dJ/dX)$  and a radial function of support the disk of radius  $L$  centered at the node  $(i, j)$ . The precise definition of  $\overline{\mathcal{P}(dJ/dX)}$  is given by equation (B.3) in Appendix B. We can then define a local criterion  $\bar{\theta}(i, j)$  and global  $\bar{\theta}$  by analogy to  $\theta(i, j)$  and  $\theta$ .

$$\bar{\theta}(i, j) = \left\| \overline{\mathcal{P}\left(\frac{dJ}{dX}\right)}_{ij} \right\| r_{i,j} \quad \bar{\theta} = \frac{1}{N_i N_j} \sum_{i=1}^{N_i} \sum_{j=1}^{N_j} \bar{\theta}(i, j)$$

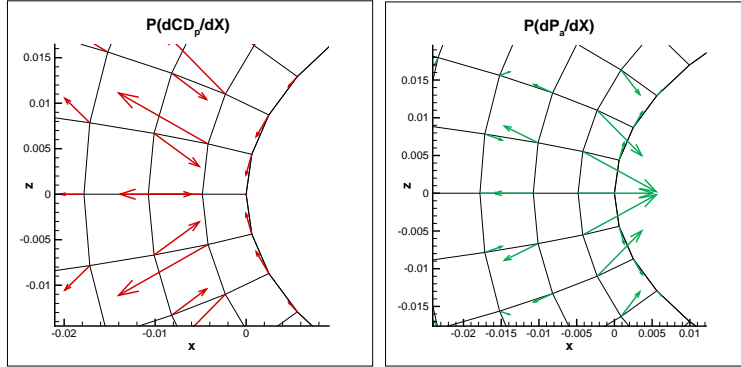


Figure 6:  $\mathcal{P}(dCD_p/dX)$  and  $\mathcal{P}(dP_a/dX)$  fields for an inviscid flow around NACA0012 airfoil ( $M_\infty = 0.8$   $AoA = 0^\circ$ , Jameson's scheme).

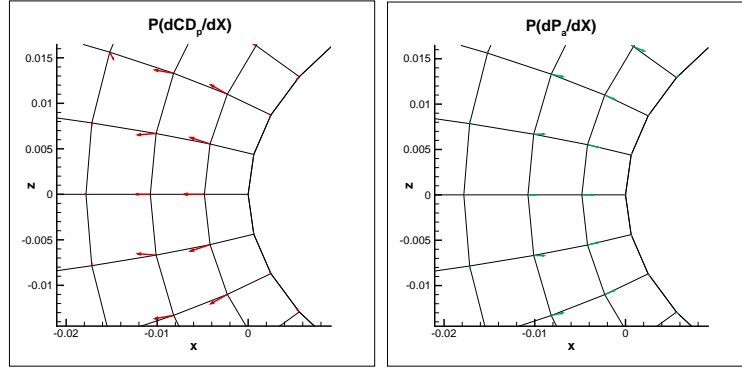


Figure 7:  $\overline{\mathcal{P}(dCD_p/dX)}$  and  $\overline{\mathcal{P}(dP_a/dX)}$  fields for an inviscid flow around NACA0012 airfoil ( $M_\infty = 0.8$   $AoA = 0^\circ$ , Jameson's scheme), with radius  $2/100$  of the chord length for the mean.

#### 4. Local mesh adaptation

The following section presents the remeshing method considered in this study. This method is built up in order to increase the node density at the mesh locations detected by the previously introduced criteria.

##### 4.1. Mesh generation and adaptation using an elliptic system of PDEs

Elliptic systems of PDEs are widely used for structured mesh generation [23, 24, 25] and adaptation [26, 27]. Most often these methods consider the following system:

$$\sum_{i,j=1}^3 g^{ij} x_{\xi^i} x_{\xi^j} + \sum_{k=1}^3 g^{kk} P_k x_{\xi^k} = 0 \quad (7)$$

where the unknown is the position vector  $x = (x_1, x_2, x_3)$  and  $\xi^i$  ( $i = 1, 2, 3$ ) are the curvilinear coordinates and  $g^{ij}$  ( $i, j = 1, 3$ ) the contravariant metric tensor and  $P_k$  the control functions. The generated mesh is entirely defined by these control functions. The construction of this system of PDEs is detailed in Appendix C. In this framework, Soni *et al.* [26] have proposed a mesh adaptation method that consists in modifying the control functions thanks to a criterion defined by the user. More precisely the control functions used to generate the adapted mesh are:

$$P_k = P_k^{initial} + \epsilon P_k^{adapt}$$

where  $P_k^{initial}$  are the control functions that define the initial mesh,  $P_k^{adapt}$  are built according to the user's criterion, and  $\epsilon$  a constant factor. It is important to notice that the functions  $P_k^{initial}$  can be computed even if the initial mesh was not generated by the elliptic system of PDEs (7), indeed these functions can be found directly by solving (7). The construction of the control functions  $P_k^{adapt}$  is the main difficulty of this method. Soni *et al.* have proposed to build these functions from the state variables in order to capture flow features such as shocks. At first, several fields  $s^{(i)} : X \rightarrow [0, 1]$  ( $i = 1, 2, 3$ ) are considered, each one connected to a specific direction. These are defined to be large in areas where the mesh needs to be refined and this in a directional way. From these fields, another one (denoted by  $s$ ) is built

to have large values in the areas where the mesh needs to be refined. Soni *et al.* suggest to use the following formula:

$$s = 1 + s^{(1)} \oplus s^{(2)} \oplus s^{(3)}$$

where the symbol  $\oplus$  is the Boolean sum (defined by  $q_1 \oplus q_2 = q_1 + q_2 - q_1 q_2$  with  $0 \leq q_1, q_2 \leq 1$ ), this sum have the property to have high values if one of its argument is high and not only if both are high. Finally the control functions for the adaptation are defined as the relative variation of this scalar field in each topological direction:

$$P_k^{adapt} = \frac{s_{\xi_k}}{s} \quad (8)$$

This definition comes from the application of the equidistribution principle of the weight functions to the one-dimensional form of (7). Indeed the equidistribution principle is satisfied if we have the relation  $s x_\xi = cste$ , this gives to  $s_\xi x_\xi + s x_{\xi\xi} = 0$ . This last relation combined with the one-dimensional form of (7) leads to (8) for each topological directions.

#### 4.2. Construction of a $\theta$ -based control function

In this work, the field  $s^{(i)}$  is defined as the norm of  $\mathcal{P}(dJ/dX)$  (or  $\overline{\mathcal{P}(dJ/dX)}$ ) times a characteristic length in the  $i^{th}$  geometrical direction. Unfortunately the resulting control functions for the adaptation are not directly usable. Indeed they present very important irregularities caused by several nodes where the values of  $P_k^{adapt}$  are significantly above the average. Consequently the sensor  $s$  is smoothed before computing the control functions. The chosen smoothing method consists in computing at each step a regularity estimator at each node in all topological directions and then to smooth the value of  $s$  at this node using the values at its neighbours in the less regular direction. The regularity estimator is an approximation of the second derivative in each topological direction. When the smoothing direction is selected the new value is computed by under-relaxation between the previous value of  $s$  and the one that would make the regularity estimator equals to zero (mean of the values at the neighbouring nodes).

## 5. Numerical assessment of $dJ/dX$ asymptotic behavior

The following section presents a numerical study of  $dJ/dX$  asymptotic behavior for two bidimensional Eulerian flows and two functional outputs. These test cases are also considered for mesh adaptations that are presented in the next section.

### 5.1. Test cases and numerical scheme

Two inviscid flows around a slightly modified NACA0012 airfoil at zero angle of attack are considered. This airfoil has been considered by Vassberg *et al.* [28, 29]. The first considered flow is subcritical ( $M_\infty = 0.5$ ) and the second one is transonic ( $M_\infty = 0.8$ ). Lastly, the two functions of interest considered here are the discrete expressions of pressure drag ( $CD_p$ ) and the integral at the airfoil contour of the stagnation pressure ( $P_a$ ):

$$CD_p = \oint_{\Gamma} \frac{2}{\gamma M_\infty^2} \left( \frac{p}{p_\infty} - 1 \right) \vec{n} \cdot \vec{e}_\infty dl \quad P_a = \frac{1}{L(\Gamma)p_{a\infty}} \oint_{\Gamma} p_a dl$$

where  $\Gamma$  is the contour of the airfoil and  $L(\Gamma)$  its length,  $\vec{n}$  is the normal vector to the solid wall and  $\vec{e}_\infty$  is the unit vector tangential to the upstream velocity,  $p$  is the static pressure,  $p_a$  the stagnation pressure and  $\gamma$  is the specific heat ratio. The numerical scheme used is the classical centered Jameson-Schmidt-Turkel scheme with artificial dissipation [17]. In practice we work with structured meshes with the *elsA* code [30], a finite-volume cell-centered code devoted to standard second order CFD analysis.

### 5.2. Mesh hierarchies and reference values for the outputs

A hierarchy of five quasi-uniform meshes provided by Vassberg *et al.* [28, 29] has been used in order to compute limiting values of the functions of interest and to compare the results of the adapted meshes with the quasi-uniform ones. Another family of meshes was built from the former, with aspect ratio 1/8 at the wall and a power law for the width of cells in the direction from wall to far-field [31]. The convergence toward the theoretical limiting values is faster on this mesh family than on the quasi-uniform one indicating the expected benefit of higher mesh density near the airfoil. These meshes are considered as standard Euler meshes and provide a reference for goal oriented mesh adaptation. Tables 1 and 2 summarise the results obtained on these meshes for subcritical and transonic flow conditions for  $CD_p$  and  $P_a$ . In the subcritical test case, the theoretical value of  $CD_p$  is

	Subcritical		Transonic	
	Regular	Stretched	Regular	Stretched
Limiting value	0.	—	83.483	—
2049 × 2049	0.067	0.002	83.454	83.410
1025 × 1025	0.271	0.004	83.539	83.402
513 × 513	1.090	0.023	84.084	83.394
257 × 257	4.276	0.185	86.124	83.981
129 × 129	16.050	1.322	94.361	88.408

Table 1: NACA0012.  $M_\infty = 0.5$  and  $M_\infty = 0.8$ . AoA=0°.  $CD_p(\times 10^4)$  for baseline and stretched grids.

	Subcritical		Transonic	
	Regular	Stretched	Regular	Stretched
Limiting value	1.	—	0.99225	—
2049 × 2049	0.99937	0.99989	0.99181	0.99299
1025 × 1025	0.99879	0.99983	0.99101	0.99268
513 × 513	0.99765	0.99970	0.98833	0.99241
257 × 257	0.99540	0.99952	0.98364	0.99235
129 × 129	0.99121	0.99918	0.97425	0.99206

Table 2: NACA0012.  $M_\infty = 0.5$  and  $M_\infty = 0.8$ . AoA=0°.  $P_a$  for baseline and stretched grids.

zero as the whole flow is subcritical and the theoretical value of  $P_a$  is one. The non-zero drag values obtained on the mesh hierarchy and the values lower than one obtained for  $P_a$

### 3.1. MESH QUALIFICATION AND LOCAL ADAPTATIONS APPLIED FOR EULERIAN FLOWS

come from numerical dissipation. The transonic test case presents two shocks located at  $x/c = 0.505$  (where  $c$  is the chord length) then the computed drag is the sum of the wave drag and the spurious drag (both positive contributions). Limiting  $CD_p$  values presented in [28, 29] range from  $83.415 \times 10^{-4}$  and  $83.423 \times 10^{-4}$ . The limiting value obtained in [19, 22] using the Roe scheme is  $83.420 \times 10^{-4}$  and the one found in this study with the Jameson *et al.* scheme is  $83.483 \times 10^{-4}$ . Lastly the limiting  $P_a$  value obtained in [19, 22] is 0.99306 and the one found in this study is 0.99225. The values of the indicators  $\theta$  and  $\bar{\theta}$  have been computed for the two functions and the two families of meshes (figures 8, 9 and tables D.3, D.4, D.5 and D.6). For both functions and both families of meshes these values decrease as the mesh size is increased. It is observed that criterion  $\theta$  is most often lower on the stretched grids than on the corresponding quasi-uniform grids whereas criterion  $\bar{\theta}$  is always lower on the stretched grids than on the corresponding quasi-uniform grids.

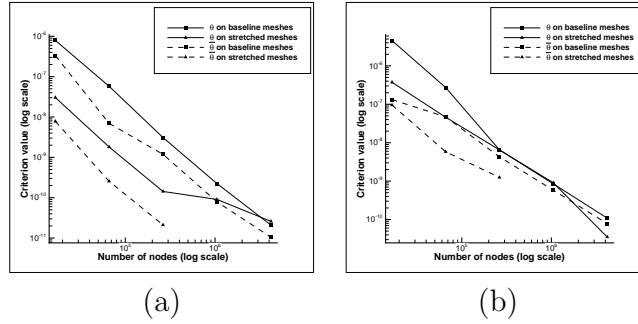


Figure 8: Criteria values on the mesh hierarchies for the subsonic test case. (a)  $CD_p$  (b)  $P_a$ .

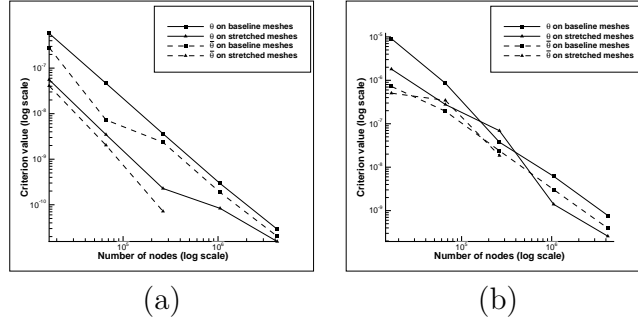


Figure 9: Criteria values on the mesh hierarchies for the transonic test case. (a)  $CD_p$  (b)  $P_a$ .

#### 5.3. Asymptotic behavior of $dJ/dX$

In Section 2 the theoretical asymptotic behavior of  $dJ/dX$  is studied. Under regularity assumptions, it was shown that the dominant term of the Taylor expansion of  $dJ/dX$  at each node is the local surface size times a term that depends on the Eulerian flux and the continuous flow-field and the limiting adjoint field (as the mesh size increases). This last term has been estimated on the quasi-uniform mesh hierarchy using the Jameson's scheme

by dividing  $dCD_p/dz_{ij}$  by the local surface  $ds_{ij}$  (for the subsonic test case). The figure 10 illustrates the evolution of the estimation of this term ( $x$ -component and  $z$ -component) on the baseline mesh hierarchy. As expected we can observe a convergence toward a limiting field.

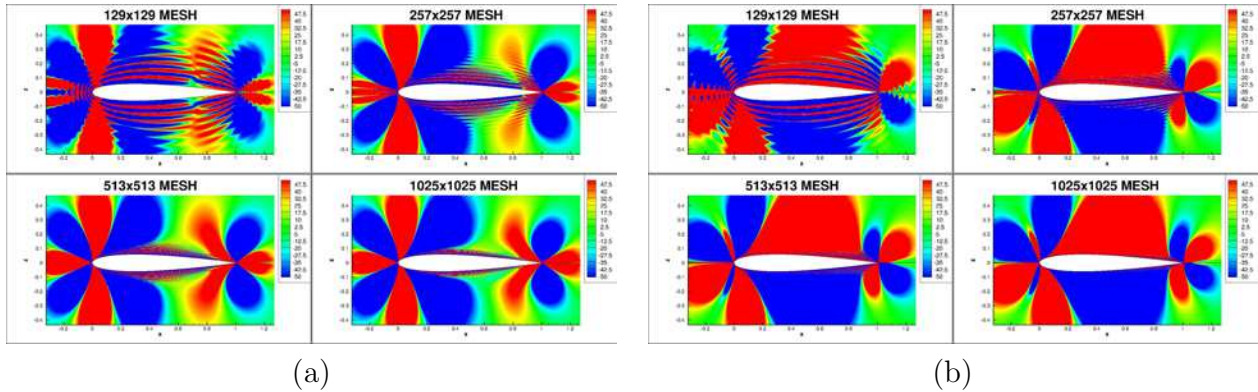


Figure 10: Estimations of the dominant term of the Taylor expansion of  $dCD_p/dX$  for quasi-regular meshes and Jameson's scheme ( $k^{(2)} = 0$  ;  $k^{(4)} = 0.016$ ). (a)  $x$ -component (b)  $z$ -component.

## 6. Numerical assessment of goal oriented mesh quality criteria

In this section we evaluate if the proposed criteria are appropriated to assess the quality of a mesh for the computation of the output  $J$ . The approach consists in considering families of parametrized meshes (that include both good meshes and bad meshes for the computation of  $J$ ) and to study the links between criteria  $\theta$  (bound of the variation of  $J$  from a mesh nodes displacement in the elementary volumes described in section 3) and  $\bar{\theta}$  (built from the  $\mathcal{P}(dJ/dX)$  spatial mean) w.r.t. the output values. More precisely, we examine if the meshes that give low values of criteria are those which give accurate values of the corresponding functions.

NB: A radial function  $\Psi_L'$  appears in the definition of the  $\mathcal{P}(dJ/dX)$  spatial mean (see appendix [Appendix B](#) for the definition). In all the study, the function used is  $\Psi_{(2/100)}^{(1/3)}$  (length  $L$  is equal to  $0.02 \times \text{chord}$ ).

6.1. *Parametrized mesh families*

6.1.1. *Mesh construction by interpolation*

The current meshes are built with bi-linear interpolation in a fine O-mesh ( $2049 \times 2049$ ) that comes from a study of Vassberg and Jameson [29]. We have chosen to define meshes whose lines are parallel to those of the fine mesh. The following function sequence defines the position of the mesh nodes (of size  $N_i \times N_j$ ). The operator chain  $\chi_{2049} \circ \Phi \circ \chi_{n_c}^{-1}$  defines the relative positions of nodes in the reference fine mesh.  $\mathcal{B}$  is a bi-linear interpolation operator.

$$\begin{array}{ccccccc} \{1, N_i\} \{1, N_j\} & \xrightarrow{\chi_{N_i, N_j}^{-1}} & [0, 1]^2 & \xrightarrow{\Phi} & [0, 1]^2 & \xrightarrow{\chi_{2049}} & [1, 2049]^2 & \xrightarrow{\mathcal{B}} & \mathbb{R}^2 \\ (i, j) & & (\bar{i}, \bar{j}) & & (\Phi^I(\bar{i}), \Phi^J(\bar{j})) & & (\chi f_i, \chi f_j) & & X(x, z) \end{array}$$

In this framework, a coarse mesh is completely defined by the two functions  $\Phi^I$  and  $\Phi^J$ . In the goal oriented mesh quality criteria study, it is necessary to consider parametrized mesh families that include meshes well or badly suited to the functions of interest computation. We will consider mesh families defined by parameterizing the functions  $\Phi^I$  and  $\Phi^J$ . In practice, in this part of the study, functions  $\Phi^I$  are function of  $\bar{i}$  only and functions  $\Phi^J$  are function of  $\bar{j}$  only.

*Remark.* In the following study, the mesh line that surrounds the airfoil is the J-line such that  $\bar{j} = 0$  and the one at the infinity is the J-line such that  $\bar{j} = 1$ . Lines  $\bar{i} = 0$  and  $\bar{i} = 1$  correspond to the connection between the trailing edge and infinity. The line at the leading edge is the I-line such that  $\bar{i} = 0.5$ .

6.1.2. *Mesh parametrization*

• *Subcritical test case.* A parametrization with two parameters has been considered (see figure 11). In the first one  $\alpha \in [0.05, 1]$ . The I-lines distribution is such that  $\alpha = 1$  corresponds to a line equidistribution ( $\Phi^I(\bar{i}) = \bar{i}$ ) and when  $\alpha$  closed to 0.05 to cases where the lines are stretched at the leading edge. A polynomial of degree two is used to parametrize the J-line distribution. The corresponding parameter is denoted by  $\beta$ . The case  $\beta = 1$  corresponds to a J-lines equidistribution whereas small values of  $\beta$  correspond to meshes where J-lines are stretched around the airfoil. The parametrization is given by:

$$\begin{aligned} \Phi_\alpha^I(\bar{i}) &= \begin{cases} 1 - 0.5(\alpha(1 - 2\bar{i}) + (1 - \alpha)(1 - 2\bar{i})^2) - 0.5 & \text{if } 0 \leq \bar{i} \leq 0.5 \\ 0.5(\alpha(2(\bar{i} - 0.5)) + (1 - \alpha)(2(\bar{i} - 0.5))^2) + 0.5 & \text{if } 0.5 \leq \bar{i} \leq 1 \end{cases} \\ \Phi_\beta^J(\bar{j}) &= \beta \bar{j} + (1 - \beta) \bar{j}^2 \end{aligned}$$

*Remark.* The parameter  $\beta$  is fixed superior to 0.5 in order to maintain an aspect ratio of 0.05 for the adjacent cells to the airfoil and avoid pathological aerodynamic solutions (small zones near the airfoil where the stagnation pressure is greater than the value at infinity). We also force  $\alpha$  to be greater than 0.05 in order to control the aspect ratio of the cells at the leading edge.

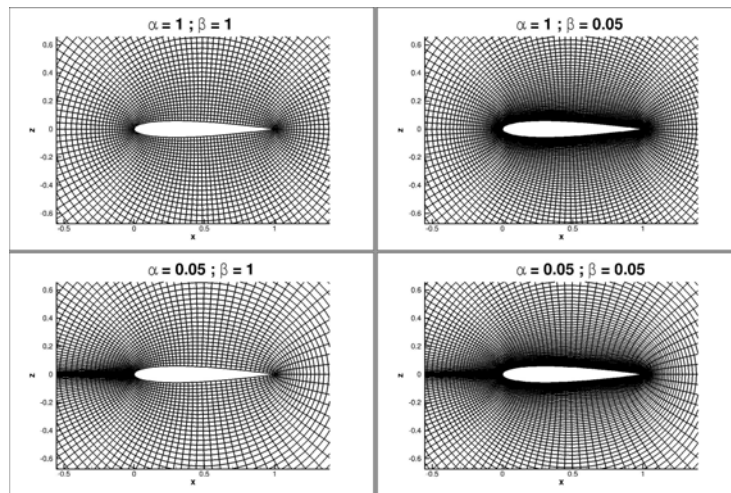


Figure 11: Meshes of the parametrization for the subcritical test case.

- *Transonic test case.* This parametrization (see figure 12), which depends on two parameters, drive the distribution of J-lines and is defined by:

$$\Phi_{\delta,\phi}^J(\bar{j}) = \delta \bar{j} + (1 - \delta - \phi) \bar{j}^2 + \phi \bar{j}^3 \quad \text{and} \quad \Phi^I(\bar{i}) = \bar{i}$$

So that  $\delta$  is the derivative of  $\Phi^J$  in 0 and affect the density of J-lines around the airfoil.

*Remark.* The parameter  $\delta$  is also fixed superior to 0.05 in order to maintain an aspect ratio of 0.05 for the adjacent cells to the airfoil and avoid pathological aerodynamic solutions as previously. The parameter  $\phi$  acts essentially in the area far from the airfoil (see figure 13).

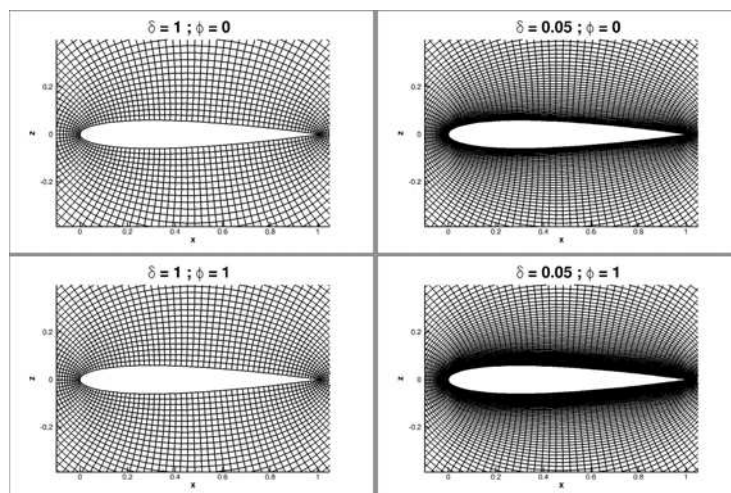


Figure 12: Meshes of the parametrization for the transonic test case near the airfoil.

### 3.1. MESH QUALIFICATION AND LOCAL ADAPTATIONS APPLIED FOR EULERIAN FLOWS

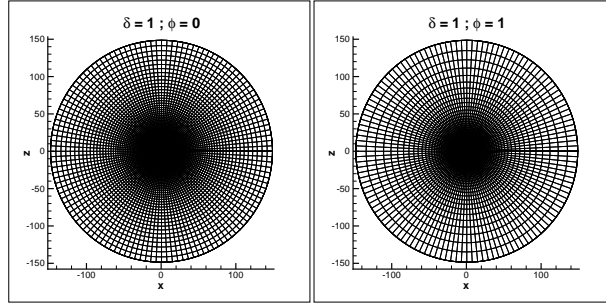


Figure 13: Meshes of the parametrization for the transonic test case.

#### 6.2. Subcritical test case

##### 6.2.1. $P_a$ evaluation and criteria on parametrized domain

Figure 14(a) presents  $P_a$  values in terms of mesh parameters  $(\alpha, \beta)$  (196 meshes are used, 14 for each parameter). The theoretical  $P_a$  value is 1. In this case numerical dissipation acts essentially monotonically on  $P_a$  by reducing its value. We notice that meshes that provide the better  $P_a$  estimations are those which are generated with the smallest value of  $\beta$  ( $\beta = 0.05$  meshes such that J-lines are closed around the airfoil). Criteria  $\theta$ , and  $\bar{\theta}$  achieve their lower values for the small values of  $\beta$  and  $\alpha$  (see figure 14(b)(c)). On the right  $\beta = 0.05$ , the variations of the function of interest  $P_a$  are very small (from 0.99938 to 0.99948). It is at  $(\alpha, \beta) = (0.05, 0.05)$  that the criteria  $\theta$  and  $\bar{\theta}$  achieve their lower values. At this point of the parameter space we have  $P_a = 0.99946$  whereas the closer value to the limiting one is obtain at  $(\alpha, \beta) = (0.6, 0.05)$  ( $P_a = 0.99948$ ). The first order variation criteria,  $\theta$  and  $\bar{\theta}$ , applied to  $P_a$  point out good meshes for the computation of  $P_a$  whereas its absolute minimum does not correspond to the best mesh but to one for which the estimation of  $P_a$  is appropriate.

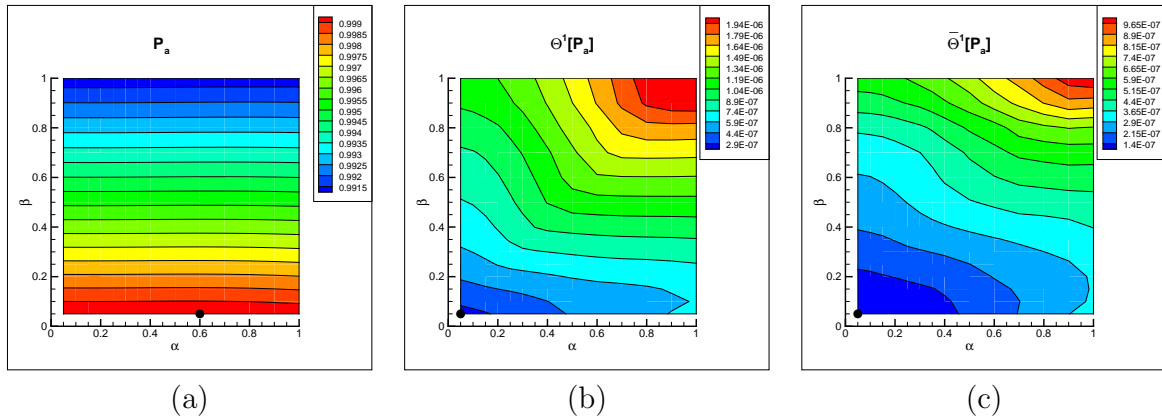


Figure 14: 2D Subcritical flow around NACA0012 (a)  $P_a$  I-lines and J-lines parametrization (b)  $\theta[P_a]$  in the parameter domain (c)  $\bar{\theta}[P_a]$  values in the parameter domain.

##### 6.2.2. $CD_p$ evaluation and criteria on parametrized domain

Figure 15(a) shows  $CD_p$  values on a mesh family parametrized by  $(\alpha, \beta)$ . The theoretical  $CD_p$  value is 0. In this case numerical dissipation act monotonically on  $CD_p$  by increasing

its value. We can notice that the best estimation of this function of interest is obtained for the lower  $\beta$  values ( $\beta = 0.05$ ). In this case, the lower  $\theta$ , and  $\bar{\theta}$  criteria values are obtained on two points of the line  $\beta = 0.05$  (see figure 15(b)(c)). On this line, the variations of the function of interest  $CD_p$  are small (from  $0.224 \times 10^{-4}$  to  $0.549 \times 10^{-4}$ ). The  $\theta$ , and  $\bar{\theta}$  minimal values are respectively located in  $(0.05, 0.05)$  and  $(0.9, 0.05)$ . The corresponding  $CD_p$  values are respectively  $0.339 \times 10^{-4}$  and  $0.419 \times 10^{-4}$  whereas the closest value to the limiting one is obtain at  $(\alpha, \beta) = (0.5, 0.05)$  ( $CD_p = 0.224 \times 10^{-4}$ ). The lower criteria values are obtained in the mesh zone that are well suited for  $CD_p$  computation ; whereas the absolute minimum does not correspond to the best mesh for  $CD_p$  computation, but leads to a mesh that provides a good estimation of the function.

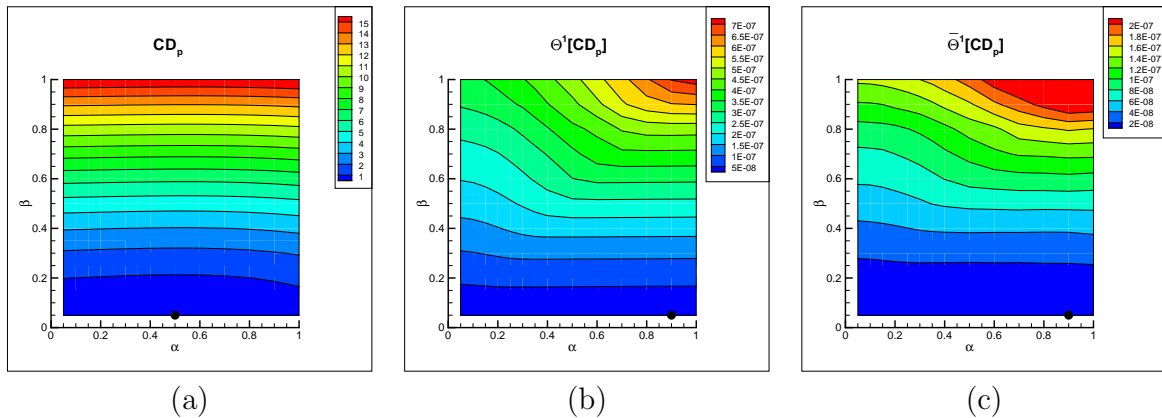


Figure 15: 2D Subcritical flow around NACA0012 (a)  $CD_p$  function. Subcritical flow. I-lines and J-lines parametrization (b)  $\theta[CD_p]$  in the parameter domain (c)  $\bar{\theta}[CD_p]$  values in the parameter domain.

### 6.3. Transonic test case

#### 6.3.1. $P_a$ evaluation. J-lines parametrization.

Figure 16(a) presents  $P_a$  values in terms of the mesh parameters  $(\delta, \phi)$  (312 meshes are used, 13 for the  $\delta$  parameter and 24 for the  $\phi$  parameter). Besides we compare the stagnation pressure curves at the wall with the one obtained on a very fine mesh (see figure 16(b)). We notice that the stagnation pressure is underestimated downstream and upstream the shock on coarse meshes for all meshes of the family. As for the subcritical flow, the better  $P_a$  values are the greater ones. The best estimations of this function are obtained for  $\delta$  close to 0.05 and  $\phi$  close to 1 corresponding to meshes such that J-lines are close around the airfoil for this parametrization (see figure 17). More precisely the best estimation obtained in  $(\delta, \phi) = (0.05, 1)$  is  $P_a = 0.99245$ .

For this family and this function of interest,  $\theta$  and  $\bar{\theta}$  maps are well linked to  $P_a$  values (*ie* the lower values are obtained for small  $\delta$  values, a zone that corresponds to good values of the function of interest  $P_a$ ). More precisely the  $\theta$  and  $\bar{\theta}$  minimal values are respectively obtained in  $(\delta, \phi) = (0.1, 1)$  and  $(0.15, 1)$ , the corresponding  $P_a$  values are 0.99128 and 0.99022.

### 3.1. MESH QUALIFICATION AND LOCAL ADAPTATIONS APPLIED FOR EULERIAN FLOWS

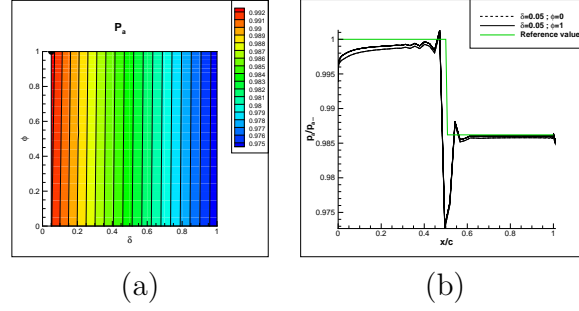


Figure 16: Transonic test case. (a)  $P_a$  J-lines parametrization (b) Limiting curves of stagnation pressure.

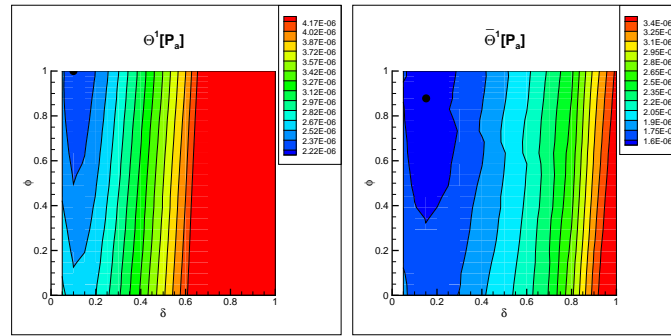


Figure 17:  $P_a$  function. Transonic test case. J-lines parametrization.  $\theta[P_a]$  and  $\bar{\theta}[P_a]$  criteria.

#### 6.3.2. $CD_p$ evaluation. J-lines parametrization.

Drag is subject to a particular attention and analyzed by a method called far-field breakdown because it has a specific importance in aeronautical applications. Otherwise, we know that numerical dissipation can lead to overestimate (with high spurious drag) or underestimate drag (with weak shock) on a transonic flow. In order to qualify meshes for  $CD_p$  computation, we introduce a special indicator associated to drag, the spurious drag is obtained in the framework of far-field drag breakdown, for two-dimensional inviscid flow, by subtracting the wave drag to the drag computed by pressure integral.

Figure 18(a) presents  $CD_p$  as a function of the mesh parameters  $(\delta, \phi)$ . Near-field drag  $CD_p$  is mainly function of  $\delta$  (decreasing with  $\delta$ ). All the values obtained are greater than the limiting one obtained on a very fine mesh ( $82.483 \times 10^{-4}$ ). Moreover the spurious drag has precisely its minimal value for small  $\delta$  (see figure 18(b)). According to these two observations, we consider that the best value on this mesh family is the lowest one. So  $CD_p = 83.734 \times 10^{-4}$  obtained for  $(\delta, \phi) = (0.05, 0.73)$ .

As for the subcritical test case, the  $\theta$ , and  $\bar{\theta}$  lower value zones correspond to accurate  $CD_p$  estimations (and to small  $\delta$ , see figure 19). More precisely the  $\theta$ , and  $\bar{\theta}$  minimal values are respectively located at  $(0.05, 0.93)$  and  $(0.1, 0.98)$ . The corresponding  $CD_p$  values are two satisfactory estimations among those reachable with the considered meshes ( $83.738 \times 10^{-4}$  and  $83.792 \times 10^{-4}$ ).

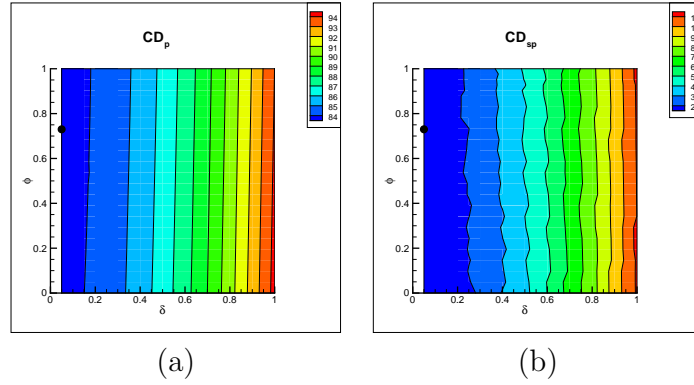


Figure 18: Transonic test case. J-lines parametrization. (a)  $CD_p$  values (b)  $CD_{sp}$  values (far-field analysis).

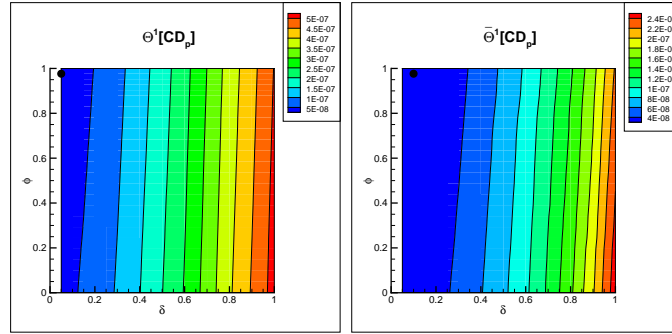


Figure 19:  $CD_p$  function. Transonic test case. J-lines parametrization.  $\theta[CD_p]$  and  $\bar{\theta}[CD_p]$  criteria.

#### 6.4. Conclusions

The results obtained in both subcritical and transonic test cases indicate a satisfactory but not perfect match between the accuracy of the functions values and the criteria  $\theta$  and  $\bar{\theta}$ . This may come from the fact that these criteria are based on a first-order estimation of the variation of  $J$ . However the overall low values of these criteria are obtained for the meshes that provide the best estimations of the function of interest in these mesh families. Thus these criteria are appropriate to assess the general quality of a mesh for the computation of the output  $J$ .

### 7. Numerical assessment of goal oriented criteria for mesh adaptation

The mesh adaptation method of section 4 has been applied to improve the quality of  $129 \times 129$  w.r.t. both  $CD_p$  and  $P_a$  computation in both subcritical and transonic test cases. The initial mesh was the quasi-regular one. The adaptation has been interrupted when the improvement in the estimation of the output is less than  $10^{-5}$  for the  $CD_p$  oriented adaptation and less than  $5 \times 10^{-5}$  for  $P_a$  oriented adaptation.

### 3.1. MESH QUALIFICATION AND LOCAL ADAPTATIONS APPLIED FOR EULERIAN FLOWS

#### 7.1. Subcritical test case

##### 7.1.1. Adaptation for $P_a$ computation

The initial mesh has been adapted in nine iterations. The corresponding results are summarized in the figure 20. The initial value of  $P_a$  was 0.99121 to be compared with the theoretical value of one. The final  $P_a$  value was 0.99949 which is more accurate than the value obtained on the stretched mesh of same size (0.99918) or to the value obtained on the quasi regular mesh of size  $2049 \times 2049$  (0.99937). The  $CD_p$  value on the adapted mesh was 0.348 which is more accurate than the value obtained on the quasi regular mesh of size  $513 \times 513$  ( $1.090 \times 10^{-4}$ ) or the value obtained on the mesh previously adapted for  $CD_p$  ( $0.584 \times 10^{-4}$ ). The adapted mesh is illustrated on figure 24(a). We notice that the adaptation has led to a refinement at the leading edge and also to an increase of mesh density all around the airfoil. The adaptation resulted in a significant reduction of the parameter  $\bar{\theta}$  which decreased from  $2.01 \times 10^{-6}$ , for the initial mesh, to  $1.06 \times 10^{-7}$  for the adapted mesh. Similarly, the parameter  $\theta$  decreased from  $4.55 \times 10^{-6}$  to  $1.09 \times 10^{-7}$ .

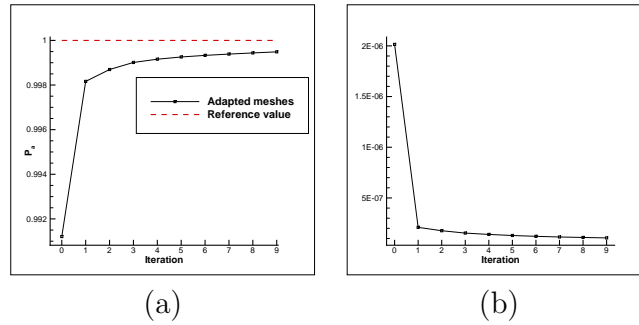


Figure 20: Results over the adaptation process for the computation of  $P_a$  for the subsonic test case. (a)  $P_a$  values (b)  $\bar{\theta}[P_a]$  values.

##### 7.1.2. Adaptation for $CD_p$ computation

The initial mesh has been adapted in six iterations. The corresponding results are summarized in the figure 21. The initial  $CD_p$  value was  $16.050 \times 10^{-4}$  that is entirely due to numerical dissipation since the theoretical value is zero. The final  $CD_p$  value was  $0.584 \times 10^{-4}$  which is more accurate than the value obtained on the stretched mesh of same size ( $1.322 \times 10^{-4}$ ) or to the value obtained on the quasi regular mesh of size  $513 \times 513$  ( $1.090 \times 10^{-4}$ ). The theoretical  $P_a$  value in this case is one. The computed  $P_a$  value on the adapted mesh was 0.99852 which is more accurate than the value obtained on the initial mesh (0.99121) or the value obtained on the quasi regular mesh of size  $513 \times 513$  (0.99765) thus we notice an indirect improvement of the estimation of this output. But this estimation was not as accurate as the one obtained on the stretched mesh of same size (0.99918). The adapted mesh is illustrated on figure 24(b). We notice that the adaptation has led to a refinement at the leading edge. The adaptation resulted in a significant reduction of the parameter  $\bar{\theta}$  which decreased from  $3.33 \times 10^{-7}$ , for the initial mesh, to  $6.88 \times 10^{-8}$  for the adapted mesh. Similarly, the parameter  $\theta$  decreased from  $7.92 \times 10^{-7}$  to  $8.10 \times 10^{-8}$ .

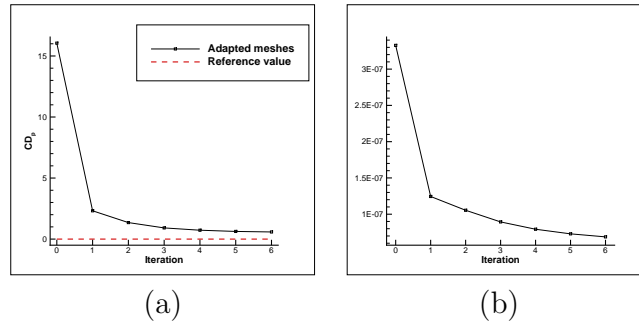


Figure 21: Results over the adaptation process for the computation of  $CD_p$  for the subsonic test case. (a)  $CD_p$  values (b)  $\theta[CD_p]$  values.

## 7.2. Transonic test case

### 7.2.1. Adaptation for $P_a$ computation

The initial mesh has been adapted in nine iterations. The corresponding results are summarized in the figure 22. The initial value of  $P_a$  was 0.97425 to be compared with the limiting value of 0.99225. The final  $P_a$  value was 0.99179 which is more accurate than the value obtained on the quasi regular mesh of size  $1025 \times 1025$  (0.99101) and close to the one obtained on the stretched mesh of same size (0.99206). Moreover the  $CD_p$  value on the adapted mesh was  $83.498 \times 10^{-4}$  which is more accurate than the value obtained on the quasi regular mesh of size  $2049 \times 2049$  and also more accurate than the value obtained on the stretched mesh of size  $2049 \times 2049$  ( $83.410 \times 10^{-4}$ ). So we observe an improvement of the solution accuracy. Moreover in order to check that this improvement is actually due to an improvement of the solution quality, the stagnation pressure at the wall has been studied. We observe an improvement of the estimation of the stagnation pressure before and after the shocks. This is also confirmed by a far-field drag extraction that estimate the spurious drag as  $CD_{sp} = 11.122 \times 10^{-4}$  for the initial mesh and  $CD_{sp} = 1.410 \times 10^{-4}$  for the final mesh. The adapted mesh is illustrated on figure 25(a). We notice refinement essentially close to and around the airfoil and slightly at the leading edge and in the neighborhood of the shocks. The adaptation resulted in a significant reduction of the parameter  $\bar{\theta}$  which decreased from  $5.24 \times 10^{-6}$ , for the initial mesh, to  $5.66 \times 10^{-7}$  for the adapted mesh. Similarly, the parameter  $\theta$  decreased from  $9.09 \times 10^{-6}$  to  $7.83 \times 10^{-7}$ .

### 3.1. MESH QUALIFICATION AND LOCAL ADAPTATIONS APPLIED FOR EULERIAN FLOWS

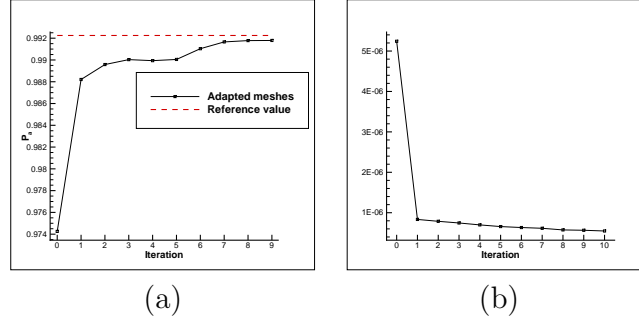


Figure 22: Results over the adaptation process for the computation of  $P_a$  for the transonic test case. (a)  $P_a$  values (b)  $\theta[P_a]$  values.

#### 7.2.2. Adaptation for $CD_p$ computation

The initial mesh has been adapted in five iterations. The corresponding results are summarized in the figure 23. The initial  $CD_p$  value was  $94.361 \times 10^{-4}$  to be compared with the limiting value of  $83.483 \times 10^{-4}$ . The final  $CD_p$  value was  $83.422 \times 10^{-4}$  which is clearly more accurate than the value obtained on the stretched mesh of same size ( $88.408 \times 10^{-4}$ ) and almost as accurate as the one obtained on the quasi regular mesh of size  $2049 \times 2049$  ( $83.454 \times 10^{-4}$ ). The limiting  $P_a$  value is 0.99225. The computed  $P_a$  value on the adapted mesh was 0.98984 and was 0.97425 on the initial one then we also notice an indirect improvement of the estimation of this output. This estimation is more accurate than the one obtained on the quasi-regular mesh of size  $513 \times 513$  (0.98833) but not than the one obtained on the stretched mesh of same size (0.99206). As in the previous case, the wall stagnation pressure has been studied in order to check the quality of the solutions and an improvement of the solution quality has been observed. Moreover a far-field drag extraction estimates the spurious drag as  $CD_{sp} = 0.829 \times 10^{-4}$  for the adapted mesh and was  $CD_{sp} = 11.122 \times 10^{-4}$  for the initial mesh. The adapted mesh is illustrated on figure 25(b). We notice that the method has led to refinement essentially at the leading edge and at the neighborhood of the shocks and also at the trailing edge. The adaptation resulted in a significant reduction of the parameter  $\bar{\theta}$  which decreased from  $2.83 \times 10^{-7}$ , for the initial mesh, to  $1.34 \times 10^{-7}$  for the adapted mesh. Similarly, the parameter  $\theta$  decreased from  $5.80 \times 10^{-7}$  to  $1.49 \times 10^{-7}$ .

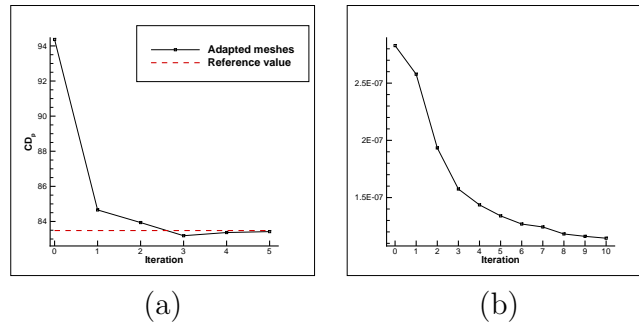
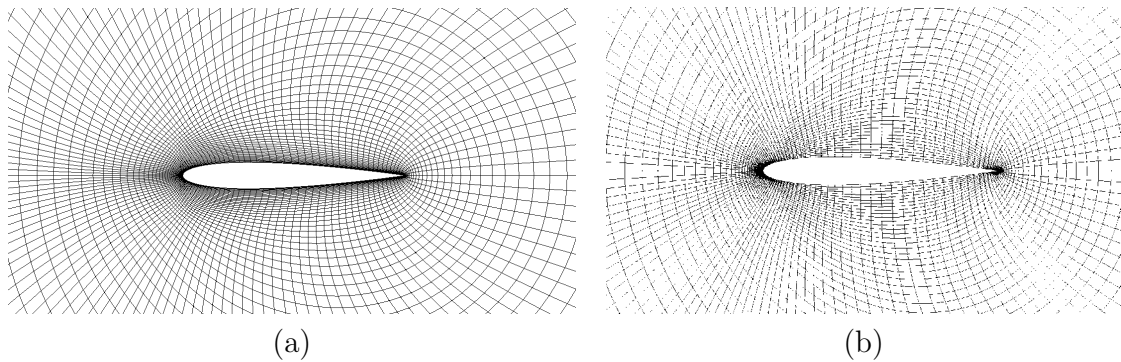
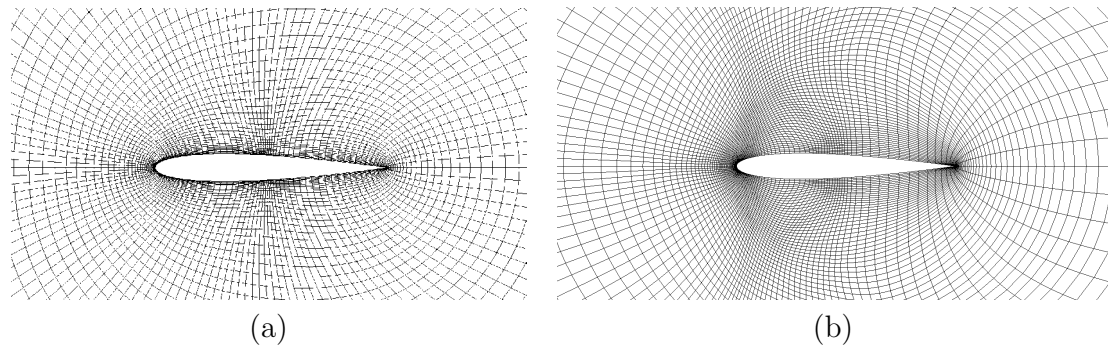


Figure 23: Results over the adaptation process for the computation of  $CD_p$  for the transonic test case. (a)  $CD_p$  values (b)  $\theta[CD_p]$  values.

Figure 24: Subcritical test case (a) Mesh adapted for  $P_a$  (b) Mesh adapted for  $CD_p$ .Figure 25: Transonic test case (a) Mesh adapted for  $P_a$  (b) Mesh adapted for  $CD_p$ .

### 7.3. Conclusions

The mesh adaptations conducted for the outputs computations for these two test cases has led to successful results as the accuracy of the outputs computation has been increased while improving the quality of the simulations. On the other hand the behaviour of the criterion  $\bar{\theta}$  during the adaptation process confirms that it is an adequate mesh quality indicator even if, as shown previously, it does not provide a perfect correlation with accuracy of the output computation.

## 8. Conclusions

In the first part of this work, we have studied the total derivative of aerodynamic functions w.r.t. mesh coordinates. In particular the asymptotic behaviour of this derivative has been analysed. It appeared that the derivative  $dJ/dX$  can be well approximated on a given mesh using a solution originating from a coarser-mesh computation hence all indicators based on  $dJ/dX$  can be interpolated from coarse grid to fine grid. The construction of mesh quality criteria based on  $dJ/dX$  has been carried out. These criteria can be used adequately for local mesh adaptation as they provide the most sensitive mesh locations for the output estimation taking into account the admissible node displacements. These criteria have been studied

### 3.1. MESH QUALIFICATION AND LOCAL ADAPTATIONS APPLIED FOR EULERIAN FLOWS

in order to analyse the correlations between its lower values and the best estimations of the outputs. It has been emphasized that these criteria are appropriate indicators of mesh quality for the computation of the outputs even if the match is not perfect between its lower values and the best estimations of the outputs. Local structured mesh adaptations has been carried out using the local form of the criterion  $\bar{\theta}$ . These adaptations have provided good meshes for the computations of the outputs through local refinement at location of high  $\bar{\theta}$  values. These results confirm that the criterion  $\bar{\theta}$  is a relevant indicator for goal oriented mesh adaptation. The extension of these methods to RANS flows will be the object of future work. This will require an accurate  $dJ/dX$  field and a careful boundary layer remeshing procedure during the adaptation process. Finally another extension will be the application of the proposed method to more complex geometries. This will require the extension of the remeshing strategy to multiblock meshes with not necessarily coincident block interfaces.

#### **Acknowledgments**

The authors warmly express their gratitude to J.C. Vassberg and A. Jameson for allowing the co-workers of D. Destarac to use their hierarchy of O-grid around the NACA0012 airfoil.

**Appendix A. Asymptotic behaviour of  $dJ/dX$  for four-point flux formulas**

The analysis of  $\Lambda^T \partial R / \partial X$  is now carried out for a four-point  $C^2$  flux formula.

$$F_{i,j-1/2} = F^{(4)}(W_{i-3/2,j-1/2}, W_{i-1/2,j-1/2}, W_{i+1/2,j-1/2}, W_{i+3/2,j-1/2}, S_{i,j-1/2}^X, S_{i,j-1/2}^Z)$$

The counter part of equation (6) is:

$$\begin{aligned} \Lambda \frac{\partial R}{\partial x_{i,j}} &= \sum_{k=1}^{k=4} T^k \\ T^k &= (\Lambda_{i+1/2,j+1/2}^k - \Lambda_{i+1/2,j-1/2}^k) \times \\ &\quad F_Z^{4,k}(w_{i+1/2,j-3/2}, w_{i+1/2,j-1/2}, w_{i+1/2,j+1/2}, w_{i+1/2,j+3/2}, S_{i+1/2,j}^X, S_{i+1/2,j}^Z) \\ &\quad - (\Lambda_{i-1/2,j+1/2}^k - \Lambda_{i-1/2,j-1/2}^k) \times \\ &\quad F_Z^{4,k}(w_{i-1/2,j-3/2}, w_{i-1/2,j-1/2}, w_{i-1/2,j+1/2}, w_{i-1/2,j+3/2}, S_{i-1/2,j}^X, S_{i-1/2,j}^Z) \\ &\quad - (\Lambda_{i+1/2,j+1/2}^k - \Lambda_{i-1/2,j+1/2}^k) \times \\ &\quad F_Z^{4,k}(w_{i-3/2,j+1/2}, w_{i-1/2,j+1/2}, w_{i+1/2,j+1/2}, w_{i+3/2,j+1/2}, S_{i,j+1/2}^X, S_{i,j+1/2}^Z) \\ &\quad + (\Lambda_{i+1/2,j-1/2}^k - \Lambda_{i-1/2,j-1/2}^k) \times \\ &\quad F_Z^{4,k}(w_{i-3/2,j-1/2}, w_{i-1/2,j-1/2}, w_{i+1/2,j-1/2}, w_{i+3/2,j-1/2}, S_{i,j-1/2}^X, S_{i,j-1/2}^Z) \end{aligned}$$

In the same mathematical framework as in the section 2 this formula is expanded in  $r$ .

3.1. MESH QUALIFICATION AND LOCAL ADAPTATIONS APPLIED FOR  
EULERIAN FLOWS

$$\begin{aligned}
T^k = & r^2 \left[ \left( (\Delta x_a - \Delta x_b) \frac{\partial \lambda^k}{\partial x} + (\Delta z_a + \Delta z_b) \frac{\partial \lambda^k}{\partial z} \right) \times \right. \\
& \left( \frac{\partial F_Z^{4,k}}{\partial w_{2L}} \left( (2\Delta x_b - \Delta x_a) \frac{\partial w}{\partial x} - (\Delta z_a + 2\Delta z_b) \frac{\partial w}{\partial z} \right) + \frac{\partial F_Z^{4,k}}{\partial w_L} \left( \Delta x_b \frac{\partial w}{\partial x} - \Delta z_b \frac{\partial w}{\partial z} \right) \right. \\
& \left. + \frac{\partial F_Z^{4,k}}{\partial w_R} \left( \Delta x_a \frac{\partial w}{\partial x} + \Delta z_a \frac{\partial w}{\partial z} \right) + \frac{\partial F_Z^{4,k}}{\partial w_{2R}} \left( (2\Delta x_a - \Delta x_b) \frac{\partial w}{\partial x} + (2\Delta z_a + \Delta z_b) \frac{\partial w}{\partial z} \right) \right) \\
& - \left( (\Delta x_a - \Delta x_b) \frac{\partial \lambda^k}{\partial x} + (\Delta z_a + \Delta z_b) \frac{\partial \lambda^k}{\partial z} \right) \times \\
& \left( \frac{\partial F_Z^{4,k}}{\partial w_{2L}} \left( (\Delta x_b - 2\Delta x_a) \frac{\partial w}{\partial x} - (2\Delta z_a + \Delta z_b) \frac{\partial w}{\partial z} \right) + \frac{\partial F_Z^{4,k}}{\partial w_L} \left( -\Delta x_a \frac{\partial w}{\partial x} - \Delta z_a \frac{\partial w}{\partial z} \right) \right. \\
& \left. + \frac{\partial F_Z^{4,k}}{\partial w_R} \left( -\Delta x_b \frac{\partial w}{\partial x} + \Delta z_b \frac{\partial w}{\partial z} \right) + \frac{\partial F_Z^{4,k}}{\partial w_{2R}} \left( (\Delta x_a - 2\Delta x_b) \frac{\partial w}{\partial x} + (\Delta z_a + 2\Delta z_b) \frac{\partial w}{\partial z} \right) \right) \\
& - \left( (\Delta x_a + \Delta x_b) \frac{\partial \lambda^k}{\partial x} + (\Delta z_a - \Delta z_b) \frac{\partial \lambda^k}{\partial z} \right) \times \\
& \left( \frac{\partial F_Z^{4,k}}{\partial w_{2L}} \left( -(\Delta x_a + 2\Delta x_b) \frac{\partial w}{\partial x} - (\Delta z_a - 2\Delta z_b) \frac{\partial w}{\partial z} \right) + \frac{\partial F_Z^{4,k}}{\partial w_L} \left( -\Delta x_b \frac{\partial w}{\partial x} + \Delta z_b \frac{\partial w}{\partial z} \right) \right. \\
& \left. + \frac{\partial F_Z^{4,k}}{\partial w_R} \left( \Delta x_a \frac{\partial w}{\partial x} + \Delta z_a \frac{\partial w}{\partial z} \right) + \frac{\partial F_Z^{4,k}}{\partial w_{2R}} \left( (2\Delta x_a + \Delta x_b) \frac{\partial w}{\partial x} + (2\Delta z_a - \Delta z_b) \frac{\partial w}{\partial z} \right) \right) \\
& + \left( (\Delta x_a + \Delta x_b) \frac{\partial \lambda^k}{\partial x} + (\Delta z_a - \Delta z_b) \frac{\partial \lambda^k}{\partial z} \right) \times \\
& \left( \frac{\partial F_Z^{4,k}}{\partial w_{2L}} \left( -(2\Delta x_a + \Delta x_b) \frac{\partial w}{\partial x} - (2\Delta z_a - \Delta z_b) \frac{\partial w}{\partial z} \right) + \frac{\partial F_Z^{4,k}}{\partial w_L} \left( -\Delta x_a \frac{\partial w}{\partial x} - \Delta z_a \frac{\partial w}{\partial z} \right) \right. \\
& \left. + \frac{\partial F_Z^{4,k}}{\partial w_R} \left( \Delta x_b \frac{\partial w}{\partial x} - \Delta z_b \frac{\partial w}{\partial z} \right) + \frac{\partial F_Z^{4,k}}{\partial w_{2R}} \left( (\Delta x_a + 2\Delta x_b) \frac{\partial w}{\partial x} + (\Delta z_a - 2\Delta z_b) \frac{\partial w}{\partial z} \right) \right) \Big] \\
& + o(r^2)
\end{aligned}$$

As in the previous calculation the terms  $\frac{\partial \lambda^k}{\partial x} \frac{\partial w}{\partial x}$  and  $\frac{\partial \lambda^k}{\partial z} \frac{\partial w}{\partial z}$  cancel. The remaining terms are

$$\begin{aligned}
T^k = & -2r^2 (\Delta x_a \Delta z_b + \Delta x_b \Delta z_a) \frac{\partial \lambda^k}{\partial x} \left( \frac{\partial F_Z^{4,k}}{\partial w_{2L}} + \frac{\partial F_Z^{4,k}}{\partial w_L} + \frac{\partial F_Z^{4,k}}{\partial w_R} + \frac{\partial F_Z^{4,k}}{\partial w_{2R}} \right) \frac{\partial w}{\partial z} \\
& + 2r^2 (\Delta x_a \Delta z_b + \Delta x_b \Delta z_a) \frac{\partial \lambda^k}{\partial z} \left( \frac{\partial F_Z^{4,k}}{\partial w_{2L}} + \frac{\partial F_Z^{4,k}}{\partial w_L} + \frac{\partial F_Z^{4,k}}{\partial w_R} + \frac{\partial F_Z^{4,k}}{\partial w_{2R}} \right) \frac{\partial w}{\partial x}
\end{aligned}$$

Hence using the same arguments as in the section 2 the asymptotic behaviour of  $dJ/dX$  outside the support of  $J$  is:

$$\frac{dJ}{dX_{ij}} = ds_{ij} \sum_{k=1}^4 \left[ \begin{array}{c} \frac{\partial \lambda^k}{\partial z} \frac{\partial \mathcal{F}_Z^k}{\partial x} - \frac{\partial \lambda^k}{\partial x} \frac{\partial \mathcal{F}_Z^k}{\partial z} \\ -\frac{\partial \lambda^k}{\partial z} \frac{\partial \mathcal{F}_X^k}{\partial x} + \frac{\partial \lambda^k}{\partial x} \frac{\partial \mathcal{F}_X^k}{\partial z} \end{array} \right]_{ij} + o(r^2)$$

**Appendix B. Definition of  $\overline{\mathcal{P}(dJ/dX)}$ , the spatial mean of  $\mathcal{P}(dJ/dX)$** 

A discrete convolution based spatial mean  $\overline{\mathcal{P}(dJ/dX)}$  of  $\mathcal{P}(dJ/dX)$  is built. A 2D problem is considered. The extension to 3D is straightforward. It is assumed that the discrete values of a realistic mesh displacement field  $dX$  are the values of a  $C^1$  regular function noted  $dXC$  taken at the nodes of the mesh. It is also assumed that  $dXC$  is well approximated by its first-order Taylor expansion on all circles of radius  $L$ . Finally,  $\mathcal{D}_{(C,L)}$  denotes the disk centered in  $C$  with radius  $L$  and  $\Psi_L$  denotes a radial function of support  $\mathcal{D}(O, L)$  and integral 1 on this disk. Using all these properties, it is easily checked that the displacement of the node  $(i, j)$  (denoted  $dX_{ij}$ ) can be estimated by the following relation:

$$\int_{\mathcal{D}(X_{ij}, L)} dXC(u) \Psi_L(u - X_{ij}) du \simeq dXC(X_{ij}) \int_{\mathcal{D}(X_{ij}, L)} \Psi_L(u - X_{ij}) du = dX_{ij} \quad (\text{B.1})$$

Although this property is available for all radial function  $\Psi_L$  of support  $\mathcal{D}(O, L)$  and integral 1, it is desirable to use a decreasing function of the norm of its argument. In practice, the following kind of functions is used

$$\Psi_L^\nu(u) = \frac{(L^2 - \|u\|^2)^\nu}{2\pi \int_0^L (L^2 - r^2)^\nu dr} \quad \text{for } \|u\| \leq L \quad \text{and} \quad \Psi_L^\nu(u) = 0 \quad \text{for } \|u\| \geq L$$

The simplest discretization on the mesh of the left-hand-side of equation (B.1) is

$$\sum_{X_{i'j'} \in \mathcal{D}(X_{ij}, L)} dX_{i'j'} \Psi_L(X_{i'j'} - X_{ij}) ds_{i'j'}$$

where  $ds_{ij}$  is the surface of the mesh element associated with the point  $X_{ij}$  (plotted on B.26(a)). However this relation is not exact on a constant field and inconsistent for coarse

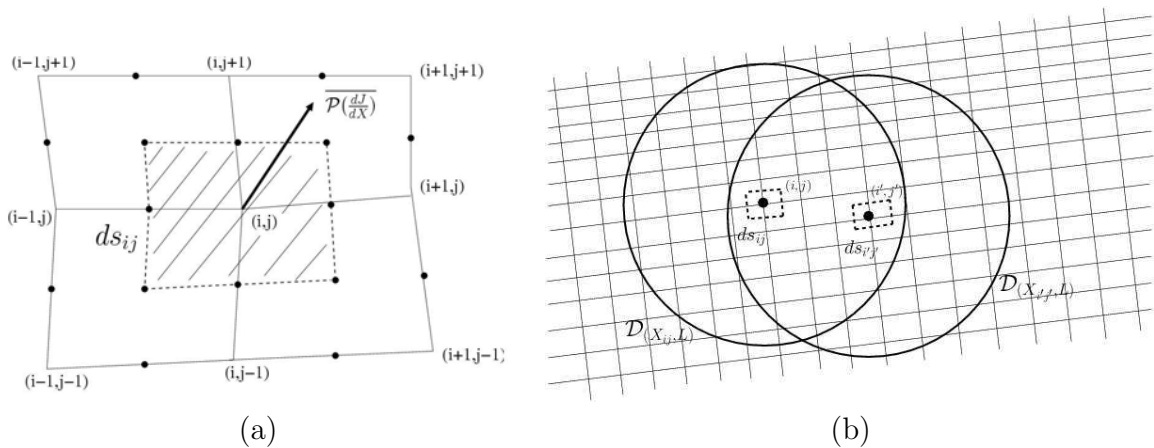


Figure B.26: (a) Surface  $ds_{ij}$  associated to node  $(i, j)$  in the definition of  $\overline{\mathcal{P}(dJ/dX)}$  (b) Disks  $\mathcal{D}(X_{ij}, L)$  and  $\mathcal{D}(X_{i'j'}, L)$

mesh zones. So the following discretization is preferred

$$\frac{\sum_{X_{i'j'} \in \mathcal{D}(X_{ij,L})} dX_{i'j'} \Psi_L(X_{i'j'} - X_{ij}) ds_{i'j'}}{\sum_{X_{i'j'} \in \mathcal{D}(X_{ij,L})} \Psi_L(X_{i'j'} - X_{ij}) ds_{i'j'}} \quad (\text{B.2})$$

Henceforth we note  $\gamma_{ijL}$  the denominator of the expression (B.2)

( $\gamma_{ijL} = \sum_{X_{i'j'} \in \mathcal{D}(X_{ij,L})} \Psi_L(X_{i'j'} - X_{ij}) ds_{i'j'}$ ). The dot product of interest ( $\mathcal{P}(dJ/dX) \cdot dX$ ) can then be rewritten using the proposed discretization of the mesh displacement field  $dX$ :

$$\begin{aligned} \mathcal{P} \left( \frac{dJ}{dX} \right) \cdot dX &= \sum_{i=1}^{N_i} \sum_{j=1}^{N_j} \mathcal{P} \left( \frac{dJ}{dX} \right)_{ij} dX_{ij} \\ &\simeq \sum_{i=1}^{N_i} \sum_{j=1}^{N_j} \frac{1}{\gamma_{ijL}} \mathcal{P} \left( \frac{dJ}{dX} \right)_{ij} \sum_{X_{i'j'} \in \mathcal{D}(X_{ij,L})} dX_{i'j'} \Psi_L(X_{i'j'} - X_{ij}) ds_{i'j'} \end{aligned}$$

It is interesting to switch the indices  $(i, j)$  and  $(i', j')$  (noticing that  $X_{i'j'} \in \mathcal{D}(X_{ij,L})$  is equivalent to  $X_{ij} \in \mathcal{D}(X_{i'j',L})$ , see figure B.26(b))

$$\mathcal{P} \left( \frac{dJ}{dX} \right) \cdot dX \simeq \sum_{i'=1}^{N_i} \sum_{j'=1}^{N_j} \left( ds_{i'j'} \sum_{X_{ij} \in \mathcal{D}(X_{i'j',L})} \left( \frac{1}{\gamma_{ijL}} \mathcal{P} \left( \frac{dJ}{dX} \right)_{ij} \Psi_L(X_{i'j'} - X_{ij}) \right) \right) dX_{i'j'}$$

So we build a mean field with the following relation (switching again the indices with and without prime):

$$\overline{\mathcal{P} \left( \frac{dJ}{dX} \right)_{ij}} = ds_{ij} \sum_{X_{i'j'} \in \mathcal{D}(X_{ij,L})} \frac{1}{\gamma_{i'j'L}} \mathcal{P} \left( \frac{dJ}{dX} \right)_{i'j'} \Psi_L(X_{i'j'} - X_{ij}) \quad (\text{B.3})$$

However the equations (B.1) and (B.2) are inaccurate for all the nodes  $(i, j)$  such that the circle  $\mathcal{D}(X_{ij,L})$  is not entirely included in the fluid domain. Therefore the previous definition of the mean field  $\overline{\mathcal{P}(dJ/dX)}$  is used only for the nodes  $(i, j)$  such that the circle  $\mathcal{D}(X_{ij,L})$  is entirely included in the fluid domain. For the other nodes, the proposed definition of  $\overline{\mathcal{P}(dJ/dX)}$  can be extended by changing the shape of the integration domain.

### Appendix C. Construction of the mesh generation elliptic system of PDEs

The construction of a mesh generation elliptic system of PDEs is presented in the particular case of a single block mesh. More details can be found in the literature (for example in [23, 24]). At first, we define a computational space (denoted by  $C$ ) which is a unit square and the coordinates are denoted by  $\xi_i$  ( $i = 1, 3$ ). We also define a parameter space (denoted by  $P$ ) which is also a unit square and the coordinates are denoted by  $t_i$  ( $i = 1, 3$ ). And finally we consider the physical space (denoted by  $D$ ) with Cartesian coordinates  $x = (x_1, x_2, x_3)$ . The mesh is built through to a mapping  $x : C \rightarrow D$  such that:

$$X_{ijk} = x \left( \frac{i-1}{N_i-1}, \frac{j-1}{N_j-1}, \frac{k-1}{N_k-1} \right) \quad (\text{C.1})$$

where  $X_{ijk}$  is the coordinates of the node  $(i, j, k)$  and  $N_i, N_j, N_k$  are the number of nodes in each topological direction. The mapping  $x : C \rightarrow D$  is defined as the combination of a mapping  $t : C \rightarrow P$  which have the property to prescribe the boundaries nodes distribution and another one  $x : P \rightarrow D$  which only depends on the shape of  $D$  and has the property that the corresponding inverse mapping  $t : D \rightarrow P$  is harmonic:

$$\Delta t_i = \sum_{k=1}^3 \frac{\partial^2 t_i}{\partial x_k^2} = 0 \quad (\text{C.2})$$

This relation is needed in order to generate a smooth mesh. Indeed it can be checked that the function  $t$  satisfying (C.2) is the one that minimize the functional:

$$K[t] = \int_D |\nabla t_1|^2 + |\nabla t_2|^2 + |\nabla t_3|^2 dx \quad (\text{C.3})$$

This functional can be seen as a smoothness measure of the generated mesh so the one built thanks to the function  $t$  solution of (C.2) is expected to be the smoother one that can be obtained using (C.1) with  $x : C \rightarrow D$  (which is the combination of  $t : C \rightarrow P$  and  $x : P \rightarrow D$ ). Finally for a given shape  $D$  the resulting mapping  $x : C \rightarrow D$  only depends on the mapping  $t : C \rightarrow P$ . One has to find the system of PDEs such that  $x : C \rightarrow D$  is the solution in order to generate the mesh thanks to the equations (C.1). At first we consider the covariant and contravariant base vectors respectively given by:

$$g_i = \frac{\partial x}{\partial \xi_i} = x_{\xi_i} \quad \text{and} \quad g^i = \frac{\partial \xi}{\partial x_i} = \xi_{x_i} \quad i = 1, 3 \quad (\text{C.4})$$

We consider the covariant and contravariant metric tensors respectively defined by:

$$A_{ij} = g_{ij} = (g_i, g_j) \quad \text{and} \quad B^{ij} = g^{ij} = (g^i, g^j) \quad i, j = 1, 3 \quad (\text{C.5})$$

We notice that we have the well known relation:

$$B = A^{-1} \quad (\text{C.6})$$

On the other hand, by considering an arbitrary function  $\psi(x) = \bar{\psi}(\xi(x))$ , it can easily be checked that we have:

$$\Delta \psi = \sum_{i,j=1}^3 g^{ij} \bar{\psi}_{\xi_i \xi_j} + \sum_{k=1}^3 \Delta \xi_k \cdot \bar{\psi}_{\xi_k} \quad (\text{C.7})$$

Then by applying this relation to equation (C.2) with  $\psi = t$ , one can check that the expression of  $\Delta \xi$  takes the form:

$$\Delta \xi = \sum_{i,j=1}^3 g^{ij} \tilde{P}_{ij} \quad (\text{C.8})$$

where  $\tilde{P}_{ij}$  are the control functions that only depend on the first and second derivatives of  $t_i$  ( $i = 1, 2, 3$ ) with respect to  $\xi_j$  ( $j = 1, 2, 3$ ). The next step consists in substituting  $\psi$  by  $x$  in

### 3.1. MESH QUALIFICATION AND LOCAL ADAPTATIONS APPLIED FOR EULERIAN FLOWS

equation (C.7) and to use the previous expression of  $\Delta\xi$  and the fact that  $\Delta x = 0$  then we obtain:

$$\sum_{i,j=1}^3 g^{ij} x_{\xi_i \xi_j} + \sum_{k=1}^3 \sum_{i,j=1}^3 g^{ij} \tilde{P}_{ij}^k x_{\xi_k} = 0 \quad (\text{C.9})$$

This equation takes the form of (7) with the relation:

$$P_k = \sum_{i,j=1}^3 \frac{g^{ij}}{g^{kk}} \tilde{P}_{ij}^k \quad (\text{C.10})$$

Finally one can notice that for the solution of system (C.9), one can use the relations (C.5) and (C.6) in order to express the system of PDEs with covariant vectors.

#### Appendix D. Numerical results on the mesh hierarchies

The following tables summarizes the numerical results obtained on the mesh hierarchies for both the outputs and the criteria. The tables D.3 and D.4 summarizes the results for the subsonic test case and the tables D.5 and D.6 for transonic one.

	$CD_p (\times 10^4)$	$\theta[CD_p]$	$\bar{\theta}[CD_p]$	$P_a$	$\theta[P_a]$	$\bar{\theta}[P_a]$
Limiting value	0.	—	—	1.	—	—
$2049 \times 2049$	0.067	$2.09 \cdot 10^{-11}$	$1.05 \cdot 10^{-11}$	0.99937	$1.09 \cdot 10^{-10}$	$7.82 \cdot 10^{-11}$
$1025 \times 1025$	0.271	$2.24 \cdot 10^{-10}$	$7.90 \cdot 10^{-11}$	0.99879	$8.48 \cdot 10^{-10}$	$5.80 \cdot 10^{-10}$
$513 \times 513$	1.090	$3.10 \cdot 10^{-9}$	$1.19 \cdot 10^{-9}$	0.99765	$6.51 \cdot 10^{-9}$	$4.28 \cdot 10^{-9}$
$257 \times 257$	4.276	$5.78 \cdot 10^{-8}$	$6.96 \cdot 10^{-9}$	0.99540	$2.73 \cdot 10^{-7}$	$4.72 \cdot 10^{-8}$
$129 \times 129$	16.050	$7.92 \cdot 10^{-7}$	$3.33 \cdot 10^{-7}$	0.99121	$4.55 \cdot 10^{-6}$	$1.32 \cdot 10^{-7}$

Table D.3: NACA0012.  $M_\infty = 0.5$  AoA=0°.  $CD_p$  and  $P_a$  for baseline.

	$CD_p (\times 10^4)$	$\theta[CD_p]$	$\bar{\theta}[CD_p]$	$P_a$	$\theta[P_a]$	$\bar{\theta}[P_a]$
$2049 \times 2049$	0.002	$2.59 \cdot 10^{-11}$	*	0.99989	$3.51 \cdot 10^{-11}$	*
$1025 \times 1025$	0.004	$9.07 \cdot 10^{-11}$	*	0.99983	$9.04 \cdot 10^{-10}$	*
$513 \times 513$	0.023	$1.43 \cdot 10^{-10}$	$2.12 \cdot 10^{-11}$	0.99970	$6.51 \cdot 10^{-9}$	$1.25 \cdot 10^{-9}$
$257 \times 257$	0.185	$1.81 \cdot 10^{-9}$	$2.56 \cdot 10^{-10}$	0.99952	$4.61 \cdot 10^{-8}$	$5.82 \cdot 10^{-9}$
$129 \times 129$	1.322	$3.04 \cdot 10^{-8}$	$7.83 \cdot 10^{-9}$	0.99918	$3.74 \cdot 10^{-7}$	$9.56 \cdot 10^{-8}$

Table D.4: NACA0012.  $M_\infty = 0.5$  AoA=0°.  $CD_p$  and  $P_a$  for stretched meshes. The sign \* corresponds to calculations that could not be achieved due to huge CPU and memory requirements.

	$CD_p(\times 10^4)$	$\theta[CD_p]$	$\bar{\theta}[CD_p]$	$P_a$	$\theta[P_a]$	$\bar{\theta}[P_a]$
Limiting value	83.483	—	—	0.99225	—	—
$2049 \times 2049$	83.454	$2.91 \cdot 10^{-11}$	$2.03 \cdot 10^{-11}$	0.99181	$7.72 \cdot 10^{-10}$	$3.94 \cdot 10^{-10}$
$1025 \times 1025$	83.539	$2.93 \cdot 10^{-10}$	$1.87 \cdot 10^{-10}$	0.99101	$6.18 \cdot 10^{-9}$	$3.06 \cdot 10^{-9}$
$513 \times 513$	84.084	$3.63 \cdot 10^{-9}$	$2.35 \cdot 10^{-9}$	0.98833	$3.76 \cdot 10^{-8}$	$2.39 \cdot 10^{-8}$
$257 \times 257$	86.124	$4.64 \cdot 10^{-8}$	$7.30 \cdot 10^{-9}$	0.98364	$8.57 \cdot 10^{-7}$	$1.95 \cdot 10^{-7}$
$129 \times 129$	94.361	$5.80 \cdot 10^{-7}$	$2.83 \cdot 10^{-7}$	0.97425	$9.09 \cdot 10^{-6}$	$7.24 \cdot 10^{-7}$

 Table D.5: NACA0012.  $M_\infty = 0.8$  AoA=0°.  $CD_p$  and  $P_a$  for baseline.

	$CD_p(\times 10^4)$	$\theta[CD_p]$	$\bar{\theta}[CD_p]$	$P_a$	$\theta[P_a]$	$\bar{\theta}[P_a]$
2049x2049	83.410	$1.56 \cdot 10^{-11}$	*	0.99299	$2.58 \cdot 10^{-10}$	*
1025x1025	83.402	$8.34 \cdot 10^{-11}$	*	0.99268	$1.40 \cdot 10^{-9}$	*
$513 \times 513$	83.394	$2.28 \cdot 10^{-10}$	$7.19 \cdot 10^{-11}$	0.99241	$6.91 \cdot 10^{-8}$	$1.85 \cdot 10^{-8}$
$257 \times 257$	83.981	$3.47 \cdot 10^{-9}$	$2.03 \cdot 10^{-9}$	0.99235	$2.78 \cdot 10^{-7}$	$3.46 \cdot 10^{-8}$
$129 \times 129$	88.408	$5.57 \cdot 10^{-8}$	$4.08 \cdot 10^{-8}$	0.99206	$1.81 \cdot 10^{-6}$	$5.06 \cdot 10^{-7}$

 Table D.6: NACA0012.  $M_\infty = 0.8$  AoA=0°.  $CD_p$  and  $P_a$  for stretched meshes. The sign \* corresponds to calculations that could not be achieved due to huge CPU and memory requirements.

## References

- [1] D. Venditti, D. Darmofal, Adjoint error estimation and grid adaptation for functional outputs: Application to quasi-one-dimensional flow, *Journal of Computational Physics* 164 (2000) 204–227.
- [2] D. Venditti, D. Darmofal, Grid adaptation for functional outputs: application to two-dimensional inviscid flows, *Journal of Computational Physics* 176 (2002) 40–69.
- [3] D. Venditti, D. Darmofal, Anisotropic grid adaptation for functional outputs: application to two-dimensional viscous flows, *Journal of Computational Physics* 187 (2003) 22–46.
- [4] C. Johnson, R. Rannacher, M. Boman, Numerics and hydrodynamics theory: towards error control in CFD, *SIAM Journal of Numerical Analysis* 32 (1995) 1058–1079.
- [5] R. Becker, R. Rannacher, *Weighted a posteriori error control in FE methods*, ENUMATH-97, Heidelberg (1998).
- [6] R. Becker, R. Rannacher, An optimal control approach to *a posteriori* error estimation in finite element methods, *Acta Numerica* 10 (2001) 1–102.
- [7] M. Giles, M. Larson, J. Levenstam, E. Süli, Adaptive error control for finite element approximation of lift and drag coefficient in viscous flow, Tech. Rep. NA-97/06, Comlab, Oxford University (1997).
- [8] S. Prudhomme, J. Oden, On goal oriented error estimation for elliptic problems: application to the control of pointwise error, *Computers Method in Applied Mechanics and Engineering* (1999) 313–331.
- [9] M. Larson, T. Barth, *A posteriori* error estimation for discontinuous galerkin approximation of hyperbolic systems, NAS Technical Report. NAS 99-010 (1999).
- [10] L. Machiels, J. Peraire, A. Patera, *A posteriori* finite element output bounds for the incompressible navier-stokes equations; application to a natural convection problem, *Journal of Computational Physics* 172 (2001) 401–425.
- [11] R. Hartmann, P. Houston, Adaptive discontinuous galerkin methods for the compressible euler equations, *Journal of Computational Physics* 182(2) (2002) 508–532.
- [12] T. Leicht, R. Hartmann, Error estimation and anisotropic mesh refinement for 3d laminar aerodynamic flow simulations, *Journal of Computational Physics* 229 (2010) 7344–7360.
- [13] R. Hartmann, J. Held, T. Leicht, Adjoint-based error estimation and adaptive mesh refinement for the rans and (k- $\omega$ ) turbulence model equations, *Journal of Computational Physics* 230 (2011) 4268–4284.
- [14] A. Loseille, A. Dervieux, F. Alauzet, Fully anisotropic goal-oriented mesh adaptation for 3d steady euler equations, *Journal of Computational Physics* 229(2) (2010) 2860–2897.

- [15] R. Dwight, Goal-oriented mesh adaptation using a dissipation based error indicator, *International Journal for Numerical Methods in Fluids* 56 (2007) 1193–2000.
- [16] R. Dwight, Heuristic *a posteriori* estimation of error due to dissipation in finite volume schemes and application to mesh adaptation, *Journal of Computational Physics* 227 (2008) 2845–2863.
- [17] A. Jameson, W. Schmidt, E. Turkel, Numerical solutions of the Euler equations by finite volume methods using runge-kutta time-stepping schemes, *AIAA paper* 81-1259 (1981).
- [18] K. Fidkowski, D. Darmofal, Output-based error estimation and mesh adaptation in computational fluid dynamics: overview and recent results, *AIAA Journal* 49 (2011) 673–694.
- [19] J. Peter, M. Nguyen-Dinh, P. Trontin, Goal oriented mesh adaptation using the total derivative of aerodynamic functions with respect to mesh coordinates, *AIAA Paper* 158 (2012).
- [20] E. Nielsen, M. Park, Using an adjoint approach to eliminate mesh sensitivities in computational design, *AIAA Journal* 44 (2005) 948–53.
- [21] M. Widhalm, J. Brezillon, C. Ilic, T. Leicht, Investigation on adjoint based gradient computations for realistic 3d aero-optimization, *AIAA Paper* 9129 (2010).
- [22] J. Peter, M. Nguyen-Dinh, P. Trontin, Goal oriented mesh adaptation using the total derivative of aerodynamic functions with respect to mesh coordinates. With applications to euler flows, *Computers and Fluids* 66 (2012) 194–214.
- [23] J. Thomson, Z. Warsi, C. Mastin, *Numerical grid generation: Foundations and applications*, Elsevier, Amsterdam 1 (1985) 985.
- [24] S. Spekreijse, Elliptic grid generation based on Laplace equations and algebraic transformations, *Journal of Computational Physics* 118 (1995) 38–61.
- [25] J. Thomson, B. Soni, N. Weatherill, *Handbook of grid generation*, CRC, 1998.
- [26] B. Soni, R. Koomullil, D. Thompson, H. Thornburg, Solution adaptive grid strategies based on point redistribution, *Computer Methods in Applied Mechanics and Engineering* 189 (2000) 1183–1204.
- [27] J. Bin, A. Uzun, Y. Hussaini, Adaptive mesh redistribution method for domains with complex boundaries, *Journal of Computational Physics* 230 (2011) 3178–3204.
- [28] J. Vassberg, A. Jameson, In pursuit of grid convergence, part I: Two dimensional Euler solutions, *AIAA Paper* 4114 (2009).
- [29] J. Vassberg, A. Jameson, In pursuit of grid convergence for two-dimensional Euler solutions, *Journal of Aircraft* 47 (2010) 1152–1166.

### 3.1. MESH QUALIFICATION AND LOCAL ADAPTATIONS APPLIED FOR EULERIAN FLOWS

- [30] L. Cambier, J. Veillot, Status of the *elsA* CFD software for flow simulation and multidisciplinary applications, AIAA Paper 664 (2008).
- [31] A. Rizzi, Computational mesh for transonic airfoils, Numerical methods for the computation of inviscid transonic flows with shock waves.(A 82-12601 02-02) Braunschweig, Friedr. Vieweg und Sohn, 1981, (1981) 222–263.

## 3.2 Enhancement of the elliptic remeshing method

The previous sections were a presentation of the development and the study of more reliable criteria of mesh quality and the use of the local form of these criteria for mesh adaptation. These adaptations were performed using a method based on an elliptic system of PDEs that carried out the adaptations according to the local criterion. The whole study was performed for two-dimensional flows described by the Euler equations. Moreover the meshes used were single block O-type grids. Hence the next step is to extend the study to flows described by the RANS equations and solved on multiblock meshes. The selected test case is a two-dimensional flow around the RAE2822 airfoil and is presented in the next section. The considered meshes are C-type multiblock grids.

It appears that the methodology presented in the previous section cannot be directly applied to these cases because of specificities of this topology. Fortunately the mesh adaptation method can be improved in order to become more robust and efficient. Subsection 3.2 is devoted to the presentation of this mesh adaptation method. Details about the test case are presented in subsection 3.3.1 and the corresponding results are described in subsection 3.3.2.

In Section 3.1 the method was developed and applied in the context of Eulerian flows computation over an O-type mesh. The extension of this method to RANS flows computation over C-type meshes raises three new issues. The first one is the treatment of the anisotropy of the initial mesh that leads to irregular meshes. The second one is the treatment of the mesh zones around walls. The third one is the necessary improvement of the robustness of the remeshing method. All the adopted techniques to solve these issues are now presented.

### 3.2.1 The issue of mesh anisotropy

The initial meshes can exhibit anisotropy in areas of high node density: for example, the mesh nodes at the trailing edge of C-type meshes around an airfoil. These zones of high node density usually arise from the employed mesh generation method. But these refined areas are not necessary of interest for the computation of the functional output. Moreover these mesh locations would lead to low values of the criterion  $\theta$  or  $\bar{\theta}$  because the local characteristic length is taken into account. Thus the control functions  $P_k^{adapt}$  built up for the remeshing would have low values in these regions and hence the complete control functions  $(P_k^{initial} + \epsilon P_k^{adapt})$  would be close to the initial ones. Consequently the initial mesh anisotropy would be conserved from a mesh adaptation iteration to another. This can lead to significant mesh irregularities.

A way to avoid this issue is to define a threshold value for the scalar field  $s$  that is used for the construction of the control function  $P_k^{adapt}$ . For the nodes that present a value of  $s$  lower than the specified threshold value, the complete control function  $P_k^{initial} + \epsilon P_k^{adapt}$  used for the remeshing is set to zero. Then the adaptation method equidistributes the nodes in regions with low values of the sensor.

Nevertheless this treatment is not efficient at every step of the mesh adaptation process. Indeed, mesh areas that are refined at a specific step lead to low values of the sensor at the next step. Thus the control functions would be set to zero in mesh areas refined at the previous step, and operate a mesh coarsening in the corresponding regions. There-

fore this treatment is applied only at the first adaptation step. Subsequently, the control functions are set to the initial one in mesh areas where the sensor values are under the threshold in order to keep the refinement of previous steps.

### 3.2.2 Treatment of the mesh close to solid walls

The mesh node density at the neighbourhood of solid wall is usually important in order to well resolve the boundary layer. The criteria defined in the previous section may not have high enough values and the method may induce an undesirable local coarsening. Moreover it is also often required to have mesh orthogonality at the walls. All these considerations incite to amend the remeshing method in these areas.

First of all, the nodes located near the walls are selected. For all those nodes the treatment described in the previous paragraph is not applied. In other words if the sensor has low values (lower than the specified threshold) then the control functions used for the remeshing is maintained to the initial ones, thus avoiding mesh coarsening. Moreover the control functions associated to the topological directions tangential to the wall are set to the same value in order to locally induce the same displacement and then to keep the mesh orthogonality.

### 3.2.3 The mesh folding issue

Another issue is that the elliptic method *a priori* does not prevent mesh folding especially near corners of the domain (*e.g.* the trailing edge of an airfoil). This behavior was noticed by many authors, for example [66, 64, 19]. In order to have a better understanding of the elliptic remeshing method it is useful to examine the discretization of the system at a particular node  $(i, j, k)$ . Recall that the elliptic mesh generation system of PDEs is the following one (equation (7) of the subsection 3.1):

$$\sum_{i,j=1}^3 g^{ij} x_{\xi^i \xi^j} + \sum_{k=1}^3 g^{kk} P_k x_{\xi^k} = 0 \quad (3.1)$$

As presented in Appendix C of Section 3.1, for single block meshes, the function  $x$  is a mapping from the computational space  $C = [0, 1]^3$  into the physical space  $D \subset \mathbb{R}^3$ . However in the framework of multiblock meshes it is convenient to define the computational space by  $C = [1, N_i] \times [1, N_j] \times [1, N_k]$  in order to simplify the computation of the derivatives at the block interfaces. Actually two adjacent blocks do not necessarily have the same number of mesh planes (or lines in 2D). Hence, using this new definition of  $C$ , the derivatives of  $x$  can be computed by finite differences independently of  $N_i$ ,  $N_j$  and  $N_k$ . Moreover, these considerations do not change the elliptic PDEs presented for single block meshes. Indeed it can be checked that the elliptic PDEs obtained with the new definition of the computational space  $C$  is equivalent to (3.1) using the following change of variables:

$$\begin{aligned} [1, N_i] \times [1, N_j] \times [1, N_k] &\rightarrow [0, 1]^3 \\ (i, j, k) &\mapsto \left( \frac{i-1}{N_i-1}, \frac{j-1}{N_j-1}, \frac{k-1}{N_k-1} \right) \end{aligned}$$

Therefore the first order derivatives are computed using central finite difference formulas:

$$\begin{aligned} x_{\xi^1}(i, j, k) &\simeq \frac{1}{2}(X_{i+1,j,k} - X_{i-1,j,k}) \\ x_{\xi^2}(i, j, k) &\simeq \frac{1}{2}(X_{i,j+1,k} - X_{i,j-1,k}) \\ x_{\xi^3}(i, j, k) &\simeq \frac{1}{2}(X_{i,j,k+1} - X_{i,j,k-1}) \end{aligned}$$

Similarly, the second order central derivatives are computed as follows

$$\begin{aligned} x_{\xi^1\xi^1}(i, j, k) &\simeq X_{i-1,j,k} - 2X_{i,j,k} + X_{i+1,j,k} \\ x_{\xi^2\xi^2}(i, j, k) &\simeq X_{i,j-1,k} - 2X_{i,j,k} + X_{i,j+1,k} \\ x_{\xi^3\xi^3}(i, j, k) &\simeq X_{i,j,k-1} - 2X_{i,j,k} + X_{i,j,k+1} \end{aligned}$$

and the cross derivatives are computed by means of the following formulas

$$\begin{aligned} x_{\xi^1\xi^2}(i, j, k) = x_{\xi^2\xi^1}(i, j, k) &\simeq \frac{1}{4}(X_{i+1,j+1,k} - X_{i+1,j-1,k} + X_{i-1,j-1,k} - X_{i-1,j+1,k}) \\ x_{\xi^2\xi^3}(i, j, k) = x_{\xi^3\xi^2}(i, j, k) &\simeq \frac{1}{4}(X_{i+1,j,k+1} - X_{i+1,j,k-1} + X_{i,j-1,k-1} - X_{i,j-1,k+1}) \\ x_{\xi^1\xi^3}(i, j, k) = x_{\xi^3\xi^1}(i, j, k) &\simeq \frac{1}{4}(X_{i+1,j,k+1} - X_{i+1,j,k-1} + X_{i-1,j,k-1} - X_{i-1,j,k+1}). \end{aligned}$$

From all these relations, the coordinates of the node  $(i, j, k)$  at the step  $n + 1$  is computed using the following equation:

$$\begin{aligned} X_{i,j,k}^{n+1} = &\frac{\bar{g}^{11}(\bar{X}_{\xi^1\xi^1}^n + \frac{1}{2}P_1X_{\xi^1}^n) + \bar{g}^{22}(\bar{X}_{\xi^2\xi^2}^n + \frac{1}{2}P_2X_{\xi^2}^n) + \bar{g}^{33}(\bar{X}_{\xi^3\xi^3}^n + \frac{1}{2}P_3X_{\xi^3}^n)}{\bar{g}^{11} + \bar{g}^{22} + \bar{g}^{33}} + \quad (3.2) \\ &\frac{\bar{g}^{12}X_{\xi^1\xi^2}^n + \bar{g}^{13}X_{\xi^1\xi^3}^n + \bar{g}^{23}X_{\xi^2\xi^3}^n}{\bar{g}^{11} + \bar{g}^{22} + \bar{g}^{33}} \end{aligned}$$

where  $\bar{g}^{ij}$  are the contravariant base vectors expressed with the covariant base vectors

$$\begin{aligned} \bar{g}^{11} &= g_{22}g_{33} - g_{23}^2 & ; & \quad \bar{g}^{12} = g_{13}g_{23} - g_{12}g_{33} \\ \bar{g}^{13} &= g_{12}g_{23} - g_{13}g_{22} & ; & \quad \bar{g}^{22} = g_{11}g_{33} - g_{13}^2 \\ \bar{g}^{23} &= g_{13}g_{12} - g_{11}g_{23} & ; & \quad \bar{g}^{33} = g_{11}g_{22} - g_{12}^2, \end{aligned}$$

and where  $X_{\xi^l}$  stands for the discretized expression of  $x_{\xi^l}$ . In the same way  $X_{\xi^l\xi^m}$  is the discretization of  $x_{\xi^l\xi^m}$  and finally:

$$\bar{X}_{\xi^1\xi^1} = \frac{X_{i-1,j,k} + X_{i+1,j,k}}{2} \quad ; \quad \bar{X}_{\xi^2\xi^2} = \frac{X_{i,j-1,k} + X_{i,j+1,k}}{2} \quad ; \quad \bar{X}_{\xi^3\xi^3} = \frac{X_{i,j,k-1} + X_{i,j,k+1}}{2}$$

The first term of the equation (3.2) is the barycenter of the points  $(\bar{X}_{\xi^1\xi^1}^n + \frac{1}{2}P_1X_{\xi^1}^n)$ ,  $(\bar{X}_{\xi^2\xi^2}^n + \frac{1}{2}P_2X_{\xi^2}^n)$  and  $(\bar{X}_{\xi^3\xi^3}^n + \frac{1}{2}P_3X_{\xi^3}^n)$  with the respective weights  $\bar{g}^{11}$ ,  $\bar{g}^{22}$  and  $\bar{g}^{33}$  as illustrated on the following figures in two dimensions.

### 3.2. ENHANCEMENT OF THE ELLIPTIC REMESHING METHOD

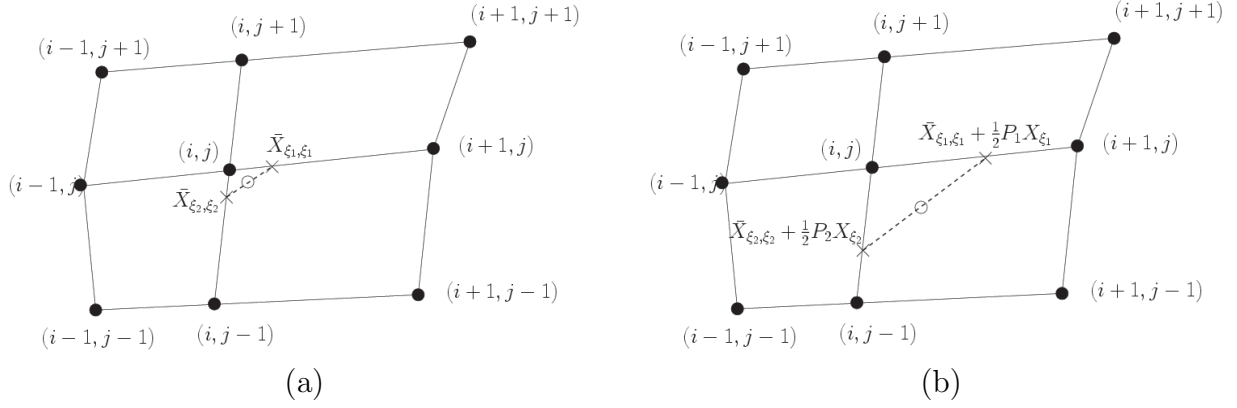


Figure 3.1: (a) Position of the new node without control functions ; (b) Position of the new node with control functions

Moreover the contravariant base vectors  $\bar{g}^{ij}$  are non negative thanks to the Cauchy-Schwarz inequality. Hence this barycenter is to stay inside the convex hull of the points  $(\bar{X}_{\xi^1 \xi^1}^n + \frac{1}{2}P_1 X_{\xi^1}^n)$ ,  $(\bar{X}_{\xi^2 \xi^2}^n + \frac{1}{2}P_2 X_{\xi^2}^n)$  and  $(\bar{X}_{\xi^3 \xi^3}^n + \frac{1}{2}P_3 X_{\xi^3}^n)$ . Finally if the control functions  $P_k$  belong to  $[-1, 1]$  then these points are inside the convex hull of the nodes  $(i-1, j, k)$ ,  $(i+1, j, k)$ ,  $(i, j-1, k)$ ,  $(i, j+1, k)$ ,  $(i, j, k-1)$  and  $(i, j, k+1)$ .

Besides it has been observed that the second term of equation (3.2) that depends on the crossed derivatives  $X_{\xi^1 \xi^2}^n$ ,  $X_{\xi^1 \xi^3}^n$  and  $X_{\xi^2 \xi^3}^n$ , has most often low values in comparison to the first term and can be neglected [19]. Therefore the position of the node  $X_{ijk}^n$  is essentially defined by the first term of equation (3.2) so we impose to  $P_k$  values to be in  $[-1, 1]$  in order to avoid mesh folding inside the volume mesh.

The nodes located on solid walls are projected on the surface in order to ensure mesh orthogonality of the first layer of mesh. However some nodes may have to be fixed during the adaptation process to avoid a change of the solid object shape (*e.g.* the trailing edge of an airfoil). Unfortunately mesh folding can occur near these nodes even if the control functions are bounded as illustrated on the following figure.

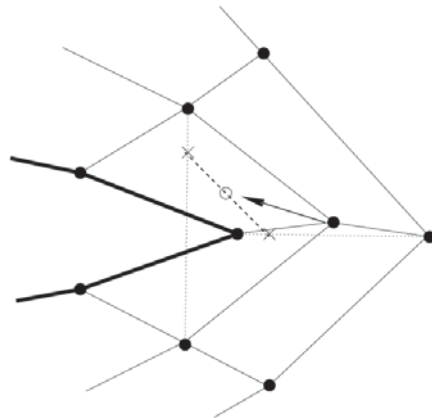


Figure 3.2: Configuration that could lead to mesh folding with the elliptic remeshing method

A way to reduce this effect and to improve the robustness of the method was to impose bounds on the allowable variations of the control functions.

### 3.2.4 Construction of the control functions for mesh adaptation

The elliptic method used for mesh adaptation in 3.1 presents a user specified constant weight factor  $\epsilon$ . The generated meshes depend on this constant and it appeared to be useful to determine its value automatically. In this context, a different constant is built for each topological direction. The constant is chosen such that  $-0.7 \leq P_k^{adapt} \leq 0.7, \forall 1 \leq k \leq 3$  and such that there exists a node for which  $P_k^{adapt}$  is 0.7 or  $-0.7$ .

## 3.3 Local adaptations for RANS flows

The present section is devoted to the application of this more efficient remeshing methodology for a two-dimensional RANS flow.

### 3.3.1 RAE2822 test case

The selected two-dimensional test case is a turbulent RANS flow over an RAE2822. The Spalart-Allmaras turbulence model has been used and the linearization has been done with the frozen  $\mu_t$  assumption. The upstream Mach number is  $M_\infty = 0.725$ , the Reynolds number per meter is  $Re.m^{-1} = 6.5 \times 10^6$  and the angle of attack is  $\alpha = 2.466^\circ$ . This test case is considered in [75] for anisotropic mesh adaptations. The flow presents a shock wave located near the mid-chord position of the airfoil on the upper surface. The iso Mach number of iso  $-C_p$  are illustrated on the following figures.

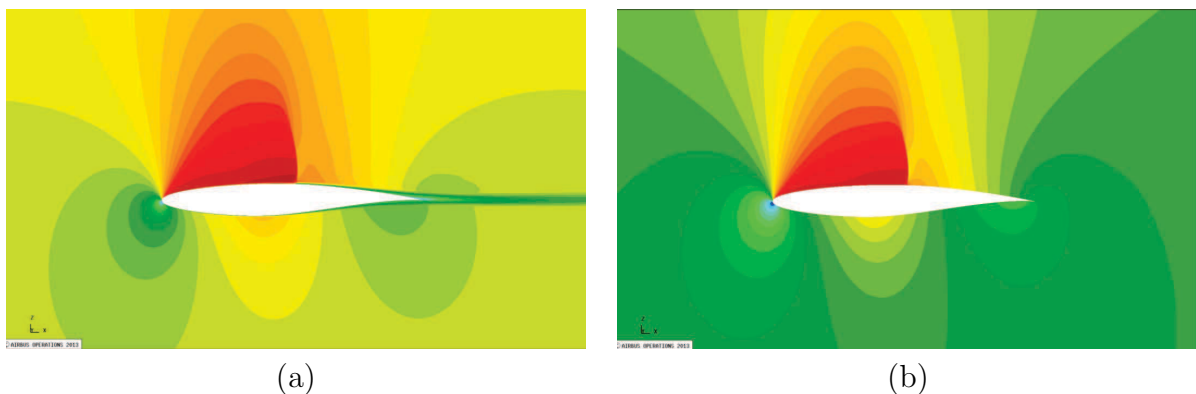


Figure 3.3: RAE2822.  $M_\infty = 0.725$ .  $Re.m^{-1} = 6.5 \times 10^6$ . AoA =  $2.466^\circ$ . (a) Iso Mach number ; (b) Iso  $-C_p$

A hierarchy of five embedded meshes was built (size ranging from 16,705 to 4,199,425 nodes) in order to evaluate reference values for the outputs. These meshes are structured C-type grids such that the far-field boundary is placed at a hundred chords. A far-field drag analysis was carried out in order to assess the quality of the solutions.

### 3.3. LOCAL ADAPTATIONS FOR RANS FLOWS

The considered functions of interest were the drag coefficient  $Cd$  and the pressure lift coefficient  $CL_p$ . Table 3.1 summarizes the values of these outputs on this mesh hierarchy with the near-field approach. The values obtained on the two finest meshes are in agreement with the reference values provided in [75].

Mesh size	$CL_p$	$Cd (\times 10^{-4})$	$CD_p (\times 10^{-4})$	$CD_f (\times 10^{-4})$
Limiting value	0.75615	118.60	60.42	58.18
$4097 \times 1025$	0.75571	118.51	60.32	58.19
$2049 \times 513$	0.75446	118.33	60.09	58.24
$1025 \times 257$	0.75029	118.84	59.96	58.88
$513 \times 129$	0.73950	123.93	62.02	61.91
$257 \times 65$	0.71837	142.61	74.36	68.26

Table 3.1: RAE2822.  $M_\infty = 0.725$ .  $Re.m^{-1} = 6.5 \times 10^6$ .  $AoA = 2.466^\circ$ .  $CL_p$ ,  $Cd$ ,  $CD_p$  and  $CD_f$  on the mesh hierarchy.

The values of the functional outputs  $Cd$  and  $CL_p$  are also summarized as plots on the following figures.

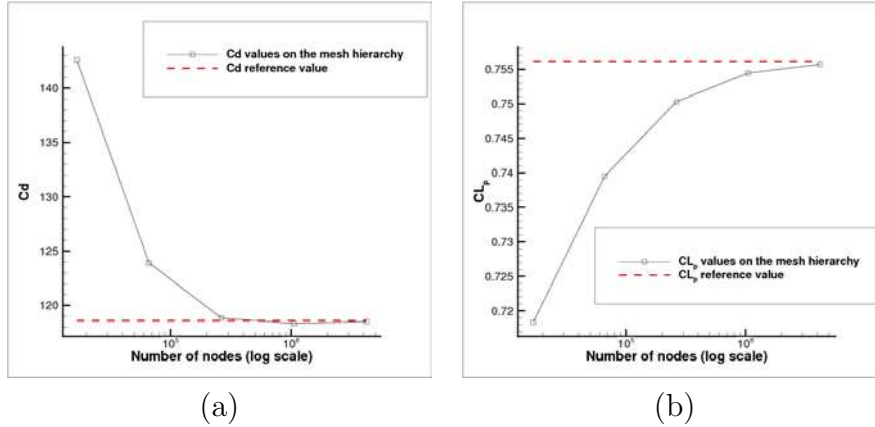


Figure 3.4: RAE2822.  $M_\infty = 0.725$ .  $Re.m^{-1} = 6.5 \times 10^6$ .  $AoA = 2.466^\circ$ . (a)  $Cd$  values ; (b)  $CL_p$  values

The table 3.2 summarizes the output values with the far-field approach.

Mesh size	$Cd (\times 10^{-4})$	$CD_w (\times 10^{-4})$	$CD_{vp} (\times 10^{-4})$	$CD_{sp,irr} (\times 10^{-4})$	$CD_{sp,rev} (\times 10^{-4})$
$4097 \times 1025$	114.27	14.30	41.78	0.19	4.04
$2049 \times 513$	114.16	13.90	42.01	0.21	3.96
$1025 \times 257$	114.50	12.69	42.92	0.60	3.74
$513 \times 129$	117.66	10.09	45.66	2.95	3.32
$257 \times 65$	125.07	6.89	49.92	15.07	2.47

Table 3.2: RAE2822.  $M_\infty = 0.725$ .  $Re.m^{-1} = 6.5 \times 10^6$ .  $AoA = 2.466^\circ$ . Far-field drag breakdown on the mesh hierarchy.

The criteria  $\theta$  and  $\bar{\theta}$  introduced in section 3.1 have been computed on the mesh hierarchy. Table 3.3 summarizes these values. The same behavior is observed in comparison to the results obtained with Eulerian flows.

Mesh size	$\theta[CL_p]$	$\bar{\theta}[CL_p]$	$\theta[Cd]$	$\bar{\theta}[Cd]$
$4097 \times 1025$	$1.4377 \cdot 10^{-12}$	*	$3.9035 \cdot 10^{-9}$	*
$2049 \times 513$	$1.5534 \cdot 10^{-11}$	$9.5707 \cdot 10^{-12}$	$1.7117 \cdot 10^{-8}$	$1.1343 \cdot 10^{-8}$
$1025 \times 257$	$1.0175 \cdot 10^{-10}$	$6.6908 \cdot 10^{-11}$	$7.5014 \cdot 10^{-8}$	$4.9641 \cdot 10^{-8}$
$513 \times 129$	$7.7841 \cdot 10^{-10}$	$5.2253 \cdot 10^{-10}$	$4.2915 \cdot 10^{-7}$	$2.9110 \cdot 10^{-7}$
$257 \times 65$	$6.1390 \cdot 10^{-9}$	$4.0369 \cdot 10^{-9}$	$3.2756 \cdot 10^{-6}$	$2.2802 \cdot 10^{-6}$

Table 3.3: RAE2822.  $M_\infty = 0.725$ .  $Re.m^{-1} = 6.5 \times 10^6$ . AoA =  $2.466^\circ$ .  $\theta$  and  $\bar{\theta}$  values for both  $Cd$  and  $CL_p$  on the mesh hierarchy. The sign \* corresponds to calculations that could not be achieved due to huge CPU and memory requirements.

These values are summarized as plots on the following figures.

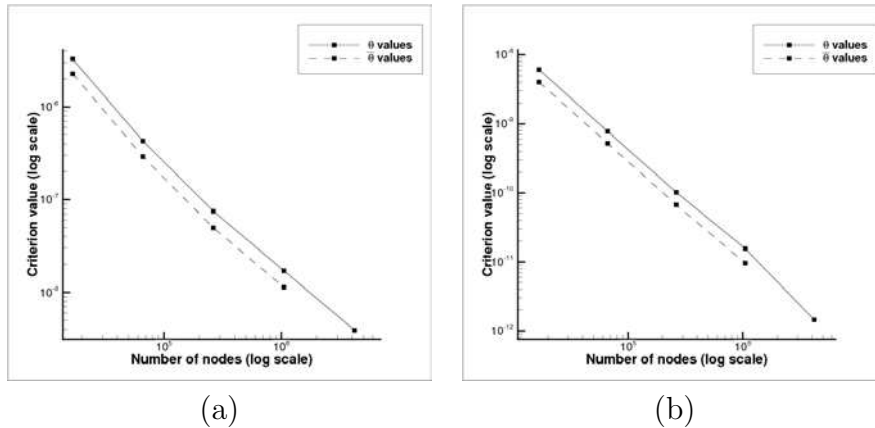


Figure 3.5: RAE2822.  $M_\infty = 0.725$ .  $Re.m^{-1} = 6.5 \times 10^6$ . AoA =  $2.466^\circ$ . (a)  $\theta$  and  $\bar{\theta}$  values for  $Cd$ ; (b)  $\theta$  and  $\bar{\theta}$  values for  $CL_p$

### 3.3.2 Mesh adaptations

The  $513 \times 129$  mesh was adapted to the computation of the outputs. The initial mesh is illustrated on figure 3.6. The local criterion used for these adaptations is  $\bar{\theta}_J(i, j)$ . It appeared that a good termination criterion is to interrupt the process whenever the value of the criterion  $\bar{\theta}_J$  increases from its value at the previous step.

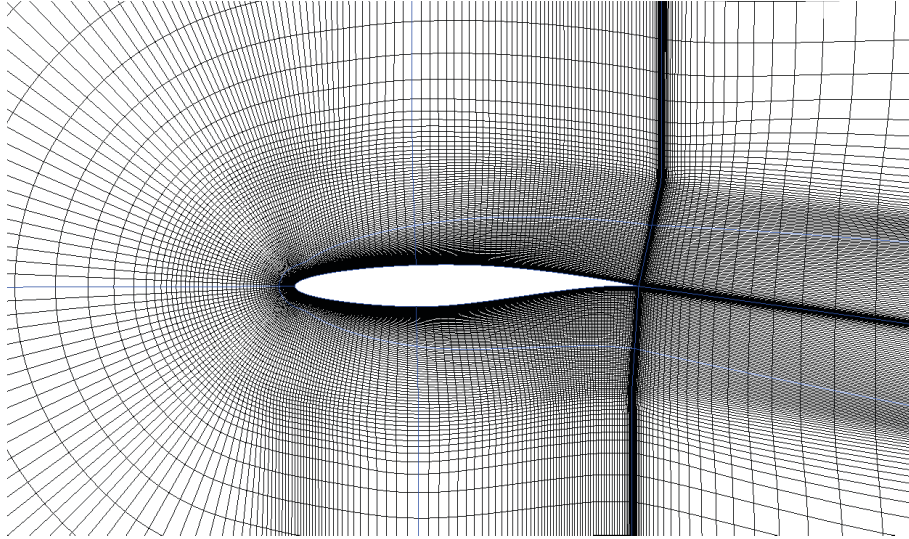
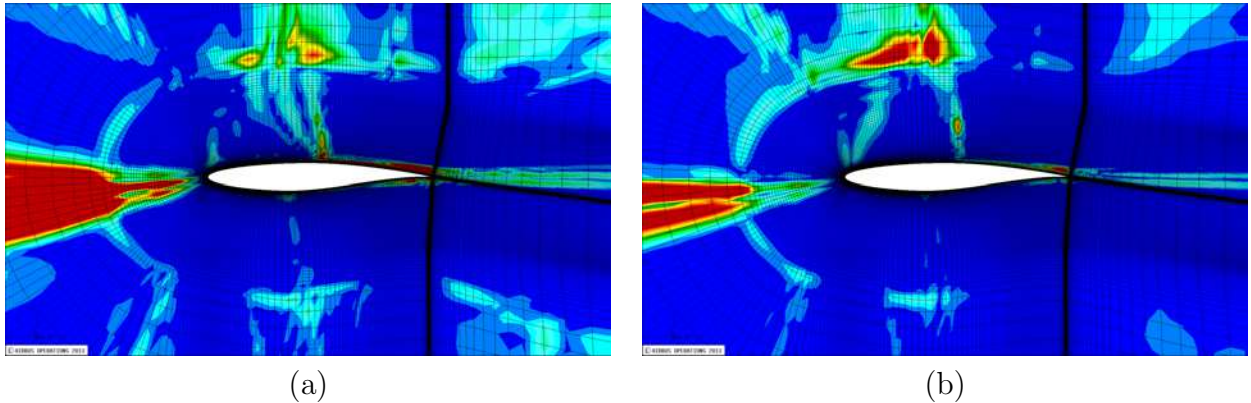


Figure 3.6: Initial C-type mesh around the RAE2822 airfoil

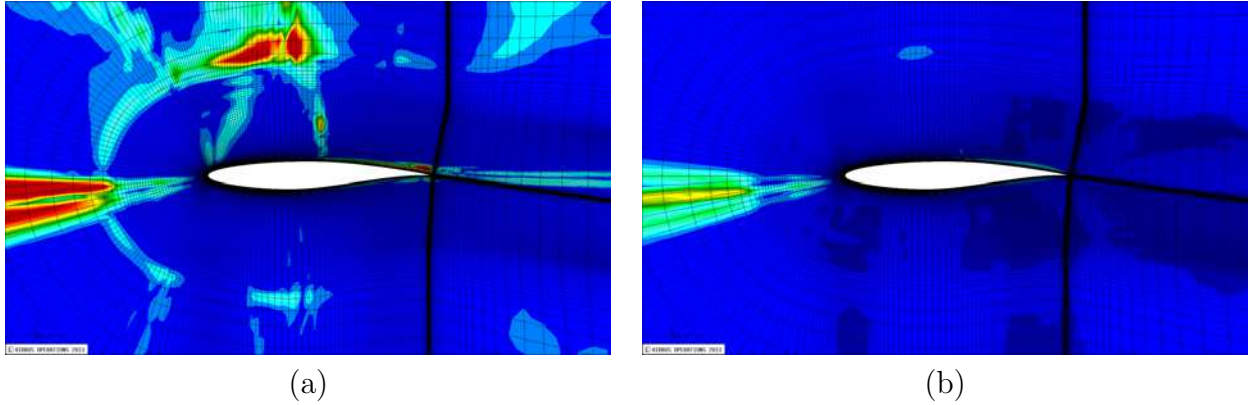
### Criterion $\bar{\theta}$ on the initial mesh

The following figures illustrate the criterion  $\bar{\theta}$  on the initial mesh for both  $CL_p$  (figure 3.7(a)) and  $Cd$  (figure 3.7(b)).

Figure 3.7: (a) Criterion  $\bar{\theta}[CL_p]$  ; (b) Criterion  $\bar{\theta}[Cd]$ 

It can be noticed that for both functions, the sensor detects the zones upstream the airfoil. The shock wave and the wake areas are also detected but with a lower intensity. Moreover the mesh nodes located above the shock are also detected. This is the area where the cell size starts to increase from the airfoil towards the far-field.

The drag coefficient  $Cd$  is the sum of the pressure drag coefficient  $CD_p$  and the friction drag coefficient  $CD_f$ . The following figures illustrates the criterion  $\bar{\theta}$  on the initial mesh for these two components.


 Figure 3.8: (a) Criterion  $\bar{\theta}[CD_p]$  ; (b) Criterion  $\bar{\theta}[CD_f]$ 

We notice that the  $\bar{\theta}[Cd]$  values (figure 3.7(b)) are quite close to the  $\bar{\theta}[CD_p]$  values (figure 3.8(a)). The criterion  $\bar{\theta}[CD_f]$  actually only detects the upstream and the nodes close to the airfoil.

### Mesh adaptation for $Cd$

The initial mesh has been adapted in three iterations. The initial  $Cd$  value,  $123.93 \cdot 10^{-4}$ , is to be compared with the limiting value of  $118.60 \cdot 10^{-4}$ . The final  $Cd$  value is  $119.41 \cdot 10^{-4}$  corresponding to a reduction of 85% of the near-field drag estimation. The limiting value of  $CL_p$  is 0.75615. The computed  $CL_p$  value on the adapted mesh is 0.74194 to be compared to 0.73950 on the initial one. We hence notice an indirect improvement of the estimation of this output. Moreover we also notice that both  $CD_p$  value and  $CD_f$  value are improved. The values computed with the near-field approach are summarized in the following table.

Mesh	$CL_p$	$Cd (\times 10^{-4})$	$CD_p (\times 10^{-4})$	$CD_f (\times 10^{-4})$
Limiting value	0.75615	118.60	60.42	58.18
Fine mesh	0.75571	118.51	60.32	58.19
Initial mesh	0.73950	123.93	62.02	61.91
Adapted mesh	0.74194	119.41	60.90	58.51

 Table 3.4: RAE2822. Adaptation for  $Cd$ . Near-field drag breakdown.

A slight increase of the spurious reversible drag was observed on the adapted mesh ( $CD_{sp,rev} = 3.42 \cdot 10^{-4}$  to be compared to the initial mesh value  $CD_{sp,rev} = 3.32 \cdot 10^{-4}$ ). However this component of the spurious drag is proportional to the square of  $CL_p$  that has been increased on the adapted mesh. The spurious irreversible drag is almost the same on the adapted mesh ( $CD_{sp,irr} = 2.84 \cdot 10^{-4}$ ) as on the initial mesh ( $CD_{sp,irr} = 2.95 \cdot 10^{-4}$ ). And the corresponding far-field drag value is improved on the adapted mesh in comparison to the initial mesh value.

### 3.3. LOCAL ADAPTATIONS FOR RANS FLOWS

The values computed with the far-field approach are summarized in the following table.

Mesh	$Cd$ ( $\times 10^4$ )	$CD_w$ ( $\times 10^4$ )	$CD_{vp}$ ( $\times 10^4$ )	$CD_{sp,irr}$ ( $\times 10^4$ )	$CD_{sp,rev}$ ( $\times 10^4$ )
Fine mesh	114.27	14.30	41.78	0.19	4.04
Initial mesh	117.66	10.09	45.66	2.95	3.32
Adapted mesh	113.16	10.52	44.13	2.84	3.42

Table 3.5: RAE2822. Adaptation for  $Cd$ . Far-field drag breakdown.

We observe an improvement of the viscous drag coefficient  $CD_v$  (that is the sum of  $CD_f$  and  $CD_{vp}$ ) from 107.57 to 102.64 in comparison to the value obtained on the fine mesh (99.97). However the wave drag is not improved as well (from 10.09 to 10.52) in comparison to the value obtained on the fine mesh (14.30). It appears that even if the adaptation leads to an increase of the mesh density close to the shock, it is not enough to compute accurately the wave drag. This is the reason why the drag coefficient computed with the far-field approach is lower for the adapted mesh than for the fine mesh. The adaptation essentially succeeds in improving the viscous drag component of the far-field drag breakdown.

The method leads to a reduction of the criteria values. The value of the criterion  $\bar{\theta}[Cd]$  decreases from  $2.9110 \cdot 10^{-7}$ , for the initial mesh, to  $2.4371 \cdot 10^{-7}$  for the adapted mesh. Similarly, the criterion  $\theta[Cd]$  decreases from  $4.2915 \cdot 10^{-7}$  to  $3.6385 \cdot 10^{-7}$ . We also noticed a reduction of the corresponding criteria for  $CL_p$ . The value of the criterion  $\bar{\theta}[CL_p]$  decreases from  $5.2251 \cdot 10^{-10}$  to  $4.2025 \cdot 10^{-10}$  and  $\theta[CL_p]$  decreases from  $7.7840 \cdot 10^{-10}$  to  $6.6698 \cdot 10^{-10}$ . The evolution of  $Cd$  and  $\bar{\theta}[Cd]$  during the adaptation process is plotted on the following figures.

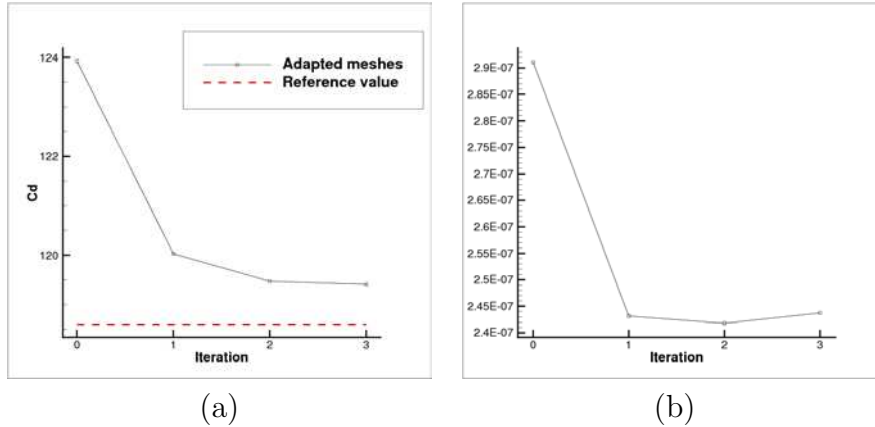
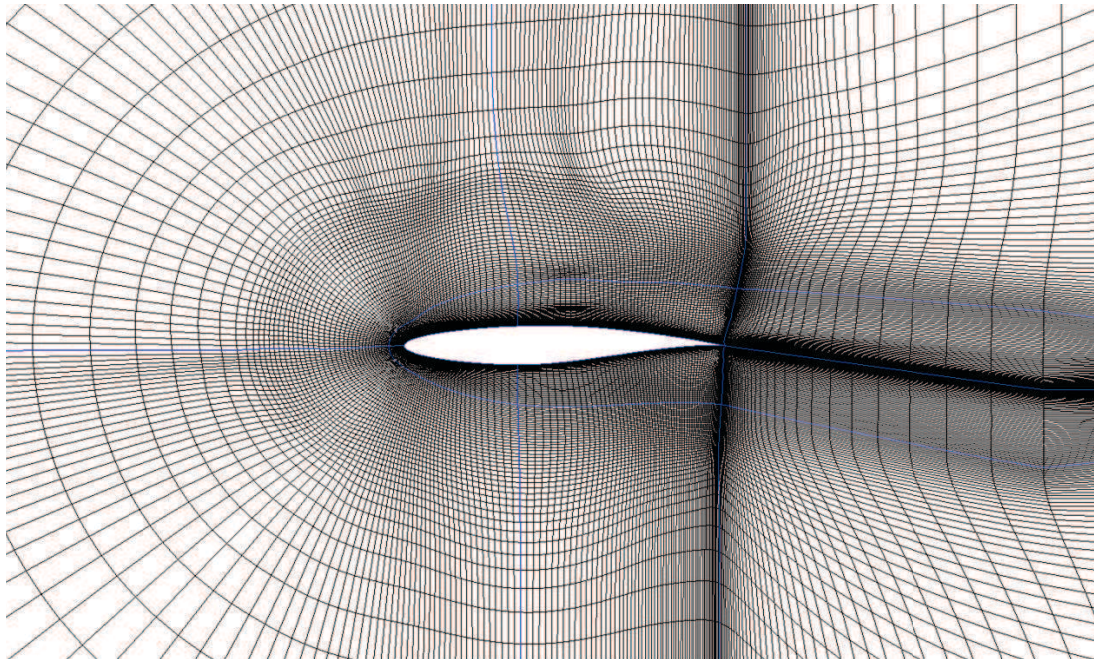
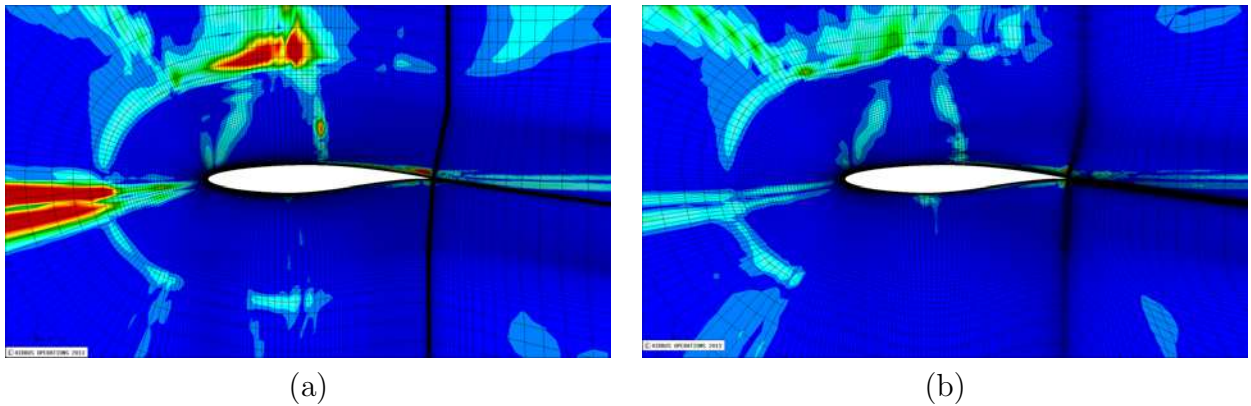


Figure 3.9: Evolution of  $Cd$  and  $\bar{\theta}[Cd]$  during the adaptation process (a)  $Cd$  values (b) Criterion  $\bar{\theta}[Cd]$

Figure 3.10 presents the adapted mesh. The method has led to an important refinement around the airfoil in particular at the leading edge. The wake has also been refined as well as the shock location.

Figure 3.10: Adapted mesh for  $Cd$ 

The following figures illustrate the criterion  $\bar{\theta}[Cd]$  on the initial mesh (figure 3.11(a)) and on the adapted one with the same scale (figure 3.11(b)). A reduction of the sensor values is noticed. This is obviously in agreement with the reduction of the global criterion between the initial mesh and the adapted mesh.

Figure 3.11: (a) Criterion  $\bar{\theta}[Cd]$  on the initial mesh ; (b) Criterion  $\bar{\theta}[Cd]$  on the adapted mesh

### Mesh adaptation for $CL_p$

The initial mesh has been adapted in four steps. The initial  $CL_p$  value is 0.73950 to be compared to the limiting value of 0.75615. The  $CL_p$  value on the adapted mesh is 0.74775, it corresponds to a reduction of 50% of the error. Moreover this value is close to the one obtained on the mesh of size  $1025 \times 257$ , equal to 0.75029. An improvement of the  $Cd$  value was noticed ( $123.93 \cdot 10^{-4}$  on the initial mesh and  $119.99 \cdot 10^{-4}$  on the adapted

### 3.3. LOCAL ADAPTATIONS FOR RANS FLOWS

one, to be compared with the limiting value of  $118.60 \cdot 10^{-4}$ ). The values computed with the near-field approach are summarized in the following table.

Mesh	$CL_p$	$Cd (\times 10^{-4})$	$CD_p (\times 10^{-4})$	$CD_f (\times 10^{-4})$
Limiting value	0.75615	118.60	60.42	58.18
Fine mesh	0.75571	118.51	60.32	58.19
Initial mesh	0.73950	123.93	62.02	61.91
Adapted mesh	0.74775	119.99	61.44	58.54

Table 3.6: RAE2822. Adaptation for  $CL_p$ . Near-field drag breakdown.

As observed for the adaptation for  $Cd$ , the spurious reversible drag has been slightly increased (from  $3.32 \cdot 10^{-4}$  to  $3.57 \cdot 10^{-4}$ ). However we observed a slight reduction of the irreversible drag whose value is  $2.49 \cdot 10^{-4}$  on the adapted mesh and  $2.95 \cdot 10^{-4}$  on the initial mesh. Thus the corresponding far-field drag estimate is more accurate on the adapted mesh. The values computed with the far-field approach are summarized in the following table. The same conclusions can be done in comparison to the mesh adaptation for  $Cd$ .

Mesh	$Cd (\times 10^{-4})$	$CD_w (\times 10^{-4})$	$CD_{vp} (\times 10^{-4})$	$CD_{sp,irr} (\times 10^{-4})$	$CD_{sp,rev} (\times 10^{-4})$
Fine mesh	114.27	14.30	41.78	0.19	4.04
Initial mesh	117.66	10.09	45.66	2.95	3.32
Adapted mesh	113.93	10.99	44.39	2.49	3.57

Table 3.7: RAE2822. Adaptation for  $CL_p$ . Far-field drag breakdown.

The criteria values have decreased during the adaptation process. The value of the criterion  $\bar{\theta}[CL_p]$  decreased from  $5.2251 \cdot 10^{-10}$ , for the initial mesh, to  $3.6104 \cdot 10^{-10}$  for the adapted mesh. In the same way,  $\bar{\theta}[Cd]$  decreased from  $2.9110 \cdot 10^{-7}$  to  $2.3458 \cdot 10^{-7}$ . Moreover, the criterion  $\theta[CL_p]$  decreased from  $7.7840 \cdot 10^{-10}$  to  $5.8779 \cdot 10^{-10}$  and the criterion  $\theta[Cd]$  decreased from  $4.2915 \cdot 10^{-7}$  to  $3.5135 \cdot 10^{-7}$ . The evolution of  $CL_p$  and  $\bar{\theta}[CL_p]$  during the adaptation process is plotted on the following figure.

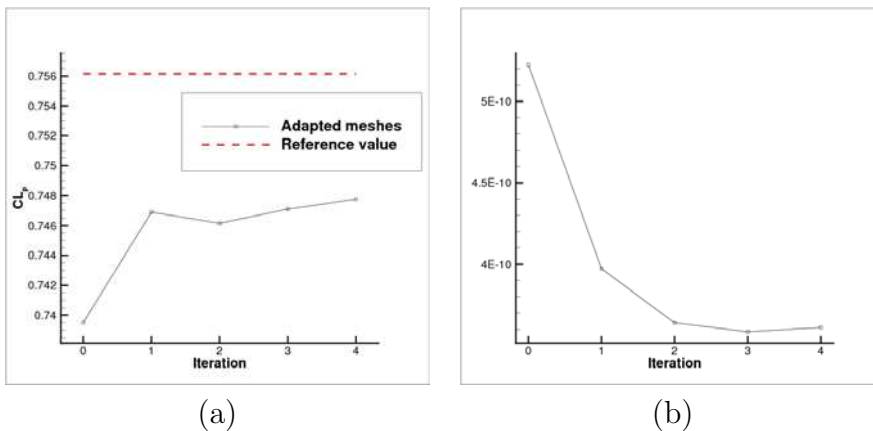


Figure 3.12: Evolution of  $CL_p$  and  $\bar{\theta}[CL_p]$  during the adaptation process (a)  $CL_p$  values (b) Criterion  $\bar{\theta}[CL_p]$

Figure 3.13 illustrates the adapted mesh. As in the previous case, the method has led to a refinement around the airfoil especially at the leading edge. The wake was also refined.

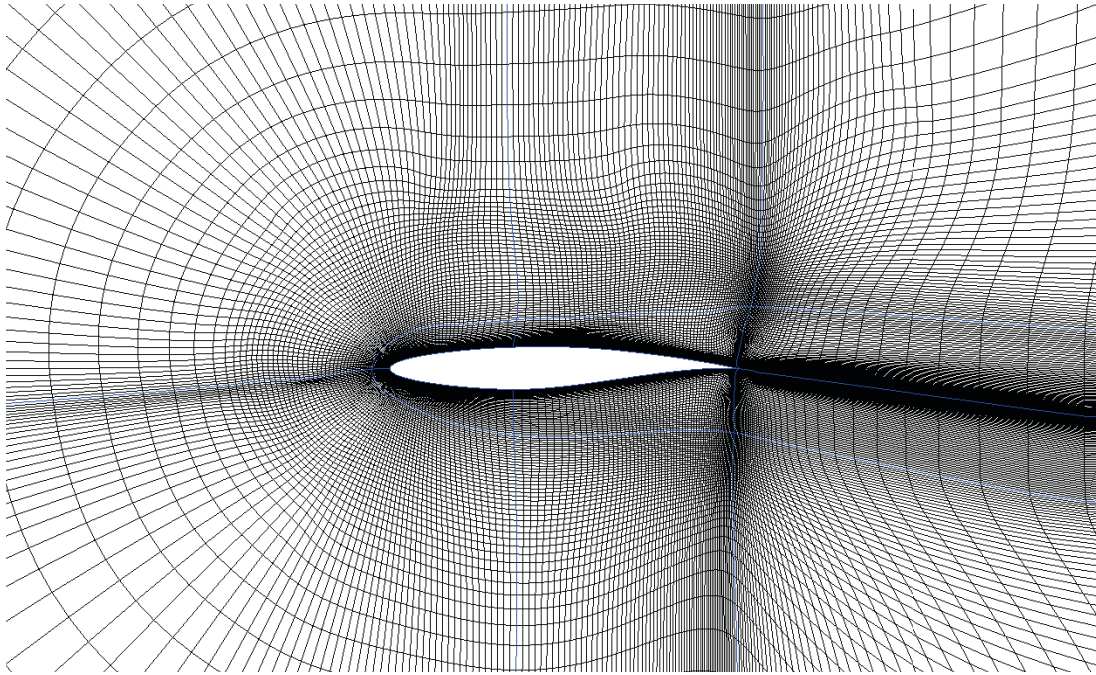


Figure 3.13: Adapted mesh for  $CL_p$

The following figures illustrate the criterion  $\bar{\theta}[CL_p]$  on the initial mesh (figure 3.14(a)) and on the adapted one with the same scale (figure 3.14(b)). As for the previous case, we notice a reduction of the sensor values between the initial mesh and the adapted mesh.

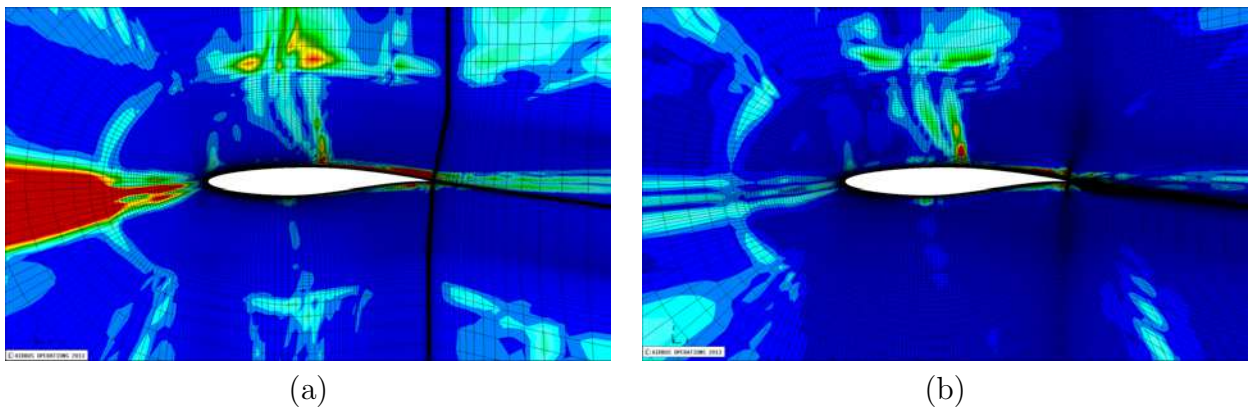


Figure 3.14: (a) Criterion  $\bar{\theta}[CL_p]$  on the initial mesh ; (b) Criterion  $\bar{\theta}[CL_p]$  on the adapted mesh

However, one can notice a slight increase of  $\bar{\theta}[CL_p]$  values at several nodes close to the shock location in comparison to corresponding values on the initial mesh. This shows up the difficulty to achieve a reduction of the criterion values for all mesh nodes using a node displacement remeshing method.

### 3.3.3 The remeshing method influence

At this step of the work, an important remark has to be done about the impact of the remeshing method on the adaptation process efficiency. This chapter presented a classical remeshing strategy based on an elliptic system of PDEs. This remeshing strategy has been used in order to perform local mesh refinement. As expected, this approach was observed to be more efficient than the one used in the previous chapter that required both a mesh parametrization and a functional output that is monotonically affected by the numerical dissipation. This was already noticed in the previous chapter (section 2.3.2). Nevertheless the elliptic remeshing method presents several drawbacks, as mentioned in the section 3.2. These drawbacks have been identified and solutions have been proposed for application to two-dimensional test cases. The use of structured meshes motivated the choice to use remeshing methods by node displacement. Moreover the choice to use the elliptic method was motivated by the ability to implement it quickly according to the tools available in this thesis. However we can notice that many other strategies exist, even for structured meshes, for example using B-splines.

## 3.4 Conclusions

The results of chapter 2 have proved that the derivative  $dJ/dX$  can be efficiently used for goal oriented mesh adaptations and also to define scalar criteria of mesh quality. Nevertheless these results also showed that the remeshing strategies have a significant impact on the method efficiency and that the irregularities of the field  $dJ/dX$  prevent a direct use for mesh adaptation or qualification. Following these remarks an elliptic mesh adaptation method has been used in order to allow more local refinement and thus to improve the remeshing efficiency. In the same way, a new criterion that takes into account the regularity of the field  $dJ/dX$  through a spatial mean using the local admissible node displacements has been developed and studied. It has appeared that a satisfactory correlation exists between the accuracy of the function estimates and the low values of this criterion. Nevertheless it also appeared that, actually, the connection is not perfect. This may be due to the fact that the criterion  $\bar{\theta}$  is based on a Taylor's expansion of  $J$  only at the first order. However the criterion appeared to be accurate enough for being used for mesh adaptation.

The approach has been applied at first to Eulerian flow computations. The adaptations performed in this case have led to improvements of the output values and also to a reduction of the criteria values. The methodology was then applied to a RANS flow using a multiblock topology. It was necessary to improve the remeshing method in order to take into account several specificities of such a test case. In particular the treatment of the possible anisotropy of the initial mesh and the treatment of the mesh near the solid walls. This method has provided meshes leading to more accurate estimations of the functions of interest with a reduction of the global criterion  $\bar{\theta}_J$ . A reduction of the corresponding local criterion was also observed during the mesh adaptation process.

In addition, a study of the asymptotic behavior of  $dJ/dX$  as the characteristic cell length decreases has been carried out in the case of two-dimensional Eulerian flows and finite volume scheme with two-point and four-point flux formulas. It has been shown that  $dJ/dX$  can be approximated on a current grid using computations performed on a

## CHAPTER 3. MESH QUALIFICATION AND LOCAL ADAPTATIONS

coarser one. The interest is that the proposed criteria for goal oriented mesh quality can be based on coarser mesh flow solution and adjoint calculation. These properties have been studied for a particular test case and deserve a deeper study.

The next step is the application of this methodology to three-dimensional industrial cases. This is the topic of the next chapter. The objective being to demonstrate that the proposed criteria can be successfully used on three-dimensional cases with complex geometries.

### 3.4. CONCLUSIONS

# Chapitre 4

## Application à des cas industriels tridimensionnels

### Résumé :

Le chapitre précédent a montré qu'une méthode elliptique de remaillage peut être efficacement utilisée pour effectuer des adaptations locales de maillages. Cette méthode a été appliquée avec succès pour des écoulements bidimensionnels décrits par les équations d'Euler et RANS. L'étape suivante consiste à mettre en œuvre cette méthode pour des cas tests tridimensionnels d'intérêt industriel. Le cas test considéré pour l'application de la méthode d'adaptation de maillages est un écoulement autour de la configuration XRF-1. Le critère local a également été calculé sur un maillage autour de la configuration "Generic Modern Aircraft" pour différentes fonctions d'intérêt afin d'illustrer l'efficacité de ce critère pour détecter les zones d'intérêt d'un maillage pour le calcul de fonctions sur des configurations complexes réalistes.

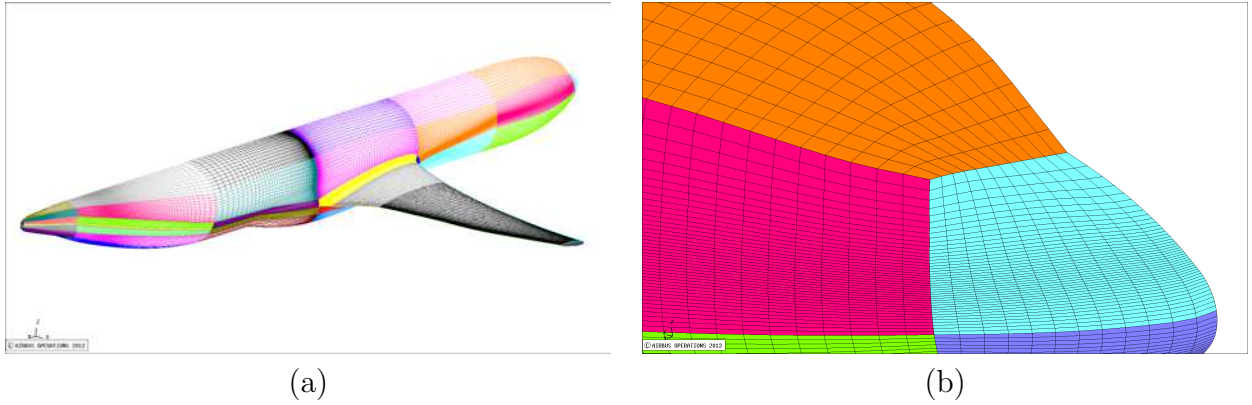
### 1. Adaptation de maillage autour de la configuration XRF-1

#### 1.1 Cas test et maillages

La configuration XRF-1 est composée d'une aile et d'un fuselage. L'écoulement considéré dans cette étude autour de cette configuration est un écoulement transsonique de fluide visqueux où le nombre de Reynolds par mètre est  $Re.m^{-1} = 7800000$ , le nombre de Mach à l'infini est  $M_\infty = 0,83$  et l'angle d'attaque est  $\alpha = 2,607^\circ$ . Le schéma numérique utilisé est le schéma de Roe [58] étendu à l'ordre deux par la méthode MUSCL [70] et le limiteur de pente est celui de van Albada [69].

Les fonctions d'intérêt considérées sont le coefficient de traînée de pression  $CD_p$  et le coefficient de portance de pression  $CL_p$ . Comme pour les cas précédents, une hiérarchie de maillages a été construite afin d'évaluer des valeurs de référence pour les fonctions ainsi que pour étudier le comportement des valeurs de critères. La hiérarchie de maillages a été construite en suivant les recommandations données dans [34]. Elle est composée de cinq maillages dont la taille est de  $3,2M$  de points et 143 blocs pour le plus grossier et  $100M$  de points et 334 blocs pour le plus fin. Les figures suivantes illustrent le maillage à la peau.

## 4. APPLICATION À DES CAS INDUSTRIELS TRIDIMENSIONNELS



- (a) Décomposition des blocs à la peau.  
 (b) Interface de blocs au niveau de la pointe avant.

### 1.2 Prise en compte des particularités 3D

Contrairement aux cas bidimensionnels considérés jusqu'à présent, ce cas présente des spécificités topologiques qui imposent un traitement particulier. Bien que tous les raccords de bloc sont coïncidents, certains d'entre-eux sont particuliers comme illustré sur la figure (b) précédente. Ainsi la valeur de  $dJ/dX$  associée aux nœuds des interfaces de bloc est la somme des valeurs calculées pour chacun des nœuds coïncidents en chacun des blocs adjacents. La seconde particularité à prendre en compte est le coût de calcul de la moyenne spatiale  $\bar{\theta}(i, j)$  occasionné par la taille des maillages considérés. Ainsi une autre moyenne a été introduite. Celle-ci (notée  $\tilde{\theta}(i, j)$ ) est un lissage itératif des composantes de  $\mathcal{P}(dJ/dX)$  par directions topologiques.

### 1.3 Résultats numériques sur la hiérarchie de maillages

#### 1.3.1 Valeurs de référence pour les fonctions et critère global

Les valeurs des fonctions considérées ( $CD_p$  et  $CL_p$ ) ont été calculées sur la hiérarchie de maillage. Pour des raisons de confidentialité, les valeurs exactes ne peuvent être données dans ce document et toutes les valeurs sont données par rapport à celles obtenues sur le maillage le plus fin à  $100M$  de points (les valeurs de fonctions obtenues sur ce maillage sont notées  $J^{ref}$ ). Les résultats obtenus sur la hiérarchie de maillages sont résumés dans le tableau suivant:

Nombre de nœuds	$CL_p/CL_p^{ref}$	$CD_p/CD_p^{ref}$	$\tilde{\theta}[CL_p]$	$\tilde{\theta}[CD_p]$
$100M$	1	1	$1,53 \cdot 10^{-13}$	$1,19 \cdot 10^{-10}$
$74M$	0,99666	0,99608	$1,93 \cdot 10^{-13}$	$1,15 \cdot 10^{-10}$
$13,5M$	0,98498	1,05849	$2,10 \cdot 10^{-12}$	$1,36 \cdot 10^{-9}$
$10M$	0,98429	1,06562	$2,91 \cdot 10^{-12}$	$1,94 \cdot 10^{-9}$
$3,2M$	0,96491	1,29034	$1,05 \cdot 10^{-11}$	$8,66 \cdot 10^{-9}$

Valeurs adimensionnées de  $CL_p$  et  $CD_p$  sur la hiérarchie de maillages et valeur du critère global  $\tilde{\theta}$ .

## 4. APPLICATION À DES CAS INDUSTRIELS TRIDIMENSIONNELS

### 1.3.2 Comportement des critères sur la hiérarchie de maillages

Les critères globaux  $\bar{\theta}$  et  $\tilde{\theta}$  ont également été évalués sur la hiérarchie de maillages (les valeurs de  $\tilde{\theta}$  sont résumées dans le tableau précédent). Les mêmes variations des coefficients que dans les cas précédents sont observées. D'autre part la visualisation de ces critères dans le maillage volumique montre que les zones détectées comme étant sensibles pour le calcul des fonctions sont la zone du choc, la zone proche paroi et l'amont de l'objet solide (comme pour les cas précédents).

### 1.4 Adaptation de maillage

Les adaptations de maillages ont été effectuées pour le calcul du coefficient de traînée de pression ( $CD_p$ ) ainsi que pour le coefficient de portance de pression ( $CL_p$ ). Le maillage initial est le maillage à 13,5M de nœuds de la hiérarchie. L'objectif de cette étude est d'évaluer si la qualité de maillage peut être améliorée pour un cas tridimensionnel d'écoulement RANS en augmentant la densité de nœuds dans les zones détectées par le senseur. Néanmoins le temps de calcul associé à ces cas tridimensionnels a conduit à simplifier la méthode d'adaptation.

La première simplification concerne la projection des nœuds à la peau. En effet, dans les cas bidimensionnels précédents, le déplacement des nœuds de la peau se faisait par projection orthogonale des nœuds de la rangée suivante et cette projection se faisait à chaque itération du remaillage. Dans un cas tridimensionnel, le temps de calcul nécessaire pour cette projection est trop important. Ainsi son exécution à chaque itération du remaillage est trop coûteux. Cette projection n'a donc pas été effectuée à chaque itération du remaillage dans les adaptations présentées dans les sections suivantes.

La seconde simplification est que le nombre d'étape de la procédure d'adaptation a été fixé initialement. Les adaptations présentées dans les sections suivantes ont été effectuées en trois itérations. De plus, comme il a été observé dans les cas précédents que la plus grande partie des améliorations obtenues provenait de la première itération, le nombre d'itération du remaillage était plus important pour la première étape d'adaptation que pour les suivantes.

#### 1.4.2 Adaptation pour $CD_p$

La valeur initiale de  $CD_p/CD_p^{ref}$  est 1,05849. La valeur obtenue sur le maillage adapté est 1,04886 ce qui correspond à une réduction de 16,5% de l'erreur (par rapport au maillage le plus fin). La traînée artificielle a diminuée de 5,32463 sur le maillage initial à 4,73881. Néanmoins, une légère diminution du coefficient de portance de pression a été observée (de 0,98476 à 0,98317). Les zones raffinées se trouvent essentiellement au niveau du choc et près du bord d'attaque de la voilure. Une amélioration de la solution aérodynamique dans ces zones a été observée. En revanche, bien que la valeur de  $CD_p$  a été améliorée, on ne constate pas d'amélioration des autres composantes de la traînée contrairement au cas bidimensionnels.

Concernant les valeurs des critères globaux, une légère diminution de  $\theta[CD_p]$  a été observée (de  $2,26 \cdot 10^{-9}$  à  $2,16 \cdot 10^{-9}$ ). En revanche la valeur du critère  $\tilde{\theta}[CD_p]$  (sur lequel l'adaptation était basée) n'a pas diminué (de  $1,36 \cdot 10^{-9}$  à  $1,38 \cdot 10^{-9}$ ). Les visualisations du critère local  $\tilde{\theta}[CD_p]$  montrent une diminution de la sensibilité du maillage pour le calcul de  $CD_p$  dans les zones raffinées. Cependant certaines zones restent très sensibles (essentiellement dans la couche limite). Cela peut expliquer pourquoi les critères globaux

n'ont pas diminués. D'autre part, cela montre que l'adaptation n'a pas été assez efficace dans ces zones et peut expliquer pourquoi les autres composantes de la traînée n'ont pas été améliorées.

### 1.4.3 Adaptation pour $CL_p$

L'adaptation pour  $CL_p$  n'a conduit qu'à une très faible amélioration de l'estimation de la fonction (une réduction de seulement 3,4% de l'erreur). En revanche, contrairement au cas précédent, les composantes champ proche de la traînée sont toutes indirectement améliorées. Concernant la décomposition de traînée en champ lointain, les mêmes conclusions que dans le cas précédent peuvent être faites.

De même, les observations du champ aérodynamique et du critère local montrent une amélioration de la solution dans le volume mais pas dans les zones proches de la peau.

## 2. Critère local appliqué à la configuration “Generic Modern Aircraft”

Le calcul du critère local a été effectué sur un maillage autour de la configuration “Generic Modern Aircraft”. L'objectif était de mettre en évidence l'efficacité du critère pour détecter les zones d'intérêt d'un maillage pour le calcul de fonction dans le cas d'une configuration complexe réaliste. Ainsi le maillage considéré comptait 81M de points sur 1394 blocs.

Trois fonctions d'intérêt ont été considérées : la traînée, la portance et l'intégrale de la température à la peau. La visualisation du critère montre que certaines zones sont détectées pour toutes les fonctions (comme la zone proche de la voilure ainsi que la dérive et la zone située au dessus de la pointe avant). En revanche il a également été constaté que certaines zones sont détectées uniquement pour certaines fonctions. C'est le cas notamment de l'intégrale surfacique de la température qui est la seule des trois fonctions dont le critère détecte avec intensité certaines zones proches de l'installation motrice. De même, le critère associé à cette fonction détecte plus intensément le “sillage amont” que la traînée et la portance (bien que ces dernières le détectent aussi). Ainsi l'aspect “goal oriented” du critère est très visible sur ce cas test.

## Conclusions

Ces résultats montrent que l'adaptation a été efficace pour réduire la sensibilité de maillage dans le volume à l'exception des zones proches de la peau. Ceci peut être dû au fait que la projection des nœuds à la peau n'a pas pu être effectuée à chaque itération du remaillage. Bien que la qualité globale de la solution n'a pas été autant améliorée que lors des cas 2D, les estimations des fonctions sur lesquelles les adaptations étaient basées ( $CD_p$  et  $CL_p$ ) ont bien été améliorées. Ceci conforte le fait que les zones détectées par le senseur sont pertinentes et suggère que la méthode de remaillage devrait être améliorée. En particulier, les valeurs du critère local restent fortes dans les zones proches de la peau ce qui suggère d'améliorer l'efficacité de la méthode remaillage près de la peau afin d'obtenir de meilleurs résultats.

# Chapter 4

## Application to three-dimensional industrial cases

In the previous chapter, the proposed goal oriented mesh adaptation strategy has been applied with an improved remeshing method to both Euler and RANS two-dimensional flows. The next step is to apply the methodology to three-dimensional industrial cases. The selected test case for adaptation has been a flow around the XRF-1 configuration. The test case and the meshes are presented in the section 4.1. Some specificities attached to this type of three-dimensional topology are also presented as well as the corresponding consequences for the proposed method. The results obtained on a mesh hierarchy are presented in Section 4.2 and the adaptations are described in Section 4.3. Finally the last section presents the application of the local criterion  $\theta$  to a flow around the Generic Modern Aircraft configuration. The objective was to demonstrate that the proposed method could already be efficiently applied to  $3D$  realistic configurations.

### 4.1 General presentation of the XRF-1 test case

This section is devoted to a general presentation of the considered test case for 3D mesh adaptations. The XRF-1 configuration and the hierarchy of meshes that have been used are presented in Section 4.1.1. It includes the presentation of the mesh characteristics and the treatment of particular block interfaces for the application of the proposed method. Section 4.1.2 is devoted to the presentation of another spatial mean for the field  $\mathcal{P}(dJ/dX)$  that is currently affordable for  $3D$  cases. Finally flow conditions are briefly summarized in Section 4.1.3.

#### 4.1.1 The XRF-1 configuration and the mesh hierarchy

The XRF-1 is a wide-body Airbus-type research configuration that consists of a fuselage and a wing. It is illustrated on the following figures.

#### 4.1. GENERAL PRESENTATION OF THE XRF-1 TEST CASE

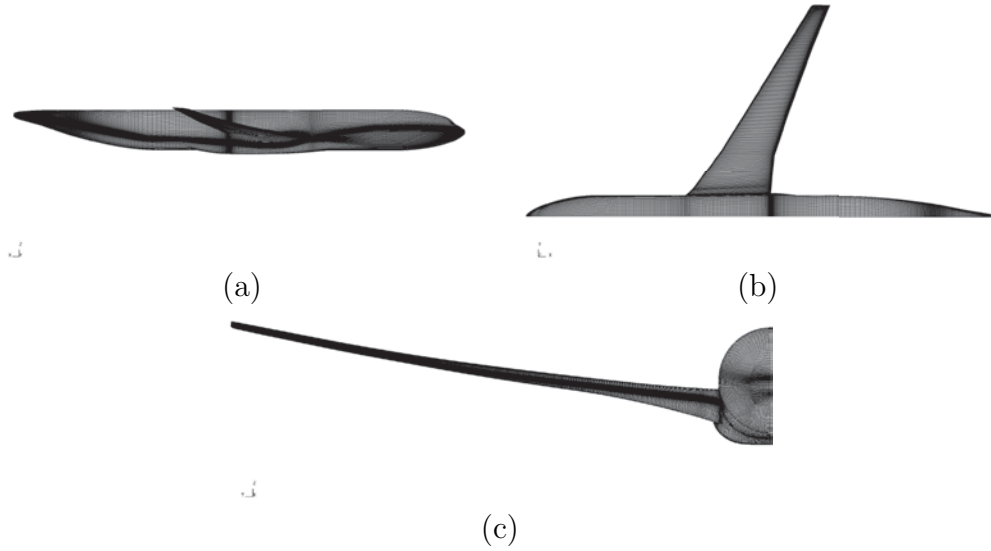


Figure 4.1: Geometry of the XRF-1 configuration (a) From the right side ; (b) From the top ; (c) From the front

**Mesh hierarchy** A hierarchy of five meshes has been built in order to evaluate the output reference values and to study the behavior of the criteria. These meshes have been constructed following the recommendations presented in [34]. The size of these meshes ranges from  $3.2M$  points for the coarsest one to  $100M$  for the finest. The characteristics of these meshes are summarized in the following table.

Mesh	Very coarse	Coarse	Medium	Fine	Extra fine
Number of nodes	$3.2M$	$10M$	$13.5M$	$74M$	$100M$
Number of block	143	143	143	206	334

Table 4.1: XRF-1 mesh hierarchy characteristics

The following figures illustrate the block decomposition on the symmetry plane 4.2(a) and the walls 4.2(b) for the medium mesh.

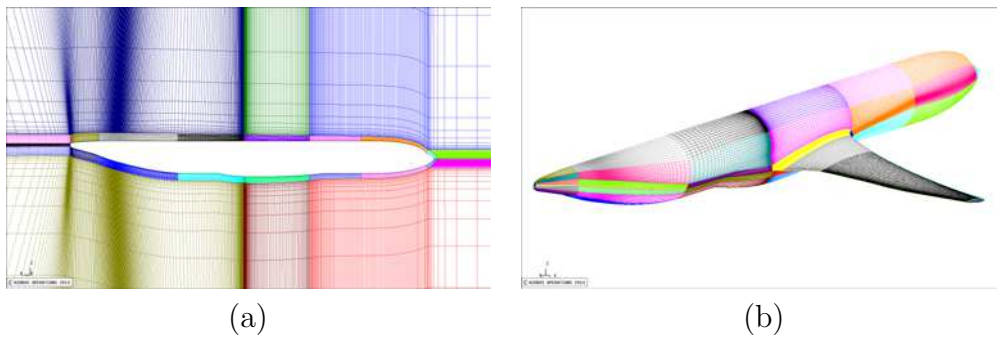


Figure 4.2: Block decomposition (a) on the symmetry plane ; (b) on the walls

The following figure illustrates different parts of a mesh plane normal to the wing.

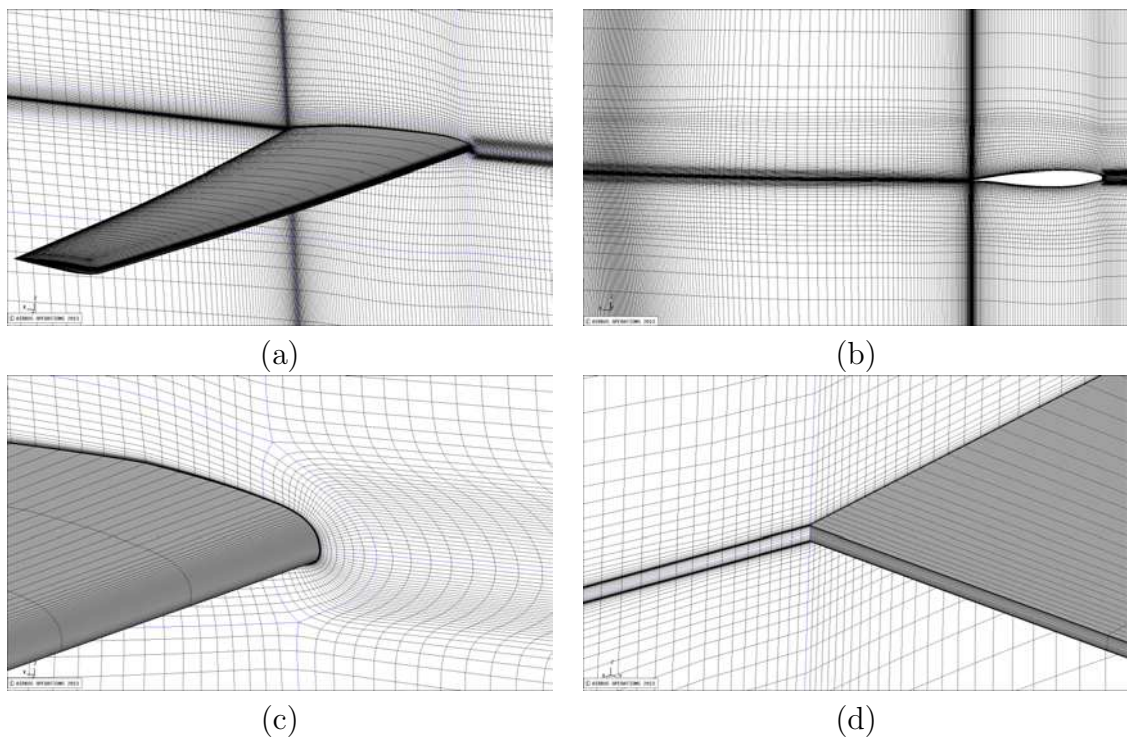


Figure 4.3: Visualization of a mesh plane normal to the wing ; (a) View with the wing mesh ; (b) View without the wing mesh ; (c) Focus at the leading edge ; (d) Focus at the trailing edge

**Particular block interfaces** All the block interfaces are coincident, however, particular junctions appear as illustrated on the figure 4.4.

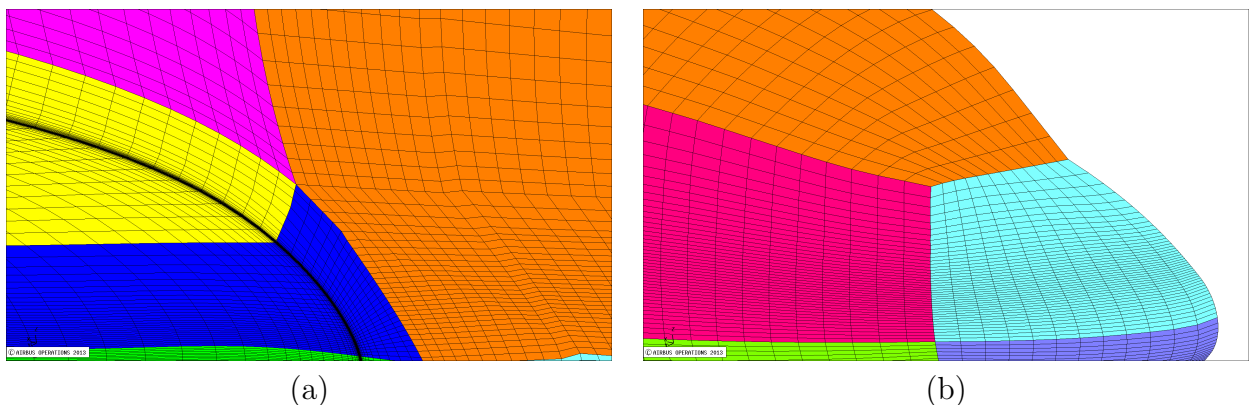


Figure 4.4: (a) Block interfaces near the junction between the fuselage and the wing ; (b) Block interfaces near nose

The value of  $dJ/dX$  for all coincident nodes is different in each block to which it belongs. Therefore it is necessary to sum up these  $dJ/dX$  values in order to build up a homogeneous  $dJ/dX$  field for all mesh nodes. This last field is then used for the computation of the criterion  $\theta$ .

### 4.1.2 Introduction of a computable spatial mean for 3D applications

The spatial mean introduced in the previous chapter (Appendix B of section 3.1) was used for the two-dimensional cases in order to take into account the irregularities of the field  $\mathcal{P}(dJ/dX)$  and the compensation effects that can occur. It has been shown that the corresponding criterion  $\bar{\theta}$  was well suited for mesh adaptation. Nevertheless this spatial mean is expensive to compute for fine meshes or meshes that present areas with important node density, since for each node, all the neighbours that are at a distance less or equal to a specified radius have to be identified.

This mean was not considered computable for the finest meshes of the hierarchy used around the RAE2822 airfoil in the previous chapter. Obviously it cannot be used for the three-dimensional case. Therefore another spatial mean was used. This alternative mean is based on an iterative process and is applied to the components of  $\mathcal{P}(dJ/dX)$ . At each step the value associated with a node is computed using the mean of the value at its six neighbours (according to the topological directions) and the value at the current.

### 4.1.3 Flow conditions and outputs

The flow considered in the applications is described by the RANS equations. The Reynolds number per meter is  $Re.m^{-1} = 7800000$ , the upstream Mach number is  $M_\infty = 0.83$  and the angle of attack is  $\alpha = 2.607^\circ$ . The considered outputs are: the pressure lift coefficient ( $CL_p$ ) and the pressure drag coefficient ( $CD_p$ ).

## 4.2 Numerical results on the XRF-1 mesh hierarchy

This section is devoted to the presentation of the numerical results obtained on the mesh hierarchy for both the output values and the behavior of the criteria  $\theta$  and  $\tilde{\theta}$ . Section 4.2.1 presents the aerodynamic solutions. The reference output values are presented in Section 4.2.2. This section details the near-field and far-field analysis for all meshes of the hierarchy. Finally the estimations of  $\theta$  and  $\tilde{\theta}$  are given and discussed in the last section.

### 4.2.1 Numerical scheme and aerodynamic flow-field

The numerical scheme used for the following computation is the same as in the previous two-dimensional RANS test cases. It is the Roe's scheme plus a MUSCL extension to the second order with the van Albada limiting function.

The plots in Figure 4.5 illustrate the iso  $-Cp$  on the wall for the meshes of the hierarchy (except for the coarsest one) with a view from the top. Figures 4.6 is analogous with a view from the bottom. We notice that a shock wave is located on the wing upper surface.

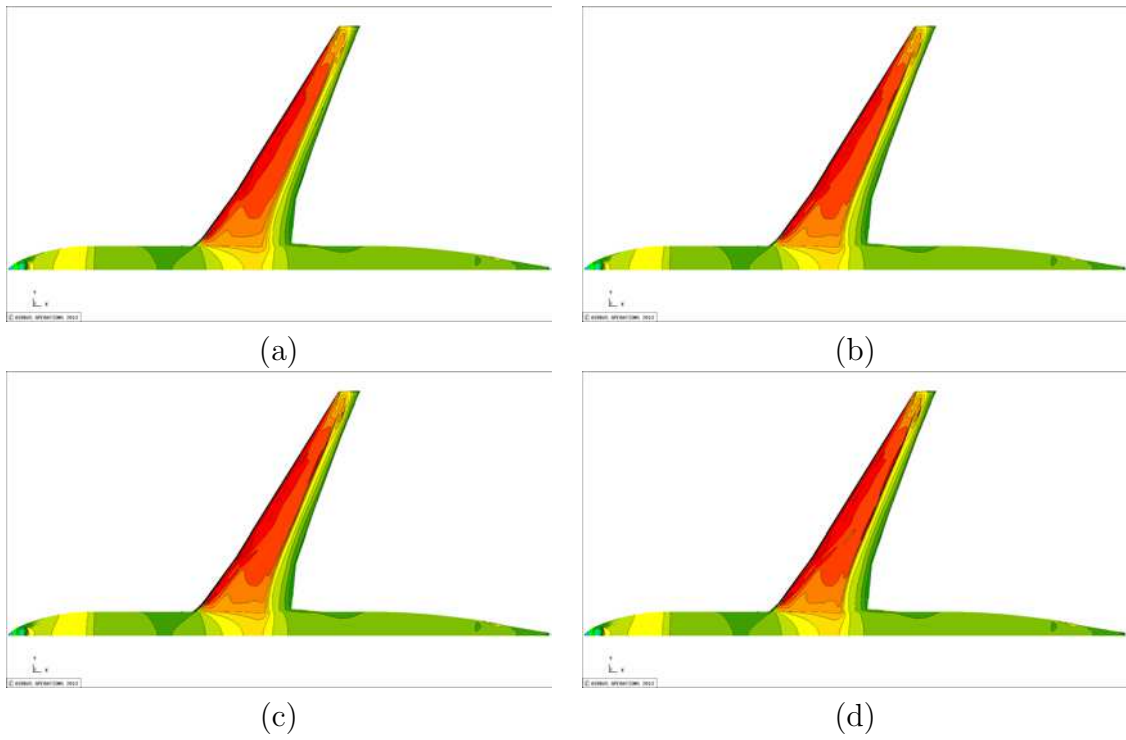


Figure 4.5: Iso  $-C_p$  on the mesh hierarchy view from the top. (a) Coarse mesh ; (b) Medium mesh ; (c) Fine mesh ; (d) Extra fine mesh

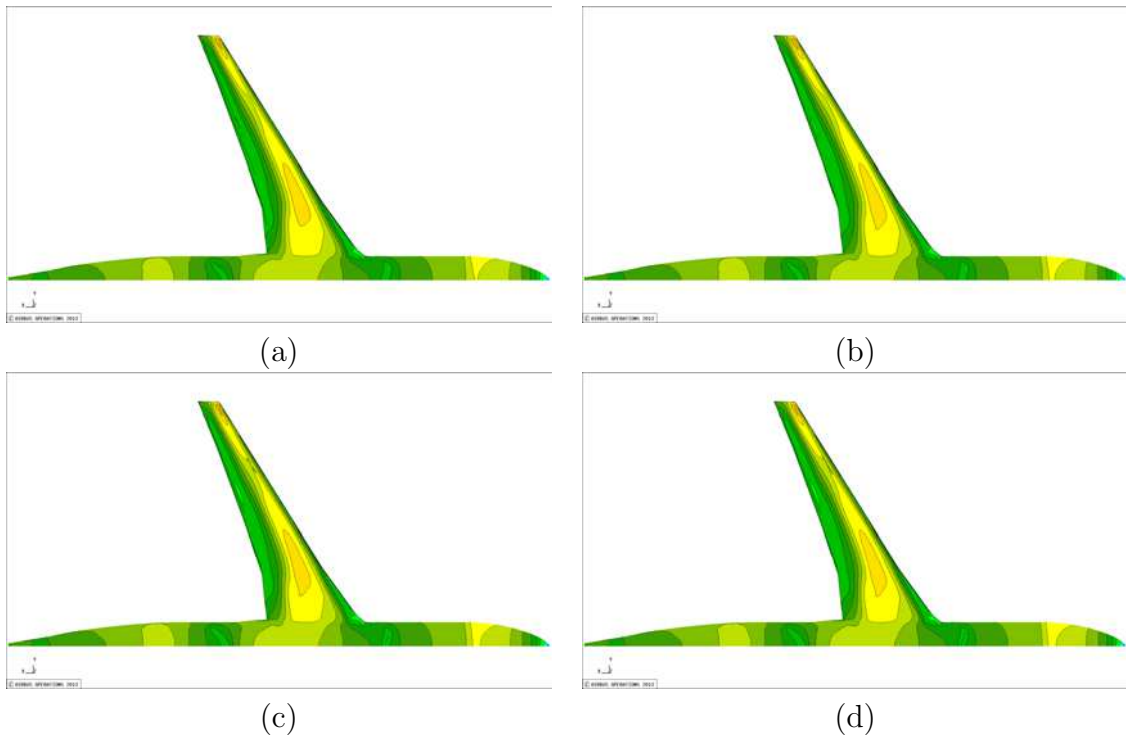


Figure 4.6: Iso  $-C_p$  on the mesh hierarchy view from the bottom. (a) Coarse mesh ; (b) Medium mesh ; (c) Fine mesh ; (d) Extra fine mesh

## 4.2. NUMERICAL RESULTS ON THE XRF-1 MESH HIERARCHY

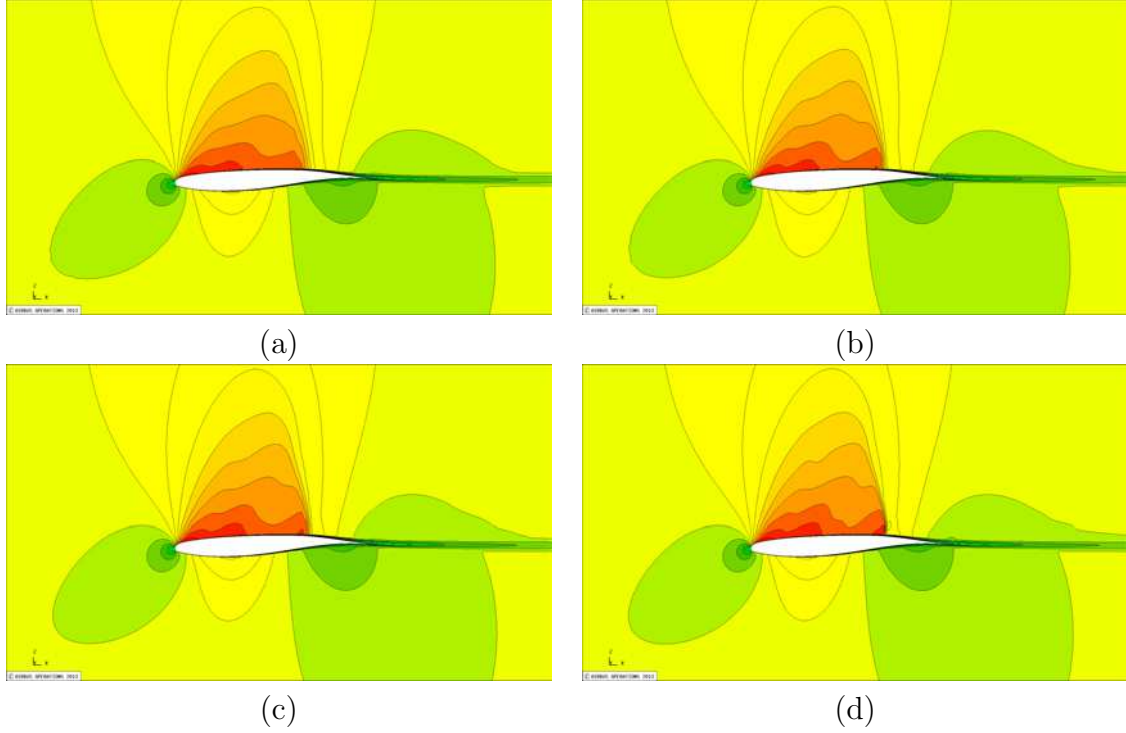


Figure 4.7: Iso Mach number on the mesh hierarchy view on a constant  $y$  plane. (a) Coarse mesh ; (b) Medium mesh ; (c) Fine mesh ; (d) Extra fine mesh

### 4.2.2 Reference values for the outputs

The considered functions of interest are the pressure drag coefficient  $CD_p$  and the pressure lift coefficient  $CL_p$ . A near-field and far-field drag analysis have been carried out on the mesh hierarchy. However, due to confidentiality requirements the exact values cannot appear in this document. All the output values are hence given relatively to the ones obtained on the finest mesh that are denoted  $J^{ref}$ .

**Near-field analysis** Table 4.2 summarizes the values of these outputs with the near-field approach for the standard mesh hierarchy.

Mesh size	$Cl/Cl^{ref}$	$CL_p/CL_p^{ref}$	$Cd/Cd^{ref}$	$CD_p/CD_p^{ref}$	$CD_f/CD_f^{ref}$
100M	1.	1.	1.	1.	1.
74M	0.99645	0.99666	0.99390	0.99608	0.98990
13.5M	0.98476	0.98498	1.04371	1.05849	1.01656
10M	0.98407	0.98429	1.04790	1.06562	1.01550
3.2M	0.96470	0.96491	1.19002	1.29034	1.00658

Table 4.2: XRF-1 ;  $M_\infty = 0.83$  ; AoA =  $2.607^\circ$  ;  $Re.m^{-1} = 7800000$ .  $Cl$ ,  $CL_p$ ,  $Cd$ ,  $CD_p$  and  $CD_f$  on the mesh hierarchy.

**Far-field analysis** Table 4.3 summarizes the output values with the far-field approach on the mesh hierarchy.

Mesh size	$Cd/Cd^{ref}$	$CD_w/CD_w^{ref}$	$CD_v/CD_v^{ref}$	$CD_i/CD_i^{ref}$	$CD_{sp}/CD_{sp}^{ref}$
100M	1.	1.	1.	1.	1.
74M	0.99341	0.92339	1.00350	0.99192	1.03731
13.5M	0.99551	0.83186	1.04077	0.96845	5.32463
10M	0.99698	0.83797	1.04462	0.96667	5.57463
3.2M	0.97163	0.66780	1.04915	0.92864	20.60448

Table 4.3: XRF-1 ;  $M_\infty = 0.83$  ; AoA =  $2.607^\circ$  ;  $Re.m^{-1} = 7800000$ . Far-field drag breakdown on the mesh hierarchy.

### 4.2.3 Criteria $\theta$ and $\tilde{\theta}$ on the mesh hierarchy

The following table summarizes the values of the criteria  $\theta$  and  $\tilde{\theta}$  on the mesh hierarchy. The same behavior as for the two-dimensional results is observed except a slight increase of the criteria for  $CD_p$  for the finest mesh.

Mesh size	$\theta[CL_p]$	$\tilde{\theta}[CL_p]$	$\theta[CD_p]$	$\tilde{\theta}[CD_p]$
100M	$2.19 \cdot 10^{-13}$	$1.53 \cdot 10^{-13}$	$1.76 \cdot 10^{-10}$	$1.19 \cdot 10^{-10}$
74M	$2.78 \cdot 10^{-13}$	$1.93 \cdot 10^{-13}$	$1.72 \cdot 10^{-10}$	$1.15 \cdot 10^{-10}$
13.5M	$3.29 \cdot 10^{-12}$	$2.10 \cdot 10^{-12}$	$2.26 \cdot 10^{-9}$	$1.36 \cdot 10^{-9}$
10M	$4.66 \cdot 10^{-12}$	$2.91 \cdot 10^{-12}$	$3.22 \cdot 10^{-9}$	$1.94 \cdot 10^{-9}$
3.2M	$1.95 \cdot 10^{-11}$	$1.05 \cdot 10^{-11}$	$1.68 \cdot 10^{-8}$	$8.66 \cdot 10^{-9}$

Table 4.4: XRF-1 ;  $M_\infty = 0.83$  ; AoA =  $2.607^\circ$  ;  $Re/m = 7800000$ . Criterion  $\theta$  and  $\tilde{\theta}$  for both  $CL_p$  and  $CD_p$  on the mesh hierarchy.

These values are summarized by the plots of Figure 4.8.

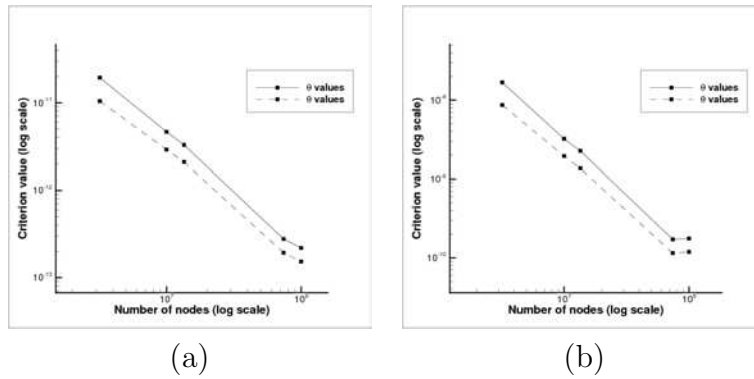


Figure 4.8: XRF-1 ;  $M_\infty = 0.83$  ; AoA =  $2.607^\circ$  ;  $Re/m = 7800000$ . Criterion  $\theta$  and  $\tilde{\theta}$ . (a)  $J = CL_p$  (b)  $J = CD_p$ .

## 4.2. NUMERICAL RESULTS ON THE XRF-1 MESH HIERARCHY

The following plots (Figure 4.9) illustrate the criterion  $\tilde{\theta}$  on several mesh planes for both  $CD_p$  and  $CL_p$  on the initial mesh (medium size of the mesh hierarchy).

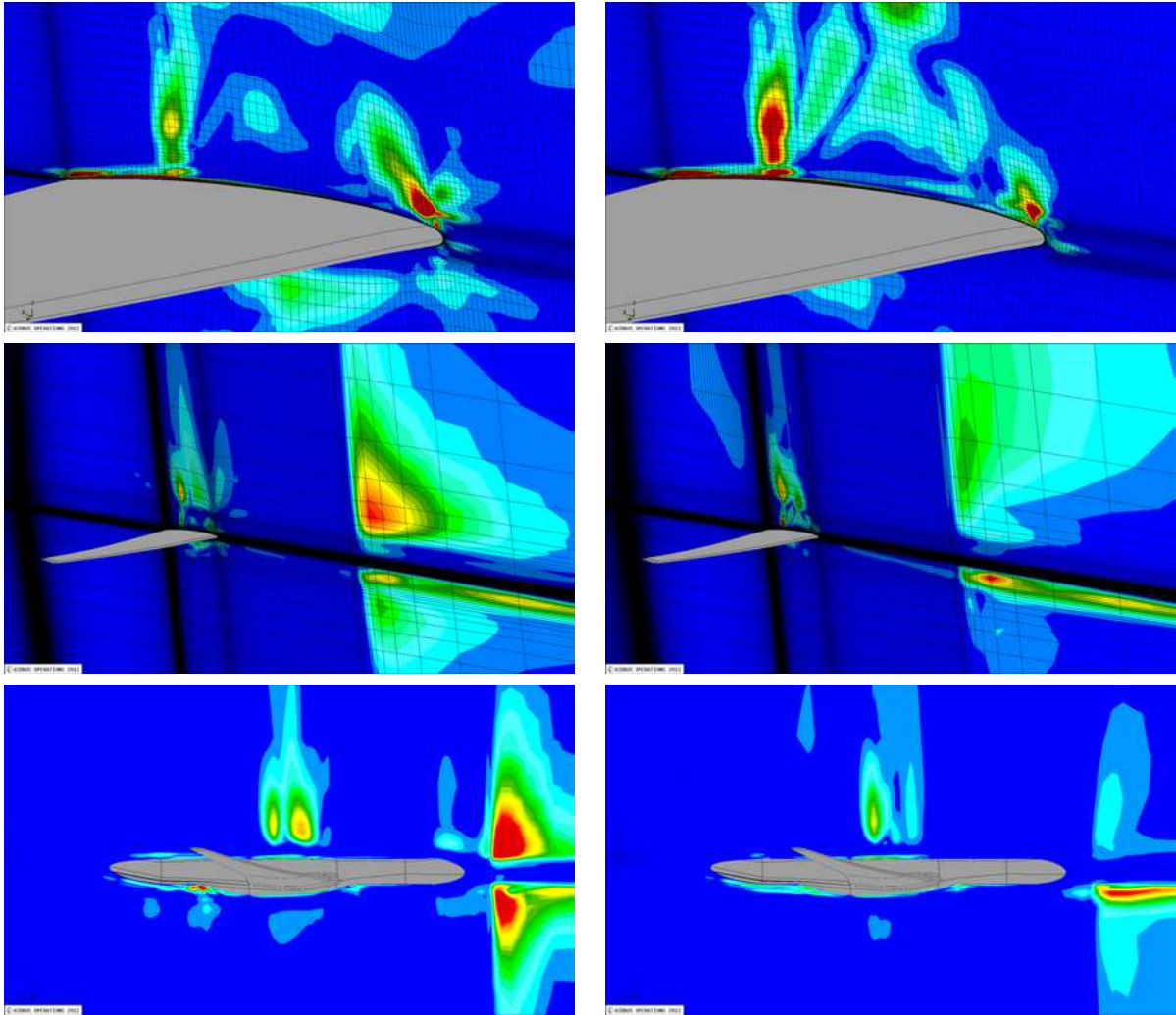


Figure 4.9: Criterion  $\tilde{\theta}$  on the initial mesh. Left: criterion for  $CD_p$  ; Right: criterion for  $CL_p$

We observe that the shock is detected by the sensor for the two functions. Moreover other locations are detected in the upstream areas where there is an important increase of the cell size. These phenomena have been already observed for the two-dimensional test cases.

Moreover we notice that the detected mesh locations are almost the same for the two functions. However it is not always the case as presented in Section 4.4 that presents a study of the criterion  $\theta$  for several functions on the Generic Modern Aircraft configuration. The next section presents the mesh adaptations carried out using these criteria.

### 4.3 Mesh adaptations on the XRF-1 configuration

Mesh adaptations have been carried out for the pressure drag coefficient ( $CD_p$ ) and the pressure lift coefficient ( $CL_p$ ). The initial mesh is the medium mesh of the hierarchy (with  $13.5M$  nodes).

In the same way as for the two-dimensional cases, the objective of this study was to evaluate if the mesh quality can be improved for a three-dimensional RANS flow by increasing the mesh node density in the locations detected by the local criterion. However due to geometry complexity and the required computation time, the remeshing process used in the previous test cases could not be applied directly.

Section 4.3.1 summarizes the specificities of the adaptation process that has been applied on the XRF-1 configuration. The corresponding results are presented in Sections 4.3.2 and 4.3.3 for mesh adaptation for the pressure drag coefficient computation and for the pressure lift coefficient computation respectively.

#### 4.3.1 Adaptation process

In the two-dimensional adaptations presented in the previous chapter, the displacement of the mesh nodes located on the wall was carried out using an orthogonal projection of the nodes located on the next node layer. This projection was applied at every step of the remeshing process based on the elliptic PDEs presented in 3.1. For the current three-dimensional case, this projection is time consuming. It was hence not performed at every step of the remeshing process.

Finally the number of adaptation steps has been fixed initially. The adaptations presented in the following sections have been done in three steps. Moreover, it was observed for the two-dimensional cases that the major part of the improvements in the function evaluation adaptation were obtained at the first step. Therefore, due to computational time requirement, the number of remeshing iterations was higher at the first step than at the others.

#### 4.3.2 Adaptation for the pressure drag coefficient

The initial  $CD_p/CD_p^{ref}$  value is 1.05849. The value obtained on the adapted mesh is 1.04886 corresponding to a reduction of 16.5% of the error (with respect to the value obtained on the finest mesh). A slight reduction of the lift coefficient (that decreased from 0.98476 to 0.98317) is observed on the adapted mesh. Besides, only the pressure drag coefficient,  $CD_p$ , has been improved. The following table summarizes the output values obtained with the near-field approach.

Mesh	$Cl/Cl^{ref}$	$CL_p/CL_p^{ref}$	$Cd/Cd^{ref}$	$CD_p/CD_p^{ref}$	$CD_f/CD_f^{ref}$
Extra fine	1.	1.	1.	1.	1.
Initial mesh	0.98476	0.98498	1.04371	1.05849	1.01656
Adapted for $CD_p$	0.98317	0.98338	1.03819	1.04886	1.01867

Table 4.5: XRF-1. Adaptation for  $CD_p$ . Near-field drag breakdown.

### 4.3. MESH ADAPTATIONS ON THE XRF-1 CONFIGURATION

The spurious drag  $CD_{sp}/CD_{sp}^{ref}$  decreased from 5.32463 on the initial mesh to 4.73881. The following table summarizes the output values obtained with the far-field approach.

Mesh	$Cd/Cd^{ref}$	$CD_w/CD_w^{ref}$	$CD_v/CD_v^{ref}$	$CD_i/CD_i^{ref}$	$CD_{sp}/CD_{sp}^{ref}$
Extra fine	1.	1.	1.	1.	1.
Initial mesh	0.99551	0.83186	1.04077	0.96845	5.32463
Adapted for $CD_p$	0.99656	0.73763	1.05744	0.96554	4.73881

Table 4.6: XRF-1. Adaptation for  $CD_p$ . Far-field drag breakdown.

Unfortunately we can notice that only far-field drag coefficient ( $Cd$ ) and the spurious drag  $CD_{sp}$  have decreased.

A mesh plane along the wing is plotted on the figure 4.10(a) as well as the corresponding one on the adapted mesh 4.10(b). We notice an increase of the mesh node density near the shock location as well as at the leading edge.

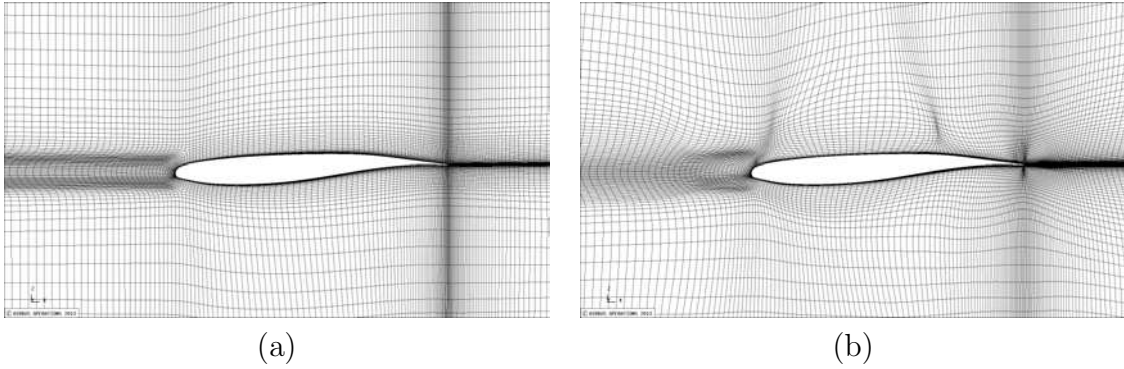


Figure 4.10: Visualization of a mesh plane along the wing. (a) Initial medium mesh ; (b) Adapted mesh for  $CD_p$

The following plots (Figure 4.11) illustrate the iso Mach number on a mesh plane for both the initial mesh and the adapted one. As expected, we notice an improvement of the solution near the shock location.

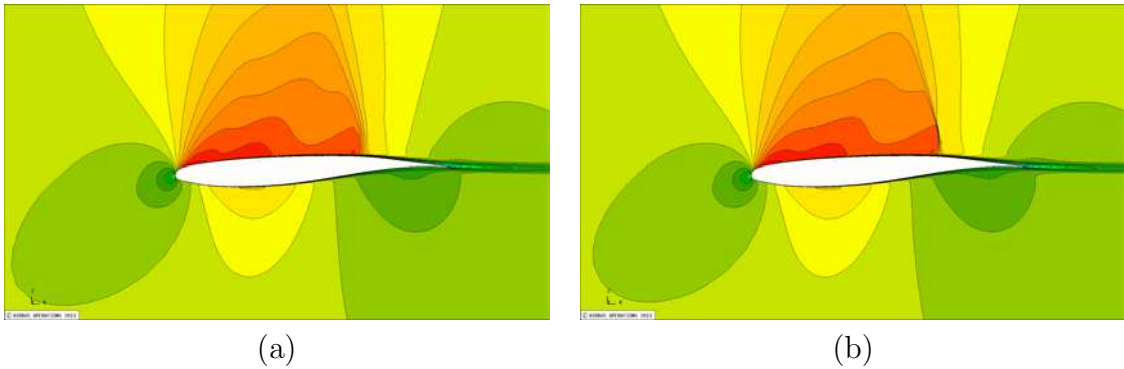


Figure 4.11: Iso Mach number view on a mesh plane along the wing. (a) Initial medium mesh ; (b) Adapted mesh for  $CD_p$

Concerning the criteria, a slight reduction of the criterion  $\theta[CD_p]$  has been observed (from  $2.26 \cdot 10^{-9}$  to  $2.16 \cdot 10^{-9}$ ). However, the value of the criterion  $\tilde{\theta}[CD_p]$  (on which the adaptation was based) has not decreased (from  $1.36 \cdot 10^{-9}$  to  $1.38 \cdot 10^{-9}$ ).

The local criterion  $\tilde{\theta}[CD_p]$  is plotted on the figures 4.12 for both the initial mesh and the adapted one. As expected, a reduction of the mesh sensitivity at several locations initially detected by the sensor (including the shock location and the leading edge) is noticed. However, it also appears that an important sensitivity remains especially in the boundary layer. This can explain why the global criteria did not diminish much while the flow field has been improved in the areas that are not close to the wall.

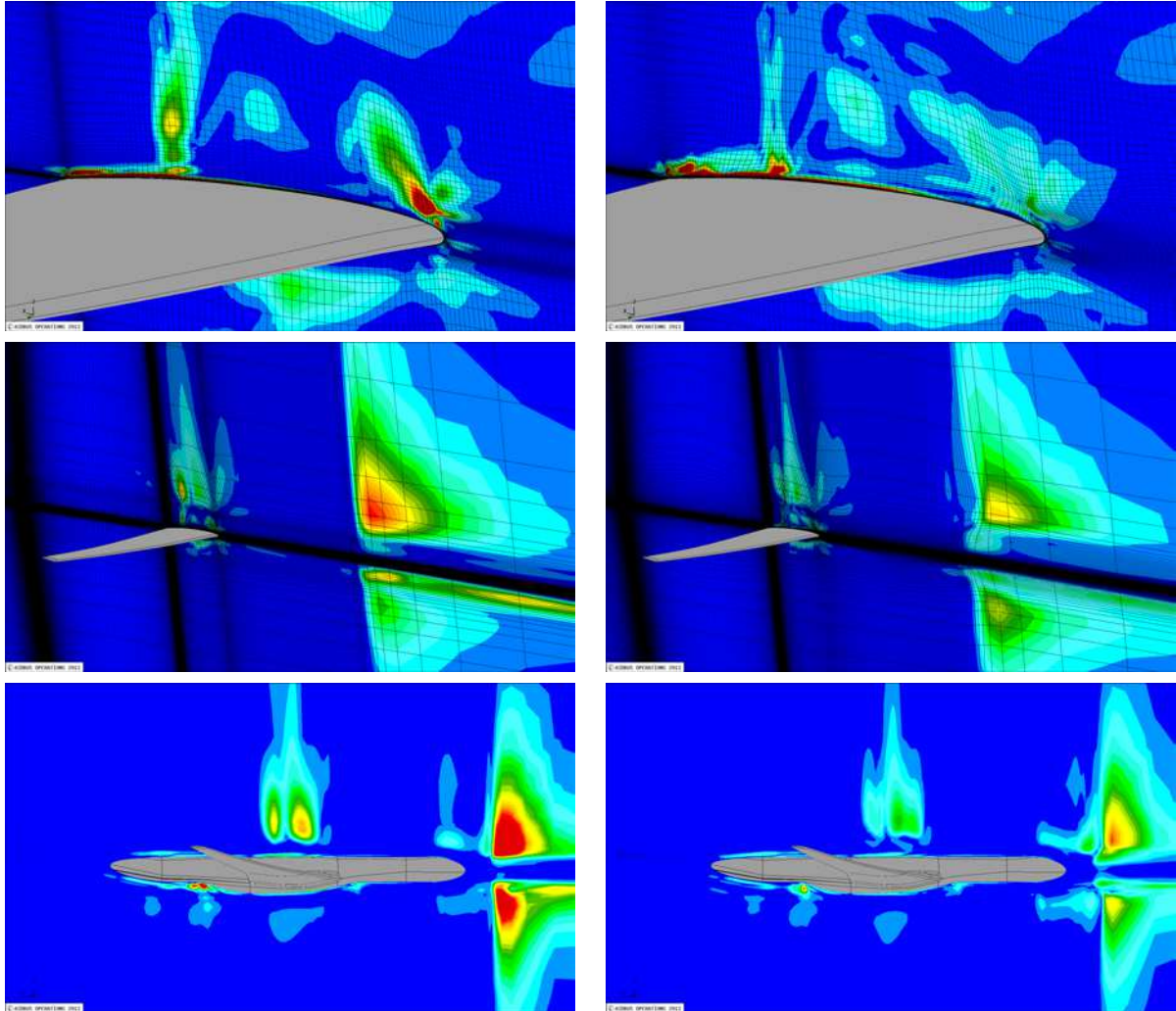


Figure 4.12: Criterion  $\tilde{\theta}[CD_p]$ . Left: initial mesh ; Right: adapted mesh for  $CD_p$

These results have shown that the current adaptation procedure was able to reduce the mesh sensitivity only in the volume mesh and not near the walls. This may be due to the fact that the wall node projection could not be done at every iteration of the remeshing process.

Concerning the evolution of the mesh quality, the adaptation has been carried out for the computation of the pressure drag coefficient and a slight improvement of the estimation of this output has been observed. Nevertheless the global quality of the solution has not been improved so much that the estimations of the other components of the drag coefficient

(and the lift coefficient) are not also improved. This is a major difference in comparison to the two-dimensional test cases. Moreover, the visualisations of the flow field have shown improvement of the solution quality inside the volume mesh, in particular close to the shock wave. However the previous two-dimensional cases already shown that the wave drag ( $CD_w$ ) is not necessarily improved while increasing the node density close to the shock location.

This tends to confirm that the remeshing was not satisfactory near the walls. These observations are in agreement with the ones done for the criterion values that remain high in these locations on the adapted mesh.

### 4.3.3 Adaptation for the pressure lift coefficient

The initial  $CL_p/CL_p^{ref}$  value is 0.98498. The value obtained on the adapted mesh is 0.98549. This corresponds to a reduction of only 3.4% of the error (with respect to the value obtained on the finest mesh). However an indirect improvement of the drag coefficient, that decreased from 1.05849 to 1.05008, is noticed. The following table summarizes the output values obtained with the near-field approach.

Mesh	$Cl/Cl^{ref}$	$CL_p/CL_p^{ref}$	$Cd/Cd^{ref}$	$CD_p/CD_p^{ref}$	$CD_f/CD_f^{ref}$
Extra fine	1.	1.	1.	1.	1.
Initial mesh	0.98476	0.98498	1.04371	1.05849	1.01656
Adapted for $CL_p$	0.98526	0.98549	1.03727	1.05008	1.01374

Table 4.7: XRF-1. Adaptation for  $CL_p$ . Near-field drag breakdown.

Besides all the near-field output values have been improved. The spurious drag  $CD_{sp}/CD_{sp}^{ref}$  decreased from 5.32463 on the initial mesh to 4.75746. The following table summarizes the output values obtained with the far-field approach.

Mesh	$Cd/Cd^{ref}$	$CD_w/CD_w^{ref}$	$CD_v/CD_v^{ref}$	$CD_i/CD_i^{ref}$	$CD_{sp}/CD_{sp}^{ref}$
Extra fine	1.	1.	1.	1.	1.
Initial mesh	0.99551	0.83186	1.04077	0.96845	5.32463
Adapted for $CL_p$	0.99542	0.76746	1.04804	0.96930	4.75746

Table 4.8: XRF-1. Adaptation for  $CL_p$ . Far-field drag breakdown.

The wave drag coefficient ( $CD_w$ ) and the viscous drag coefficient ( $CD_v$ ) have not been improved. A mesh plane along the wing is plotted on the figure 4.13(a) as well as the corresponding one on the adapted mesh 4.13(b). It appears that the mesh node density has been increased near the shock location as well as at the leading edge.

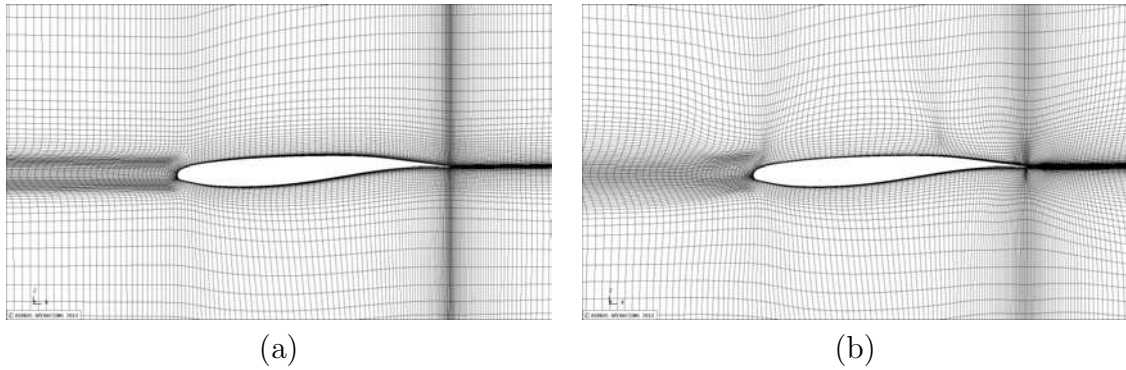


Figure 4.13: Visualization of a mesh plane along the wing. (a) Initial medium mesh ; (b) Adapted mesh for  $CL_p$

The following figure illustrate the iso Mach number on the same mesh plane for both the initial mesh and the adapted one. An improvement of the solution near the shock location is observed as well as for the mesh adapted for  $CD_p$ .

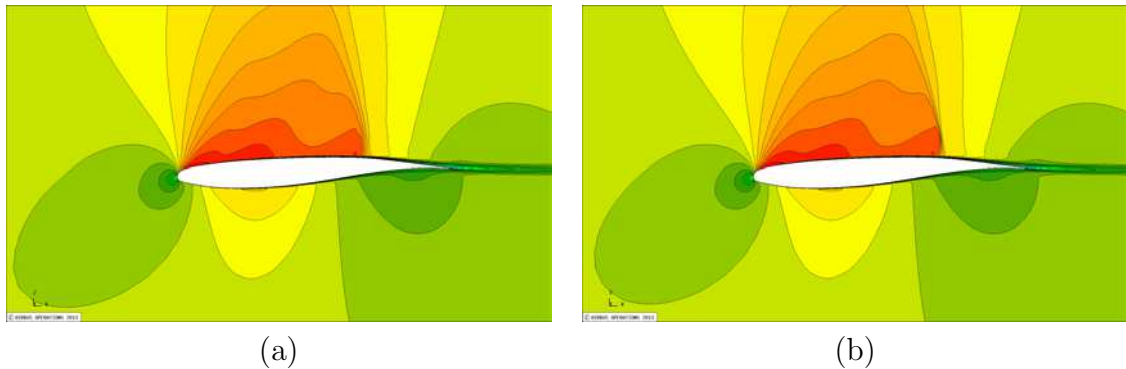


Figure 4.14: Iso Mach number view on a constant  $y$  plane. (a) Initial medium mesh ; (b) Adapted mesh for  $CL_p$

Concerning the criteria, a slight increase of the criterion  $\theta[CL_p]$  has been observed (from  $3.29 \cdot 10^{-12}$  to  $3.38 \cdot 10^{-12}$ ). The same behavior is observed for the value of the criterion  $\tilde{\theta}[CL_p]$  (from  $2.10 \cdot 10^{-12}$  to  $2.28 \cdot 10^{-12}$ ).

The local criterion  $\tilde{\theta}[CL_p]$  is plotted on the Figure 4.15 for both the initial mesh and the adapted one. As for the previous case, we can notice a reduction of the mesh sensitivity at the locations initially detected inside the volume mesh. Nevertheless, it has also appeared that an important sensitivity remains especially near the wall as in the previous case.

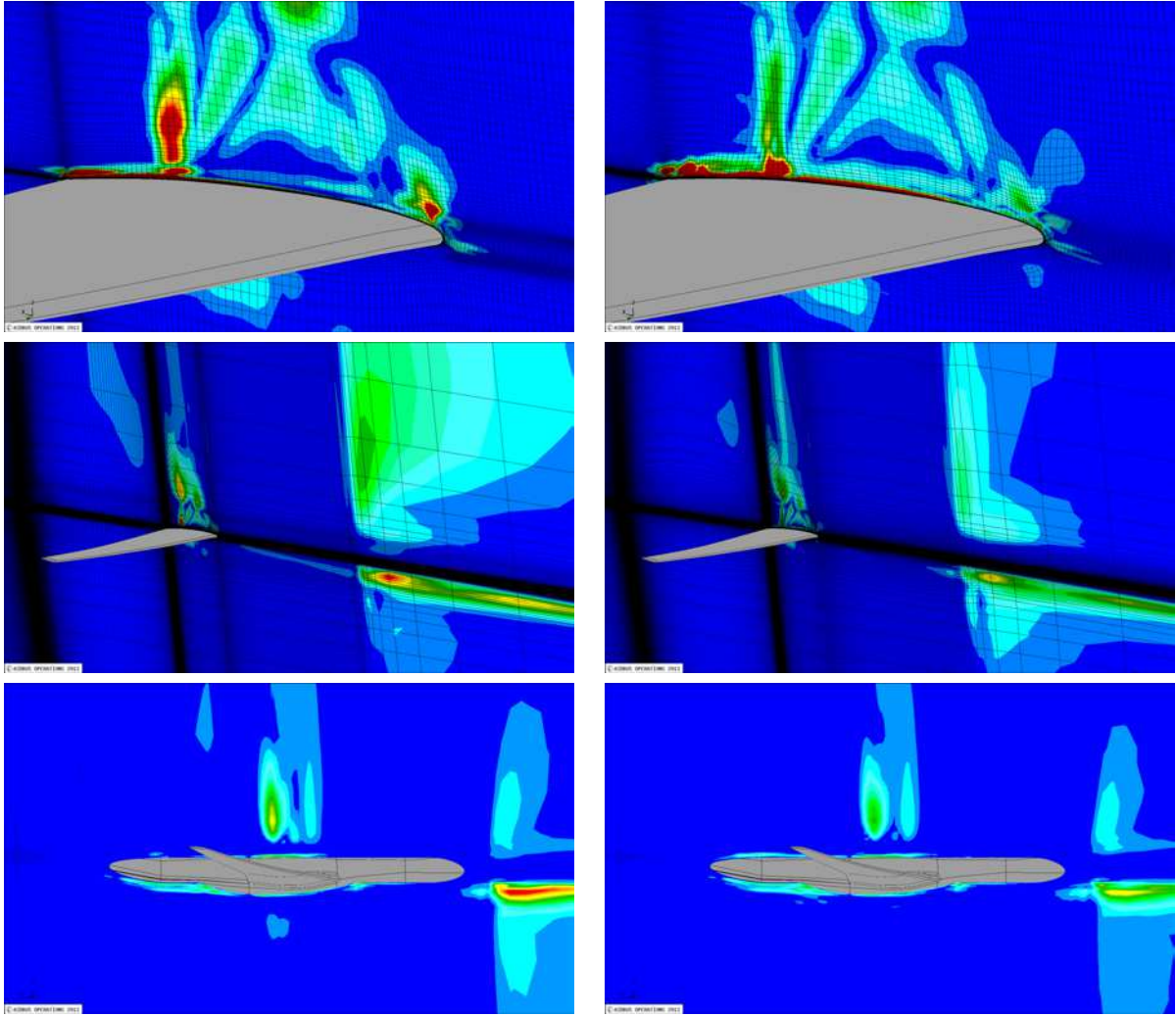


Figure 4.15: Criterion  $\tilde{\theta}[CL_p]$ . Left: initial mesh ; Right: adapted mesh for  $CL_p$

This mesh adaptation has been carried out for the computation of the pressure lift coefficient ( $CL_p$ ). The estimation of this output has been slightly improved. As for the previous case, we have noticed that the method succeeds in improving the mesh quality inside the volume mesh but not near the walls.

#### 4.3.4 Conclusions

The objective of these mesh adaptations was to evaluate if the proposed method could be applied to three-dimensional cases of viscous flows described by the RANS equations. The results are not as good as for the two-dimensional configurations: the output values have been slightly improved and the mesh locations detected by the sensor seemed to be relevant for mesh adaptation. The mesh quality was improved inside the volume mesh and less near the wall. This phenomenon is detected by the sensor in so far that its values remain high in those locations. Finally it seems that the efficiency of the remeshing method has a major importance for three-dimensional RANS test cases.

## 4.4 Application to the Generic Modern Aircraft configuration

The computation of the criterion  $\theta$  has been done for a flow around the Generic Modern Aircraft configuration. The objective was to demonstrate the efficiency of the proposed approach for the detection of mesh zones of interest in the case of 3D realistic industrial configurations. The test case is presented in Section 4.4.1. In particular it is shown that the criterion can be extended for non-coincident block interfaces (as illustrated on Figure 4.17). Finally the interest of the visualization of the criterion  $\theta$  is shown up in Section 4.4.2.

### 4.4.1 General presentation of the test case

The considered outputs are the drag coefficient, the lift coefficient and the temperature integrated over the walls. The mesh was composed by 81M points on 1394 blocks. The following figure illustrates the surface mesh.



Figure 4.16: Surface mesh of the Generic Modern Aircraft configuration

The mesh involves non-coincident block interfaces (as illustrated on Figure 4.17 which shows the mesh symmetry plane) on the contrary to the XRF-1 case presented in the previous sections. However the computation of the criterion  $\theta$  can be done. The derivative  $dJ/dX$  is projected on the non-coincident block interfaces. The characteristic length is the same but computed only using the neighbour nodes that are inside the same block.

The criteria  $\tilde{\theta}$  and  $\tilde{\theta}$  that are based on a spatial mean of  $\mathcal{P}(dJ/dX)$  are not computed for this case. Since further development would be necessary to take into account the non-coincident block junctions. Nevertheless, from the theoretical point of view, these means can be extended for these cases.

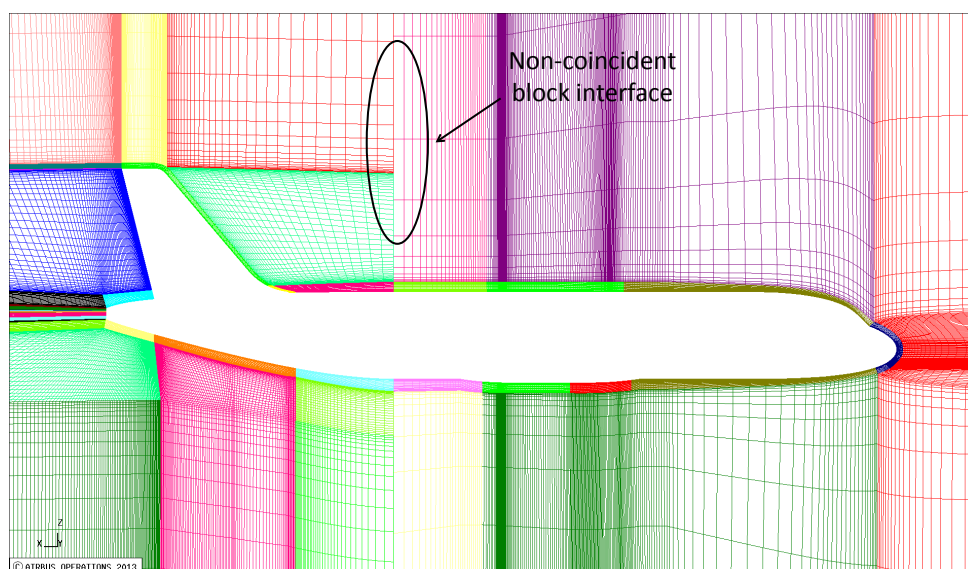


Figure 4.17: Symmetry plane of the Generic Modern Aircraft configuration

#### 4.4.2 Visualization of mesh sensitivities

It has been shown, in the previous chapters, that the visualization of the criterion  $\theta$  provides relevant information about the most sensitive mesh locations for the computation of a given output. The following paragraphs illustrates this approach for the three considered outputs. First of all the iso Mach number lines are plotted.

**Flow field** The following figure illustrates the iso Mach number for several planes of the computation domain.

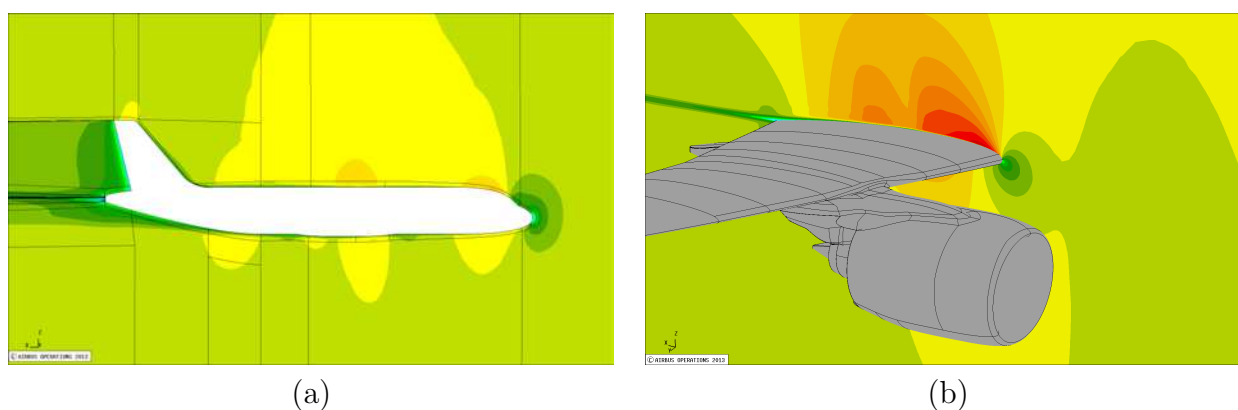


Figure 4.18: Iso Mach number ; (a) Symmetry plane ; (b) Plane between the engine and the fuselage

The following figure illustrate the iso Mach number on a geometrical plane near the engine.

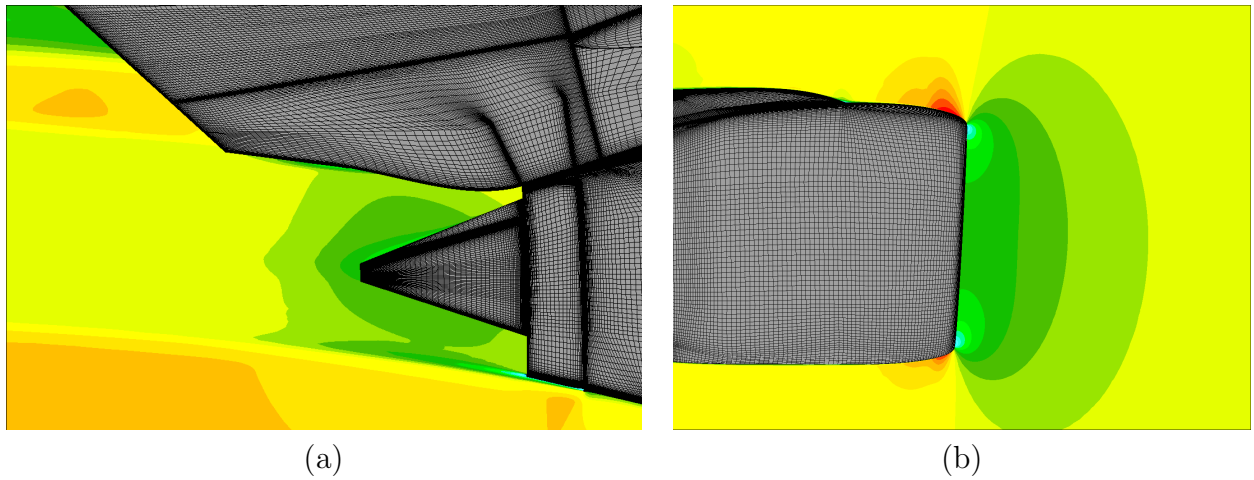


Figure 4.19: Iso Mach number ; (a) Back of the engine ; (b) Front of the engine

**Sensor for the lift coefficient** The following figure illustrates the criterion  $\theta$  for the lift on the planes illustrated Figure 4.18. Figure 4.20(a) shows that the zone above the fuselage after the nose is detected to be sensitive. Moreover high sensitivity near the non-coincident block interface located under the fuselage are noticed. Figure 4.20(b) shows that the shock area is detected just like the leading edge and the boundary layer after the shock. Besides a sensitive mesh area near a non-coincident block interface under the body is observed.

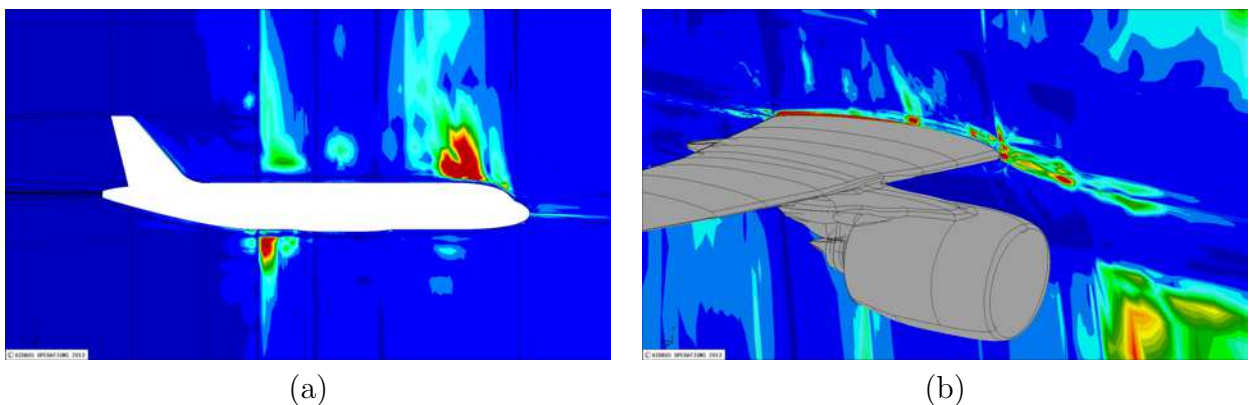


Figure 4.20: Criterion  $\theta$  for the lift ; (a) Symmetry plane ; (b) Plane between the engine and the fuselage

The next figure illustrates the criterion  $\theta$  for the lift on the geometrical plane already illustrated on Figures 4.19. No important sensitivity on the back side of the engine is observed (Figure 4.21(a)). However a sensitive mesh location at the upper side of the engine is noticed (Figure 4.21(b)).

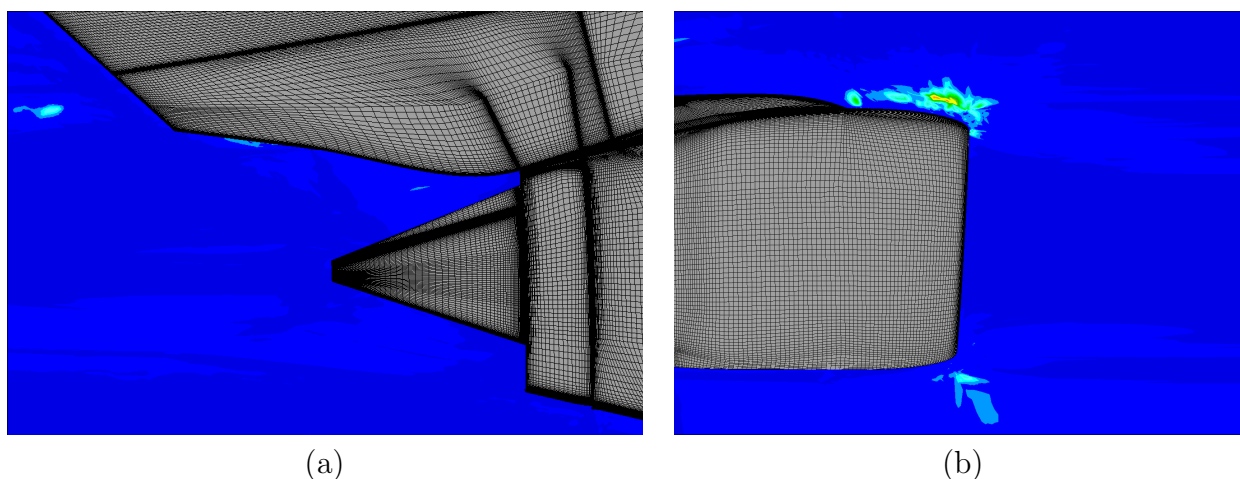


Figure 4.21: Criterion  $\theta$  for the lift ; (a) Back of the engine ; (b) Front of the engine

**Sensor for the drag coefficient** The following figure illustrates the criterion  $\theta$  for the drag on the symmetry plane (figure 4.22(a)) and on the already considered plane between the fuselage and the wing (figure 4.22(b)). The mesh area above the fuselage after the nose is detected just as the previous case for the lift. The same observation can be done for the non-coincident block interface located under the fuselage. However, the zone upwind to the tailplane is detected whereas it was not for the lift. Concerning the sensitivity on the selected plane between the engine and the fuselage, the same areas as for the lift are detected.

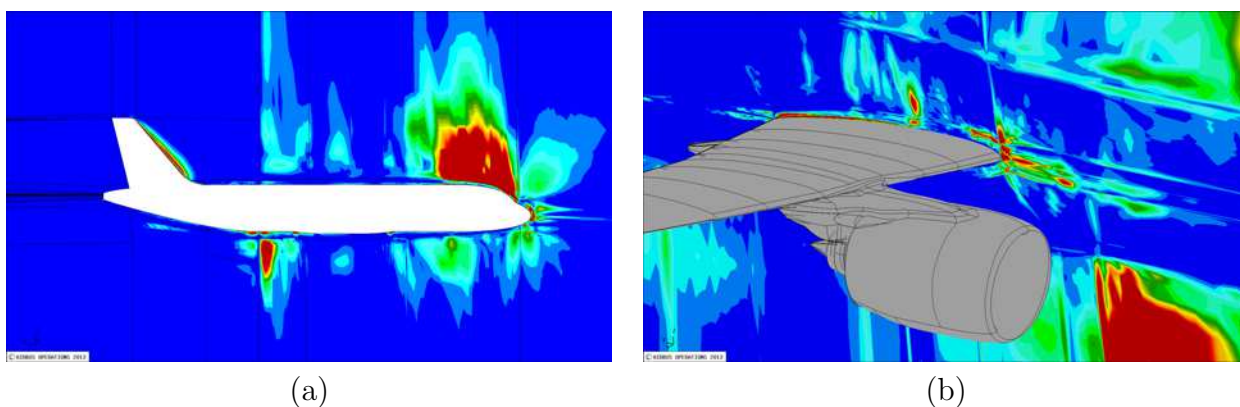


Figure 4.22: Criterion  $\theta$  for the drag ; (a) Symmetry plane ; (b) Plane between the engine and the fuselage

The next figure illustrates the criterion  $\theta$  for the drag on a constant  $y$  plane located close to the engine. There is no important sensitivity on the back side of the engine (Figure 4.23(a)). The same phenomenon was observed for the lift (Figure 4.21(a)). Concerning the front of the engine (Figure 4.21(b)), the upper side is detected by the sensor as in the previous case but with higher intensity. Moreover, the lower side is also detected to be a sensitive zone which was not the case for the lift (Figure 4.21(b)).

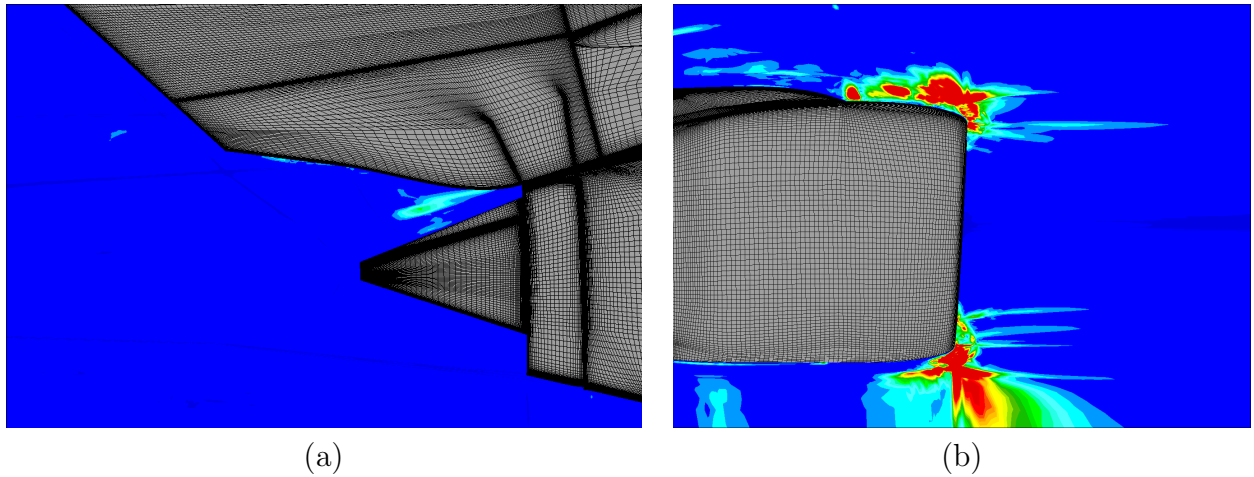


Figure 4.23: Criterion  $\theta$  for the drag ; (a) Back of the engine ; (b) Front of the engine

**Sensor for the temperature** The following figure illustrates the criterion  $\theta$  for the temperature on the symmetry plane (Figure 4.24(a)) and on the already considered constant  $y$  plane between the fuselage and the wing (Figure 4.24(b)). The area above the fuselage after the nose is detected again (like the two previous cases). The fluid zone upwind the tailplane is detected like the drag. Moreover, non-coincident block interfaces are detected above the fuselage. Whereas in the previous cases it was the block interface under the fuselage that was detected. Concerning the sensor in the plane located between the engine and the fuselage, the upstream area is detected as well as the near wall zone. In this case, the sensor close to the shock is not as strong as in the previous cases and the non-coincident block interface that was sensitive for the previous cases is not detected for temperature.

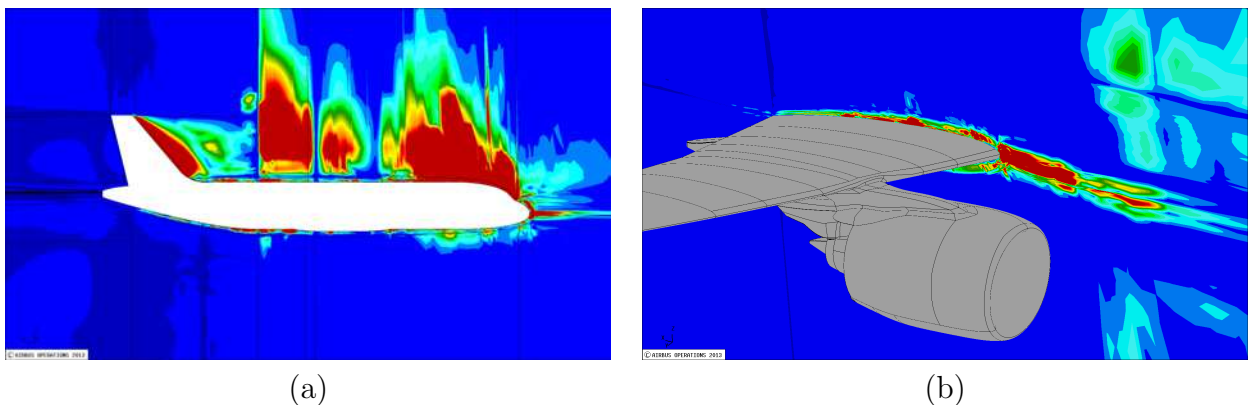


Figure 4.24: Criterion  $\theta$  for the temperature ; (a) Symmetry plane ; (b) Plane between the engine and the fuselage

The next figure illustrates the criterion  $\theta$  for the temperature on the constant  $y$  plane located close to the engine. There is a mesh area presenting important values of the sensor on the back side of the engine 4.25(a) which was not the case for both the lift and the drag. Finally, the figure 4.25(b) illustrates the sensor values at the front of the engine. High values are observed at both the upper and lower side of the casing like for the drag.

Besides the upstream location of these two mesh areas are detected with a higher intensity for the temperature than for the drag.

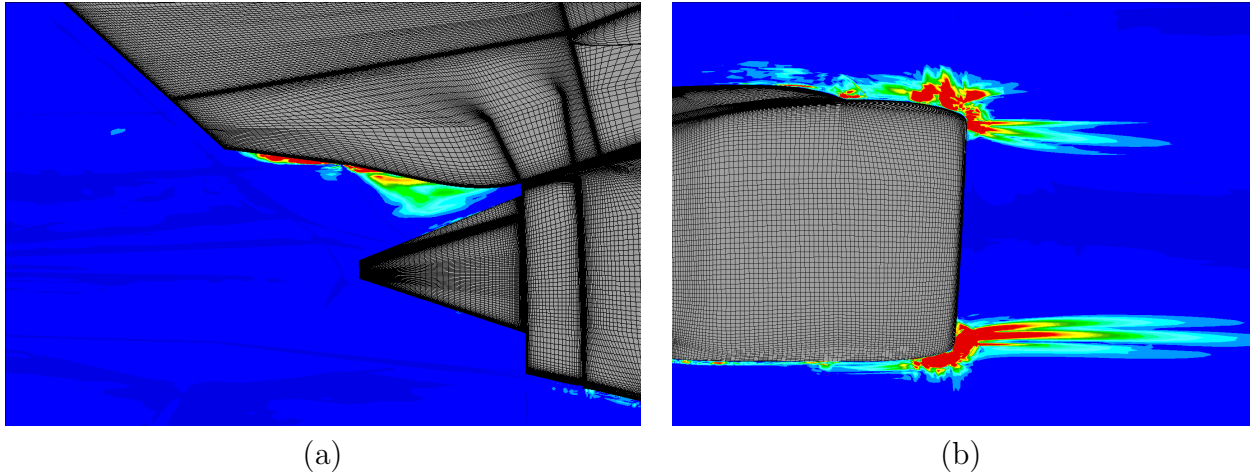


Figure 4.25: Criterion  $\theta$  for the temperature ; (a) Back of the engine ; (b) Front of the engine

### 4.4.3 Conclusions

The visualization of the local criterion  $\theta$  on this industrial case confirms the efficiency of the tool for the evaluation of the local mesh quality for the computation of a given output. The goal oriented aspect of the proposed criterion has been clearly highlighted. Since it detected mesh areas for the computation of the drag or lift that have not been detected for the computation of the temperature and conversely.

## 4.5 Conclusions

The objective of this chapter was to assess the method proposed in the previous chapters in the more complex context of three-dimensional flows described by the RANS equations. The method used for the two-dimensional cases (presented in the previous chapter) could not be applied directly; it was necessary to improve the adaptation process as well as the definition of the spatial mean of  $dJ/dX$  because the computational cost associated to the three-dimensional cases.

The mesh adaptations were carried out for a RANS flow around the XRF-1 configuration for the computation of both the pressure drag coefficient ( $CD_p$ ) and the pressure lift coefficient ( $CL_p$ ). These adaptations did not lead to significant improvements of the output estimations. However, for both cases the value of the output (on which the adaptation was based) has been slightly improved. Therefore it seems that the mesh locations detected by the sensor are relevant as it was for the two-dimensional cases. Besides it appeared that the remeshing is efficient inside the volume mesh where both the aerodynamic field quality and the local criterion values are improved. Unfortunately the criteria

values remain high near the walls on the adapted meshes. This shows up that the criteria detect that the remeshing should be improved in these mesh locations.

The extension to three-dimensional RANS test cases of the proposed method is not straightforward. However the numerical results presented in this chapter show that the proposed criteria seems to be relevant as well as for the previous cases but that the remeshing method has a critical importance for the adaptation efficiency. Therefore the remeshing strategy should be improved for efficient three-dimensional mesh adaptations.

In this context the sensor computations performed on the Generic Modern Aircraft configuration show promising results. Indeed it shows that the sensor seems to be able to provide the relevant sensitive mesh locations for the computation of a given output even for realistic configurations.

## 4.5. CONCLUSIONS

# Conclusions

Les objectifs de cette thèse étaient d'une part l'étude de méthodes d'adaptation de maillages pour le calcul de fonctions et d'autre part la construction d'indicateurs globaux de qualité de maillage. La dérivée totale de la fonction d'intérêt par rapport aux coordonnées du maillage était à la base des méthodes proposées.

La première étape était le développement et l'application de méthodes d'adaptation de maillages pour des écoulements de fluides parfaits. L'objectif de cette étude était de mettre en évidence le fait que la dérivée  $dJ/dX$  est une quantité pertinente en adaptation de maillages pour le calcul de fonctions. À ce moment deux stratégies de remaillages ont été considérées : l'ajout de nœuds et le déplacement de nœuds qui étaient basés sur des paramétrisations de maillages. Concernant la méthode d'ajout de nœuds, la détection des rangées de cellules où un raffinement est nécessaire a été basée sur la norme de  $dJ/dX$ . Concernant la méthode de déplacement de nœuds, il était supposé que les fonctions d'intérêt étaient affectées de façon monotone par la dissipation numérique. Ainsi la méthode consistait à maximiser (ou minimiser) les fonctions d'intérêt. La moyenne de  $\|dJ/dX\|$  pour tous les nœuds du maillage a été étudiée tout comme la moyenne de  $\|dJ/dX\|$  multiplié par une longueur caractéristique associée à chaque nœud. Ces critères globaux ont été corrélés à la qualité des évaluations de fonction sur les différents maillages considérés. Il est apparu que c'est  $\|dJ/dX\|r$  qui est faible sur les maillages bien adaptés au calcul de  $J$ .

Les résultats obtenus dans cette première étude ont confirmé l'intérêt d'utiliser  $dJ/dX$  pour atteindre nos objectifs. Ainsi l'étape suivante a consisté à fixer les critères (locaux et globaux) tout comme la stratégie de remaillage. Concernant les critères, il y a deux phénomènes doivent être pris en compte. Le premier est que, comme mentionné ci-dessus, les déplacements admissibles de nœuds doivent être utilisés. Ceci a conduit au critère local  $\theta(i, j)$  qui est en chaque nœud la norme de  $dJ/dX$  multipliée par la moitié de la distance au nœud voisin le plus proche. Le second phénomène à prendre en compte est la régularité du champ  $dJ/dX$ . En effet, ce champ peut présenter d'importantes irrégularités. Ainsi qu'un mouvement local d'un ensemble de nœuds peut avoir un faible impact sur l'estimation de la fonction à cause d'un effet de compensation. Cet effet peut être pris en compte à l'aide d'une moyenne spatiale de  $dJ/dX$ ,  $\overline{\mathcal{P}(dJ/dX)}$ , qu'on a fait intervenir dans un critère local  $\bar{\theta}(i, j)$  et du critère global  $\bar{\theta}$  définis par analogie à  $\theta(i, j)$  et  $\theta$ . Le lien entre la précision des valeurs de fonctions et les faibles valeurs du critère a été étudié sur des familles de maillages paramétrées pour des écoulements de fluides parfaits. Il a été observé une bonne corrélation entre les maillages qui fournissent de bonnes valeurs de fonction et ceux qui ont de faibles valeurs des critères. Ainsi, même si cette corrélation n'est pas parfaite, le critère local  $\bar{\theta}(i, j)$  a été utilisé pour détecter les zones du maillage à raffiner.

Concernant la méthode de remaillage, l'approche par déplacements de nœuds a été considérée. Cependant la méthode utilisée tout d'abord ne pouvait être généralisée car

elle suppose que les fonctions d'intérêt sont affectées de façon monotone par la dissipation numérique. De plus cette méthode utilisait une paramétrisation de maillage et la qualité des résultats dépendait donc de la qualité de cette paramétrisation. Une autre approche a donc été considérée : cette méthode s'appuie sur un système d'équations aux dérivées partielles elliptiques et permet des raffinements locaux. Cette technique a été appliquée pour des écoulements de fluides parfaits autour du profil NACA0012 et pour un écoulement RANS autour du profil RAE2822. Les résultats ont montré une amélioration des estimations de fonctions ainsi qu'une réduction du critère global.

La dernière étape a été l'étude de la méthode proposée pour des cas industriels tridimensionnels. La méthode d'adaptation de maillages a été appliquée pour un écoulement RANS autour de la configuration XRF-1. Le critère local a aussi été calculé sur un maillage autour de la configuration "Generic Modern Aircraft" pour évaluer son efficacité à détecter les zones sensibles d'un maillage pour le calcul de fonctions sur une configuration complexe. Les résultats obtenus pour trois fonctions (coefficient de portance, coefficient de traînée et intégrale surfacique de la température) confirment que le senseur proposé est capable de fournir des zones cohérentes du maillage à raffiner. De plus l'aspect "goal oriented" du critère est bien mis en évidence dans la mesure où les zones détectées dépendent de la fonction considérée.

Ces travaux ont confirmé l'efficacité de l'utilisation de  $dJ/dX$  pour adapter et qualifier des maillages. Une bonne corrélation entre les faibles valeurs du critère et les bonnes valeurs de fonctions a été mise en évidence. Cependant cette corrélation n'est pas parfaite et peut donc possiblement être améliorée. Plusieurs voies d'étude peuvent être considérées : l'amélioration de la longueur caractéristique (pour estimer plus finement les déplacements admissibles des nœuds) ; l'amélioration de la moyenne spatiale du champ  $\mathcal{P}(dJ/dX)$  (pour améliorer l'efficacité de la prise en compte des éventuels effets de compensations dues aux irrégularités du champ  $\mathcal{P}(dJ/dX)$ ). De plus, ce critère ne fournit pas d'information sur le gain potentiel que l'on peut obtenir si une adaptation de maillage est effectuée.

À ces améliorations possibles de la méthode proposée, il est important de remarquer qu'il y a aussi d'autres axes d'étude intéressants à considérer : une étude plus approfondie de la méthode appliquée en multipoint mérite d'être menée dans la mesure où la construction de maillages adaptés pour plusieurs points du domaine de vol a un intérêt industriel particulier dans le cadre de l'évaluation des performances aérodynamiques des aéronefs. Une autre voie d'étude est l'amélioration du critère global par exemple en utilisant un champ  $dJ/dX$  plus précis (qui inclus le terme  $\lambda_6(\partial R_6/\partial X)$ ). L'influence de la méthode de remaillage utilisée a été observée au cours de cette étude ainsi l'amélioration des techniques de remaillage où l'utilisation de nouvelles techniques est aussi un voie d'étude. L'intégration de la méthode à une chaîne d'optimisation et l'évaluation de l'amélioration des résultats que cela peut occasionner est aussi un axe d'étude à considérer. Et enfin, on peut noter que la méthode proposée peut s'étendre aux maillages non-structurés pour lesquels les possibilités de remaillages sont plus vastes.

# Conclusions

The objectives of this thesis were to study goal oriented methods for both mesh adaptation and mesh quality assessment. The total derivative of the functional output w.r.t. the mesh nodes coordinates was at the basis of all the proposed methods.

The first step was the development and the application of a mesh adaptation method to Eulerian flows. The objective of this study was to show that the derivative  $dJ/dX$  is actually a relevant field for goal oriented mesh adaptations. At that time two remeshing strategies were considered: node addition where new mesh lines were added (or mesh planes in three dimensions) and node displacement that was based on mesh parameterizations. Concerning the node addition method, the detection of the mesh cell rows where a refinement was necessary has been done using a sensor based on the norm of  $dJ/dX$ . Concerning the node displacement method, it was supposed that the output estimations were monotonically affected by the numerical dissipation. Therefore the method consisted of a maximization (or minimization) of the functional outputs. This study also demonstrated that  $dJ/dX$  can be used to bring up global criteria of mesh quality. In this way the mean of  $\|dJ/dX\|$  over all mesh nodes was studied as well as the mean of  $\|dJ/dX\|$  times a local characteristic length (associated to each node). These global criteria are connected to the quality of the meshes for the output computations.

The results obtained in this first study confirmed the interest of the derivative  $dJ/dX$  for our purpose. Hence the next step consisted in improving both criteria (local and global) and the remeshing strategy. Concerning criteria, it appeared that two phenomena have to be taken into account. The first one is that the local admissible node displacements have to be used. This led to the local criterion  $\theta(i, j)$  that is for each node the norm of  $dJ/dX$  times half the distance to the nearest neighbour node. The second phenomenon that has to be taken into account is the regularity of the  $dJ/dX$  field. Indeed, in actual fact the  $dJ/dX$  field can present important irregularities. Thus a local node movement could have little impact on the functional estimation due to the compensation effects. These effects are taken into account through a spatial mean of  $dJ/dX$ . This new field led to the definition of the local criterion  $\bar{\theta}(i, j)$  and the corresponding global one  $\bar{\theta}$ . The connection between the accuracy of the outputs and the low criteria values has been studied on parametrized mesh families for Eulerian flows. It appeared that a good correlation exists between the meshes that provided good function estimates and those that provided low criteria values. Therefore, even if this correlation was not perfect, the local criterion  $\bar{\theta}(i, j)$  was used to detect the mesh locations to refine.

Concerning the remeshing method, we considered adaptations by nodes displacement. However the previously used method could not be used. Indeed this approach supposed that the functions are monotonically affected by the numerical dissipation. Moreover this method used mesh parameterizations and thus the quality of the results depends on the quality of this parametrization. Therefore another approach was considered. The chosen

method was based on an elliptic system of PDEs and allowed more local refinements. This new method was applied for Eulerian flows around the NACA0012 airfoil and for a RANS flow around the RAE2822 airfoil. The results demonstrated improvements of the output estimates and reduction of the global criterion values.

The last step was to study the proposed approach in three-dimensional industrial cases. The mesh adaptation method has been applied to a RANS flow around the XRF-1 configuration. The proposed local criterion has been computed on a mesh around the Generic Modern Aircraft configuration in order to assess its relevancy to detect the sensitive mesh locations for output estimations on a complex configuration. The results obtained for three functions (lift coefficient, drag coefficient and the integrated temperature) confirm that the proposed sensor was able to provide coherent mesh locations to refine. Moreover the goal oriented aspect of the criterion was clearly highlighted as the detected mesh locations depended on the considered output.

Finally these works have confirmed the efficiency of the use of  $dJ/dX$  for both mesh adaptation and qualification. A good connection has been shown up between the low criterion values and the good output values. However the connection was not perfect hence the criterion may be improved. Several ways of investigation can be considered: improvement of the characteristic length (in order to use a better estimation of the local admissible nodes displacement) ; improvement of the spatial mean of the field  $\mathcal{P}(dJ/dX)$  (in order to efficiently take into account the possible compensation effects that may occur in a local mesh adaptation due to the  $\mathcal{P}(dJ/dX)$  field irregularities). Moreover, this criterion does not provide information about the potential benefit from a mesh adaptation.

In addition to these possible improvements to the proposed method, it is important to notice that there are also interesting ways forward to consider. A study of the multipoint use of the proposed method deserves to be carried out in so far that the construction of well suited meshes for several points of the flight domain has a particular industrial interest for the assessment of aircraft aerodynamic performances. Another way forward is the improvement of the global criteria for example using more accurate  $dJ/dX$  fields (that include the term  $\lambda_6(\partial R_6/\partial X)$ ). The remeshing method influence has been observed in this study hence the improvement of these remeshing techniques or the use of new techniques is also a way to be investigated. The integration of the proposed approach in a shape optimization process and the assessment of the induced results improvements is also a way forward. Finally one can notice that the proposed method could be extended to unstructured meshes.

# Appendix A

## The anisotropic smoothing method

The remeshing method based on an elliptic system of PDEs used in the chapters 3 and 4 requires to build up control functions for adaptation (denoted  $P_k^{adapt}$ ). These functions come from a scalar field  $s$  built up in order to have high values where the mesh needs to be refined and lower values where the node density is adequate. The control function  $P_k^{adapt}$  are defined as the relative variation of this scalar field for each topological direction. The field  $s$  has to be smooth enough since an irregular field would lead to irregular control functions  $P_k^{adapt}$  that would obviously lead to an irregular mesh at the next step of the adaptation process. Unfortunately the scalar field  $s$  involves the fields  $\theta$  or  $\bar{\theta}$  that are very irregular. It is hence necessary to use a smoothing operator in order to build up a regular smoothed field that has its higher values at the same location as the initial field  $s$ . The current appendix is devoted to the presentation of the smoothing operators that have been developed to achieve this goal. The test case is the RANS flow over the RAE2822 airfoil considered in the chapter 3 ( $M_\infty = 0.725$ ,  $Re.m^{-1} = 6.5 \times 10^6$  and  $AoA = 2.466^\circ$ ). The considered output is the pressure drag coefficient  $CD_p$ .

### A.1 Isotropic smoothing operator

The smoothed field is built through an iterative process. At each step and for all nodes, a new sensor value is computed by a mean using the values of the sensor at the neighbour nodes in all the topological direction. Figure A.1 illustrates the initial field  $s$  and the smoothed field using this isotropic operator.

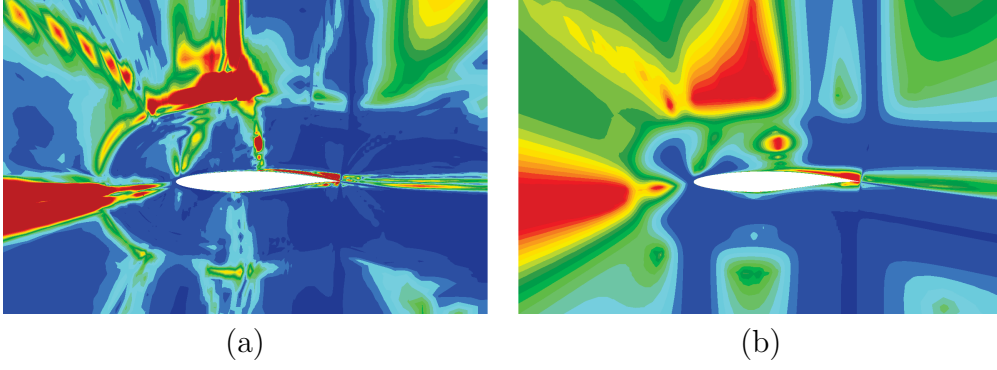


Figure A.1: (a) Sensor field  $\bar{\theta}$ ; (b) Smoothed field  $s$  using an isotropic smoothing

We notice that the isotropic smoothing operator preserves the mesh locations where the sensor has high values but it fails to remove some irregularities of the initial field.

## A.2 Anisotropic smoothing operator

This smoothing method is also an iterative operator process. At each step and for each node, a new value of the field  $s$  is computed according to the topological direction on which the sensor is the less regular. More precisely at each step the following values are computed (in a 2D case, the generalization to 3D is straightforward):

$$\tilde{s}_i = s_{i-1,j} - 2s_{ij} + s_{i+1,j} \quad \text{and} \quad \tilde{s}_j = s_{i,j-1} - 2s_{ij} + s_{i,j+1}$$

The values  $\tilde{s}_i$  and  $\tilde{s}_j$  are estimations of the second derivative of  $s$  in the different topological directions. Then the field is smoothed only in the direction that presents the higher value of  $\tilde{s}_i$  or  $\tilde{s}_j$ . To do that, an intermediate value  $s_{ij}^{n+\frac{1}{2}}$  is computed from the values of the field  $s$  at the current step  $n$ :

$$s_{ij}^{n+\frac{1}{2}} = \begin{cases} \frac{1}{2}(s_{i-1,j} + s_{i+1,j}) & \text{if } \tilde{s}_i \geq \tilde{s}_j \\ \frac{1}{2}(s_{i,j-1} + s_{i,j+1}) & \text{if } \tilde{s}_j \geq \tilde{s}_i \end{cases}$$

This intermediate value  $s_{ij}^{n+\frac{1}{2}}$  corresponds to the value of  $s$  that would have led to a value of  $\tilde{s}$  equal to zero. The value of  $s_{ij}^{n+1}$  at the step  $n+1$  is given by:

$$s_{ij}^{n+1} = (2 - s_{ij}^n)s_{ij}^{n+\frac{1}{2}} + (s_{ij}^n - 1)s_{ij}^n$$

This formula was built up in order to smooth with less intensity the values of the scalar field  $s$  at the nodes that present the higher values of  $s$ . Indeed one of the requirement for this smoothing operator is to preserve the mesh locations where the sensor has high values. The following figure illustrates the application of the new smoothing operator.

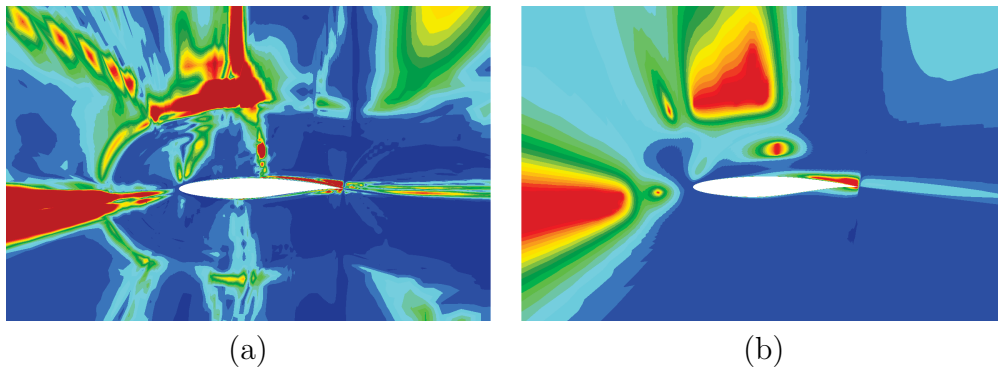


Figure A.2: (a) Sensor field  $\bar{\theta}$  ; (b) Smoothed field  $s$  using an anisotropic smoothing

We notice that the sensor field obtained with this smoothing process keeps only the more important locations of the fluid domain where the initial sensor has its highest values. Nevertheless some oscillations also occur. Therefore it appeared that an efficient smoothing operator uses both the isotropic and the anisotropic smoothing processes. More precisely the isotropic smoothing is used first in order to build a smoother sensor field than the initial one. Then the anisotropic smoothing is applied (with less iterations) in order to reduce the remaining irregularities. Finally the isotropic smoothing is applied again with less iterations in order to smooth the oscillations that may occur from the anisotropic smoothing. The following figure illustrates the smoothed field that comes out this smoothing process.

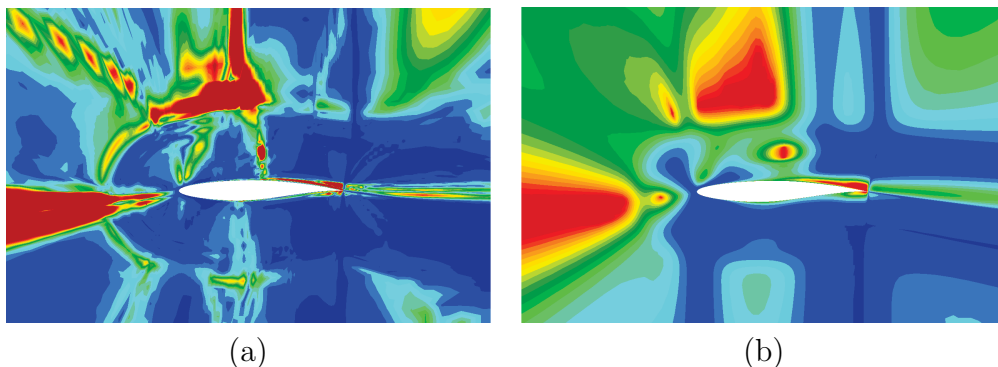


Figure A.3: (a) Sensor field  $\bar{\theta}$  ; (b) Smoothed field  $s$  using an anisotropic smoothing

We notice that the smoothed field presents more mesh areas with high sensor values in comparison to the field calculated by the anisotropic smoothing only (figure A.2). This is due to the use of the isotropic smoothing. We also notice that this sensor field presents less irregularities than the one obtained with the isotropic smoothing only (figure A.1) and that no oscillation appears.

### A.3 Impact of the smoothing on the remeshing

This smoothing operator has been designed to construct regular sensor fields in order generate regular new meshes. The following figures show the mesh obtained with the

### A.3. IMPACT OF THE SMOOTHING ON THE REMESHING

isotropic smoothing operator only A.4(a) and using the anisotropic smoothing operator only A.4(b).

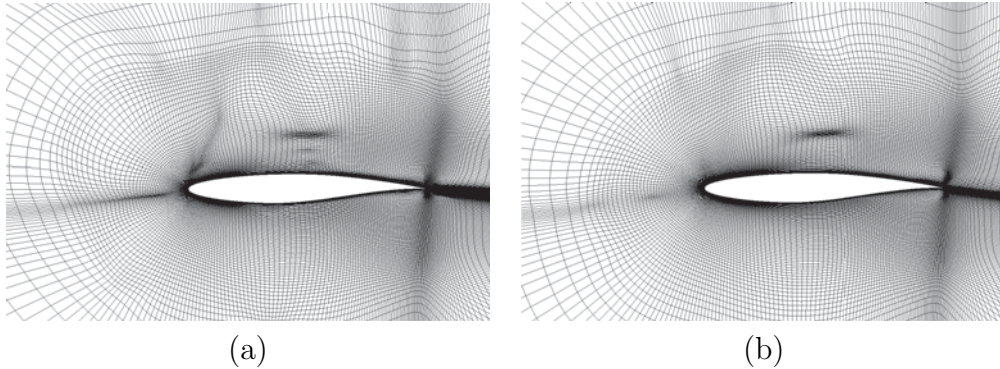


Figure A.4: (a) Mesh built using the isotropic smoothing only ; (b) Mesh built using the anisotropic smoothing only

As expected, we notice that the mesh build up using the isotropic smoothing presents some irregularities in comparison to the mesh obtained with the anisotropic smoothing. These irregularities become stronger during the mesh adaptation process. However we also notice that the mesh built up using the anisotropic smoothing is less refined in several areas (see the leading edge for example).

The following figure illustrates the mesh obtained with the smoothing operator based on both the isotropic and anisotropic operators.

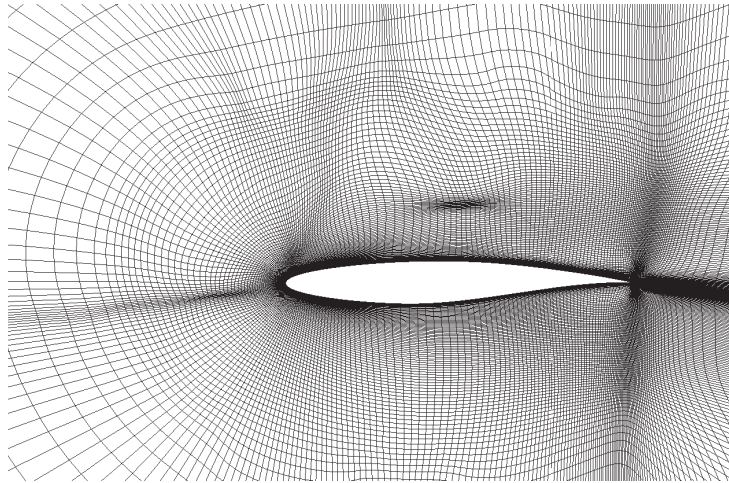


Figure A.5: Mesh built using the smoothing based on both the isotropic and anisotropic operators

We can notice that this mesh is similar to the one obtained with the isotropic smoothing operator. However this mesh is slightly more regular and, actually, the meshes created by the adaptation process are more regular.

# Appendix B

## Comparison with feature-based mesh adaptation

The following appendix is devoted to the presentation of a mesh adaptation carried out on the RAE2822 test case which has been presented in the chapter 3. However the sensor used in the following adaptation is based on the feature of the flows instead of the local criterion  $\theta_{ij}$  (or  $\bar{\theta}_{ij}$ ). This approach is a classical and the objective of this appendix is to provide a comparison between this method and the one proposed in this thesis. The idea of the feature-based method is to increase the node density where some variables present high gradients. In this study the Mach number gradient was used to identify the locations of the mesh that have to be refined.

### B.1 Construction of a feature-based sensor

The norm of the Mach number gradient was used instead of the norm of  $\overline{\mathcal{P}(dJ/dX)}$  in the definition of the local criterion. This lead to the feature-based sensor  $\theta_{ij}^{FB}$ :

$$\theta^{FB}(i, j) = \|\nabla M_{i,j}\| r_{i,j}$$

where  $M_{i,j}$  is the Mach number at the node  $(i, j)$  and  $r_{i,j}$  is the characteristic length associated to this node (as presented in the section 3.1). Moreover a global value can be associated to the entire mesh too. This is done using the same definition of the global criterion  $\theta$  in function of the local one  $\theta(i, j)$ . This leads to:

$$\theta^{FB} = \frac{1}{N_i N_j} \sum_{i,j} \theta^{FB}(i, j)$$

In the following example, the Mach number gradients are evaluated at first at the cells. The following relation is used (for the cell  $l$ ).

$$\nabla M_l = \frac{1}{Vol_l} \sum_{m \in neigh_l} \frac{M_l + M_m}{2} \vec{n}_{l,m}$$

where  $Vol_l$  is the volume of the cell  $l$ ,  $neigh_l$  is the set of the cells that are adjacent to the cell  $l$  and  $n_{l,m}$  is the unit normal vector of the interface between the cell  $l$  and the cell

## B.1. CONSTRUCTION OF A FEATURE-BASED SENSOR

$m$  (oriented from the cell  $l$  to the cell  $m$ ). The gradients were then interpolated at the nodes using these values computed at the cells.

The following figure illustrates the iso Mach number and the its gradient on the initial mesh.

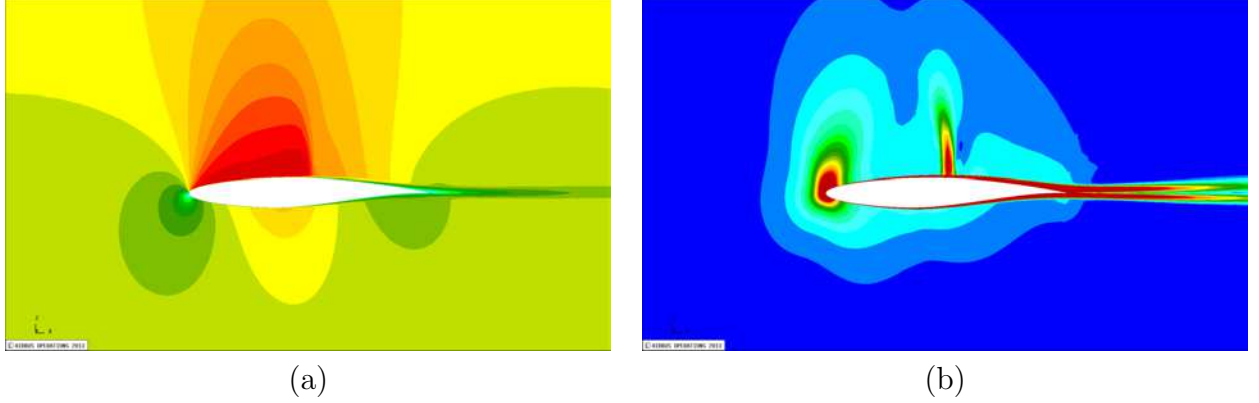


Figure B.1: RAE2822,  $M_\infty = 0.725$ ,  $\text{AoA} = 2.466^\circ$ ,  $\mathcal{R}e/m = 6.5 \cdot 10^6$ . (a) Iso Mach number ; (b) Mach number gradient

The following figure shows the corresponding feature-based criterion  $\theta^{FB}(i, j)$  (Figure B.2(a)) and the corresponding criterion  $\bar{\theta}[Cd]$  (Figure B.2(b)) that was computed on this mesh in the adaptation for  $Cd$  presented in Section 3.3.

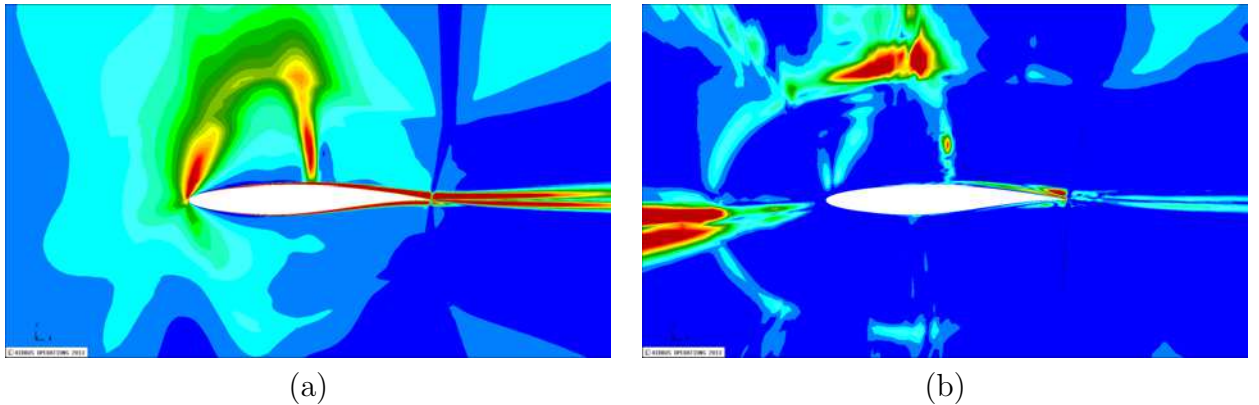


Figure B.2: RAE2822,  $M_\infty = 0.725$ ,  $\text{AoA} = 2.466^\circ$ ,  $\mathcal{R}e/m = 6.5 \cdot 10^6$ . (a) Criterion  $\theta^{FB}$  ; (b)  $\bar{\theta}[Cd]$

We notice that these two sensors do not detect the same mesh areas. The feature-based sensor detects only the leading edge, the shock location and the wake. The goal oriented sensor (built up from  $dCd/dX$ ) detects these areas too but with less intensity. Moreover the later sensor also detects the zone upstream the airfoil which is not flagged by the feature-based sensor. It can also be noticed that the mesh location above the shock where the cell size begin to increase are detected by the two sensors but with a higher intensity for the goal oriented sensor.

## B.2 Feature-based mesh adaptation

Three iterations of the feature-based mesh adaptation process has been carried out. The results are summarized in the following table.

Iteration	$CL_p$	$Cd (\times 10^{-4})$	$Cd_{sp,irr} (\times 10^{-4})$	$Cd_{sp,rev} (\times 10^{-4})$	$\theta^{FB}$
0	0.73950	123.93	2.95	3.32	$2.2426 \cdot 10^{-6}$
1	0.74350	120.27	2.19	3.35	$2.1350 \cdot 10^{-6}$
2	0.74178	118.86	2.84	3.38	$2.3095 \cdot 10^{-6}$
3	0.73859	117.95	2.86	3.40	$2.3866 \cdot 10^{-6}$

Table B.1: RAE2822,  $M_\infty = 0.725$ ,  $\text{AoA} = 2.466^\circ$ ,  $\mathcal{Re}/m = 6.5 \cdot 10^6$ . Outputs values and criterion  $\theta^{FB}$  during the feature-based mesh adaptation process

We can notice that good values are obtained for the near-field drag estimations. Nevertheless the  $Cd$  value is under the limiting one for the last iteration. The quality of the  $CL_p$  estimations is improved at the first step and is degraded at the next steps. The spurious drag values are stable. However the  $Cd$  value given by the far-field drag breakdown is far from the one obtained with the fine meshes of the hierarchy in comparison to the ones obtained with the goal oriented adaptations. Finally the value of the criterion  $\theta^{FB}$  is lower than the initial one only at the first step. Hence this criterion seems to not be well suited to evaluate the global quality of the solution. The following figure illustrates the meshes obtained during the feature-based adaptation process.

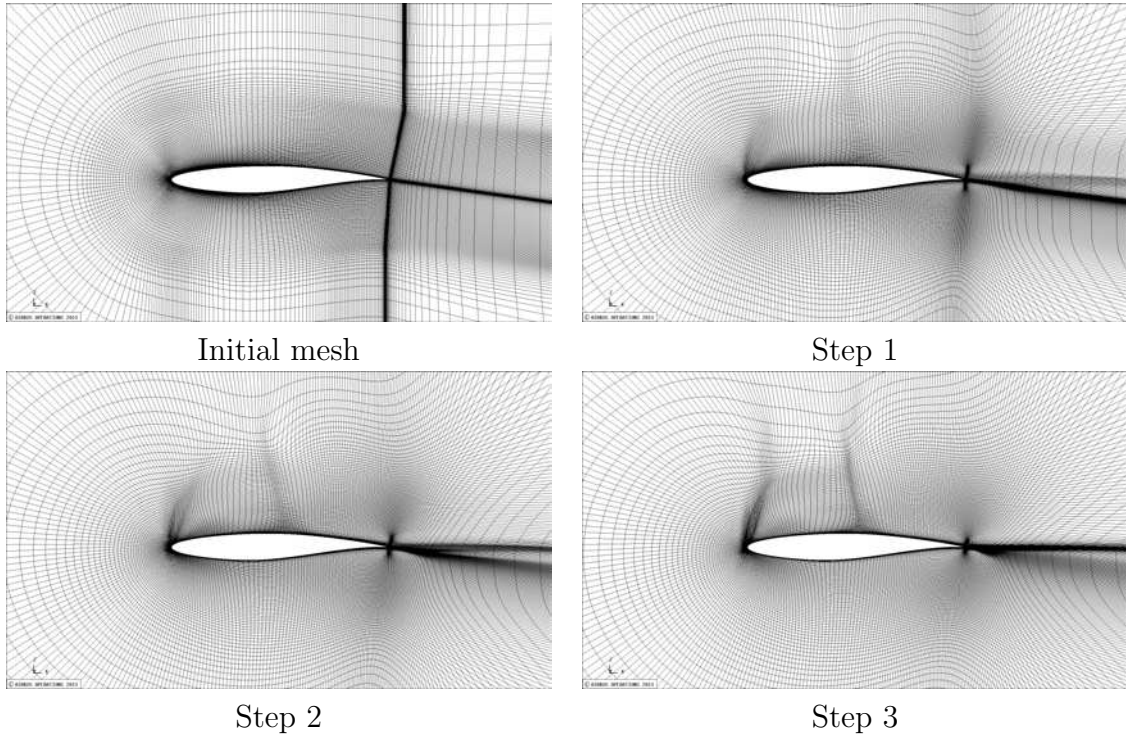


Figure B.3: Meshes during the feature-based adaptation process,  $M_\infty = 0.725$ ,  $\text{AoA} = 2.466^\circ$ ,  $\mathcal{Re}/m = 6.5 \cdot 10^6$

We notice that the method leads to refinements only in the locations that are initially detected by the sensor. In comparison to the goal oriented meshes obtained in Section 3.3, we notice that there is no increase of node density at the upstream. Moreover it appears that the refinements are done with a higher intensity for the feature-based adaptations. All these remarks can be explained by the evolution of the sensor during the adaptation process. The following figures illustrates these fields on the different meshes of the adaptation steps.

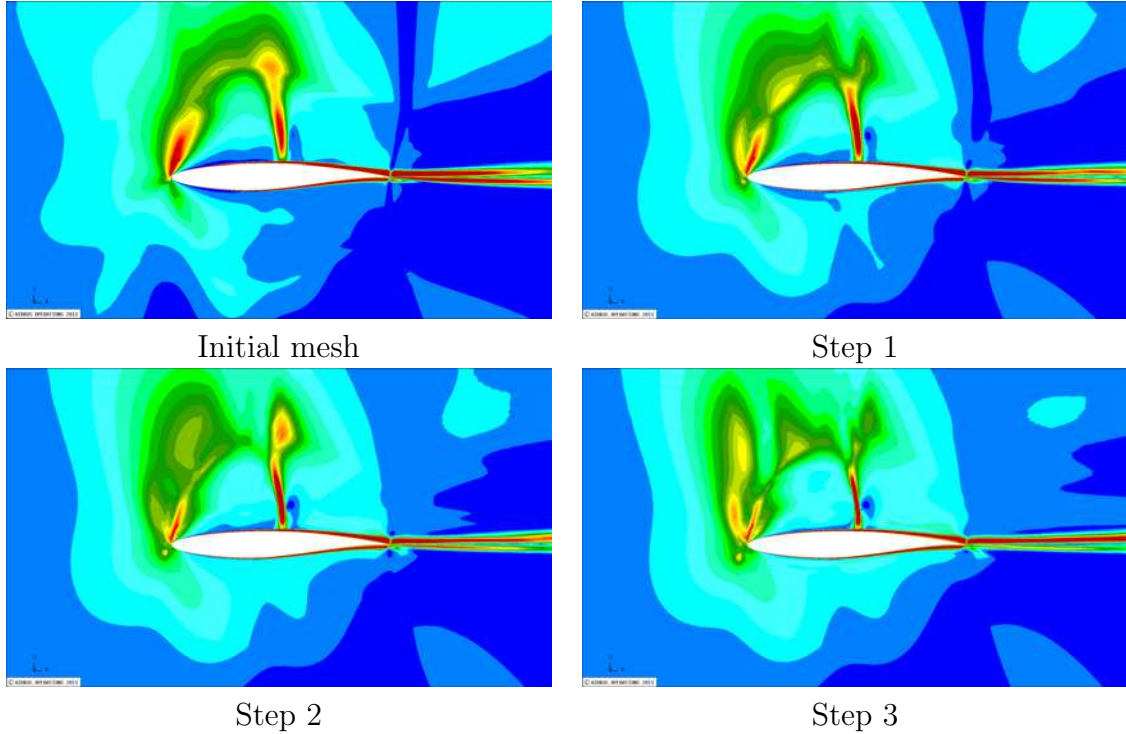


Figure B.4: Criterion  $\theta^{FB}$  during the feature-based adaptation process,  $M_\infty = 0.725$ ,  $\text{AoA} = 2.466^\circ$ ,  $\text{Re}/m = 6.5 \cdot 10^6$

We notice that the same areas are detected by the sensor at each step. Indeed the feature-based sensor is connected to the Mach number gradient on which the high values are always in the same locations. It appears that the reduction of the characteristic length on the nodes that present high values of the Mach number gradients is not enough to reduce the values of the sensor  $\theta^{FB}$ . This is another major difference between the feature-based approach and the goal oriented one. Indeed as presented in Section 3.3.2 (Figures 3.11 and 3.14), the goal oriented sensor fields present lower values on the adapted meshes than on the initial one. Therefore the goal oriented approach is more efficient to evaluate the quality of the meshes.

In conclusion even if the feature-based adaptations can provide improvements of the outputs estimations (as it was already observed in [50]), these adaptations can fail to converge toward satisfactory solutions. Indeed it can be noticed that the error in the computed outputs begin to increase since the second iteration. And as the sensor does not decrease during the adaptation process (as illustrated previously on Figures B.4), the solution error would continue to increase if more iteration would have been done. Moreover this approach is, by construction, not connected to the functional outputs neither to any error indicator. Thus the goal oriented method appears to be more reliable and efficient.

# Bibliography

- [1] F. Alauzet, S. Borel-Sandou, L. Daumas, A. Dervieux, Q. Dinh, and S. Kleinveld et. al. Multimodel design strategies applied to sonic boom reduction. *European Journal for Computational Mechanics*, 10(1):1–20, 2007.
- [2] R. Balasubramanian and J.C. Newman III. Comparison of adjoint-based and feature-based grid adaptation for functional outputs. *International Journal for Numerical Methods in Fluids*, 53:1541–1569, 2007.
- [3] A. Barthet. *Amélioration de la prévision des coefficients aérodynamiques autour de configurations portantes par méthode adjointe*. PhD thesis, Institut National Polytechnique de Toulouse, 2007.
- [4] A. Barthet, C. Airiau, M. Braza, and L. Tourrette. Adjoint-based error correction applied to far-field drag breakdown on structured grid. *AIAA Paper*, 2006-3315, 2006.
- [5] O. Baysal and M. Eleshaky. Aerodynamic design sensitivity analysis methods for the compressible Euler equations. *Journal of Fluids Engineering*, 113(4):681–8, 1991.
- [6] R. Becker and R. Rannacher. Weighted *a posteriori* error control in FE methods. *ENUMATH-97, Heidelberg*, 1998.
- [7] R. Becker and R. Rannacher. An optimal control approach to *a posteriori* error estimation in finite element methods. *Acta Numerica*, 10:1–102, 2001.
- [8] J. Bin, A. Uzun, and M.Y. Hussaini. Adaptive mesh redistribution method for domains with complex boundaries. *Journal of Computational Physics*, 230:3178–3204, 2011.
- [9] M. Bompard and J. Peter. Local search methods for design in aeronautics. *RTO-AVT-167 lecture series on strategies for optimization and automated design of gas turbine engines*, 2010.
- [10] L. Cambier and J.P. Veuillot. Status of the *elsA* CFD software for flow simulation and multidisciplinary applications. *AIAA Paper*, 2008-664, 2008.
- [11] M. de la Llave Plata, V. Couaillier, C. Marmignon, M.C. Le Pape, M. Gazaix, and B. Cantaloube. Further developments in the multiblock hybrid CFD solver *elsA-H*. *AIAA Paper*, 2012-1112, 2012.
- [12] D. Destarac. Far-field/near field drag balance and applications of drag extraction in *cfD*. *VKI Lecture Series*, pages 3–7, 2003.

- [13] R.P. Dwight. Goal-oriented mesh adaptation using a dissipation based error indicator. *International Journal for Numerical Methods in Fluids*, 56(8):1193–2000, 2007.
- [14] R.P. Dwight. Heuristic *a posteriori* estimation of error due to dissipation in finite volume schemes and application to mesh adaptation. *Journal of Computational Physics*, 227:2845–2863, 2008.
- [15] K.J. Fidkowski and Darmofal D.L. Output-based error estimation and mesh adaptation in computational fluid dynamics: overview and recent results. *AIAA Journal*, 49(4):673–94, 2011.
- [16] K.J. Fidkowski and P.L. Roe. An entropy adjoint approach to mesh refinement. *SIAM Journal on Scientific Computing*, 32(3):1261–1287, 2010.
- [17] P. Frank and G. Shubin. A comparison of optimisation based approaches for a model computational aerodynamics design problem. *Journal of Computational Physics*, 98:74–89, 1992.
- [18] M. Giles, M.G. Larson, J.M. Levenstam, and E. Süli. Adaptive error control for finite element approximation of lift and drag coefficient in viscous flow. *Tech. Rep. NA-97/06, Comlab, Oxford University*, 1997.
- [19] G.H. Hansen, R.W. Douglass, and A. Zardecki. *Mesh enhancement*. Imperial College Press, 2005.
- [20] R. Hartmann, J. Held, and T. Leicht. Adjoint-based error estimation and adaptive mesh refinement for the rans and (k- $\omega$ ) turbulence model equations. *Journal of Computational Physics*, 230:4268–4284, 2011.
- [21] R. Hartmann and P. Houston. Adaptive discontinuous galerkin methods for the compressible euler equations. *Journal of Computational Physics*, 182(2):508–532, 2002.
- [22] J.E. Hicken and D.W. Zingg. Aerodynamic optimization algorithm with integrated geometry parametrization and mesh movement. *AIAA Journal*, 48(2):400–13, 2010.
- [23] A. Jameson. Aerodynamic design via control theory. *Journal of Scientific Computing*, 3:233–60, 1988.
- [24] A. Jameson, W. Schmidt, and E. Turkel. Numerical solution of the Euler equations by finite volume methods using runge-kutta time stepping schemes. *AIAA Paper*, 1981-1259, 1981.
- [25] C. Johnson, R. Rannacher, and M. Boman. Numerics and hydrodynamics theory: towards error control in cfd. *SIAM Journal of Numerical Analysis*, 32:1058–1079, 1995.
- [26] W.T. Jones, E.J. Nieslsen, and M.A. Park. Validation of 3d adjoint-based error estimation and mesh adaptation for sonic boom prediction. *AIAA Paper*, 2006-1150, 2006.
- [27] S. Kapadia, W.K. Anderson, and C. Burdyslaw. Channel shape optimization of solid oxide fuel cells using advanced numerical techniques. *Computers and Fluids*, 41(1):41–50, 2011.

## BIBLIOGRAPHY

- [28] H.J. Kim and K. Nalahashi. Output-based error estimation and adaptative mesh refinement using viscous adjoint method. *AIAA Paper*, 2006-1395, 2006.
- [29] N. Kroll, H. Bieler, H. Deconinck, V. Couaillier, H. van der Ven, and K. Sorensen. A european adaptative on the development of adaptative higher-order methods variational methods for aerospace applications. *ADIGMA*, 2010.
- [30] N. Kroll, N. Gauger, J. Brezillon, K. Becker, and V. Schultz. Ongoing activities in shape optimization within the german project megadesign. *In Proceedings of ECCOMAS Congress, Jyvaskyla*, 2004.
- [31] M.G. Larson and T.J. Barth. *A posteriori* error estimation for discontinuous galerkin approximation of hyperbolic systems. *NAS Technical Report. NAS 99-010*, 1999.
- [32] E.M. Lee-Rausch, M.A. Park, W.T. Jones, D.P. Hammond, and E.J. Nielsen. Application of parallel adjoint-based error estimation and anisotropic grid adaptation for three-dimensional aerospace configurations. *AIAA Paper*, 2005-4842, 2005.
- [33] T. Leicht and R. Hartmann. Error estimation and anisotropic mesh refinement for 3d laminar aerodynamic flow simulations. *Journal of Computational Physics*, 229:7344–7360, 2010.
- [34] D.W. Levy, Labin K.R., Tinoco E.D., Vassberg J.C., Mani M.M., Rider B., Rumsey C.L., Wahls R.A., Morrison J.H., Brodersen O.P., Crippa S., Mavriplis D.J., and Murayama M. Summary of Data from the Fifth AIAA CFD Drag Prediction Workshop. *AIAA Paper*, 2013-0046, 2013.
- [35] A. Loseille, A. Dervieux, and F. Alauzet. Fully anisotropic goal-oriented mesh adaptation for 3d steady euler equations. *Journal of Computational Physics*, 229(2):2860–2897, 2010.
- [36] L. Machiels, J. Peraire, and A.T. Patera. *A posteriori* finite element output bounds for the incompressible navier-stokes equations; application to a natural convection problem. *Journal of Computational Physics*, 172:401–425, 2001.
- [37] M. Nemeć and M.J. Aftosmis. Adjoint error estimation and adaptative refinement for embedded-boundary cartesian mesh. *AIAA Paper*, 2007-4187, 2007.
- [38] M. Nemeć, M.J. Aftosmis, and M. Wintzer. Adjoint-based adaptative mehs refinement for complex geometries. *AIAA Paper*, 2008-725, 2008.
- [39] M. Nguyen-Dinh, J. Peter, R. Sauvage, M. Meaux, and J.A. Désidéri. Mesh quality assessment based on aerodynamic functional output total derivatives. *European Journal of Mechanics - B/Fluids*, 45:51–71, 2014.
- [40] M. Nguyen-Dinh, P. Trontin, M. Meaux, J. Peter, and F. Renac. Total derivative of aerodynamics functions w.r.t. volume or wall mesh nodes for shape optimization and mesh adaptation. *Proceedings of ODAS congress, Toulouse*, 2011.
- [41] E. Nielsen and B. Kleb. Efficient construction of discrete adjoint operators on unstructured grids by using complex variables. *AIAA Paper*, 2005-0324, 2005.

- [42] E. Nielsen, E.M. Lee-Rausch, and W.T. Jones. Adjoint-based design of rotors in a non-inertial reference frame. *Journal of Aircraft*, 47(2):638–46, 2010.
- [43] E. Nielsen and M.A. Park. Using an adjoint approach to eliminate mesh sensitivities in aerodynamic design. *AIAA Journal*, 44(5):948–53, 2005.
- [44] M.A. Park. Three-dimensionnal turbulent RANS adjoint-based error correction. *AIAA Paper*, 2003-3849, 2003.
- [45] M.A. Park. Adjoint-based, three-dimensional error prediction and grid adaptation. *AIAA Journal*, 42(9):1854–1862, 2010.
- [46] M.A. Park and D.L. Darmofal. Output-adaptative tetrahedral cut-cell validation for sonic boom prediction. *AIAA Paper*, 2008-6594, 2008.
- [47] J. Peter and R.P. Dwight. Numerical sensitivity analysis: a survey of approaches. *Computers and Fluids*, 39(3):373–91, 2010.
- [48] J. Peter, M. Lazareff, and V. Couaillier. Verification, validation and error estimation in cfd. *International Journal of Systems Modelling and Simulation*, 2(1/2):75–86, 2010.
- [49] J. Peter, M. Nguyen-Dinh, and P. Trontin. Goal oriented mesh adaptation using the total derivative of aerodynamic functions with respect to mesh coordinates - With applications to Euler flows. *Computers and Fluids*, 66:194–214, 2012.
- [50] J. Peter, M. Nguyen-Dinh, and P. Trontin. Goal oriented mesh adaptation using total derivative of aerodynamic functions with respect to mesh coordinates. *AIAA Paper*, 2012-158, 2012.
- [51] J. Peter, P. Trontin, and M. Nguyen-Dinh. Goal oriented mesh adaptation using total derivative of aerodynamic functions with respect to mesh coordinates. *AIAA Paper*, 2011-30, 2011.
- [52] N.A. Pierce and M.B. Giles. Improved lift and drag estimates using adjoint Euler equations. *AIAA Paper*, 1999-3293, 1999.
- [53] N.A. Pierce and M.B. Giles. Adjoint recovery of superconvergent functionals for pde approximations. *SIAM Review*, 42:247–264, 2000.
- [54] N.A. Pierce and M.B. Giles. Adjoint and defect error bounding and correction for functional estimates. *AIAA Paper*, 2003-3846, 2003.
- [55] S. Prudhomme and J. Oden. On goal oriented error estimation for elliptic problems: application to the control of pointwise error. *Computers Method in Applied Mechanics and Engineering*, pages 313–331, 1999.
- [56] G. Puigt, M. Gazaix, M. Montagnac, M.C. Le Pape, M. de La Llave Plata, C. Marmignon, J.F. Boussuge, and V. Couaillier. Development of a new hybrid compressible solver inside the CFD elsA software. *AIAA Paper*, 2011-3379, 2011.
- [57] A Rizzi. Computational mesh for transonic airfoils. *Numerical methods for the computation of inviscid transonic flows with shock waves. (A 82-12601 02-02) Braunschweig, Friedr. Vieweg und Sohn, 1981.,* pages 222–263, 1981.

## BIBLIOGRAPHY

- [58] P.L. Roe. Approximate Riemann solvers, parameter vectors and difference schemes. *Journal of Computational Physics*, 43:357–72, 1981.
- [59] G. Rogé and S. Borel-Sandou. Improvement of observations, error estimation and mesh adaptation using an adjoint based approach for aeroerodynamic calculations. *Proceedings of RTO-MP-AVT-147 symposium*, 2007.
- [60] G. Rogé and L. Martin. Goal oriented anisotropic grid adaptation. *C.R. Acad. Sci. Paris, Ser. I 346*, pages 1109–1112, 2008.
- [61] V Schmitt and A. Charpin. Pressure distributions on the ONERA-M6-Wing at transonic Mach numbers. experimental data for computer program assessment. *AGARD-R-138*, page 179.
- [62] B. Soni, R. Koomullil, D. Thompson, and H. Thornburg. Solution adaptive grid strategies based on point redistribution. *Computer Methods in Applied Mechanics and Engineering*, 189:1183–1204, 2000.
- [63] P.R. Spalart and Allmaras S.R. A one-equation turbulence model for aerodynamic flows. *AIAA Paper*, 1992-0439, 1992.
- [64] S. Spekreijse. Elliptic grid generation based on Laplace equations and algebraic transformations. *Journal of Computational Physics*, 118:38–61, 1995.
- [65] A. Taylor III, V Korivi, and G. Hou. Sensitivity analysis applied to the Euler equations: a feasibility study with emphasis on variation of geometric shape. *AIAA Paper*, 1991-0173, 1991.
- [66] J.F. Thompson, B. Soni, and N. Weatherill. *Handbook of grid generation*. CRC Press, 1998.
- [67] J.F. Thompson, Z.U.A. Warsi, and C.W. Mastin. *Numerical grid generation: Foundations and applications*. 1985.
- [68] A.H. Truong, C.A. Oldfield, and D.W. Zingg. Mesh movement for discrete-adjoint Newton-Krylov algorithm for aerodynamic optimization. *AIAA Journal*, 46(7):1695–704, 2008.
- [69] G.D. van Albada, B. van Leer, and W.W. Roberts. A comparative study of computational methods in cosmic gas dynamics. *Astronomy and Astrophysics*, 108:76–84, 1982.
- [70] B. van Leer. Towards the ultimate conservative difference scheme. V-A second order sequel to Godunov’s method. *Journal of Computational Physics*, 32:101–36, 1979.
- [71] J.C. Vassberg and A. Jameson. In pursuit of grid convergence, part I: two-dimensional Euler solution. *AIAA Paper*, 2009-4114, 2009.
- [72] J.C. Vassberg and A. Jameson. In pursuit of grid convergence for two-dimensional Euler solution. *Journal of Aircraft*, 47(4):1152–66, 2010.
- [73] D.A. Venditti and D.L. Darmofal. Adjoint error estimation and grid adaptation for functional outputs: Application to quasi-one-dimensional flow. *Journal of Computational Physics*, 164(1):204–227, 2000.

- [74] D.A. Venditti and D.L. Darmofal. Grid adaptation for functional outputs: application to two-dimensional inviscid flows. *Journal of Computational Physics*, 176(1):40–69, 2002.
- [75] D.A. Venditti and D.L. Darmofal. Anisotropic grid adaptation for functional outputs: application to two-dimensional viscous flows. *Journal of Computational Physics*, 187(1):22–46, 2003.
- [76] M. Widhalm, L. Brezillon, C. Ilić, and T. Leicht. Investigation of adjoint-based gradient computation for realistic 3D aero-optimization. *AIAA Paper*, 2010-9129, 2010.
- [77] N.K. Yamaleev, B. Diskin, and K. Pathak. Error minimization via adjoint-based anisotropic grid adaptation. *AIAA Paper*, 2010-4436, 2010.